九州大学学術情報リポジトリ
Kyushu University Institutional Repository

Development of Novel Near-Infrared Light Responsive Metal-Organic Frameworks Based on N-Confused Porphyrin

楊, 雨峰

https://hdl.handle.net/2324/2236189

出版情報：九州大学, 2018, 博士（工学）, 課程博士
バージョン：
権利関係：

Doctoral Thesis

Development of Novel Near-Infrared Light Responsive Metal-Organic Frameworks Based on N-Confused Porphyrin

N-混乱ポルフィリンを基体とした近赤外応答性を有する金属有機構造体の開発

楊　雨峰

2019.01

Content

Content i

Chapter 1. Introduction 1

1.1 Metal-Organic Frameworks 1

1.1.1 MOFs as Active Catalysts 1

1.1.2 MOFs as Photosensitizers 3

1.1.3 MOFs as Anion Sensor 3

1.1.4 Hybrid MOFs 4

1.2 Porphyrin 8

1.2.1 Metalloporphyrin as Catalyst 10

1.2.2 Metalloporphyrin as Photocatalyst 11

1.2.3 Metalloporphyrin as Photosensitizers for Photodynamic Therapy 12

1.2.4 Porphyrin Derivatives for Anion-Binding 13

1.2.5 MOFs Based on Porphyrins 14

1.3 N-Confused Porphyrin (NCP) 17

1.3.1 NCP as Catalyst 19

1.3.2 NCP as Anion Receptor 20

1.4 Anion Transporter 20

1.4.1 Common Anions in Human Body 20

1.4.2 Transmembrane Transport of Ions 23

1.4.3 Synthetic Transport System 25

1.4.4 Design for Anion Transporter 29

1.5 Overview of This Thesis 31

References 32

Chapter 2. Synthesis and Properties of Metal-Organic Frameworks Based on N-Confused Porphyrin 36

2.1 Introduction 36

2.1.1 Zirconium MOFs 36

2.1.2 Porphyrin as Organic Ligands 36

2.1.3 Purpose of This Chapter 38

2.2 Synthesis of MOFs Based on NCP....39
2.2.1 Synthesis of NCP Ligand....39
2.2.2 Synthesis of MOFs....39
2.3 Characterization....40
2.4 Porosity....42
2.5 Stability of Zr-MOFs....43
2.5.1 Thermostability....43
2.5.2 Chemical Stability....44
2.6 Optical Properties....45
2.7 Conclusion....46
2.8 Experimental Section....47
2.8.1 Materials and Instruments....47
2.8.2 Synthesis of Ligand....47
2.8.3 Synthesis of Metal-Organic Frameworks....50
2.8.4 Characterization....50
2.9 Supporting Data....51
References....55
Chapter 3. Hierarchical Hybrid Metal-Organic Frameworks: Tuning the Visible/Near Infrared Optical Properties by Combination of Isomeric Porphyrin Ligands....57
3.1 Introduction....57
3.1.1 MOFs Based on N-Confused Porphyrin....57
3.1.2 Hybridized MOFs....58
3.1.3 Purpose of This Chapter....59
3.2 Synthesis of Hybrid MOFs....59
3.2.1 Synthesis of Porphyrin Ligands....59
3.2.2 Synthesis of MOFs and Characterization....60
3.3 Porosity....65
3.4 Thermogravimetric Analysis....66
3.5 Photophysical Properties....67
3.6 Photoinduced Singlet Oxygen Generation....74
3.7 Conclusion....76
3.8 Experimental Section....76

3.8.1 Materials and Instruments 76
3.8.2 Synthesis of Hybrid MOFs 77
3.9 Supporting Data 79
References 83
Chapter 4. Dissecting the Chloride–Nitrate Anion Transport Assay 85
4.1 Introduction 85
4.1.1 Binding Affinity—Hofmeister Series 85
4.1.2 Transport Selectivity 85
4.1.3 Purpose of This Chapter 88
4.2 Molecular Design and Synthesis of Anion Transporters 88
4.3 Binding affinity 89
4.4 Transport Selectivity 90
4.4.1 Transport Selectivity Analysis 90
4.4.2 Theoretical Calculation 93
4.5 Conclusion 94
4.6 Experimental Section 94
4.6.1 General 94
4.6.2 Synthetic Procedures 95
4.6.3 Ion Selective Electrode (ISE assay) 97
4.6.4 HPTS Assay 97
4.6.5 Osmotic Assay 98
4.7 Supporting Data 100
4.7.1 Characterization of Compounds 100
4.7.2 Titration Experiments and Calculation of Binding Constants 101
4.7.3 Transport Kinetic Results 107
References 121
Chapter 5. Conclusion 124
List of Publication 126
Acknowledgment 127

Chapter 1. Introduction

1.1 Metal-Organic Frameworks

Metal-Organic Frameworks (MOFs) are a type of porous coordination polymers constructed through the coordination of organic ligands and metal ions (Figure 1-1).[1] Due to the high porosity, stability and flexible design by changing the building units, it is considered extremely versatile materials with high potential in the filed of catalysis[2], gas storage[3], sensors[4], photosensitizers[5] and so forth.

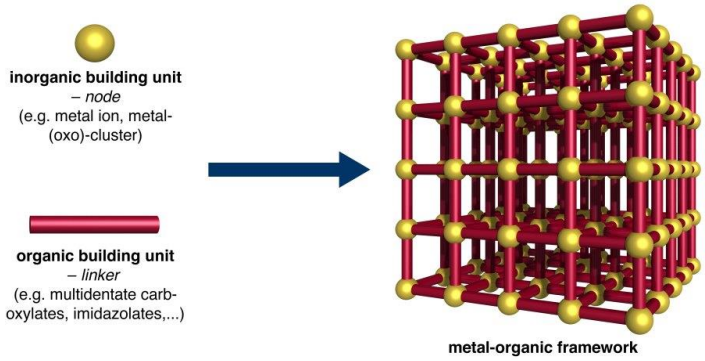

Figure 1-1. The process of MOF synthesis.[1a]

As one of the porous materials, MOFs have demonstrated the flexibility in topology and function directed structure design by varying the building block of organic ligands or metal ions, which has hardly been reported in other porous materials like zeolite.[6] For example, by simply varying the molecular size, the surface area of the MOFs can be tuned, leading to a higher gas intake volume.[7]

1.1.1 MOFs as Active Catalysts

As a porous material, one of MOFs' applications is catalysis due to the high intake of guest molecules in the pores, which are not only the catalyst molecules but also the substrates. Especially, in the case of a gas reaction, due to the high gas storage ability, MOFs with great stability and recyclability are considered to be the next green heterogeneous catalyst for gas reaction.[2]

In this application, MOFs can function as both the reactor where catalyst and substrates are adsorbed at high concentrations and the catalyst with the active center to conduct a chemical reaction. The crystalline structure also provides MOFs with an assured high reactivity, which cannot be found in amorphous structure due to the random morphology where catalyst molecules are likely to react with substrates insufficiently. For example, Yaghi and coworkers have applied MOF-47 and MOF-48 in the catalysis of the oxidation reaction of methane to acetic acid in the presence of $K_2S_2O_8$ and carbon oxide. In comparison with the reaction without

the application of MOF, the turnover number increased more than two-fold.[8] (Figure 1-2)

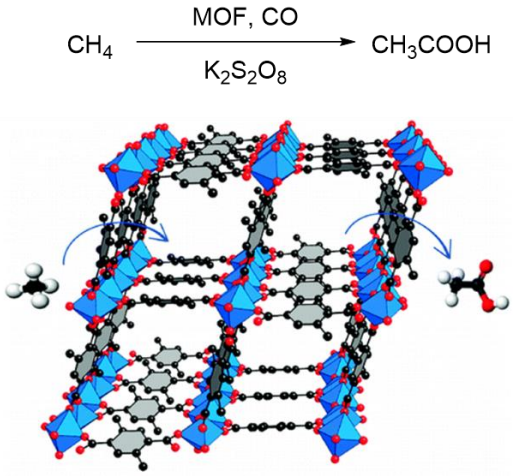

Figure 1-2. Catalysis of CH_4 to acetic acid in the presence of CO in MOF-48.[8]

Hong-Cai Zhou and coworkers synthesized PCN-700 using zirconium as the metal center due to its catalytic reactivity. They revealed that the catalytic reactivity of MOFs highly depends on their pore sizes by synthesizing the MOF using various organic ligand to obtain a switchable MOF. In this report, PCN-700 was applied in a reduction reaction of carbon dioxide, where Zr(IV) is the active site. Compared with $ZrCl_4$, the turnover number increased 1.5-fold. In addition, it was found that pores of PCN-700 shrink when it is desolvated, with the catalytic reactivity decreasing drastically. After treatment of solvent along with acid, the pores recovered and high reactivity was observed, leading to a switch in the catalytic activity. The authors explained that the difference in the catalytic activity results from the variation of the diffusion rate of the substrate in the pores.[9] (Figure 1-3)

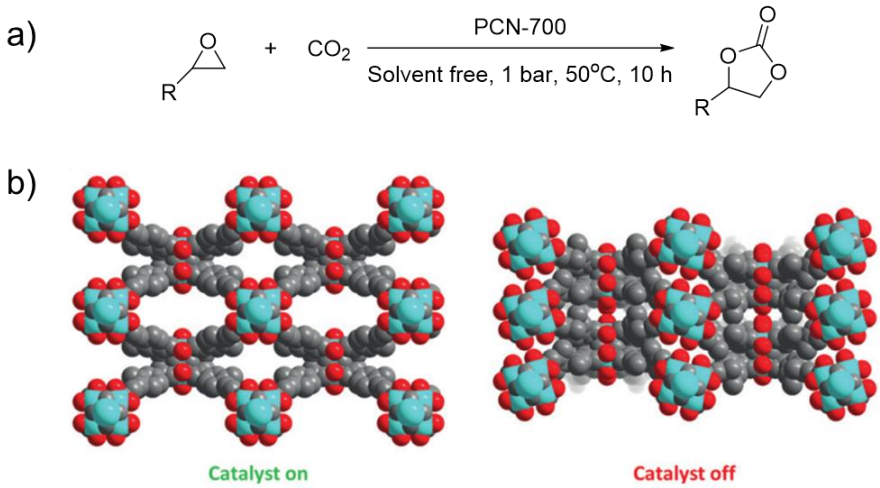

Figure 1-3. a) The reduction of carbon dioxide with epoxide in the presence of PCN-700, b) the catalyst on and catalyst off state of PCN-700.[9]

1.1.2 MOFs as Photosensitizers

MOFs have been utilized as highly efficient photosensitizers. With a crystalline morphology, MOFs are considered to have the potential to function in a solar cell or photocatalyst where crystallinity and hierarchical topology are found necessary for the electron transfer between various phases. In addition, the close distance between organic ligand and the metallic active center allows the efficient electron transit after it is excited in the organic ligand, which is another advantage of MOFs as the photosensitizer.[10] Thus, with an appropriate choice of organic ligand, fast electron transfer from ligands to metals occur after the ligand is irradiated, followed by the electron transit between the hierarchical structure to the edge of the MOFs. The difference of potential is induced, which then can be used in other devices in the presence of a suitable conductor.

For example, Lin and coworkers synthesized MOFs using derivatives of $[Ir(ppy)_2(bpy)]^+$ and $[Ru(bpy)_3]^{2+}$ with nickel-containing polyoxometalates ($[Ni_4(H_2O)_2(PW_9O_{34})_2]^{10-}$) in the pores as the guest and active site. The two organic ligands (**$[Ir(ppy)_2(bpy)]^+$** and **$[Ru(bpy)_3]^{2+}$**) are both effective photosensitizers that have been reported to be applied in solar cell, organic light emitting diode (OLED) and so forth. The excitation of electrons occurs once irradiated with visible light. Then the excited electrons transfer to the polyoxometalates, resulting in a water-splitting reaction to give H_2 effectively.[10a] (Figure 1-4)

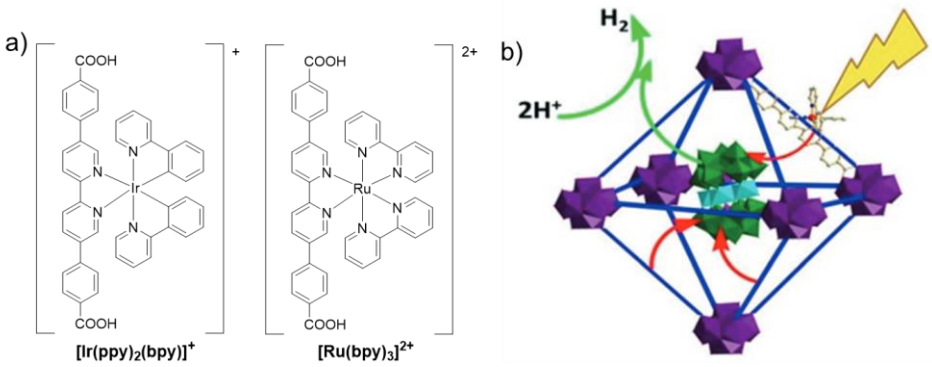

Figure 1-4. a) The structures of the organic ligands ($[Ir(ppy)_2(bpy)]^+$ and $[Ru(bpy)_3]^{2+}$) used in the MOF synthesis. B) Water splitting reaction under light irradiation in the presence of MOF.[10a]

1.1.3 MOFs as Anion Sensor

MOFs are also considered to be one good material for sensing due to the high intake of guest molecules such as gas and organic solvents. With an organic ligand responsive to the environmental changes in the pores resulting from various gas molecules, output signals such as absorption or fluorescent spectral changes are detected, which is a common idea for sensor design based on MOFs. Surprisingly, MOFs have also been researched as chemical sensors for species such as anions, cations and so forth.[4] This features again shows the flexibility and infinite possibility for MOFs as highly crystalline materials.

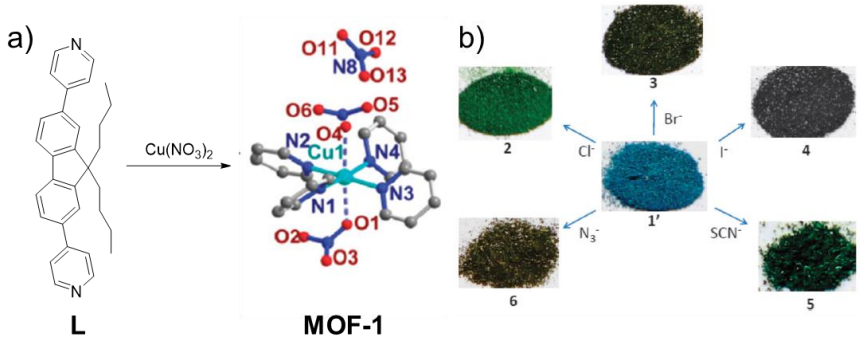

Figure 1-5. a) Synthesis of **MOF-1** by ligand **L** and Cu^{2+}, b) color change resulted from the anion exchange.[11]

For instance, Dong and coworkers synthesized **MOF-1** using fluorene-based ligand L and Cu^{2+}. **MOF-1** was found to be a two-dimensional non-interpenetrating net containing extra NO_3^- in the pore, which can be exchanged by other anions. After being soaked in aqueous solutions of different anionic salts, the anion exchange reaction occurs with an obvious color change, which is found to be related to different interactions with the ligand fluorene.[11] (Figure 1-5)

These examples have demonstrated the potential of MOFs as functional materials, in addition to the significant role that organic ligands play in the dynamically responsive MOFs.

1.1.4 Hybrid MOFs

So far, the flexibility of MOFs has been discussed by introducing the design and variation of building blocks. Whereas there is more than one way to functionalize MOFs. Hybridization is one of the widely used methods to design highly functional MOFs.[12] Hybridization is simply a synthesis of MOFs with more than one component. For example, MOFs containing two or more types of metal center or organic ligands are one of hybrid MOFs. With more components included in the frameworks, new topology or dynamic process involving two different components other than the interactions between metal centers and ligands.

Kitagawa and coworkers have studied the researches on hybrid MOFs till this year and classified them into three classes as is shown below.[12] (Figure 1-5)

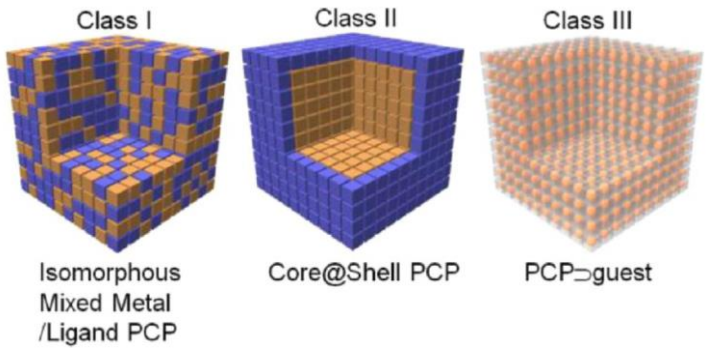

Figure 1-6. Reported hybrid MOFs so far.[12]

Class I is MOFs with two or more metal centers or organic ligands randomly distributed inside. It requires the components to be structurally similar to obtain a perfect crystallinity. This type seems the easiest to synthesize by simply mixing all the components. However, by innovative design and discrete fabrication, novel structures like 2D-MOF pillared by another type of organic linker can be achieved. Another advantage of hybridization is the utilization of the interaction between the two components inside. For example, Lee and coworkers synthesized a class I hybrid MOF using Zn-porphyrin and pyrene as the organic linkers. Due to the excellent photophysical properties and the overlap between the emission of pyrene and the absorption of porphyrin, an efficient energy transfer occurs when the MOF is irradiated, resulting in increasing light-harvesting properties at the visible light region, and thus a high efficiency of singlet oxygen generation.[13] (Figure 1-7)

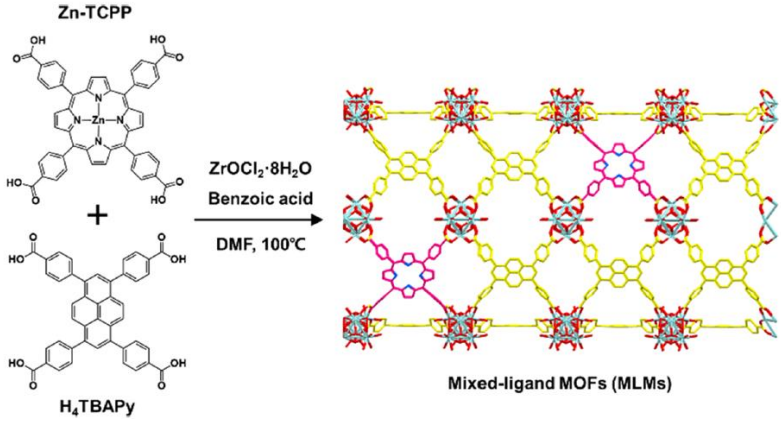

Figure 1-7. Synthesis of class I hybrid MOF with Zn-porphyrin and pyrene as the organic linkers.[13]

In another report, Zhou and coworkers synthesized hybrid MOF also using porphyrin and 1,2-bis(2-methyl-5-(pyridin-4-yl)thiophen-3-yl)cyclo-pent-1-ene (BPDTE). The photoinduced switching properties of BPDTE (open and close) and the overlap between absorption of porphyrin and emission of close BPDTE provides the hybrid MOF with a dynamic switching function. The switchable singlet oxygen generation was achieved by irradiation of UV and visible light to turn on and off.[14] (Figure 1-8)

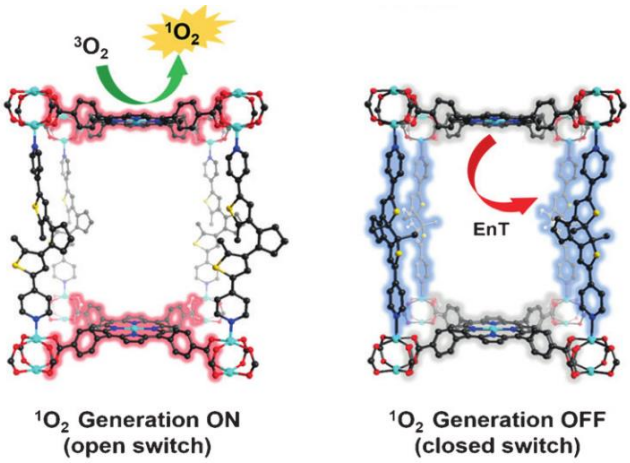

Figure 1-8. Switch-on and off of the singlet oxygen generation of hybrid MOF.[14]

Class II is a MOF possessing core/shell structure. This type requires special synthesis method such as seed-mediated synthesis. A seed-mediated synthesis is widely used to synthesize phase-pure particles or core/shell structure. The mechanism of the method is to put a crystalline particle in a reaction as a seed crystal to grow shell phase on the surface[12]. (Figure 1-9).

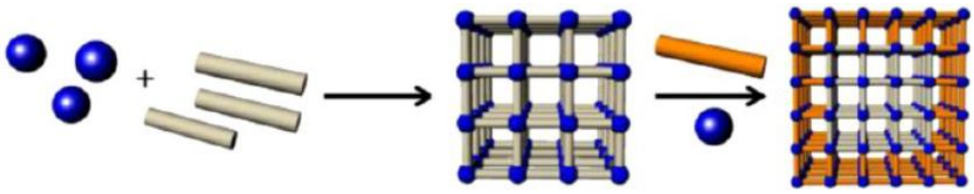

Figure 1-9. Schematic illustration of seed-mediated synthesis.[12]

Core/shell structure has the advantages of simplicity in structure characterization. The higher-level hierarchical structure gives a challenge of function-directed topology design. However, the core does not need to be MOF necessarily. Other crystalline nanoparticles can be included inside the pore. For example, a nanoparticle capable of converting low-energy light to high energy light efficiently ($NaYF_4$: Yb, Tm) was included in MIL-53, a MOF possessing Fe as the metal center. The upconversion properties allow the core to convert near-infrared (NIR) with long wavelength to UV-vis with a short wavelength, which is then absorbed by MIL-53 through energy transfer. This design demonstrated a new possibility of MOF as an optical unit.[15] (Figure 1-10)

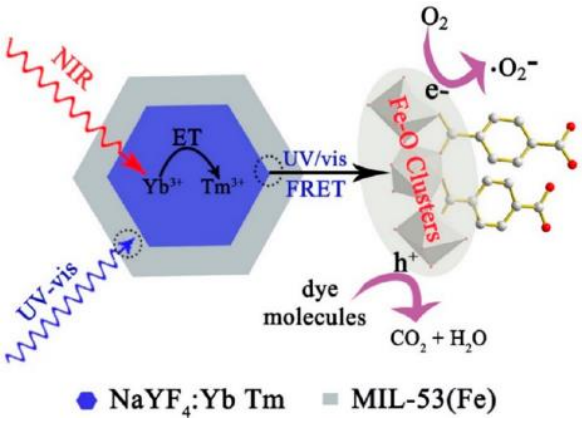

Figure 1-10. Upconversion of the core nanoparticle and energy transfer between core and shell in the Class II hybrid MOF.[15]

Class III is MOFs with other particles inside the pores. Unlike class I and II which have other components engraved in the composition, class III has the host-guest chemistry which highlights the porosity of MOFs.[16] In the class III hybrid MOFs, the storage and transport functions are valued and studies have been conducted so far. For instance, ZJU-28⊃cationic dyes are fabricated. By introducing a red-light-emitting dye 4-(*p*-dimethylaminostyryl)-1-methyl-pyridinium (DSM) and a green-light emitting dye acriflavine into the pores of blue light emitting MOF, a white light emitting hybrid MOF was facilitated, which also offers a simple mechanism of white light emitting material design.[17] (Figure 1-11)

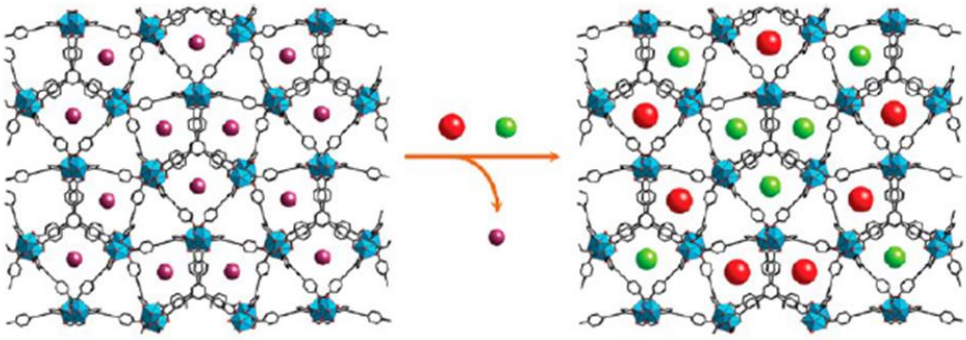

Figure 1-11. Organic dyes are encapsulated in ZJU-28.[17]

In another report, sulfur was confined in MOF-525 to give high-performance lithium-sulfur batteries. The rigid structure of MOF-525 with effective Lewis acidic sites are chosen to encapsulate polysulfides (Li_2S_8, Li_2S_6, Li_2S_4, and Li_2S_3) and prevent them from dissolving into the electrolyte in order to maintain the high energy density and capacity. Metalloporphyrin in MOF-525 provides the central metal to stabilize the polysulfides.[18] (Figure 1-12)

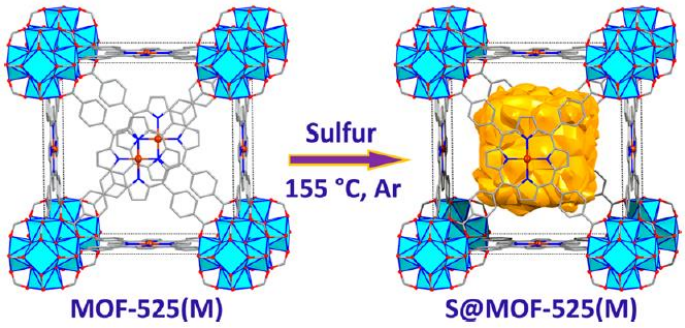

Figure 1-12. Schematic illustration of S@MOF-525 synthesized through the melt-diffusion method at 155 °C under an Ar atmosphere.[18]

So far, hybridization has been an attracting method to design novel functional MOFs. By incorporating various functional building unit or guest molecules, high performance can be facilitated intentionally. In this thesis, the author focuses on the variation that the organic ligand brings to MOFs, and has chosen porphyrin and its isomer to construct novel MOF and studied its properties. Porphyrin will be introduced in the next section.

1.2 Porphyrin

Porphyrins are a series of organic compounds consisting of four pyrrole rings bonded by four sp^2 hybridized carbons (*meso*-position) as shown in Figure 1-13. The discovery of porphyrin can be dated back to 1867 when Scherer extracted an unknown purple-red fluid from dried blood powder with concentrated sulfuric acid. Since then, other existence of porphyrins has been found and their structure has been studied. For example, the porphyrin-like structure was also founded in chlorophyll as a magnesium complex in 1884 by Hoppe Seyler.[19] (Figure 1-13)

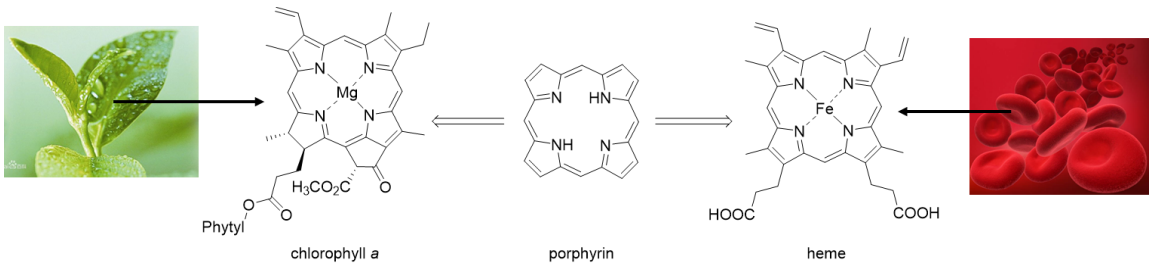

Figure 1-13. The structure of porphyrin (middle), heme (right) and chlorophyll *a* (left).

The name of porphyrin is from a Greek word “porphura”, meaning purple because the solid of porphyrin is usually purple-red in color. In 1883, the spectroscopic feature of porphyrin was studied. Swiss chemist Jacques-Louis Soret found the strong absorption at around 400 nm for hemoglobin. Therefore, this absorption band is still called the Soret band. From 500 to 700 nm, there are also four small absorption peaks called Q

bands. Q bands come from the forbidden excitation starting from ground state (S_0) to the first excited state (S_1), unlike Soret band (from S_0 to S_2).[20] Porphyrins have also been found to be fluorescent molecules, from which the strong decay from S_1 to S_0 was observed due to a rapid internal conversion from S_2 to S_1. (Figure 1-14)

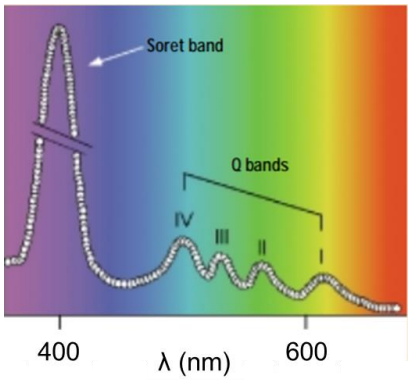

Figure 1-14. Normal UV/vis absorption spectrum of porphyrin.[21]

Porphyrin shows a 18π electrons aromatic macrocyclic system. Therefore, it has the typical features like other aromatic molecules, such as high stability, structural planarity, magnetically induced ring currents and averaging of bond lengths. Moreover, with a macrocyclic organic skeleton, porphyrin is capable of coordinating with metal ions in the center to form various stable metal complexes, such as the iron complex in heme and magnesium complex in chlorophyll *a*, which has expanded the porphyrin family. When coordinated with metals, the d orbitals of metal ions, especially metals with d^m (m = 6~9), have significant interaction with porphyrin π orbitals, resulting in a huge change in the spectral features.[20]

In terms of the modification, there are normally two types of position that have been used in the previous reports. One is the β-carbon of pyrroles which are called β-position, the other is the carbon connecting every two pyrrole rings, which is called *meso*-position on porphyrin. Modified porphyrins have been a hot research field in chemistry and material, even in biology and medical science. With the development of porphyrin research, artificial utilization has also caught scientists' attention due to its photophysical properties, singlet oxygen generation ability, metal coordination as well as the flexibility in molecular design and modification. So far, nine ways of modifying and functionalizing porphyrin have been studied (Figure 1-15).

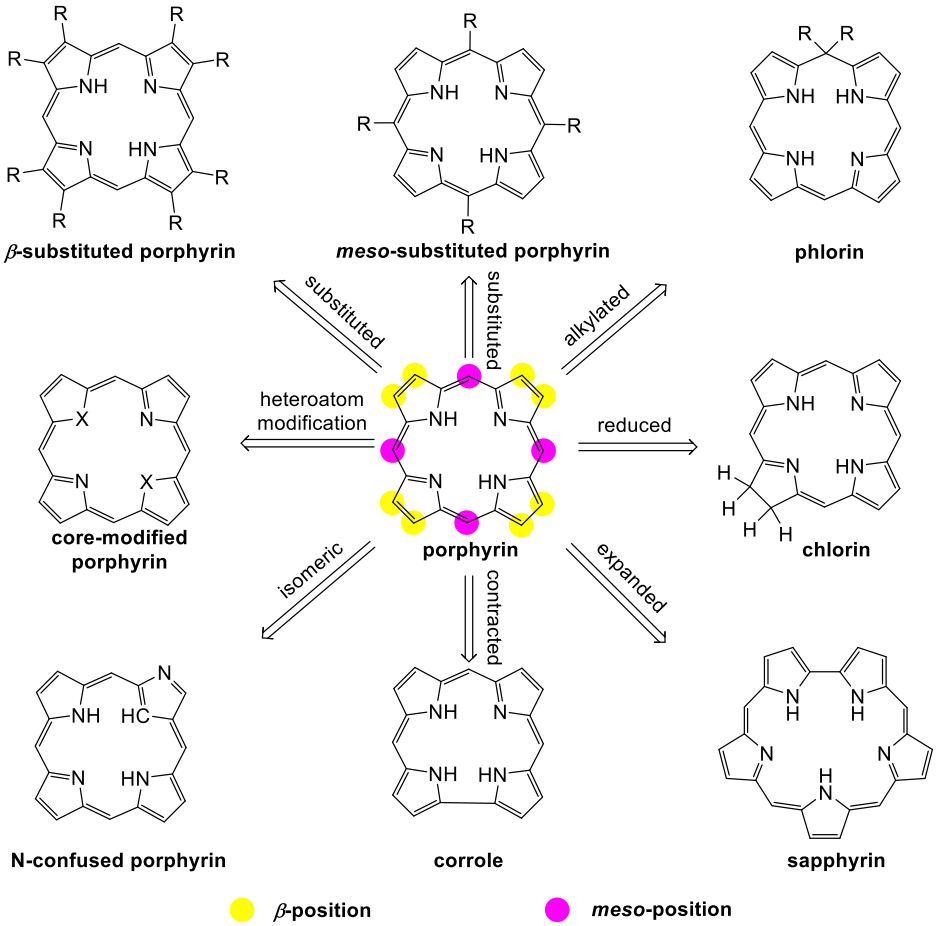

Figure 1-15. Representative modification strategies of porphyrin structure.

After classification, there are four different strategies, which are substitution, backbone modification (core modification and N-confusion), expansion or contraction, and reduction. They have all been proved very effective in novel functional molecule design. In this chapter, a few applications of porphyrin will be introduced.

1.2.1 Metalloporphyrin as Catalyst

It has been a field with a long history to use metalloporphyrin as catalysts. The two amine N atoms and two imine N atoms at the center make porphyrin a quadridentate divalent ligand that can stabilize many types of ions. The planarity and symmetry provide porphyrin complex with the ability to further coordinate with axial ligands, with the help of which, more metal ions can be stabilized. In the application of catalysis, metal center is essential to adsorb the substrate to induce chemical reactions.

Dehydrogenation is one of the reactions that need the catalyst of metal ions. Due to the industrial significance, many catalysts based on non-noble metal have been developed, including the ones coordinated with porphyrin ligands. Recently, Chen and coworkers reported the dehydrogenation and aromatization of

9,10-dihydroanthracene and other organic chemicals.[22] In the paper, they elucidated the reaction pathway as shown below (Figure 1-16).

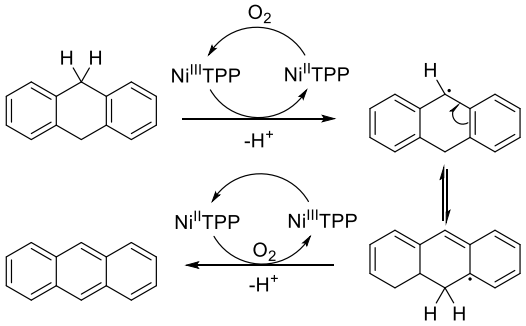

Figure 1-16. A possible reaction pathway for the aerobic dehydrogenation of 9,10-dihydroanthracene.[22]

Among various metalloporphyrins (MTPP, M = Ni, Fe, Co, and Cu), NiTPP demonstrated the highest catalytic activity, because Ni(II) was first oxidized to Ni(III) which was considered a highly reactive chemical species due to the electron deficiency character and the tendency to accept single electron during the activation of the substrate. NiTPP was also proven versatile toward various substrates. In terms of stability, NiTPP remained its structure after the reaction by spectral monitoring.

1.2.2 Metalloporphyrin as Photocatalyst

A photocatalyst is also a type of catalyst, which is only activated when it is irradiated. The energy from irradiation can facilitate more reaction that requires high activation energy. An optimal photocatalyst must meet the following requirements: 1) having a bandgap that absorbs light in the visible range; 2) remaining stable when given light; 3) non-toxicity (environmental friendliness); 4) being abundant and easily processable into a desirable shape.[23]

Inspired by the natural photocatalysts such as chlorophyll a, artificial photocatalysts have been researched and even put into actual use so far. As derivatives of chlorophyll *a*, porphyrins have received much attention. When used as a photocatalyst, porphyrins have a huge advantage—high absorbance in the visible light region. Although in most reports, porphyrins are used as photosensitizers, the high absorbance and suitable bandgaps also function well with many inorganic semiconductors in photocatalysis. Besides, the flexibility in molecular design enables researchers to incorporate porphyrins into many materials through physical adsorption or chemical bonding.

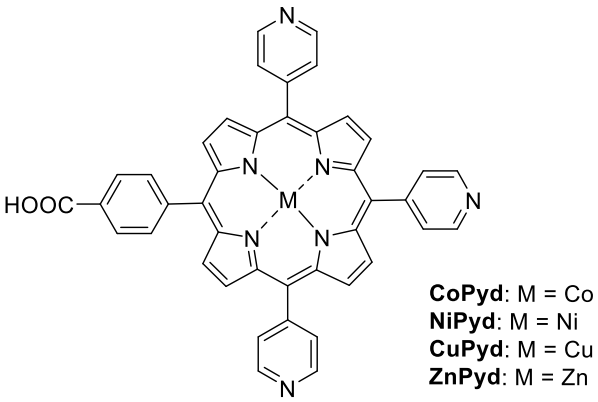

Figure 1-17. Structures of **MPyd**s.[24]

Lately, Zhou and coworkers reported the effects of the central metal ions on the photosensitization of metalloporphyrins (**MPyd**s, M = Co, Ni, Cu, and Zn), in which **MPyd**s are adopted onto Pt-loaded carbon nitride (C_3N_4) for visible light responsive H_2 reduction from water splitting[24] (Figure 1-17). **ZnPyd** exhibited the highest apparent quantum yield (AQY). By measuring the transient photocurrent curves of **MPyd**s/C_3N_4 suspensions when irradiated by visible light, the same order of photocurrent as the photocatalytic activity was obtained (**CoPyd** < **NiPyd** < **CuPyd** < **ZnPyd**). It is also confirmed that by adding Pt-loaded C_3N_4 into the DMF solution of **MPyd**s, the emission intensities were quenched and decay lifetimes decreased in the same order, suggesting an increased electron injection rate according to the migration path from **MPyd** molecules to C_3N_4. Experimental results showed that all these metal complexes have more negative LUMO level, which means excited electrons transferring from the photosensitizers into the conduction band of C_3N_4 is feasible. Nevertheless, theoretical calculation pointed out that **ZnPyd** is easy to conduct MLCT which helps the charge further transfer to C_3N_4, while others show more inclined to conduct LMCT.

1.2.3 Metalloporphyrin as Photosensitizers for Photodynamic Therapy

Photodynamic therapy (PDT) is a relatively new type of cancer treatment that utilizes the reactive oxygen species (ROS) excited by PDT photosensitizer through light irradiation to selectively kill cancer cells. For the purpose of improvement of patients' quality of life (QOL), it is considered a promising novel cancer treatment. In the last century, many countries, including US, Japan, have approved PDT in the public medication, and PDT has been researched and used in the treatment of skin diseases, cancers and so forth.[25]

Porphyrin (Phlorin or porfimer sodium) is one of the commonly used PDT photosensitizers due to its strong light-harvesting ability and singlet oxygen (one of ROS) generation ability resulted from the long decay lifetime. Therefore, triplet oxygen is excited to singlet oxygen through a fluorescence resonance energy transfer (FRET). However, the low efficiency and the photosensitivity disorders after the operation have been the main factors keeping PDT from being put into more practical cancer treatment. Hence, the development

of novel PDT photosensitizer has been the main research focus[26].

In 2015, Ventura and coworkers reported a novel conjugation system based on porphyrin that is capable of two-photon absorption and singlet oxygen generation (Figure 1-18).[27] The molecular design is to conjugate Zn-porphyrin (ZnP) to diketopyrolopyroles (DPPs), a molecule attracting attention for its high stability and light-harvesting. It has been reported that DPP is also capable of two-photon absorption, thus the application of DPP in dye-sensitized solar cell (DSSC) was studied. By conjugating DPP to porphyrin, a PDT system capable of two-photon absorption can be constructed. Consequently, the two molecules both demonstrated two-photon absorption and phototoxicity under irradiation at 910 nm.

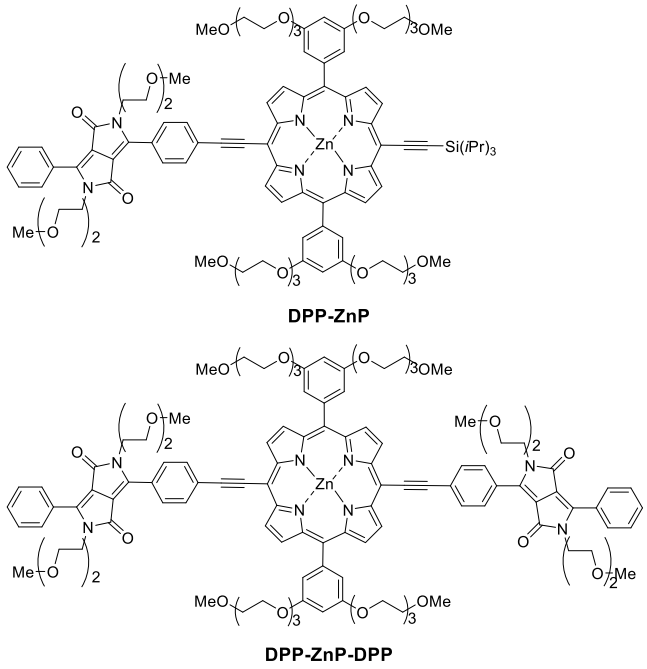

Figure 1-18. Structure of the DPP-porphyrin conjugates.[27]

So far, the defect of porphyrin has caught researchers' attention, which is the absorption in visible light is not suitable for practical use such as PDT or DSSC[28] due to the weak penetration of visible light in human body and the consumption of much energy. Therefore, modification of porphyrin has been a major research focus.

1.2.4 Porphyrin Derivatives for Anion-Binding

Another application of porphyrin and its derivatives is anion binding.[29] A strong anion receptor is considered having potentials to be used as anion probe or transporter in terms of diagnosing and treating diseases, thus new molecular designs have been studied so far. As an aromatic compound possessing 18π-electrons, porphyrin shows theoretical anion binding after protonation through hydrogen bond of four NH

moieties. Whereas due to the small ring size, it is difficult to realize with porphyrin scaffold. Thus, instead of porphyrin, expanded porphyrin or reduced porphyrin have been developed.

Sapphyrin, one of the expanded porphyrin family, was studied for its anion binding ability (Figure 1-19) in the early 1990s.[30] This receptor was also found to bind with Cl^- and Br^-. In this case, protonation increased the H bonding donor, and enhance the binding through electrostatic interaction.

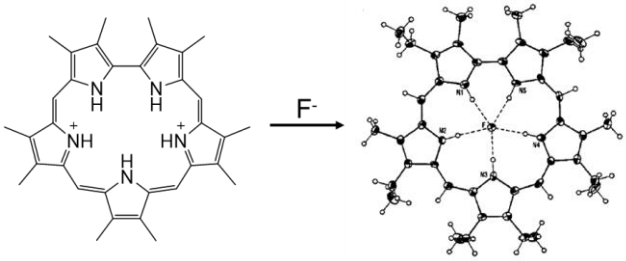

Figure 1-19. Fluoride binding using protonated sapphyrin.[30]

Another strategy is to use reduced porphyrin backbone such as calixpyrrole **1** (Figure 1-20).[31] By reduction, the molecule loses its aromaticity and planarity in structure, whereas the pyrrole moieties obtain the ability to rotate in the direction of the α-α position. In this case, by strapping the molecule with an alkyl chain containing a single 1,2,3-triazole group, the molecules (**2**-**4**) demonstrated high affinity and selectivity toward F^- over other halides. The triazoles have been confirmed to be an effective H bonding donor, thus the molecules have a high binding affinity.

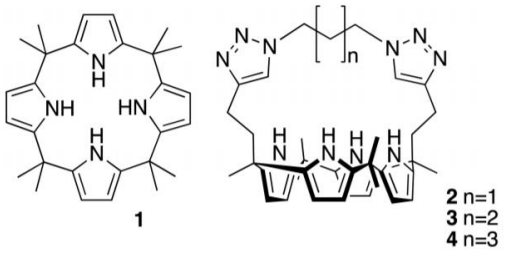

Figure 1-20. Structures of the calix[4]pyrroles **1**−**4** used in the selective fluoride binding.[31a]

So far, many anion receptors have been synthesized. However, selectivity toward specific anions has still been a problem. A study related to molecular binding intensity and binding selectivity associated with the structure is necessary for the future study.

1.2.5 MOFs Based on Porphyrins

Porphyrins are a type of well-studied ligands that possess high light-harvesting and emission ability, high

planar and symmetric geometry and metal coordination in the center. Thus, many researchers have shown interests in constructing functional materials based on porphyrin[32].

Porphyrins bearing 4-pyridyl or 4-carboxyl aryl (phenyl) on *meso*-positions are the most commonly used derivatives in MOF synthesis. Since Yaghi and coworkers reported MOF-525[33] based on porphyrin carboxylic acid derivative and zirconium (Zr) metal cluster in 2012, the focus on MOFs based on COO-Zr has continued to thrive. As a metal cluster, Zr exhibits high biocompatibility and low toxicity, which provide the MOF with the applications in vivo. In addition, the strong binding between Zr and COO^- ensures the high stability of the resulting MOFs[34]. In fact, MOF-525 have been reported to exhibit high stability toward organic solvents and acid[33].

Nevertheless, because it takes much time for the reaction to reach its balance, the reaction environment plays a crucial role in affecting the resulting crystallinity and topology. Zhou and coworkers have worked on MOFs based on porphyrin and Zr and developed a series of stable MOFs named PCN-221 to PCN-225 with different topologies[35]. (Figure 1-21)

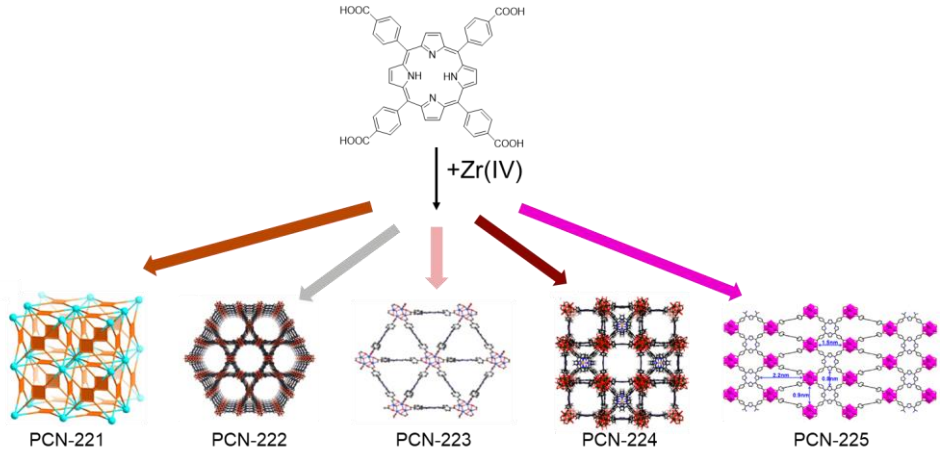

Figure 1-21. Topologies of PCN series of MOFs based on porphyrin and Zr(IV) as the building block.[35]

Table 1-1. Reported synthesis conditions for MOFs based on porphyrin and Zr(IV).

Name	Zr salt	Acid	Solvent	Temperature/°C	Time	Topology
MOF-525	$ZrOCl_2 \cdot H_2O$	HOAc	DMF	65	3 d	**ftw**
PCN-221	$ZrCl_4$	HOAc	DEF	120	12 h	**ftw**
PCN-222	$ZrCl_4$	BA	DEF	120	48 h	**csq-a**
PCN-223	$ZrCl_4$	HOAc	DMF	120	12 h	**shp-a**
PCN-224	$ZrCl_4$	BA	DMF	120	24 h	**she net**
PCN-225	$ZrCl_4$	BA + HOAc	DEF	120	12 h	**sqc net**

Acid: HOAc: CH_3COOH, BA: benzoic acid; Solvent: DMF: *N*,*N*-dimethylformamide, DEF: *N*,*N*-diethylformamide.

As is exhibited in Table 1-1, changes in synthesis conditions lead to a different topology. Nevertheless, in spite of the difficulty in phase pure crystallinity synthesis, porphyrins have demonstrating ability differing from other ligands. Due to all the exciting features mentioned above, porphyrin-MOFs have exhibited high potential in photocatalysis[36], drug delivery system (DDS)[37], photodynamic therapy (PDT) [38] etc.

The center metal coordination ability provides porphyrin with a new site for the introduction of the active site, which has benefit new design for the efficient heterogeneous iron catalyst. PCN-222 (Fe) was reported to exhibit high catalysis toward the oxidation of pyrogallol, mimicking the reaction of peroxidase enzyme. The high catalytic activity results from the high density of active site on the walls of the ultra-large open nanochannel.[35c] (Scheme 1-1)

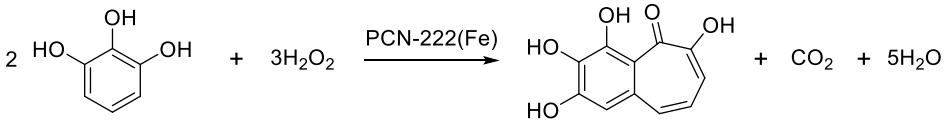

Scheme 1-1. The peroxidase-like oxidation reaction of pyrogallol catalyzed by PCN-222(Fe).[35c]

Furthermore, the strong light-harvesting ability at the visible light region enables porphyrin-based MOFs to function as a stable and crystalline photosensitizer material. **MOF-2** was synthesized with Ni-porphyrin and Ni as building blocks. While the monomer Ni-porphyrin was found to demonstrate no photocatalytic activity toward the reduction reaction of nitrobenzene, high activity was observed from with **MOF-2** as the catalyst under irradiation at 421 nm.[39] (Scheme 1-2)

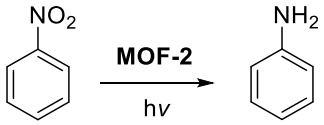

Scheme 1-2. Photoreduction reaction with the catalysis of porphyrin-based Ni(II) **MOF-2**.[39]

Lastly, the singlet oxygen generation ability has gained porphyrin-MOFs much attention as a new generation of photosensitizers for PDT. As is mentioned before (at section **1.1.3**), porphyrin is currently commercially available and permitted in the real use of on human treatment. However, the low solubility in an aqueous environment and low photostability have limited its further application. Researches have been conducted further study to address the problems, to which MOFs are considered to be the solution as MOFs possesses high stability and flexibility resulting from the crystalline structure. The rigid structure is found to benefit a stable oxygen excitation due to little aggregation observed.[40] As one of the typical MOFs possessing porphyrin as an organic ligand with an ultra large surface area, PCN-222 was experimented for its singlet oxygen generation ability[38]. $^1O_2$ was detected under visible light irradiation at high efficiency.[38] In the

experiment, photodegradation of bisphenol A (BPA) by $^1O_2$ generated from PCN-222 was conducted. (Figure 1-22) The reaction was conducted five times and the removal efficiency of BPA still remains 99.2%, demonstrating high photocatalytic activity and photostability of PCN-222.

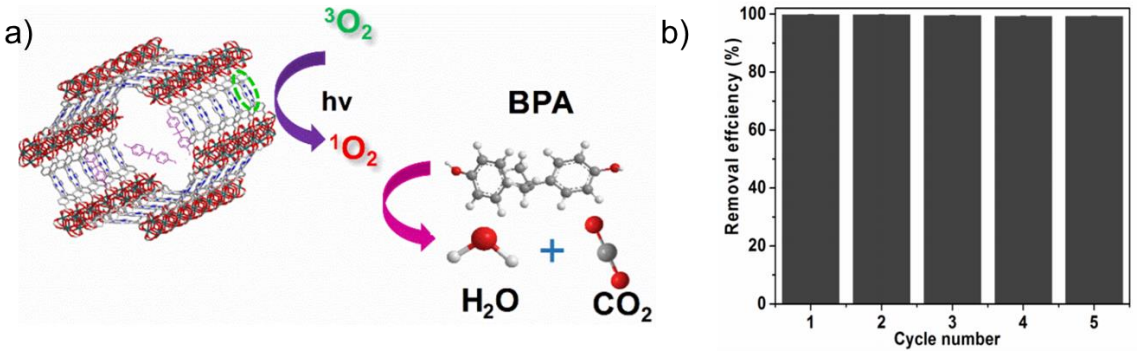

Figure 1-22. a) The proposed mechanism of photodegradation of BPA by $^1O_2$ with PCN-222; b) Removal efficiency of BPA after five-time photocatalysis.[38]

1.3 N-Confused Porphyrin (NCP)

N-confused porphyrin (NCP) is one of the porphyrin (TPP) isomers that has the pyrrolic moiety connected to the surrounding meso-carbons at the *α*- and *β*-positions (Figure 1-9).[41] Although NCP has the same backbone as porphyrins, new properties were also demonstrated attributing to the confused pyrrolic moiety. Those new properties are introduced as followed.

First, as shown in Figure 1-23, because of the periphery N atom, the tautomerism of N atoms leads to two different isomers, which are also called 3H form and 2H form according to the number of H atoms in the center.[42] The tautomerism occurs when the polarity of the chemical environment changes, which also changes the aromaticity of the molecule. By the observation of UV/vis spectra, one can differentiate them from due to the change in the absorption spectra. In highly polar solvents such as *N*,*N*-dimethylformamide (DMF) or dimethyl sulfoxide (DMSO), 2H form dominates while in lowly polar solvents such as dichloromethane (DCM) or chloroform, 3H form takes over. Because of its capability of taking these two metastable forms, NCP has a high potential in stabilizing metal ions in the highly oxidized state, which also makes NCP metal complexes more reactive catalysts due to the high reactivity of highly oxidized species.

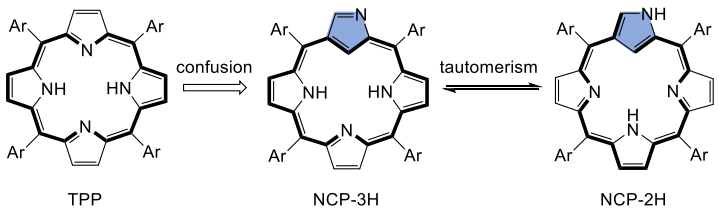

Figure 1-23. Structures of porphyrin and N-confused porphyrin and its NH-tautomerism.

Moreover, with a carbon atom introduced to the aromatic conjugation ring, a perturbation is brought to the electronic structure of the molecule due to different electronic negativities, leading to a decrease in the HOMO-LUMO bandgap.[43] Hence, the absorption and emission spectra of NCP was red-shifted compared with those of TPP (Figure 1-24).

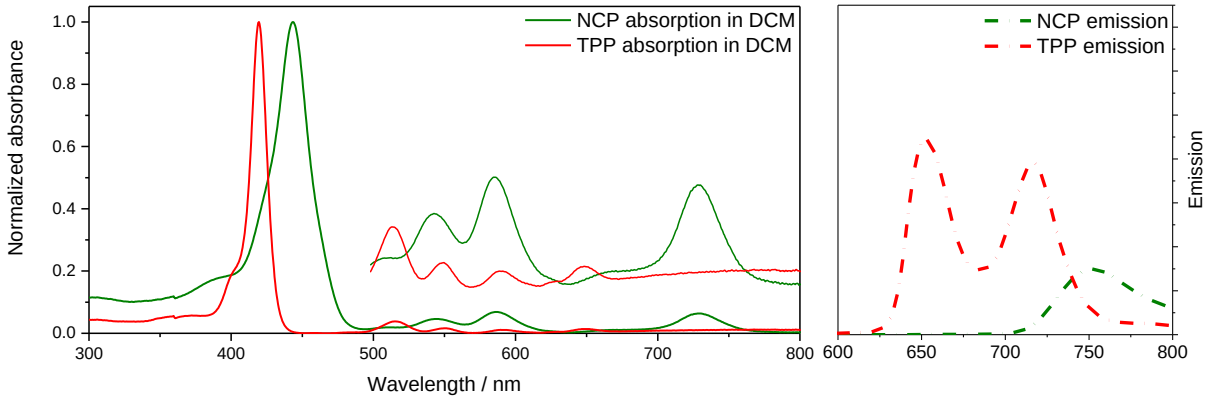

Figure 1-24. Absorption and emission spectra of TPP (red) and NCP (green) in DCM. (TPP: λ_{ex} = 420 nm, NCP: λ_{ex} = 444 nm)

Lastly, with a carbon atom facing inside the center, when coordinated with metal ions, NCP shows unique reactivity, leading to a different metal complex from the one formed by porphyrin. In the reaction, central carbon is deprotonated to carbon ion, which then coordinates with metal ions. Thus, metals without strong basicity are not capable of this reaction, resulting in a tridentate macrocycle.[44] For example, when reacted with zinc acetate, a dimer is formed bridged by two zinc acetate molecules. Then further reaction in alkali gives an intermediate of tridentate zinc complex, which is not stable and then form a dimer or coordinates with other ligands due to the quadridentate nature of zinc.[45] (Figure 1-25)

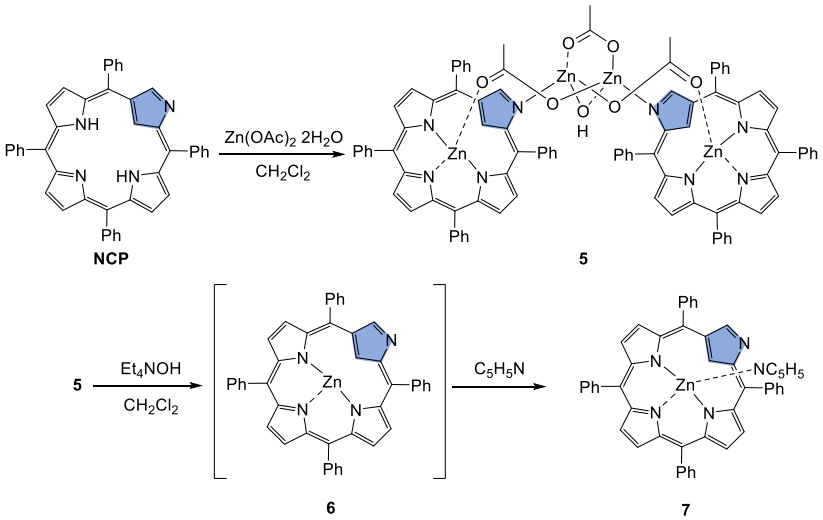

Figure 1-25. The reaction between NCP and zinc acetate.[45]

As a result of the tautomerism, different from its porphyrin isomer, NCP turns to a quadridentate trivalent ligand. Coordinated with metal ions, the center carbon anion bonds with the cation even stronger than nitrogen as it shows organometallic nature, leading to a covalent carbon-metal bond. The strong bond between carbon and metal stabilizes metal ion even in a higher oxidation state. Hence, many high oxidation state metal complexes have been reported so far. For example, NCP copper complex is usually copper (II), whereas it can be readily oxidized to copper (III) with 2,3-dichloro-5,6-dicyano-1,4-benzoquinone (DDQ) as the oxidant.[46] (Scheme 1-3)

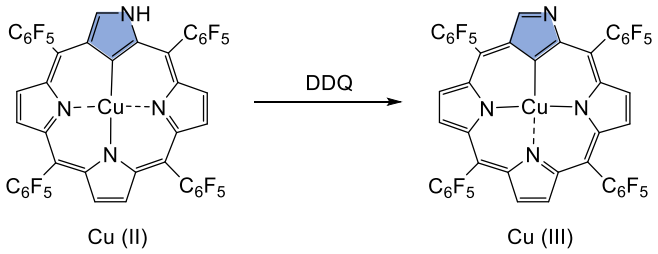

Scheme 1-3. The oxidation of Cu(II)-NCP to Cu(III)-NCP.[46]

1.3.1 NCP as Catalyst

Metalloporphyrin is a promising catalyst candidate due to the stabilization of center metal ion resulting from the coordination with the quadridentate macrocycle. As an isomer of porphyrin, NCP is also expected to work as a catalyst. In addition, a higher catalytic activity is expected from NCP complexes due to the special ability to stabilize metal ions in higher oxidation state. One example is the rhodium (Rh) complex of NCP. When coordinated with TPP, Rh shows a trivalent nature with the help of halogen as the axial ligand. But in the case of NCP, due to its central carbon atom, the Rh ion is stabilized as Rh(IV) with the axial ligand. Attributing to the higher oxidized Rh, the NCP complex demonstrated a higher catalytic activity and led to a higher yield than TPP complex in the reaction of alkane cyclopropanation (Scheme 1-4). Moreover, with NCP complex as the catalyst, a better *cis/trans* selectivity was obtained due to the steric hindrance in the transition state.[47]

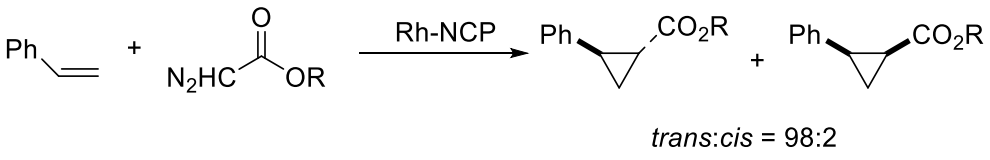

Scheme 1-4. The catalytic reaction using NCP-Rh complex as the catalyst.[47]

1.3.2 NCP as Anion Receptor

Anion receptor is popular research due to the application in medical science, biology, and environment. Although metalloporphyrin or the derivatives like calixpyrrole have been reported capable of binding with anions through the central metal, porphyrin itself shows no anion binding due to small ring size. However, with a confused pyrrole, the active nitrogen can be utilized as the binding site with anions on the outside of the macrocycle.[48] For example, the outward-facing NH moiety gives NCP the ability to bind with anions through hydrogen bonding. (Scheme 1-5) The spectral change also allows it to function as an anion sensor.

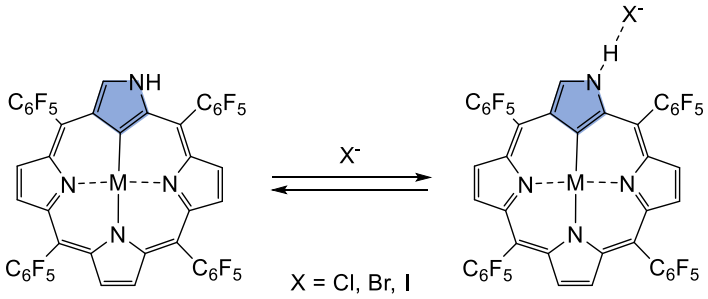

Scheme 1-5. NCP metal complex as halide receptor.[48a]

1.4 Anion Transporter

As have been introduced in the previous section, porphyrin and its N-confused isomer have been studied for their anion binding applications such as sensing and capturing. MOFs have also been catching attention for the anion sensing and encapsulation function, indicating that anion binding is a useful tool to detect or remove them as anions play significant roles in our living environment. Anions also are crucial in our body as they have influences on the vital activities such as metabolism or inner acid-base equilibrium. Studies related to biochemistry have been focusing on the problems caused by the disorder of anions and curing these problems using chemical tools such as anion binding. In this thesis, the applications of organic compounds in transporting anions through the cell membrane are conducted and discussed. Therefore, in this section, the basic information on anions and the roles they play in the human body will be introduced.

1.4.1 Common Anions in Human Body

There are various types of anions in the human body. They can be generated by metabolism or other biological reactions happening inside our body, or absorbed through food and drinks. These anions are extremely essential to our vital activities, thus the absorption, excretion of them play a very important role in our health. Furthermore, the concentration of ions provides useful information for disease diagnosis and treatment. Hence, the studies of these anions, their role, and circulation in vivo have drawn increasing

attention in the field of biochemistry and pharmacy.

Unlike their counter ions—cations, which have also been studied for biological effects and widely understood so far, anions are correspondingly important in the regulation of vital activities and yet people's awareness of them have not been leveled with their counterparts. Through years of studies, their roles have been revealed and the significance has certainly caught attention. Efforts have been put into studies of anions and their movement to further learn their relevance to diseases, whereas it is usually difficult to differentiate the effect of anions from cations.

Some typical anions and their roles are listed below.

- Chloride ion (Cl^-) is the major anion found outside cells in the body. It functions as the counterion for sodium and potassium in the extracellular fluid and for H^+ in gastric juice. The chloride ion is ingested mainly as table salt along with sodium. It is now believed that chloride ions are involved in many functions such as fluid regulation, electrolyte balance, maintaining blood pressure and acid-base and so forth. As the concentration of chloride ions plays a key role in maintaining balance and the regulation, the ingestion and excretion of chloride ions have been of critical significance when it comes to diagnosis of diseases. Moreover, although chloride ions are predominantly found outside of cells, they can get through cell membrane as self-regulation when there is an abnormality in the concentrations. Thus, transport of chloride has also intrigued many scientists in the field of pharmacy.[49]

- Bromide ion (Br^-) is one of the trace elements in the human body. It had not caught scientists' attention due to the resemblance of its role to chloride ion in biology system until it was found to be involved in the vital activities in the 1980s when fruit flies died without bromide in their diet in an experiment. Currently, it is considered that bromide assists in the process of peroxidasin to form the sulfilimine bond which acts as a connector between collagen IV molecules. Bromide is also needed to generate antiparasitic brominating compounds. Hence, bromide is one of the key factors in the immune system and tissue architecture.[50]

- Iodide ion (I^-) is known as the heaviest element needed by living organisms and second heaviest element used by any form of life. In the human body, iodide is used by the thyroid gland for the synthesis of thyroid hormones which has a dominant effect on the gene transcription mechanisms to regulate the basal metabolic rate and also helps the carbohydrate absorption and fatty acid release in intestine. As the source of iodide only depends on ingestion from food, the deficiency of it has been the main cause of diseases in some countries.[51]

- Nitrate ion (NO_3^-) is a common ion in nature as one of the nitrogen sources of some bacteria and plants, thus it has been used as fertilizers to develop agriculture. For a very long time, nitrate ion was considered

harmful to the human body as it may cause methemoglobinemia and cancers. International Agency for Research on Cancer concluded: “ingested nitrite or nitrate under conditions that result in endogenous nitrosation is probably carcinogenic to humans”. Nonetheless, in the late last century, it was reported that the methemoglobinemia is more likely to result from infective enteritis instead of nitrate, and the relations between cancer risk and intake of nitrate are still uncertain. Later on, nitrate is believed to be critical in the metabolism, host defense and even to improve cardiovascular risks at certain concentrations. So far, although nitrate is revealed to be connected to human health, the exact role of it is still in the shadow. The risk-benefit analysis of nitrate has not been easy due to the concentration-dependent effect on metabolism, which also makes the relating researches even more meaningful and challenging.[52]

- Bicarbonate ion (HCO_3^-) is another common type of anions found in all body fluid, as 70-75% of CO_2 in the body is converted into carbonic acid (H_2CO_3), which then turns to bicarbonate easily. As a buffer, bicarbonate is of high significance to maintaining acid-base homeostasis. Moreover, bicarbonate assists the generation of lactic acid after physical activities. The pH of the human body is an indicator of the health conditions, which has been widely tested for initial diagnosis. The research of bicarbonate is believed to be beneficial for athletes, as its participation in the lactic acid plays a huge part in the fatigue we feel after exercise.[53]

- Perchlorate ion (ClO_4^-) is another anion found in food and even in the air. Unlike the aforementioned anions, perchlorate is believed to be unnecessary for humans. However, perchlorate should be paid high attention because it still affects our health when ingested excessively into the body. For instance, perchlorate has a competitive effect on iodide ingestion in the thyroid gland, which leads to an abnormality in thyroid hormone generation. On the other hand, it is also an effective drug for hyperthyroidism caused by too much thyroid hormones due to malfunction of the thyroid gland. [54]

As is mentioned above, different ions have completely different functions in various tissues. Not only their existence is crucial, but also the concentrations inside and outside of the tissue play a vital part in our life activities. Lots of reports have shown that when there is a disorder in the ion concentrations, malfunction of tissue and physical symptoms will occur which then possibly lead to diseases. Hence, regulations of ion concentrations are a huge factor in maintaining our bodies functions properly. Among all the ways of ion concentration regulations, ion transport is one of the effective ways that our body utilizes actively. Ion transport is a process that involves many substances and even energy consumption, thus it is a highly delicate and normal process.

In this thesis, the author focuses on the transport of anions, the basis of which is introduced. Then, a modern technique called artificial anion transporter involving organic chemistry and supramolecular will also be

mentioned.

1.4.2 Transmembrane Transport of Ions

Before one gets to transmembrane transport, it is necessary to learn cell membrane in order to understand the mechanism.

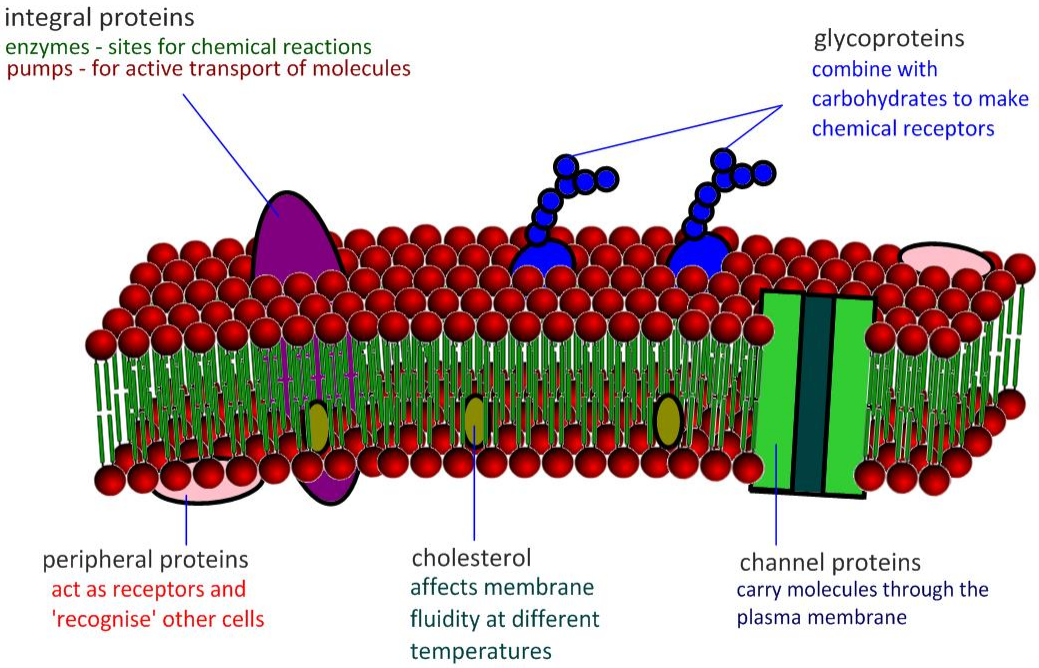

Figure 1-26. Diagram of the general cell membrane and its constitution.

As is known, cell membrane generally consists of the phospholipid bilayer. with some glycoproteins, proteins, cholesterols in, through or on the surface of it. (Figure 1-26) Although there are many types of phospholipid in the membrane of various types of cell, they all have a similar molecular structure, which composes a hydrophilic bulky phosphoric acid moiety and one or two hydrophobic aliphatic chains. Hence, in the biological environment, these phospholipid molecules are forced to assembled into bilayer membrane through a hydrophobic effect, giving a hydrophilic surface of the phosphoric acid and a highly nonpolar and hydrophobic space between the bilayer. Attributing to the phospholipid molecules, cell membrane thus forms a natural barrier that blocks the free movement of substances on either side though it.[55]

Whether a chemical species is able to pass through cell membrane depends on two factors—path and driving force. According to the different driving forces, the transport can be classified into two types. When concentration difference is the driving force, it is called passive transport. In the case of passive transport, the chemical species is always transported along the concentration gradient—from a concentrated side to diluted side. On the other hand, when the transport occurs with ATP reacted and enzyme participating—

namely energy consumed—it is called active transport. Active transport normally occurs when the chemical species is highly needed and it is transported against the concentration gradient, with the energy consumed to help with the transport that does not happen spontaneously.[56] (Figure 1-27)

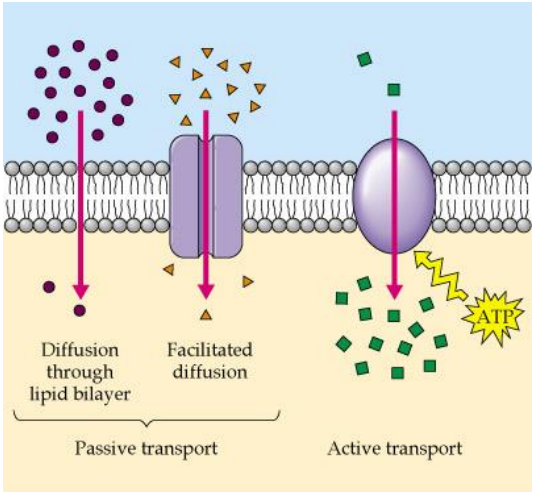

Figure 1-27. Diagram of three types of transmembrane transports.[56a]

When only passive transport is considered, in terms of the path, there are also roughly two types. As a semipermeable membrane, only small molecules such as water, oxygen, carbon dioxide etc. are allowed to pass through cell membrane freely. The free movement of small molecules through the cell membrane is called diffusion. However, with polar molecules or big molecules such as ions or proteins, diffusion is not likely to happen due to the incompatibility between these species and the low polar and hydrophobic environment inside. Hence, a special path is needed to facilitate the transport of these chemical species, which are exactly the proteins or other substance distributed in the membrane. This transport is also called facilitated diffusion. The important role is played by proteins in the membrane, which form channels, or function as carriers to help the chemical species pass through the membrane.

There are diverse channels and carriers in membranes related to hundreds of chemical species needed to be transported. For instance, one of the chloride transport channels is called Cystic fibrosis transmembrane conductance regulator, which is responsible only for chloride. (Figure 1-28).

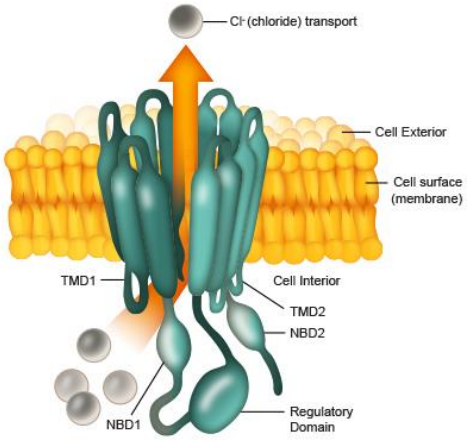

Figure 1-28. Diagram of Cl^- transport channel protein.[57]

As such, channels and transporters usually have selectivity towards a specific type of chemical species to keep the balance of every chemical species on both sides of the cell membrane. However, when there are disorders in the translation of this protein such as Cystic fibrosis transmembrane conductance regulator, tissues like lungs, pancreas, liver, kidneys and intestine will get affected, with symptoms such as difficulty breathing and coughing up mucus as a result of frequent lung infections.[57]

Researchers have been working on solutions to cure these diseases. Among them, synthetic transmembrane transporter is a simple and effective way, which will be introduced as followed.

1.4.3 Synthetic Transport System

Synthetic transport systems are groups of molecules that 1) feature significant structural motifs that do not occur in nature, and 2) mediate transport in lipid bilayer membrane. Synthetic transport systems include channels and carriers.[58] (Figure 1-29)

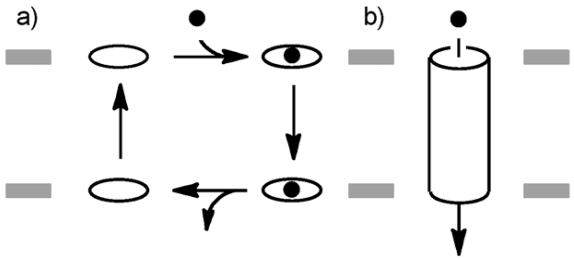

Figure 1-29. Schematic transport mechanism of a) ion carriers and b) ion channels.[58]

Ion channel has been studied for over three decades. People have been keeping trying to design and synthesize efficient channel molecules by mimicking the natural channel protein. The key to designing an ion channel is to create a molecule that is able to fit in the hydrophobic environment and maintain a

hydrophilic environment inside for ion movement in the meantime.

For example, in 1990, a channel polymer based on crown ether was reported. The effectiveness in the design and membrane-activity was confirmed by cation (Na^+ and K^+) transport experiments.[59] (Figure 1-30)

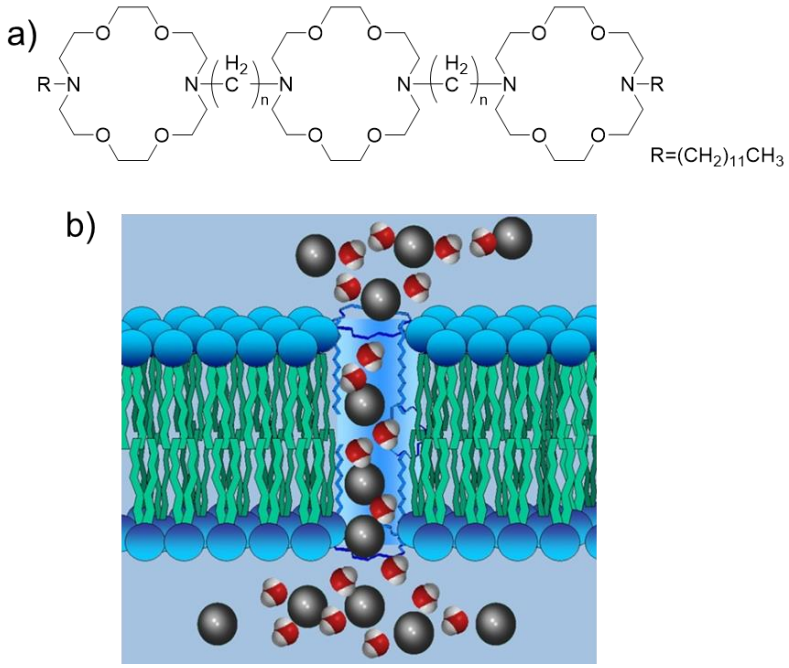

Figure 1-30. (top) The molecular structure of ion channel based on crown ether, (bottom) schematic of ion transport in cell membrane.[59]

Large molecules seem the first impression of ion channels. However, channel assembled by small molecules is also a common way of constructing a novel synthetic ion channel. For example, by a simple synthetic process, a molecule possessing both polar and nonpolar moiety self-assembles in the aliphatic chain phase, facing the polar moiety inside to create nanotube with a polar inner environment.[60] (Figure 1-31)

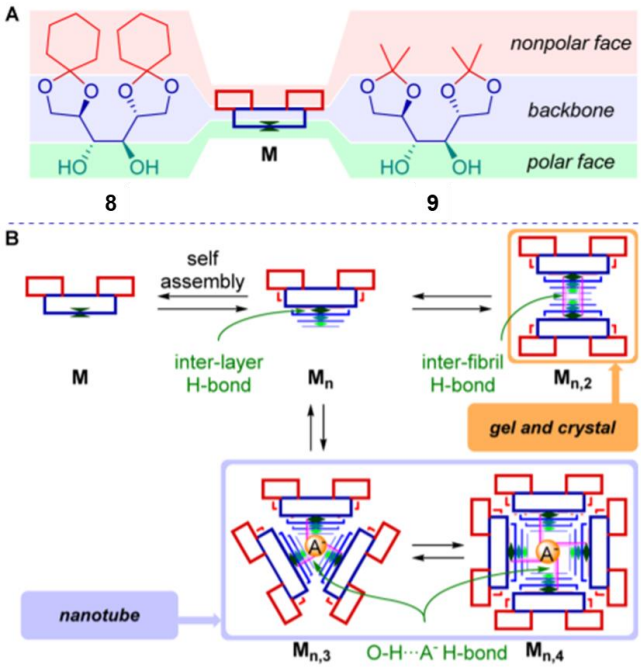

Figure 1-31. Structures of synthetic ion channels constructed from small molecules.[60] A, the molecular design of channel unit compound 8 and 9; B, the self-assembly of channel units in a hydrophobic environment.

Although channels are considered an efficient candidate for transporting ions, the huge size and complexity in molecular design have been the factor slowing down research in the area. On the other hand, ion transport transporters (carriers) are small molecules with the ability to transport ions through the cell membrane. The simplicity in design and synthesis makes them a more promising in this area.[61]

Like channel, the key in ion transporter molecule design is the hydrophobicity. First, the molecules must have a certain degree of hydrophobicity to exist in the aliphatic chain phase stably. However, in order to bond with the target ion, transporters must also have a polar moiety, which decides the binding strength and the selectivity toward ions. After bonding with a target on one side of the membrane, transporters carry target through the membrane as a chelate, and finally dissociate with the target and release it on the other side of the membrane due to concentration difference. When coordinated with hydrophobic molecules, the high polarity of the target species is neutralized, giving the chelate stability in the hydrophobic environment inside the membrane. Hence, the balance in the molecular hydrophobicity is one of the crucial factors that decide the transport efficiency. When the molecule is too hydrophobic, it does not bind with target ions well, while low hydrophobicity leads to the poor permeability and mobility in the cell membrane.[62] (Figure 1-32)

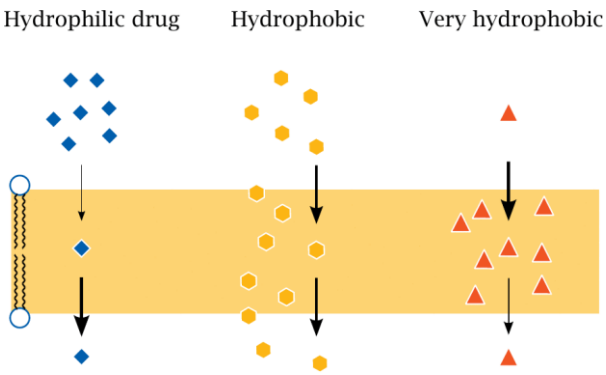

Figure 1-32. Diagram of the relationship between hydrophobicity and carrier molecule design.

For example, a group of transporters based on indoles was reported to have a strong affinity toward carboxylate. The amine groups assure the binding ability with anions while the aliphatic chains make sure the hydrophobicity. Among these compounds, the ones with urea or thiourea moiety showed stronger binding affinity toward carboxylate.[55] (Figure 1-33)

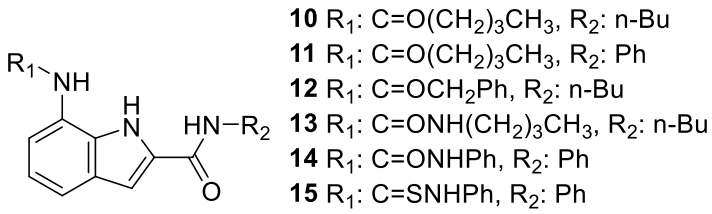

Figure 1-33. A group of simple transporters (compound **10**-**15**) based on indoles.[55]

Besides the hydrophobicity of the transporter itself, the hydrophobicity of the chelate formed by the transporter and ion is another factor that has an influence on the transport efficiency. When bonded with ions, the transporter is introduced with a certain degree of hydrophilicity, due to which the transport efficiency is likely to decrease. However, this phenomenon can be avoided by careful design of the transporters. For instance, a cyclic transporter was reported to transport fluoride selectively. The cyclic structure that binds with ions in the center is an effective way to stabilize the ion in the aliphatic chain phase and keep the hydrophobicity at the same time.[63] (Figure 1-34)

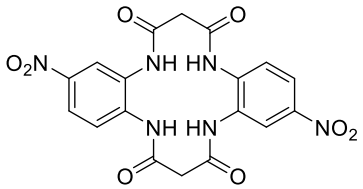

Figure 1-34. structure of cyclic transporter molecule.[63]

In this thesis, anions are the major target ion as people's attention and awareness of them are not to the level as they do to cations. Currently, development in modern supramolecular chemistry has helped with novel design of anion transporters and the comprehension of their mechanism. Therefore, a few examples will be introduced in the order of the type of interaction with anions later in the chapter.

1.4.4 Design for Anion Transporter

Transporters usually bond with anions through non-covalent bonding to ensure the dissociation. As the research on supramolecular chemistry develops, more novel interactions have been used in this field and exhibited distinct behaviors that are considered suitable for different situations. These interactions are summarized as follow.

1.4.4.1 Hydrogen Bonding

Hydrogen bonding is one of the most common non-covalent interactions that are easily included in the design due to the relatively simple synthetic strategy. Aforementioned calix[4]pyrroles are one of the examples. (Figure 1-20) The amine moieties from four pyrroles and the two CHs on triazoles in the strap chain work as hydrogen donors and bonds strongly with anions. The molecular structure provides an inner polar environment for encapsulation of anion, which contributes to the stabilization of the chelate thus a high transport efficiency. Furthermore, the length of the strap has a decisive effect on the selectivity. Hence, transporters with shorter strap demonstrated dominant selectivity toward F^- over Cl^-.

For designing an anion transporter based on hydrogen bonding, the affinity between transporters and anions plays a predominant role. Since transporter molecules serve as the hydrogen donor, a stronger affinity comes with the increase of the hydrogen acidity. For example, a series of transporters were designed and synthesized based on sqaramide, thiourea, and urea. Squaramide is a derivative of squaric acid which shows as strong acidity as sulfuric acid due to an aromatic stabilization of the anion after deprotonation, thus the amide NH on squaramide is more acid than urea and thiourea, resulting in more efficient transport of compound **1** than **2** and **3**. In addition, when more electron-withdrawing groups were attached to the transporters (**4-9**), the efficiencies were enhanced to a huge level.[64] (Figure 1-35)

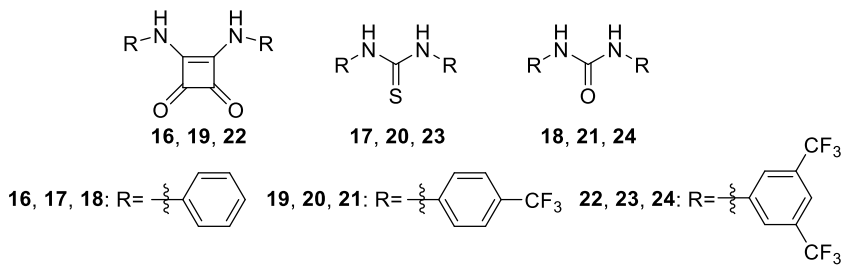

Figure 1-35. Anion transporters based on squaramide (**16**, **19**, **22**), thiourea (**17**, **20, 23**) and urea (**18**, **21**, **24**).[64]

1.4.4.2 Anion-π Interaction

Anion-π interaction is defined as nonbinding, commonly observed on the surface of π-acidic (electron-deficient) aromatic plane with positive quadrupole moments. It is, in fact, a better-studied interaction than π-cation interaction, which has also been used in the field of anion transport. However, it is not until 2010 that anion-π interaction was confirmed to exist experimentally. In this paper, Matile and coworkers synthesized a series of transporters based on naphtalenediimides (NDI) and conducted anion transport experiment along with binding affinity calculation to illustrate the existence of anion-π interaction. As a result of selectivity experiments toward various anions, halide transport selectivity was found to be $Cl^- > Br^- > I^-$, which is influenced by the π-acidity.[65] (Figure 1-36)

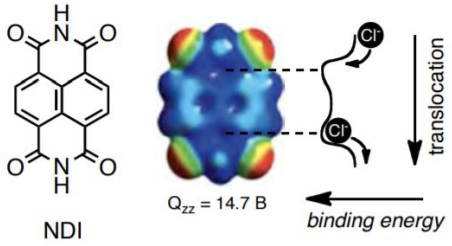

Figure 1-36. The calculation result of active sites of NDI with Cl^- and the binding energy.[65]

1.4.4.3 Halogen Bonding

Halogen bonding usually occurs between two halogens. When halogen is attached to an electron-withdrawing group, the outer electron density will be affected and attracted to the position closer to the group, leaving an electron-deficient area at the opposite direction to the electron-withdrawing interatom. This electron deficient area is called σ-hole and is the main interaction position with other anions. Because the more electrons on the halogen and the farther they are from the nucleus, the easier it is to form the σ-hole, iodide is the often used in the molecular design, nevertheless, fluoride is also reported capable of halogen bonding. Additionally, when the electron-withdrawing ability raises, the halogen bonding also strengthens.[66] (Figure 1-37)

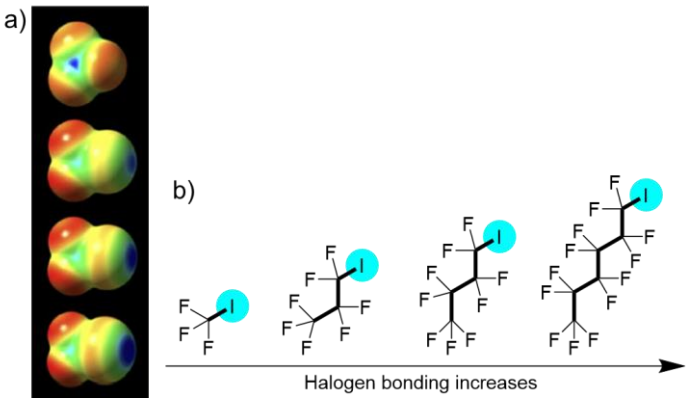

Figure 1-37. a) Electrostatic potential surfaces of CF_4, CF_3Cl, CF_3Br and CF_3I (top to bottom), b) enhancement of halogen bonding with the increase of the electron-withdrawing ability of the side chain.[66]

1.4.4.4 Chalcogen Bonding

Similarly to halogen bonding, chalcogen bonding originates from elements in group 16—namely the oxygen family. The only distinction is that there are usually two σ-hole in the opposite direction of the electron withdrawing groups. As is demonstrated in Figure, a series of transporter of Dithienothiophene was reported. This research directed a new way of designing anion transporter.[67] (Figure 1-38)

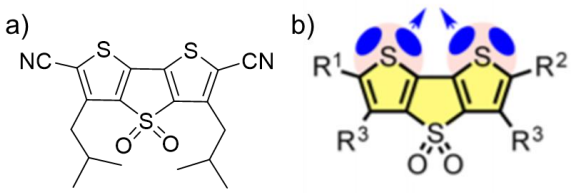

Figure 1-38. a) structure of transporter based on Dithienothiophene and b) diagram the σ-hole.[67]

1.5 Overview of This Thesis

In this thesis, the author address one of the current limitations of using porphyrin-based MOF, which is the short absorption wavelength, by tailoring the molecular structure of the organic ligand to realize a NIR-responsive MOF. Furthermore, the previous works on these isomeric ligand molecules have inspired us in the use of hybridization. Hence, taking advantages of the design flexibility of MOFs, we realized higher light harvesting ability by hybridizing two ligands to synthesize a novel class II hybrid MOF.

In chapter 2, NCP and an N-methylated derivative MeNCP -based Zr-MOFs were synthesized. The synthesis conditions were discussed and optimized in details due to the different conditions resulting from the subtle difference in structures between porphyrin and NCP. Crystallinity was verified through Powder XRD patterns, from which the theoretical cubic ftw topology was also calculated. The thermal and chemical stability was tested and these MOFs demonstrated high stability toward heat and various chemical dissolution (acid-base and organic solvents). Compared with porphyrin-based MOFs, the red-shifted absorption and

emission spectra were measured. The similar backbones of NCP to TPP allows us to obtain MOF with a similar topology to TPP-based MOF and NIR-responsiveness.

In chapter 3, novel class two hybrid MOF is constructed through a seed-mediated synthesis. The core/shell structures have also been characterized by the introduction of different metal ions to the centers of both macrocycles, followed by means of nanoparticle analyses such as SEM, TEM, EDX elementary analysis. By incorporating both TPP and NCP into one MOF, a stronger light harvesting ability is realized from visible to NIR region, which is also verified by the photophysical properties. However, due to the shorter fluorescent decay lifetime of NCP compared with TPP, the singlet oxygen generation ability decreases according to the ratio of NCP in the hybrid MOF.

In addition to the study of novel MOF, one of the widely studied applications of anion transport based on hydrogen bond is also discussed in the thesis. In particular, the relationship between binding selectivity and transport selectivity was studied. We believe that the connection between these two selectivities will shed light on the future design of novel selective anion transporters.

In chapter 4, we imitate sapphyrin or calixpyrrole to synthesize a series of novel anion receptor for transmembrane anion transport. In previous research, the transport selectivity, particularly toward Cl^- and NO_3^-, was experimented with a potential error as one of the factors has been underrated in the old assay. Therefore, we proposed and conducted two new assays to test the transport selectivities of various transporters toward anions, on phospholipid bilayer vesicles. Consequently, the tripodal compounds exhibited excellent Cl^- selectivity due to the encapsulation effect, which was different from the result of the old assay.

References

1. (a) Henke, S., **2012**; (b) Kitagawa, S., *Chem. Soc. Rev.* **2014,** *43* (16), 5415-5418; (c) Zhou, H. C.; Long, J. R.; Yaghi, O. M., *Chem. Rev.* **2012,** *112* (2), 673-674.
2. (a) Chughtai, A. H.; Ahmad, N.; Younus, H. A.; Laypkov, A.; Verpoort, F., *Chem. Soc. Rev.* **2015,** *44* (19), 6804-6849; (b) Corma, A.; García, H.; Llabrés i Xamena, F., *Chem. Rev.* **2010,** *110* (8), 4606-4655.
3. Ma, S.; Zhou, H. C., *Chem Commun (Camb)* **2010,** *46* (1), 44-53.
4. Fang, X.; Zong, B.; Mao, S., *Nano-Micro Letters* **2018,** *10* (4).
5. Chen, D.; Xing, H.; Wang, C.; Su, Z., *J. Mater. Chem. A* **2016,** *4* (7), 2657-2662.
6. (a) Lu, W.; Wei, Z.; Gu, Z.-Y.; Liu, T.-F.; Park, J.; Park, J.; Tian, J.; Zhang, M.; Zhang, Q.; Gentle III, T., *Chem. Soc. Rev.* **2014,** *43* (16), 5561-5593; (b) Stock, N.; Biswas, S., *Chem. Rev.* **2012,** *112* (2), 933-969; (c) Zhao, D.; Timmons, D. J.; Yuan, D.; Zhou, H.-C., *Acc. Chem. Res.* **2010,** *44* (2), 123-133.
7. Liu, T. F.; Feng, D.; Chen, Y. P.; Zou, L.; Bosch, M.; Yuan, S.; Wei, Z.; Fordham, S.; Wang, K.; Zhou, H. C., *J. Am. Chem. Soc.* **2015,** *137* (1), 413-419.
8. Phan, A.; Czaja, A. U.; Gándara, F.; Knobler, C. B.; Yaghi, O. M., *Inorg. Chem.* **2011,** *50* (16), 7388-7390.

9. Yuan, S.; Zou, L.; Li, H.; Chen, Y. P.; Qin, J.; Zhang, Q.; Lu, W.; Hall, M. B.; Zhou, H. C., *Angew. Chem. Int. Ed.* **2016,** *55* (36), 10776-10780.
10. (a) Kong, X. J.; Lin, Z.; Zhang, Z. M.; Zhang, T.; Lin, W., *Angew. Chem. Int. Ed.* **2016,** *55* (22), 6411-6416; (b) Zhang, Z.-M.; Zhang, T.; Wang, C.; Lin, Z.; Long, L.-S.; Lin, W., *J. Am. Chem. Soc.* **2015,** *137* (9), 3197-3200.
11. Ma, J.-P.; Yu, Y.; Dong, Y.-B., *Chem. Commun.* **2012,** *48* (24), 2946-2948.
12. Foo, M. L.; Matsuda, R.; Kitagawa, S., *Chem. Mater.* **2013,** *26* (1), 310-322.
13. Park, K. C.; Seo, C.; Gupta, G.; Kim, J.; Lee, C. Y., *ACS Appl Mater Interfaces* **2017,** *9* (44), 38670-38677.
14. Park, J.; Feng, D.; Yuan, S.; Zhou, H. C., *Angew. Chem. Int. Ed.* **2015,** *54* (2), 430-435.
15. Li, M.; Zheng, Z.; Zheng, Y.; Cui, C.; Li, C.; Li, Z., *ACS Appl. Mater. Interfaces* **2017,** *9* (3), 2899-2905.
16. Cui, Y.; Li, B.; He, H.; Zhou, W.; Chen, B.; Qian, G., *Acc. Chem. Res.* **2016,** *49* (3), 483-493.
17. Cui, Y.; Song, R.; Yu, J.; Liu, M.; Wang, Z.; Wu, C.; Yang, Y.; Wang, Z.; Chen, B.; Qian, G., *Adv. Mater.* **2015,** *27* (8), 1420-1425.
18. Wang, Z.; Wang, B.; Yang, Y.; Cui, Y.; Wang, Z.; Chen, B.; Qian, G., *ACS Appl. Mater. interfaces* **2015,** *7* (37), 20999-21004.
19. Moore, M. R., Springer: 2009; pp 1-28.
20. Hashimoto, T.; Choe, Y.-K.; Nakano, H.; Hirao, K., *J. Phys. Chem. A* **1999,** *103* (12), 1894-1904.
21. Goldoni, A., *ELETTRA highlights* **2001,** *2002* (2002), 64-65.
22. Dai, X.; Chen, D.; Zhou, W.; Yang, S.; Sun, F. a.; Qian, J.; He, M.; Chen, Q., *Catal. Commun.* **2018,** *117*, 85-89.
23. Wang, X.; Maeda, K.; Thomas, A.; Takanabe, K.; Xin, G.; Carlsson, J. M.; Domen, K.; Antonietti, M., *Nat. Mater.* **2009,** *8* (1), 76.
24. Wang, J.; Liu, D.; Liu, Q.; Peng, T.; Li, R.; Zhou, S., *Appl. Surf. Sci.* **2019,** *464*, 255-261.
25. Moan, J.; Peng, Q., *Anticancer Res.* **2003,** *23* (5A), 3591-3600.
26. O'Connor, A. E.; Gallagher, W. M.; Byrne, A. T., *Photochem. Photobiol.* **2009,** *85* (5), 1053-1074.
27. Schmitt, J.; Heitz, V.; Sour, A.; Bolze, F.; Ftouni, H.; Nicoud, J. F.; Flamigni, L.; Ventura, B., *Angew. Chem. Int. Ed. Engl.* **2015,** *54* (1), 169-173.
28. Mathew, S.; Yella, A.; Gao, P.; Humphry-Baker, R.; Curchod, B. F.; Ashari-Astani, N.; Tavernelli, I.; Rothlisberger, U.; Nazeeruddin, M. K.; Grätzel, M., *Nat. Chem.* **2014,** *6* (3), 242.
29. Sessler, J. L.; Cyr, M.; Furuta, H.; Král, V.; Mody, T.; Morishima, T.; Shionoya, M.; Weghorn, S., *Pure Appl. Chem.* **1993,** *65* (3), 393-398.
30. Sessler, J. L.; Davis, J. M., *Acc. Chem. Res.* **2001,** *34* (12), 989-997.
31. (a) Clarke, H. J.; Howe, E. N.; Wu, X.; Sommer, F.; Yano, M.; Light, M. E.; Kubik, S.; Gale, P. A., *J. Am. Chem. Soc.* **2016,** *138* (50), 16515-16522; (b) Yano, M.; Tong, C. C.; Light, M. E.; Schmidtchen, F. P.;

Gale, P. A., *Org. Biomol. Chem.* **2010,** *8* (19), 4356-4363.

32. Day, N. U.; Wamser, C. C.; Walter, M. G., *Polym. Int.* **2015,** *64* (7), 833-857.
33. Morris, W.; Volosskiy, B.; Demir, S.; Gandara, F.; McGrier, P. L.; Furukawa, H.; Cascio, D.; Stoddart, J. F.; Yaghi, O. M., *Inorg. Chem.* **2012,** *51* (12), 6443-6445.
34. (a) Bai, Y.; Dou, Y.; Xie, L. H.; Rutledge, W.; Li, J. R.; Zhou, H. C., *Chem. Soc. Rev.* **2016,** *45* (8), 2327-2367; (b) Deria, P.; Yu, J.; Balaraman, R. P.; Mashni, J.; White, S. N., *Chem Commun (Camb)* **2016,** *52* (88), 13031-13034; (c) Yuan, S.; Feng, L.; Wang, K.; Pang, J.; Bosch, M.; Lollar, C.; Sun, Y.; Qin, J.; Yang, X.; Zhang, P.; Wang, Q.; Zou, L.; Zhang, Y.; Zhang, L.; Fang, Y.; Li, J.; Zhou, H. C., *Adv. Mater.* **2018,** *30* (37), e1704303.
35. (a) Feng, D.; Chung, W. C.; Wei, Z.; Gu, Z. Y.; Jiang, H. L.; Chen, Y. P.; Darensbourg, D. J.; Zhou, H. C., *J. Am. Chem. Soc.* **2013,** *135* (45), 17105-17110; (b) Feng, D.; Gu, Z. Y.; Chen, Y. P.; Park, J.; Wei, Z.; Sun, Y.; Bosch, M.; Yuan, S.; Zhou, H. C., *J. Am. Chem. Soc.* **2014,** *136* (51), 17714-17717; (c) Feng, D.; Gu, Z. Y.; Li, J. R.; Jiang, H. L.; Wei, Z.; Zhou, H. C., *Angew. Chem. Int. Ed. Engl.* **2012,** *51* (41), 10307-10310; (d) Feng, D.; Jiang, H. L.; Chen, Y. P.; Gu, Z. Y.; Wei, Z.; Zhou, H. C., *Inorg. Chem.* **2013,** *52* (21), 12661-12667; (e) Jiang, H. L.; Feng, D.; Wang, K.; Gu, Z. Y.; Wei, Z.; Chen, Y. P.; Zhou, H. C., *J. Am. Chem. Soc.* **2013,** *135* (37), 13934-13938.
36. Johnson, J. A.; Luo, J.; Zhang, X.; Chen, Y.-S.; Morton, M. D.; Echeverría, E.; Torres, F. E.; Zhang, J., *ACS Catalysis* **2015,** *5* (9), 5283-5291.
37. Lin, W.; Hu, Q.; Jiang, K.; Yang, Y.; Yang, Y.; Cui, Y.; Qian, G., *J. Solid State Chem.* **2016,** *237*, 307-312.
38. Meng, A. N.; Chaihu, L. X.; Chen, H. H.; Gu, Z. Y., *Sci. Rep.* **2017,** *7* (1), 6297.
39. Deenadayalan, M. S.; Sharma, N.; Verma, P. K.; Nagaraja, C. M., *Inorg. Chem.* **2016,** *55* (11), 5320-5327.
40. Lismont, M.; Dreesen, L.; Wuttke, S., *Adv. Funct. Mater.* **2017,** *27* (14), 1606314.
41. (a) Chmielewski, P. J.; Latos-Grażyński, L.; Rachlewicz, K.; Glowiak, T., *Angew. Chem. Int. Ed. Engl.* **1994,** *33* (7), 779-781; (b) Furuta, H.; Asano, T.; Ogawa, T., *J. Am. Chem. Soc.* **1994,** *116* (2), 767-768.
42. Furuta, H.; Ishizuka, T.; Osuka, A.; Dejima, H.; Nakagawa, H.; Ishikawa, Y., *J. Am. Chem. Soc.* **2001,** *123* (25), 6207-6208.
43. Lee, J. S.; Lim, J. M.; Toganoh, M.; Furuta, H.; Kim, D., *Chem. Commun.* **2010,** *46* (2), 285-287.
44. Bohle, D. S.; Chen, W.-C.; Hung, C.-H., *Inorg. Chem.* **2002,** *41* (13), 3334-3336.
45. Furuta, H.; Ishizuka, T.; Osuka, A., *J. Am. Chem. Soc.* **2002,** *124* (20), 5622-5623.
46. Maeda, H.; Ishikawa, Y.; Matsuda, T.; Osuka, A.; Furuta, H., *J. Am. Chem. Soc.* **2003,** *125* (39), 11822-11823.
47. Niino, T.; Toganoh, M.; Andrioletti, B.; Furuta, H., *Chem. Commun.* **2006,** (41), 4335-4337.
48. (a) Maeda, H.; Osuka, A.; Furuta, H., *J. Incl. Phenom Macrocycl Chem.* **2004,** *49* (1-2), 33-36; (b) Toganoh, M.; Miyachi, H.; Akimaru, H.; Ito, F.; Nagamura, T.; Furuta, H., *Org. Biomol. Chem.* **2009,** *7* (15), 3027-3030.

49. Thornton, J., **1993**.
50. Cross, J. D.; Smith, H., *Forensic science* **1978,** *11* (1), 147-153.
51. Zimmermann, M. B., *Semin. Cell Dev. Biol.* **2011,** *22* (6), 645-652.
52. Lundberg, J. O.; Weitzberg, E.; Cole, J. A.; Benjamin, N., *Nat. Rev. Microbiol.* **2004,** *2* (7), 593.
53. (a) Dalmark, M., *J. Gen. Physiol.* **1976,** *67* (2), 223-234; (b) Sahlin, K.; Alvestrand, A.; Brandt, R.; Hultman, E., *J. Appl. Physiol.* **1978,** *45* (3), 474-480.
54. Soldin, O. P.; Braverman, L. E.; Lamm, S. H., *Ther. Drug Monit.* **2001,** *23* (4), 316.
55. De Riccardis, F.; Izzo, I.; Montesarchio, D.; Tecilla, P., *Acc. Chem. Res.* **2013,** *46* (12), 2781-2790.
56. (a) Stein, W., Elsevier: 2012; (b) Stein, W., Elsevier: 2012; Vol. 6.
57. Kerem, B.-s.; Rommens, J. M.; Buchanan, J. A.; Markiewicz, D.; Cox, T. K.; Chakravarti, A.; Buchwald, M.; Tsui, L.-C., *Science* **1989,** *245* (4922), 1073-1080.
58. Matile, S.; Jentzsch, A. V.; Montenegro, J.; Fin, A., *Chem. Soc. Rev.* **2011,** *40* (5), 2453-2474.
59. Gokel, G. W.; Negin, S., *Acc. Chem. Res.* **2013,** *46* (12), 2824-2833.
60. Saha, T.; Dasari, S.; Tewari, D.; Prathap, A.; Sureshan, K. M.; Bera, A. K.; Mukherjee, A.; Talukdar, P., *J. Am. Chem. Soc.* **2014,** *136* (40), 14128-14135.
61. (a) Gale, P. A.; Pérez-Tomás, R.; Quesada, R., *Acc. Chem. Res.* **2013,** *46* (12), 2801-2813; (b) Shugarts, S.; Benet, L. Z., *Pharm. Res.* **2009,** *26* (9), 2039-2054.
62. Davis, A. P.; Sheppard, D. N.; Smith, B. D., *Chem. Soc. Rev.* **2007,** *36* (2), 348-357.
63. Caltagirone, C.; Gale, P. A., *Chem. Soc. Rev.* **2009,** *38* (2), 520-563.
64. Busschaert, N.; Kirby, I. L.; Young, S.; Coles, S. J.; Horton, P. N.; Light, M. E.; Gale, P. A., *Angew. Chem.* **2012,** *124* (18), 4502-4506.
65. Dawson, R. E.; Hennig, A.; Weimann, D. P.; Emery, D.; Ravikumar, V.; Montenegro, J.; Takeuchi, T.; Gabutti, S.; Mayor, M.; Mareda, J., *Nat. Chem.* **2010,** *2* (7), 533.
66. Jentzsch, A. V.; Emery, D.; Mareda, J.; Nayak, S. K.; Metrangolo, P.; Resnati, G.; Sakai, N.; Matile, S., *Nat. Commun.* **2012,** *3*, 905.
67. Benz, S.; Macchione, M.; Verolet, Q.; Mareda, J.; Sakai, N.; Matile, S., *J. Am. Chem. Soc.* **2016,** *138* (29), 9093-9096.

Chapter 2. Synthesis and Properties of Metal-Organic Frameworks Based on N-Confused Porphyrin

2.1 Introduction

2.1.1 Zirconium MOFs

Zirconium-based metal-organic frameworks (Zr-MOFs), a class of porous coordination polymers consisting of multinuclear Zr-cluster ions, have attracted increasingly much attention due to their intrinsic chemical and thermal stability.[1] These Zr-based MOF materials have been potentially considered to apply toward catalysts[2] (driven by photoirradiation, acids, oxidants, etc.), gas storage[3], gas separation[4], molecular sensing[5] and so forth. Due to the low biotoxicity, Zr-MOFs are also studied for their potential biological applications such as photodynamic therapy (PDT)[6] and drug delivery system (DDS)[7].

2.1.2 Porphyrin as Organic Ligands

Among the various building blocks, porphyrinic Zr-based MOFs have been extensively utilized due to their large π-conjugated backbone capable of creating unique π-space for above applications.[8] With inherent large absorption coefficient values in the visible to near IR energy regions, it is indeed advantageous for developing potential near IR-responsible materials. In addition, the coordination of the dominant porphyrinic units with large varieties of metals leads to the various metal-dependent heterogeneous catalysts.[9] Hence, a near-IR light harvesting stable MOF materials have been demanded for photocatalytic systems as well.

In an effort to realize extremely stable and robust porphyrinic MOF materials (e.g., catalysts, sensors, etc), the synthesis of porphyrin-containing Zr-MOFs with a topologically pure phase is indeed important to realize the specific functions. However, due to the flexible coordination modes of the high valent zirconium (IV) clusters and the slow exchange reactions of the Zr^{4+}-cation and carboxylate ligands, the rational approaches to the topology-controlled Zr-MOF synthesis remains challenging. Zhou *et al*. have extensively studied the synthesis of various porphyrinic Zr-MOFs (e.g., a series of PCN-221-225)[10a, 10b, 3, 10c, 10d]. The change in the synthesis conditions such as substrates ratio, zirconium salts, temperature, reaction time, or solvents afforded the huge diversities in their topologies. Even the structures of porphyrinic linkers can control the crystalline topologies by adjusting the *meso*-aryl ring angles. In the meantime, Yaghi *et al*. have also independently reported the synthesis of Zr-MOFs (i.e., MOF-525)[11] with porphyrins under different conditions, which resulted in the formation of an ftw-type cubic structure with a 4,12-coordinated Zr_6 cluster. It is quite similar to PCN-221 containing 4,12-coordinated Zr_8 blocks. Thus, the topology of porphyrin-based MOFs relies on the reaction conditions to a great extent.

Porphyrin-based Zr-MOFs have been well-studied and designed for novel applications. However, when

put into the practical applications such as PDT or photocatalysis, the short absorption wavelength has limited porphyrin-based MOFs because the absorption and scattering in the human body lead to a poor permeability and little energy can reach deep tissue. On the other hand, near-infrared (NIR), with wavelengths at 700-2500 nm, have caught many researchers' attention due to the higher permeability in biological systems and lower energy involved, which also gives this area a name of "optical window". (Figure 2-1)[12] Ever since materials possessing absorption band in the near-infrared window have been studied. Among various approaches to synthesize NIR-responsive MOFs, the modification of porphyrin-based MOFs has also been discussed[13].

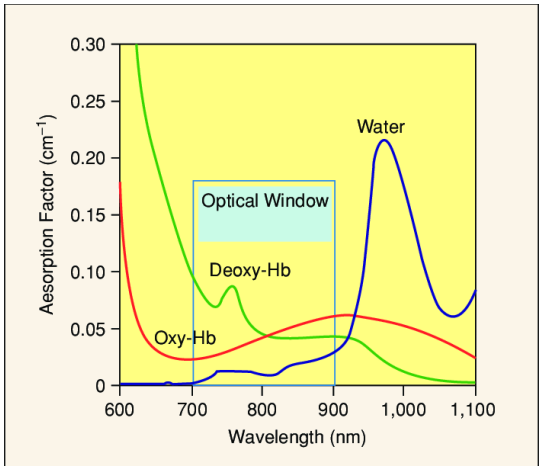

Figure 2-1. Optical window in the near-infrared area.[12]

For instance, self-assembly of porphyrin-MOF with upconversion nanoparticles (UCNPs) was reported[13a] (Figure 2-2a). The energy transfer between MOF and UCNPs was utilized, hence upon irradiation by near-infrared (NIR), the MOF can receive energy converted by UCPNs and excite $^3O_2$ to $^1O_2$. Another example also utilized energy transfer between MOF and NIR-responsive nanoparticle (Figure 2-2b)[13b].

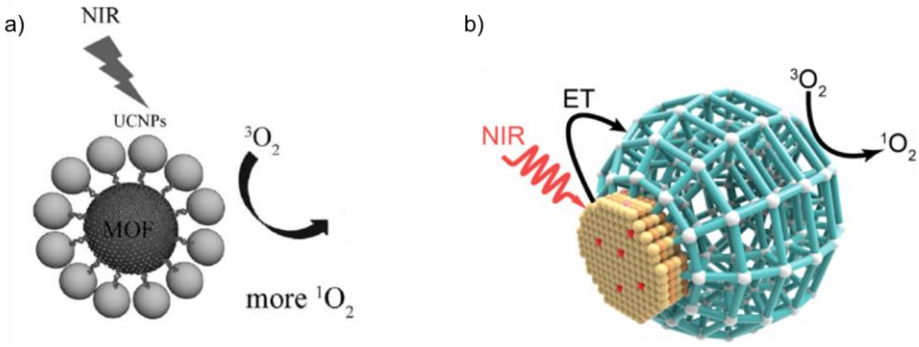

Figure 2-2. a) Self-assembled MOF–UCNP core–satellite in singlet oxygen generation, b) MOF growing on an upconversion nanoparticle.[13]

Both examples utilize the energy transfer to design NIR-responsive $^1O_2$ generator MOFs. However, the low efficiency of energy transfer resulting from the long distance between MOF and nanoparticle still poses

new problems. Therefore, new approaches for modifying porphyrin-based MOFs and designing novel NIR-responsive MOFs without the energy loss resulting from transfer are in required.

On the other hand, the author's group has been focusing on the isomer of porphyrin—N-confused porphyrin (NCP).[14] As is introduced in chapter 1, NCP has a similar tetrapyrrole macrocyclic backbone with one "confused" pyrrole rings connected within the macrocycle. This direct structural modifications of the distinct 18π conjugation core allow breaking the degeneracy of the typical HOMO and LUMO pairs. This results in the narrower HOMO-LUMO energy gaps than those of regular porphyrins which then leads to red-shifted absorption and emission spectra.[15] In addition to the NIR-responsiveness, NCP reveals conspicuous NH tautomerism that a hydrogen atom shifts between the inner and outer nitrogen sites, which reflects the difference in the optical properties as the bistable tautomers[16]. With these in mind, a new approach to construct MOF based on NCP is considerable. Due to the isomeric structures of NCP and porphyrin, a NIR-responsive can be constructed.

2.1.3 Purpose of This Chapter

In this chapter, the author develops novel "N-confused" porphyrinic MOF (**NCP_{MOF}**) containing the most substituted ftw topological Zr_6 clusters under the appropriate conditions (Scheme 2-1). For the study of "confused" pyrrole ring, a control MOF (**$MeNCP_{MOF}$**) is also developed. The Zr_6 node (i.e., $Zr_6O_4(OH)_4(COO)_{12}$) being targeted in this chapter has the highest connectivity in Zr-based MOFs, which shows excellent chemical stability. The resulting MOFs could exhibit unique near IR optical properties due to the great electronic perturbation of the porphyrinic π-block via N-confusion approach. The dynamic nature of the electronic structure of NCPs may reflect environment-dependent adsorption/emissions. The detailed structures, chemical stability, porosity, and optical properties are discussed in this chapter.

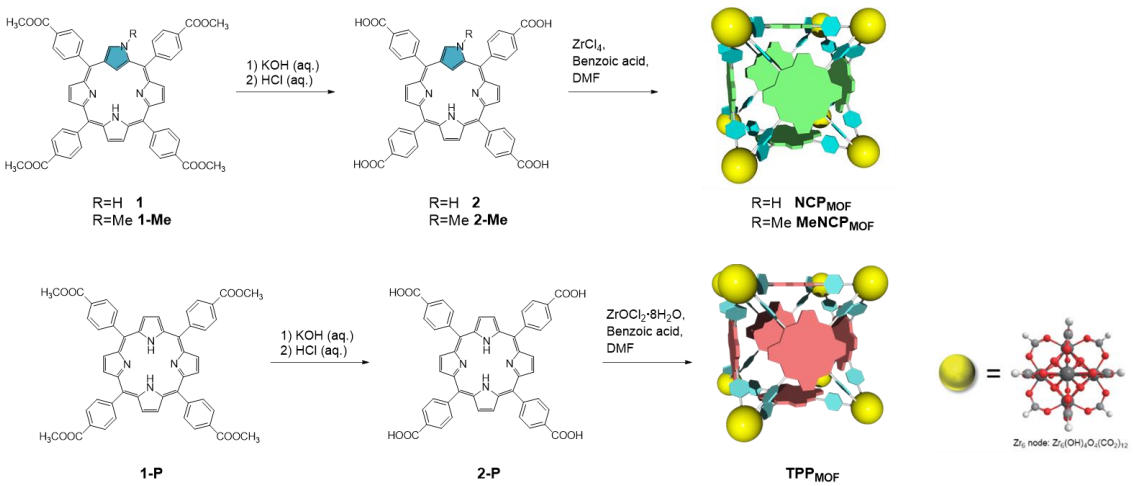

Scheme 2-1. Synthesis of **NCP_{MOF}**, **$MeNCP_{MOF}$**, and **TPP_{MOF}.** The structures of MOFs shown here are the theoretical structures based on Rietveld refinement. The structure of Zr_6 cluster present in MOF-525 is drawn

from the reference 11.

2.2 Synthesis of MOFs Based on NCP

2.2.1 Synthesis of NCP Ligand

In the synthesis of Zr-based MOFs, the corresponding NCP ester derivative (**1**) was prepared by our modified protocols.[17] The product **1** was then hydrolyzed under basic condition to give the tetracarboxylic acid derivative of NCP (**2**) quantitatively. For a comparative study, *N*-methylated NCP (**1-Me**) was also synthesized by mixing **1** with CH_3I and K_2CO_3 in the THF and DMSO mixture overnight in 83% yield. Likewise, **2-Me** was obtained by the hydrolysis of **1-Me** in 94% yield. The products, **2** and **2-Me** were characterized by NMR, mass, and absorption spectra.[18] (See details in the **2.8**)

2.2.2 Synthesis of MOFs

The solvothermal synthesis was conducted to fabricate $\mathbf{NCP_{MOF}}$ and $\mathbf{MeNCP_{MOF}}$ using zirconium(IV) salts, modulator acids, and NCPs, **2** or **2-Me** in *N,N*-dimethylformamide (DMF) (Scheme 2, and the details in Experimental Section). Under Yaghi's procedure[11], using a zirconyl(IV) chloride ($ZrOCl_2 \cdot 8H_2O$), no identical cubic crystalline products were formed (Entry 1 in Table 2-1). When a benzoic acid was used instead of acetic acid, the resulting powders showed stick-shaped crystalline blocks (Entry 2 and 3).[5b] Finally a use of zirconium(IV) chloride ($ZrCl_4$) as the metal source yielded pure-phased microcrystals according to scanning electron microscopy (SEM) experiment (Entry 4) (Figure 2-3a). Similar cubic crystalline grains with lengths of approximately 1 μm were observed as reported in MOF-525. The amount of benzoic acid and reaction time were found to be crucial for obtaining pure-phased cubic crystallinities (Entry 5-7). The combination of $ZrCl_4$ and acetic acid for MOF synthesis resulted in the mixed phase microcrystals (Entry 8). Under the optimized condition, the identical cubic shaped crystalline $\mathbf{MeNCP_{MOF}}$ was obtained as well (Figure 2-3b). In contrast, $\mathbf{TPP_{MOF}}$ was synthesized in similar conditions to $\mathbf{NCP_{MOF}}$, only the Zr reagent was replaced with 103 mg of $ZrOCl_2 \cdot 8H_2O$ (Figure 2-3c).

$\mathbf{TPP_{MOF}}$ was synthesized by a modified method, where the carboxylic acid derivative of TPP (**2-P**) was put in reaction with $ZrOCl_2 \cdot 8H_2O$ and benzoic acid in dry DMF at 120 ^oC for 48 h.

Table 2-1. Reactions for **NCP_{MOF}** fabrication.

Entry	**1** / **mg**	DMF / **mL**	Zr reagent / **mg**	Acid / **mg**	Temp / **°C**	Time / **h**	Results
1	2.5	10	12.5 [b)]	2.5 [d)]	65	72	Stick-like crystals
2	10	2	30 [b)]	400 [c)]	120	24	Stick-like crystals
3	50	8	103.7 [b)]	2700 [c)]	120	48	Stick-like crystals
4	**50**	**8**	**75** [a)]	**2700** [c)]	**120**	**48**	**Cubic crystals**
5	50	8	75 [a)]	2200 [c)]	120	48	Powders with poor crystallinity
6	50	8	75 [a)]	3200 [c)]	120	48	Solution
7	50	8	75 [a)]	2700 [c)]	120	72	Solution
8	50	26	14.7 [a)]	5 [d)]	60	48	Mixture of cube and stick crystals

Zr reagent, a) $ZrCl_4$, b) $ZrOCl_2 \cdot 8H_2O$; Acid, c) benzoic acid, d) acetic acid

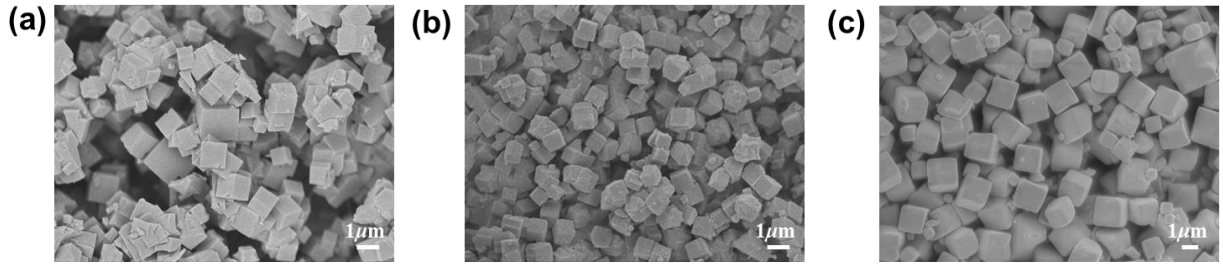

Figure 2-3. SEM images of a) **NCP_{MOF}** and b) **$MeNCP_{MOF}$**, c) **TPP_{MOF}**.

2.3 Characterization

The pure crystallinity of the resulting products was evident from powder X-ray diffraction (PXRD) analysis (Figure 2-3). The cubic **NCP_{MOF}** and **$MeNCP_{MOF}$** indeed revealed the similar patterns with characteristic peaks at 4.5, 6.4, 7.8, 9.1, 10.2, and 11.2° as observed in **TPP_{MOF}**. Using the model generated from Rietveld refinement, the theoretical patterns are in good accordance with the experimental PXRD ones. The final refined parameters for **NCP_{MOF}** and **$MeNCP_{MOF}$** are both constructed in a space group $Pm3\bar{m}$, exhibiting the similar unit cell parameters of a = 19.39 Å, with R_p = 4.35%, R_{wp}=12.38% for **NCP_{MOF}**, while, **$MeNCP_{MOF}$** possesses a = 19.54 Å, with R_p = 4.59%, R_{wp}=12.61%. Thus, the NCP-containing MOFs display three-dimensional porous structures with average pore diameters of ca 19 Å. The results suggest that both

NCP$_{MOF}$ and **MeNCP$_{MOF}$** are face-centered cubic structures with a (4,12)-connected "ftw" topological network on the zirconium cluster. The tetravalence states of zirconium cations in **NCP$_{MOF}$** were confirmed by X-ray photoelectron spectroscopy (XPS) measurement (Figure 2-4). The simple energy pattern peaks at 185 and 183 eV corresponded to the $3d_{3/2}$ and $3d_{5/2}$ peaks, respectively, are suggestive of the symmetric carboxylate coordination to the Zr (IV) centers.

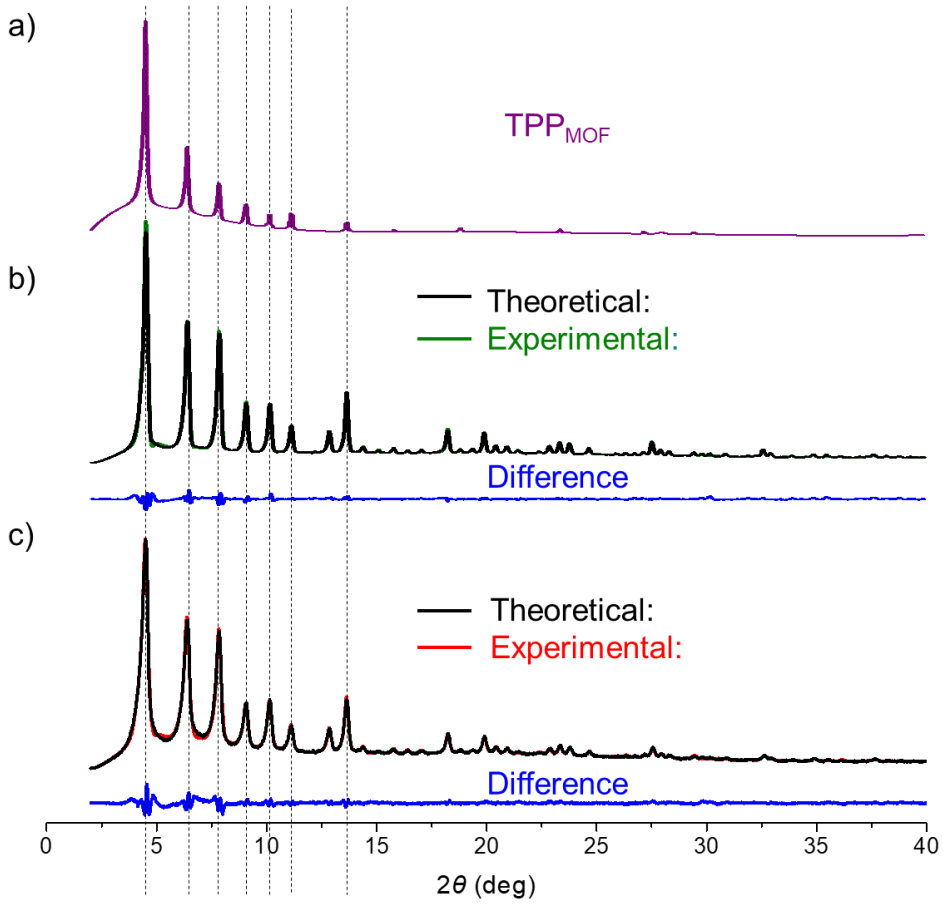

Figure 2-4. Powder X-ray diffraction patterns (black line) and theoretical simulations (red line) based on Rietveld refinement of a) **TPP$_{MOF}$**, b) **MeNCP$_{MOF}$** and c) **NCP$_{MOF}$**. The different patterns are shown in blue.

As is stated above, NCP and TPP ligand (**2** and **2-P**) shares similar structures, and yet have different synthesis conditions when it comes to the synthesis of MOF. This phenomenon is understandable when the distortion of macrocycle resulted from the N-confused pyrrole ring is taken into account. In the previous study conducted by Furuta, NCP has distorted molecular planarity due to the N-confused pyrrole ring, which is even considered rotatable in the macrocycle. This structural difference from the planar TPP ligand may force the molecule to take a changed conformation when reacting with Zr cluster, leading to different conditions.

A similar phenomenon was also found in the synthesis of DMP-UiO[17] and DBC-UiO[18], which are Hf-

based MOFs with porphyrin and chlorin as the organic ligands. The structural difference caused the variation in the synthesis of both MOFs with similar topology. (Figure 2-5) In addition, PCN-224[19, 10a] with β-position modified porphyrin demonstrated different synthesis conditions from the original report.

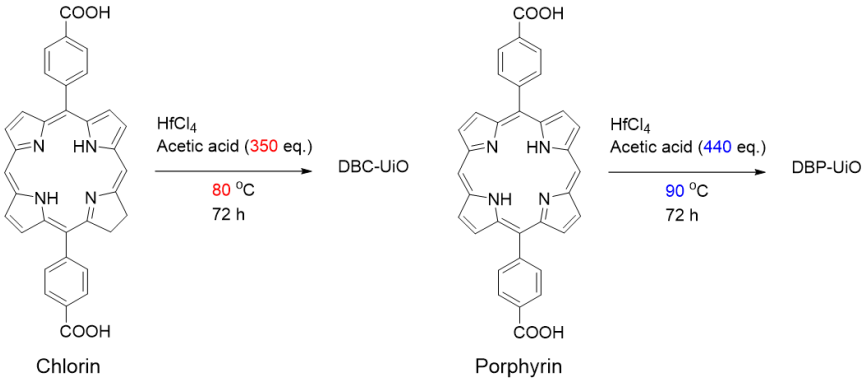

Figure 2-5. Different synthesis conditions for DBC-UiO[18] and DBP-UiO[17] with chlorin and porphyrin as the organic ligands respectively.

2.4 Porosity

The permanent porosity was determined by nitrogen gas adsorption experiment at 77 K (Figure 2-6). Both **NCP$_{MOF}$** and **MeNCP$_{MOF}$** demonstrated the type I isotherm, suggesting the microporosity. The N_2 uptake of 276 cm^3g^{-1} (STP) was determined with **NCP$_{MOF}$**, while **MeNCP$_{MOF}$** showed a value up to 422 cm^3g^{-1}. The Brunauer-Emmett-Teller (BET) surface areas are estimated to be 1040 and 1590 m^2/g, respectively. The difference between these values is probably ascribed to the interactions between the DMF molecule and the confused pyrrolic nitrogen in the NCPs. As seen in the crystal structure of DMF-complex of NCP derivative, some amounts of solvent are still persistent inside **NCP$_{MOF}$** even after the sample activation process. (Figure 2-6) While the N-protected **MeNCP$_{MOF}$** is not the case.

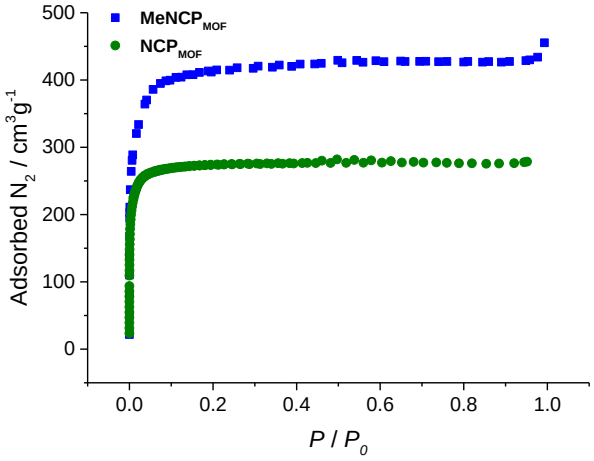

Figure 2-6. N_2 adsorption isotherms for **NCP$_{MOF}$** (blue) and **MeNCP$_{MOF}$** (black) at 77 K. N_2 adsorption

isotherms for **NCP$_{MOF}$** (blue) and **MeNCP$_{MOF}$** (black) at 77 K.

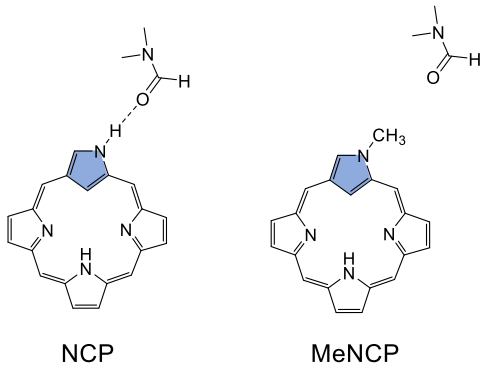

Figure 2-7. The interaction between NCP and DMF molecule through hydrogen bonding (left), and no interaction between MeNCP and DMF molecule (right).

Table 2-2. Calculated surface areas and pore volumes of NCPMOF and MOF-525

	NCP$_{MOF}$	**MOF-525**
Surface area (m^2 / g) BET	1040	2620
Pore Volume (cm^3 / g)	0.43	1.44

Compared with MOF-525 (**TPP$_{MOF}$**), **NCP$_{MOF}$** demonstrated smaller surface area and pore size because the solvent molecules adsorbed in the pore prevented the adsorption of N_2 molecules. NCP ligands bind strongly with DMF molecules through hydrogen bonding resulting from the peripheral NH moiety (Figure 2-6), which makes the porous framework more difficult to desolvate.

2.5 Stability of Zr-MOFs

2.5.1 Thermostability

The thermogravimetric (TG) analysis of both MOFs determined from 30 to 550 ^oC revealed that the weight loss of the **NCP$_{MOF}$** is more significant than that of **MeNCP$_{MOF}$** (Figure 2-8). It should be relevant to the degree of the content percentage for solvent molecules. The weight loss of **NCP$_{MOF}$** at less than 100 ^oC is the desolvation of acetone, while the same process was not observed for MeNCP$_{MOF}$, indicating an easier desolvation of **MeNCP$_{MOF}$** than **NCP$_{MOF}$**. Both MOFs are found to be thermally stable until 400 ^oC.

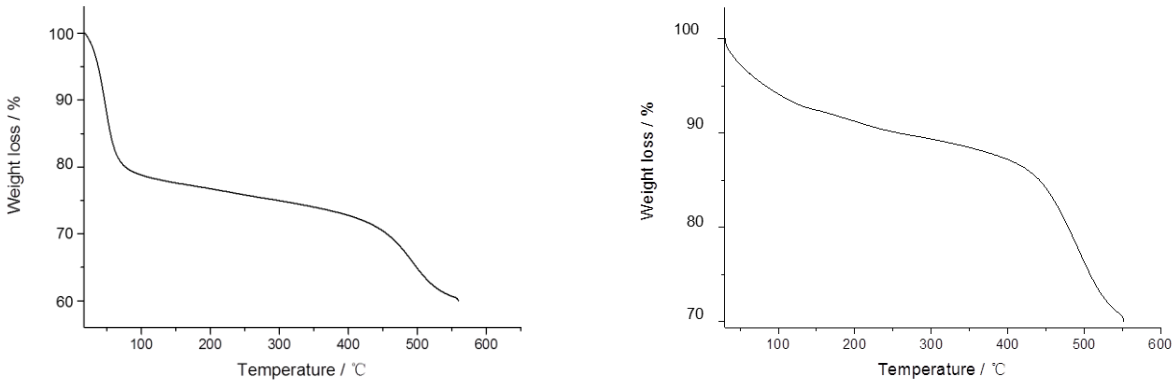

Figure 2-8. Thermogravimetric analyses of (left) **NCP$_{MOF}$** and (right) **MeNCP$_{MOF}$**.

2.5.2 Chemical Stability

In line with the porphyrinic Zr-MOFs[5, 8], the chemical stability, the microcrystalline samples of **NCP$_{MOF}$** were immersed into various organic solvents as well as aqueous solutions (1 < pH < 12) for 24 h, followed by desiccation under vacuum. Their crystallinity was assessed by PXRD experiment. Consequently, the **NCP$_{MOF}$** is stable in organic and aqueous solution up to pH 10, which is consistent with the reported MOF-525 (Figure 2-9 and 2-10).

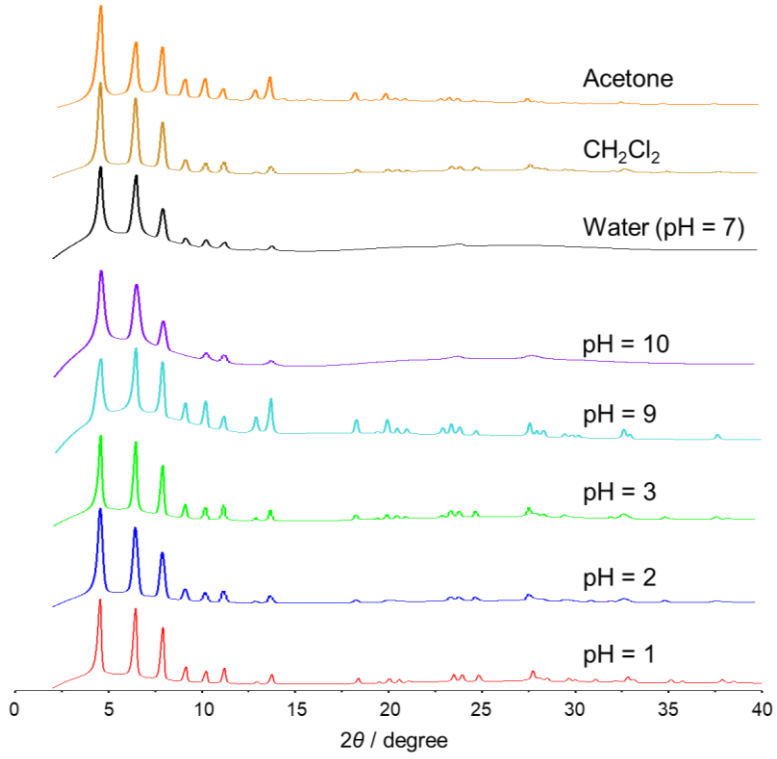

Figure 2-9. Powder X-ray diffraction patterns of **NCP$_{MOF}$** after immerse in different chemical environments for 24 h.

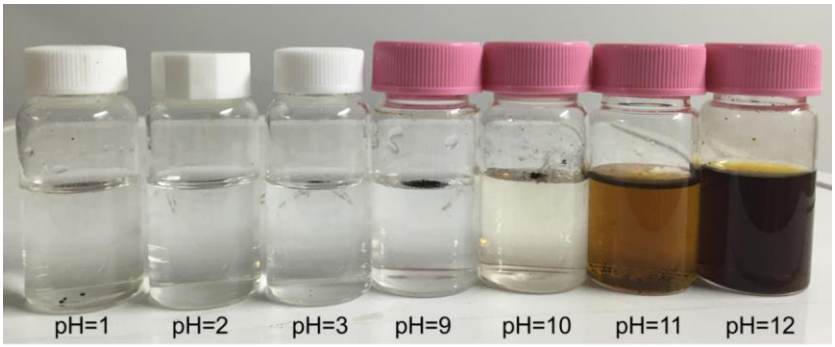

Figure 2-10. Photographs of **NCP$_{MOF}$** in aqueous solutions with different pH values.

2.6 Optical Properties

These stable Zr-MOFs demonstrated unique absorption/emission properties. The absorption spectra of **NCP$_{MOF}$** and **TPP$_{MOF}$** dispersed in KBr matrix exhibited red-shifted absorption band tailing more than 1000 nm (Figure 2-11, see Figure 2-21 for the spectra of **MeNCP$_{MOF}$**).[12] The characteristic features of the broaden Soret and Q bands of NCP derivative could be attributed to the effect of through-bond interactions of the structurally arranged NCP chromophores. Notably, the near IR emissions peaked around 900 nm were observed in the aqueous suspensions the powder samples. The N-methylated **MeNCP$_{MOF}$** exhibited a stronger emission relative to that of **NCP$_{MOF}$** (the fluorescence quantum yield of **MeNCP$_{MOF}$** is 2.39 times that of **NCP$_{MOF}$**), suggesting the proton-transfer reaction inside the macrocycle may govern the radiative decay process.

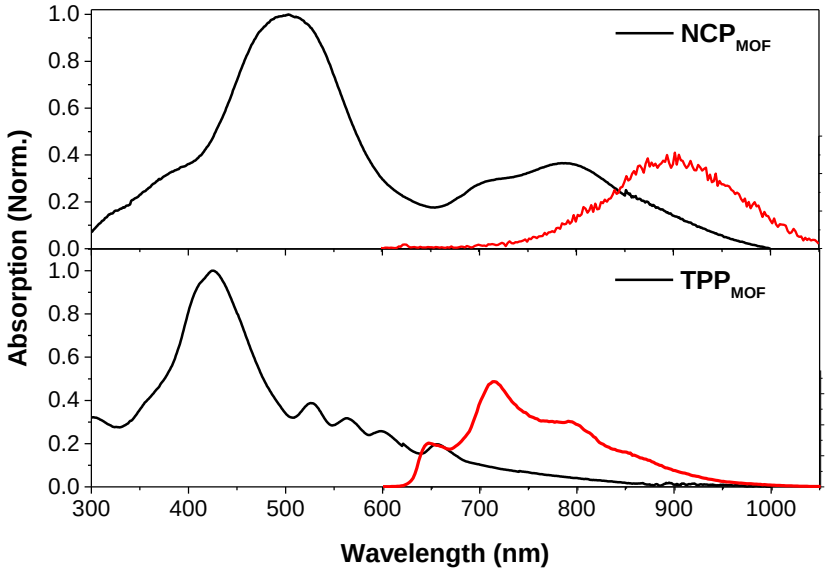

Figure 2-11. Absorption (in the KBr pellets) and emission (in the DMF suspensions) spectra of **NCP$_{MOF}$** (upper) and **TPP$_{MOF}$** (lower) (λ_{ex} = 532 nm)

Compared with the ligands, both **NCP$_{MOF}$** and **TPP$_{MOF}$** demonstrated redshifted absorption and emission spectra. This phenomenon can be understood by considering the interchromophoric interaction existing in the frameworks. In MOFs, TPP and NCP ligands are close to each other in location, leading to an interaction that is similar to the ones observed in aggregation. However, as the ligands are not bound through π-π interaction in MOFs, the distance between two macrocycles can be tuned through the design of MOF topology, which is considered one of the huge advantages of MOFs in the optical property design.

In a report of Zr-based porphyrinic MOF by S. N. White, both steady-state emission spectra and transient fluorescence decay are studied for MOF-525 and NU-902, in which redshifted and broaden absorption and emission were observed with a shorter decay lifetime compared with the monomer ligand.[20] Interchromophoric interaction was considered the cause. The coupling among excited ligand molecules results in the delocalization of excitons in MOFs in which the merges of the absorption bands occur and lead to the broadening and bathochromic shift. This delocalization also increases decay ways of excitons, causing a shorter lifetime of emission in MOF than monomers.

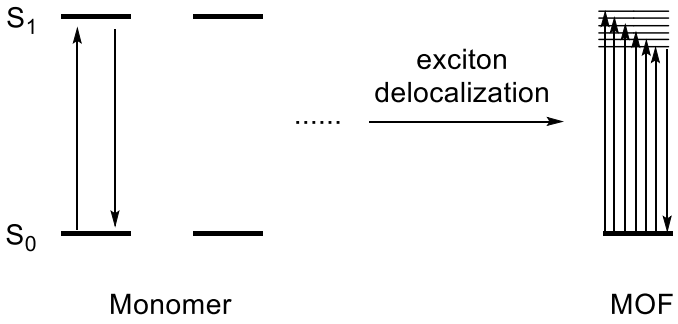

Figure 2-12. In MOFs, delocalization of exciton leads to the merge of ligand energy bands, which then causes the broadening and bathochromic shift of absorption and emission spectra.

2.7 Conclusion

In summary, novel zirconium-based metal-organic frameworks, **NCP$_{MOF}$** and **MeNCP$_{MOF}$** have been synthesized under the aforementioned reaction conditions by using N-confused porphyrin carboxylic acid derivatives. The PXRD pattern analysis with Reitveld refinement proved the compounds have face-centered cubic ftw topologies. Along with great chemical and thermal stabilities, they have demonstrated unique vis-to-near IR absorption/emission properties, which may lead to the near-IR-responsible photonic materials as well as efficient heterogeneous photocatalysts.

2.8 Experimental Section

2.8.1 Materials and Instruments

Commercially available solvents and reagents were used without further purification unless otherwise mentioned. Thin-layer chromatography (TLC) was carried out on aluminum sheets coated with silica gel 60 (Merck 5554). Preparative separations were performed by silica gel flash column chromatography (KANTO Silica gel 60N, spherical, neutral, 40–50 μm) and silica gel gravity column chromatography (KANTO Silica Gel 60N, spherical, neutral, 63–210 μm). ^{1}H NMR spectra were recorded on a JEOL JNM-ECX Series of NMR (500 MHz) using the residues of deuterated solvents as internal references. UV/vis/NIR absorption spectra were recorded on Shimadzu UV-3150PC and JASCO V-770 spectrophotometers. High-resolution mass (HRMS) spectra were obtained in fast atom bombardment (FAB mode) with 3-nitrobenzyl alcohol (NBA) as a matrix on a JEOL LMS-HX-110 spectrometer and a Bruker Autoflex-KK matrix-assisted laser desorption ionization time-of-flight (MALDI-TOF) mass spectroscopic analyzer. Scanning electron microscope (SEM) images were recorded with a JEOL JSM-6701F instrument. Powder X-ray diffractions (PXRD) were recorded with a Rigaku SmartLab Intelligent X-ray diffraction (XRD) instrument. Thermogravimetry (TG) analyses were completed with a Hitachi High-Tech Science Corporation TG/DTA7300 analyzer. Gas adsorption experiments were completed with high precision gas/vapor adsorption measurement instrument of MicrotracBEL BELSORP-aqua. The X-ray photoelectron spectroscopy (XPS) was measured at room temperature using an AXIS-ULTRA (Shimadzu) in which indium was used as the substrate. Synthesis of MOFs was carried out in an EYELA personal organic synthesizer (Chemi-station PPM-5512).

2.8.2 Synthesis of Ligand

Synthesis of 2-Aza-5,10,15,20-tetrakis(*p*-methoxycarbonylphenyl)-21-carba- porphyrin (1): [21]

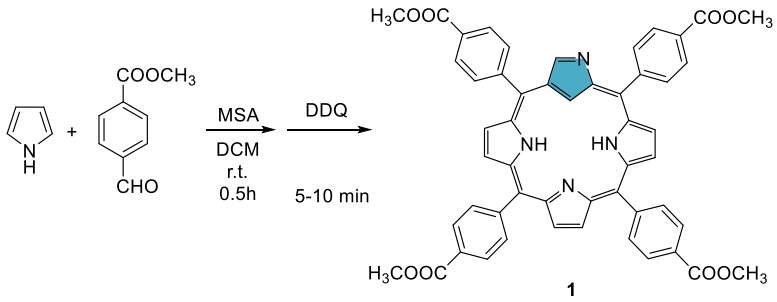

To a DCM solution (3 L) of methyl *p*-formylbenzoate (4924.8 mg, 30 mmol) was added purified pyrrole (2.08 mL, 30 mmol). After 1.36 mL of methanesulfonic acid was added, the solution was stirred for 0.5 h at room temperature. Then 6 g of DDQ was added. After 5 min, the mixture was monitored on TLC, and the triethylamine is added to quench the reaction. The solution was passed through an alumina column and then

extracted from CH_2Cl_2. Then the mixture was dissolved in a DCM/MeOH (99:1(v/v)) solution, passed through a silica gel column with an eluent of DCM/MeOH (99:1(v/v)) solution to extract the product. After drying under vacuum, the weight of the green solid is measured (1044.22 mg, 1.23 mmol, 16% yield). ^{1}H NMR (500 MHz, $CDCl_3$) δ 8.97 (d, J = 4.9 Hz, 1H), 8.91 (d, J = 4.8 Hz, 1H), 8.75 (s, 1H), 8.61 (d, J = 5.0 Hz, 1H), 8.57 (d, J = 4.8 Hz, 1H), 8.53 (dd, J = 15.2, 6.7 Hz, 6H), 8.44 (d, J = 6.5 Hz, 6H), 8.40 (d, J = 8.1 Hz, 2H), 8.24 (t, J = 8.3 Hz, 4H), 4.10 (d, J = 13.1 Hz, 12H), -2.31 – -2.62 (m, 2H), -5.06 (s, 1H).; MALDI-TOF-MS m/z = 847.119 ([M+1$^+$]).

_N_-methyl-2-Aza-5,10,15,20-tetrakis(_p_-methoxycarbonylphenyl)-21-carba- porphyrin (1-Me) [22]

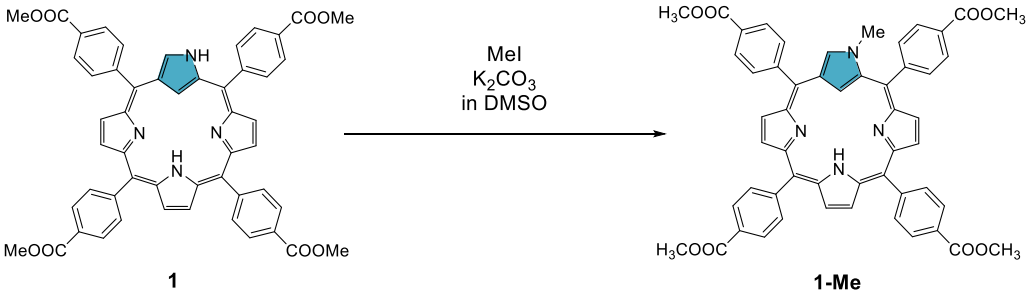

1 **1-Me**

_N_-methylation of **1** was conducted by using the reported method In a 200 mL of round flask, **1 (**300 mg, 0.35 mmol) and K_2CO_3 (147 mg, 3 equiv, 1.06 mmol) was dissolved in the mixed solution of 20 mL of THF and 0.8 mL of DMSO under N_2 atmosphere. After CH_3I (88 μL, 4 equiv, 1.41 mmol) was added into the flask, the mixture was stirred at 75 °C overnight. After completion of the reaction, the mixture was cooled down to room temperature. The resulting mixture was concentrated in vacuo. The residue was purified by silica gel column chromatography using DCM/MeOH (99:1(v/v)) as an eluent. The dark bluish solid compound **1-Me** was obtained by recrystallization. Yield 250.72 mg, 0.29 mmol, 83% yield. ^{1}H NMR (500 MHz, $CDCl_3$, ppm): δ 8.34 (d, J = 7.8 Hz, 2H, Ar-H), 8.30 (d, J = 8.0 Hz, 2H, Ar-H), 8.27 (d, J = 5.8 Hz, 4H, β-H), 8.05 (d, J = 7.8 Hz, 2H, Ar-H), 8.01 (d, J = 7.9 Hz, 2H, Ar-H), 7.91 (m, 5H, Ar-H+β-H), 7.79 (d, J = 4.6 Hz, 1H, β-H), 7.75–7.71 (m, 2H, Ar-H), 7.49 (d, J = 4.6 Hz, 1H, β-H), 7.45 (d, J = 4.6 Hz, 1H, β-H), 7.18 (s, 1H, α-H), 4.05 (s, 6H, COOMe), 4.04 (s, 6H, COOMe), 3.67 (s, 1 H, inner NH), 3.41 (s, 3H, NCH_3), 1.15 (s, 1H, CH); HRMS (FAB): calcd for $C_{53}H_{40}N_4O_8$ ([M]$^+$), 860.9230, found 860.7091; UV-vis (CH_2Cl_2, nm): λ_{max} = 365.5, 451, 661, 715.5.

Synthesis of Tetrakis(4-carboxyphenyl)_N_-Confused Porphyrin (2): [23]

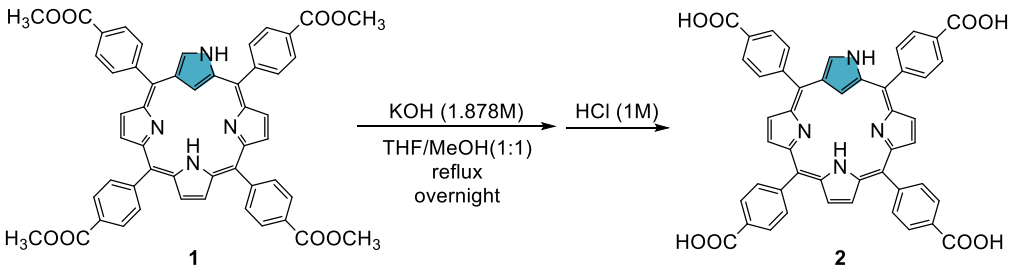

A solution of KOH (1.13 g, 20.19 mmol) in H_2O (25 mL) was added to a mixture of **1** (300 mg) in THF/MeOH (50 mL, 1:1(v/v)). The mixture was stirred and refluxed overnight. After monitoring the consumption of **1**, the reaction was cooled down to room temperature, and the organic solvents were evaporated. Additional water was added to the resulting water phase and the mixture was heated until the solid was fully dissolved, then the homogeneous solution was acidified with 1 M of HCl until no further precipitate was detected. The green solid was collected by filtration, washed with water and dried in vacuum. Then the solid was ground into powder and further washed by water three times. After filtration and drought, compound **2** was obtained (271.65 mg, 0.34 mmol, 96% yield). ^{1}H NMR (500 MHz, DMSO-d_6) δ 13.14 (d, J = 60.0 Hz, 4H), 8.29 (d, J = 8.0 Hz, 2H), 8.25 (dd, J = 13.8, 7.8 Hz, 7H), 8.07 (d, J = 7.8 Hz, 4H), 8.00 (d, J = 7.8 Hz, 7H), 7.94 (d, J = 4.5 Hz, 1H), 0.48 (s, 1H).

***N*-methyl-tetrakis(4-carboxyphenyl) N-confused porphyrin (2-Me):**

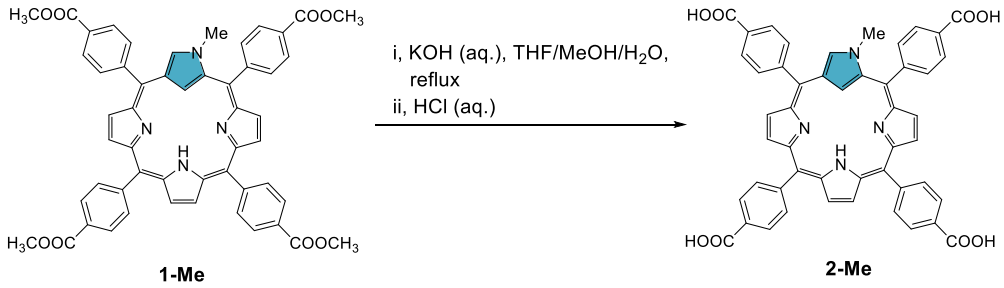

A solution of KOH (1.15 g, 20.50 mmol) in H_2O (25 mL) was added to a mixture of **1-Me** (310 mg, 0.36 mmol) in THF/MeOH (50 mL, 1:1 (v/v)). The solution was stirred overnight under reflux. The resulting reaction mixture was cooled down to room temperature, and the organic solvents were removed *in vacuo*. Water was then added to the residue to dissolve completely. The precipitates were formed via slow addition of 1 M HCl aq. to a final pH of 3. The dark green solid was collected by filtration, washed with water and dried *in vacuo*. Yield of **2-Me**; 273.07 mg, 0.34 mmol (94% yield). ^{1}H NMR (500 MHz, DMSO-d_6, ppm): δ 13.19 (s, 4H), 8.27 (s, 1H), 8.26 (s, 2H), 8.24 (s, 1H), 8.22 (d, J = 3.6 Hz, 2H), 8.21 (d, J = 3.5 Hz, 2H), 8.15 (s, 1H), 8.08–8.04 (m, 2H), 8.03 (d, J = 7.9 Hz, 2H), 7.98 (s, 1H), 7.96 (s, 2H), 7.95 (d, J = 4.2 Hz, 2H), 7.91 (s, 2H), 7.79 (d, J = 4.5 Hz, 1H), 7.53 (d, J = 4.6 Hz, 1H), 7.48 (d, J = 4.5 Hz, 1H), 3.54 (s, 3H), 2.35 (s, 1H), 0.48 (s, 1H). HRMS(FAB): calcd for $C_{49}H_{33}N_4O_8$ ([M+H]$^+$) 805.8230, found 805.2298. UV-vis (DMF, nm); λ_{max} = 364, 450, 650.5, 711.5.

2.8.3 Synthesis of Metal-Organic Frameworks

The reference sample, MOF-525 was prepared by the reported method. $ZrCl_4$ (75 mg), NCP (compound **2** or **2-Me**, 50 mg) and benzoic acid (2700 mg) were dissolved in 8 mL of DMF with ultrasonic for over 1 h. The mixture was then heated and stirred in 120 °C oven for 48 h. After cooling down to room temperature slowly, the solid was obtained by filtration.

Yield for **NCP$_{MOF}$**; 61.01 mg (48.8%). Anal. calcd. (%) for: C, 56.91; H, 2.70; N, 5.53%. Found: C, 56.97; H, 4.95; N, 5.56%.

Yield for **MeNCP$_{MOF}$**; 61.21 mg (49.0%). Anal. calcd. (%) for: C, 57.31; H, 2.86; N, 5.46%. Found: C, 57.23; H, 5.36; N, 5.37%.

2.8.4 Characterization

Crystal Structure Modeling

The structures of **NCP$_{MOF}$** and **MeNCP$_{MOF}$**, including cell parameters and atomic positions, were modeled using Crystal Studio software. The structures were generated using the relevant space group ($Pm3\bar{m}$) and the cell parameters were used as obtained from a Pawley refinement. The atomic positions were generated according to the MOF-525 containing a TCPP-H_2 and the cube octahedron $Zr_6O_4(OH_4)(CO_2)_{12}$ unit. The geometry optimization routine with the universal force field functional gave the model. The structures of the resulting models were determined by the Rietveld refinement.

Table 2-3. Statistics from **NCP$_{MOF}$** and **MeNCP$_{MOF}$**

Name	**NCP$_{MOF}$**	**MeNCP$_{MOF}$**
Composition	$Zr_6O_{32}N_{12}C_{144}$	$Zr_6O_{32}N_{12}C_{147}$
Formula (g mol^{-1})	3051.7320	3093.8130
Crystal system	Cubic	Cubic
Space group	*P*m3$\bar{m}$	*P*m3$\bar{m}$
a (Å)	19.39	19.54
V (Å^3)	7291.23	7465.30
R_p (%)	4.35	4.59
R_{wp} (%)	12.38	12.61

2.9 Supporting Data

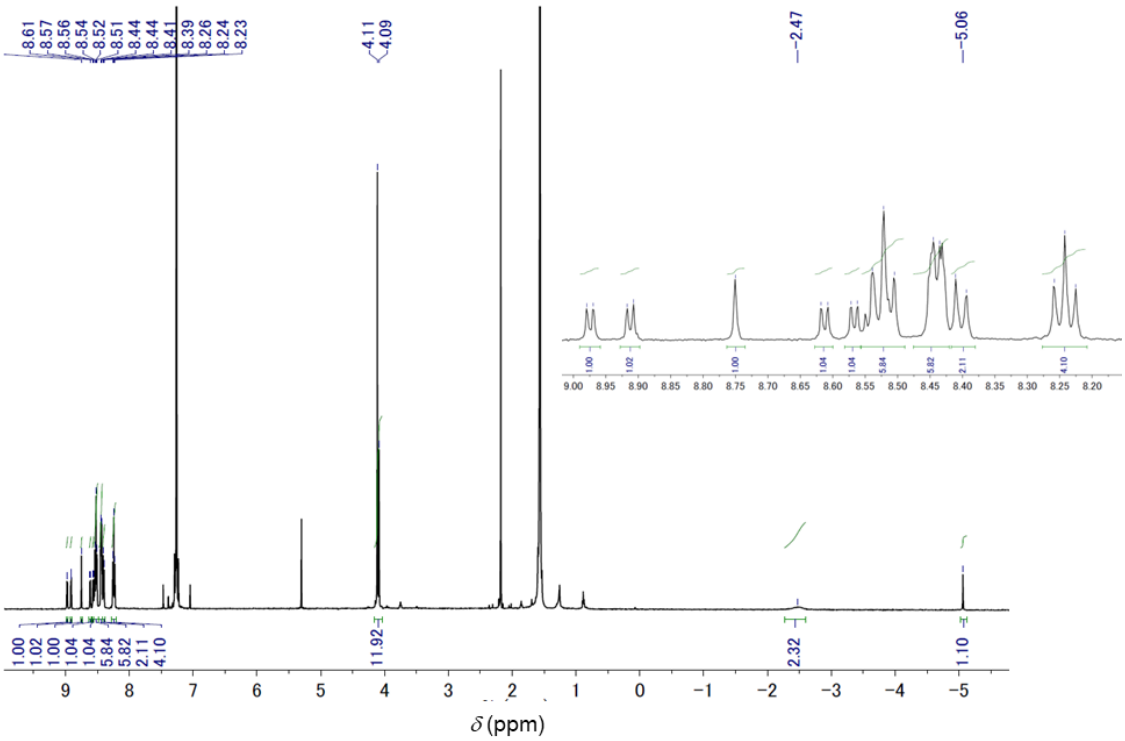

Figure 2-13. ^{1}H NMR spectrum (500 MHz) of NCTPP (**1**) in $CDCl_3$

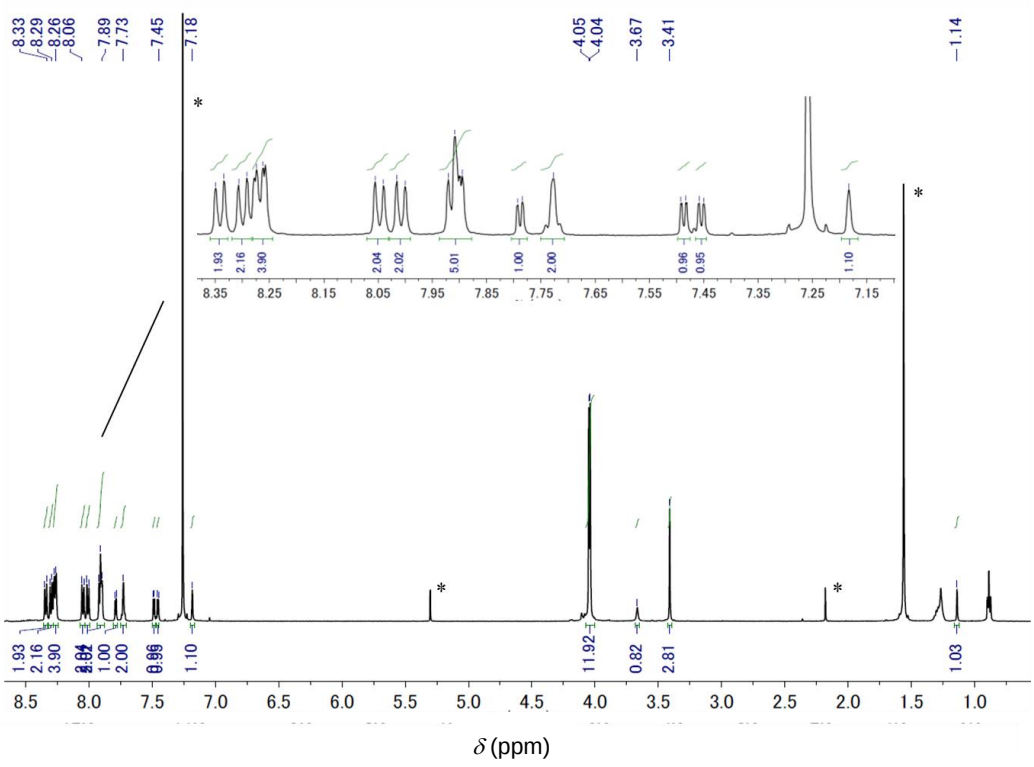

Figure 2-14. ^{1}H NMR spectrum of **1-Me** in $CDCl_3$.

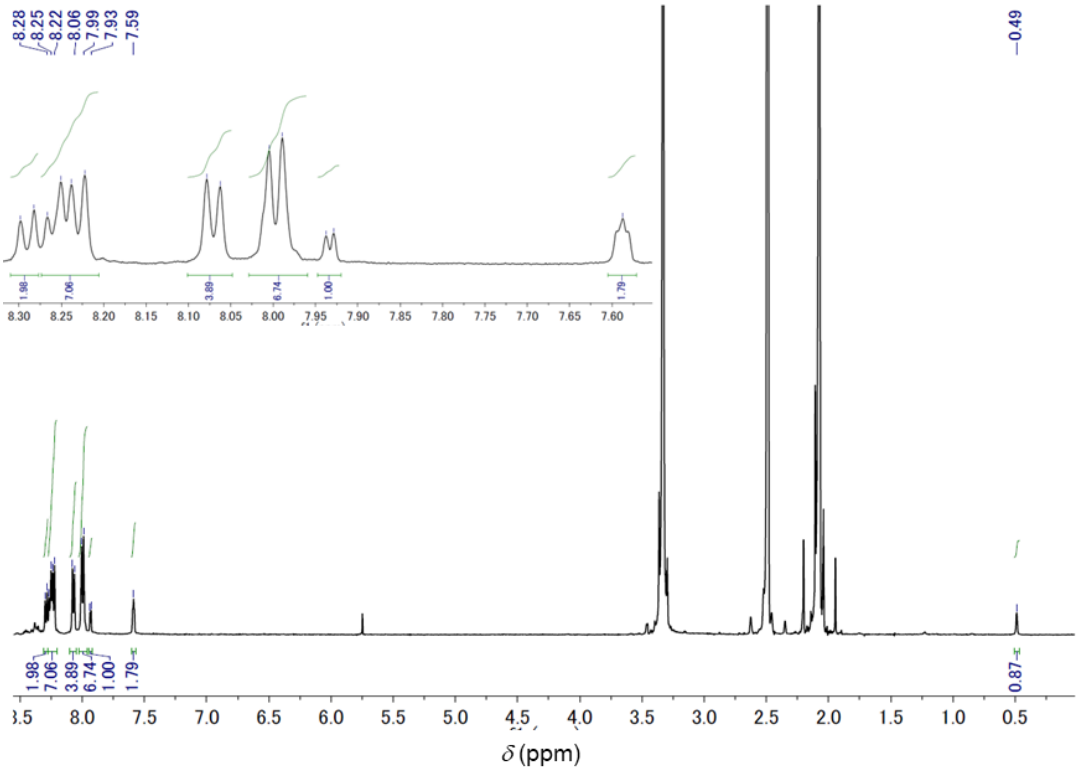

Figure 2-15. ^{1}H NMR spectrum of **2** in DMSO-d_6.

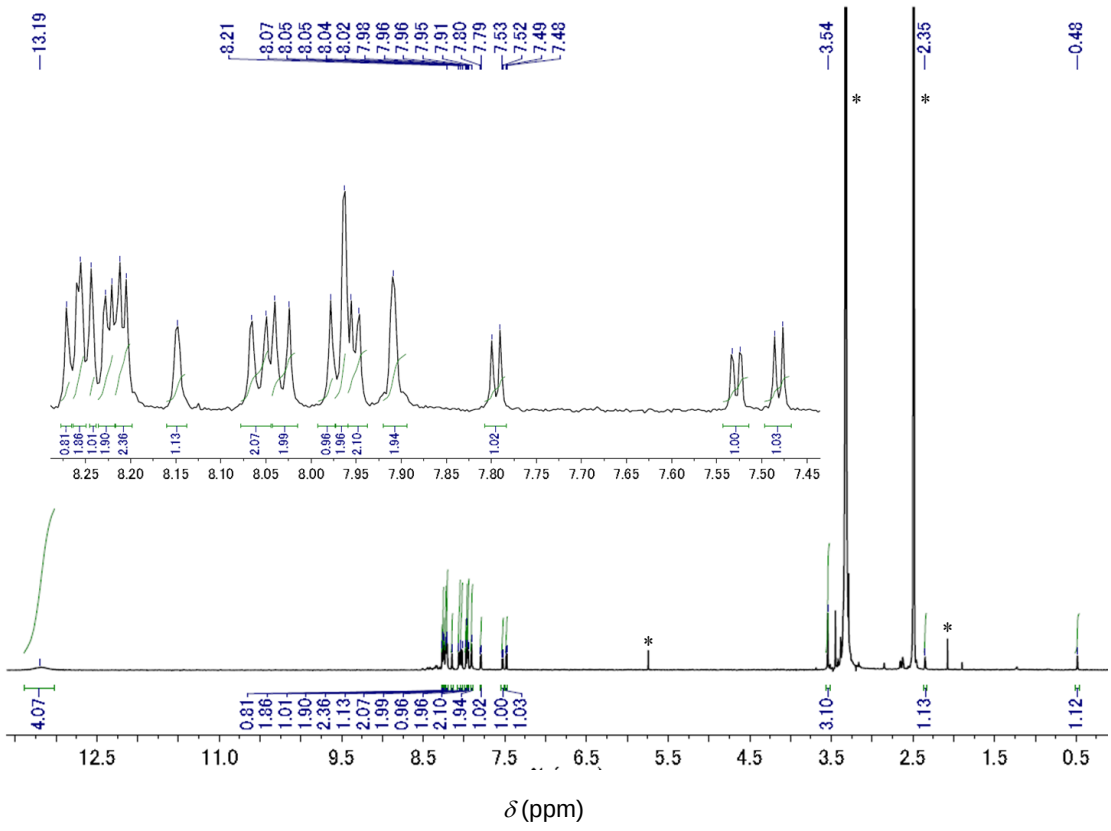

Figure 2-16. ^{1}H NMR spectrum of **2-Me** in DMSO-d_6.

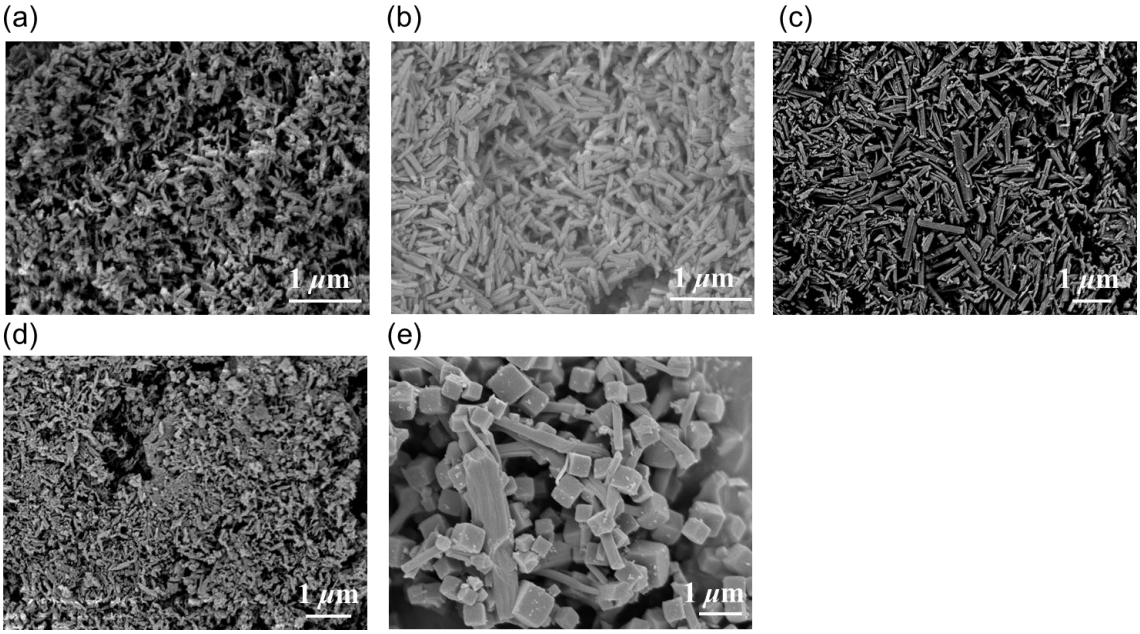

Figure 2-17. Selected SEM images of $\mathbf{NCP_{MOF}}$ fabricated under various conditions: (a) entry 1, (b) entry 2, (c) entry 3, (d) entry 5, and (e) entry 8.

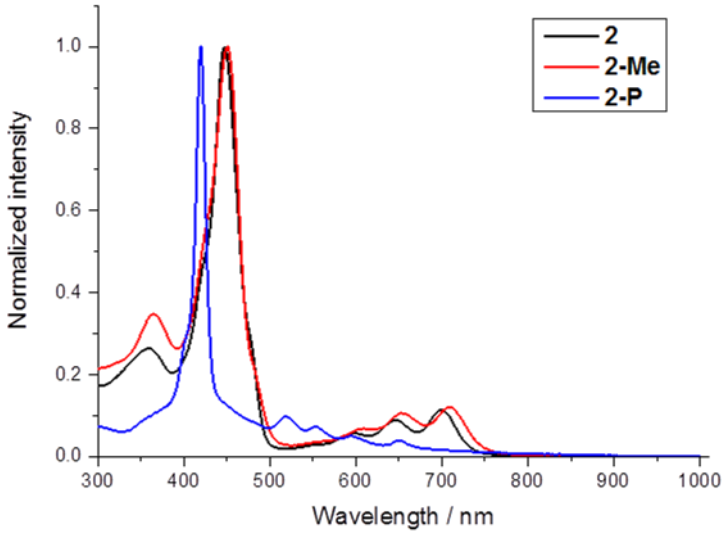

Figure 2-18. UV/vis spectra of NCP (**2**, black), **MeNCP** (**2-Me**, red), and TPP (**2-P**, blue) in DMF.

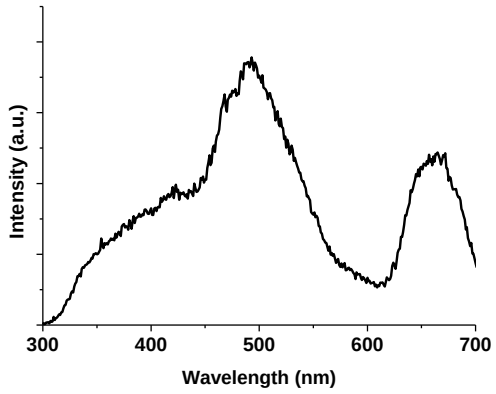

Figure 2-19. The excitation spectrum of the aqueous suspension of **MeNCP$_{MOF}$** under probing at 850 nm. Below the wavelength at 700 nm, the spectrum is not corrected.

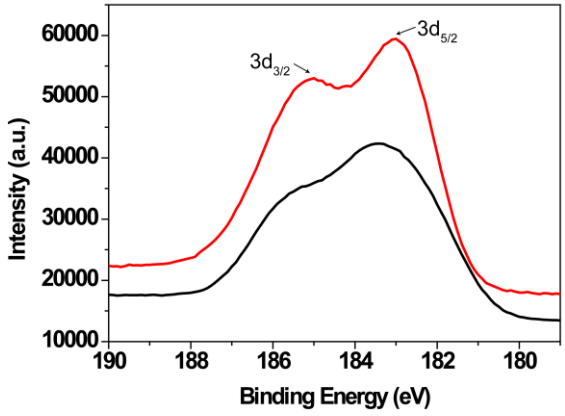

Figure 2-20. XPS spectra of **NCP$_{MOF}$** (black) and **MeNCP$_{MOF}$** (red)

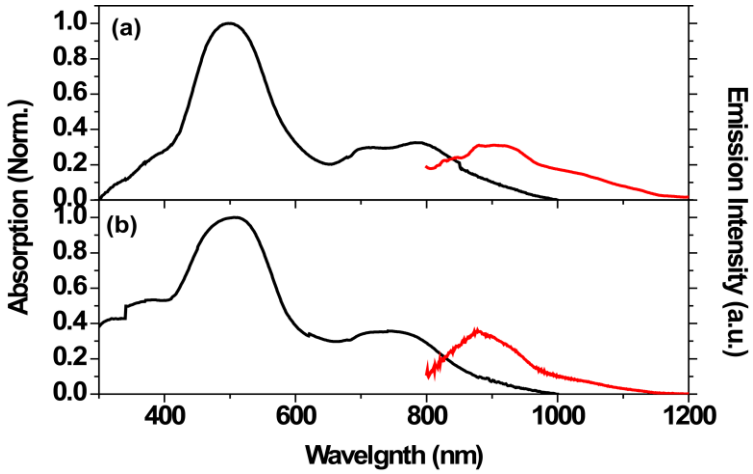

Figure 2-21. UV-vis absorption spectrum of the KBr pellet containing (a) **NCP$_{MOF}$** and (b) **MeNCP$_{MOF}$**.

References

1. Bai, Y.; Dou, Y.; Xie, L. H.; Rutledge, W.; Li, J. R.; Zhou, H. C., *Chem. Soc. Rev.* **2016,** *45* (8), 2327-2367.
2. (a) Huang, N.; Yuan, S.; Drake, H.; Yang, X.; Pang, J.; Qin, J.; Li, J.; Zhang, Y.; Wang, Q.; Jiang, D., *J. Am. Chem. Soc.* **2017,** *139* (51), 18590-18597; (b) Pereira, C.; Simões, M.; Tomé, J.; Almeida Paz, F., *Molecules* **2016,** *21* (10), 1348.
3. Feng, D.; Gu, Z. Y.; Li, J. R.; Jiang, H. L.; Wei, Z.; Zhou, H. C., *Angew. Chem. Int. Ed. Engl.* **2012,** *51* (41), 10307-10310.
4. Wang, H.; Dong, X.; Lin, J.; Teat, S. J.; Jensen, S.; Cure, J.; Alexandrov, E. V.; Xia, Q.; Tan, K.; Wang, Q., *Nat. Commun.* **2018,** *9* (1), 1745.
5. Li, C.; Huang, J.; Zhu, H.; Liu, L.; Feng, Y.; Hu, G.; Yu, X., *Sens Actuators B: Chem.* **2017,** *253*, 275-282.
6. (a) Meng, A. N.; Chaihu, L. X.; Chen, H. H.; Gu, Z. Y., *Sci. Rep.* **2017,** *7* (1), 6297; (b) Park, J.; Jiang, Q.; Feng, D.; Mao, L.; Zhou, H.-C., *J. Am. Chem. Soc.* **2016,** *138* (10), 3518-3525.
7. Lin, W.; Hu, Q.; Jiang, K.; Yang, Y.; Yang, Y.; Cui, Y.; Qian, G., *J. Solid State Chem.* **2016,** *237*, 307-312.
8. Xu, L.; Luo, Y. P.; Sun, L.; Xu, Y.; Cai, Z. S.; Fang, M.; Yuan, R. X.; Du, H. B., *Chemistry* **2016,** *22* (18), 6268-6276.
9. Deria, P.; Gomez-Gualdron, D. A.; Hod, I.; Snurr, R. Q.; Hupp, J. T.; Farha, O. K., *J. Am. Chem. Soc.* **2016,** *138* (43), 14449-14457.
10. (a) Feng, D.; Chung, W. C.; Wei, Z.; Gu, Z. Y.; Jiang, H. L.; Chen, Y. P.; Darensbourg, D. J.; Zhou, H. C., *J. Am. Chem. Soc.* **2013,** *135* (45), 17105-17110; (b) Feng, D.; Gu, Z. Y.; Chen, Y. P.; Park, J.; Wei, Z.; Sun, Y.; Bosch, M.; Yuan, S.; Zhou, H. C., *J. Am. Chem. Soc.* **2014,** *136* (51), 17714-17717; (c) Feng, D.; Jiang, H. L.; Chen, Y. P.; Gu, Z. Y.; Wei, Z.; Zhou, H. C., *Inorg. Chem.* **2013,** *52* (21), 12661-12667; (d) Jiang, H. L.; Feng, D.; Wang, K.; Gu, Z. Y.; Wei, Z.; Chen, Y. P.; Zhou, H. C., *J. Am. Chem. Soc.* **2013,** *135* (37), 13934-13938.
11. Morris, W.; Volosskiy, B.; Demir, S.; Gandara, F.; McGrier, P. L.; Furukawa, H.; Cascio, D.; Stoddart, J. F.; Yaghi, O. M., *Inorg. Chem.* **2012,** *51* (12), 6443-6445.
12. Izzetoglu, M.; Bunce, S. C.; Izzetoglu, K.; Onaral, B.; Pourrezaei, K., *IEEE Eng. Med. Biol. Mag.* **2007,** *26* (4), 38.
13. (a) He, L.; Brasino, M.; Mao, C.; Cho, S.; Park, W.; Goodwin, A. P.; Cha, J. N., *Small* **2017,** *13* (24); (b) Li, Y.; Di, Z.; Gao, J.; Cheng, P.; Di, C.; Zhang, G.; Liu, B.; Shi, X.; Sun, L. D.; Li, L.; Yan, C. H., *J. Am. Chem. Soc.* **2017,** *139* (39), 13804-13810.
14. (a) Chmielewski, P. J.; Latos‐Grażyński, L.; Rachlewicz, K.; Glowiak, T., *Angew. Chem. Int. Ed. Engl.* **1994,** *33* (7), 779-781; (b) Furuta, H.; Asano, T.; Ogawa, T., *J. Am. Chem. Soc.* **1994,** *116* (2), 767-768.
15. Lee, J. S.; Lim, J. M.; Toganoh, M.; Furuta, H.; Kim, D., *Chem. Commun.* **2010,** *46* (2), 285-287.

16. Furuta, H.; Ishizuka, T.; Osuka, A.; Dejima, H.; Nakagawa, H.; Ishikawa, Y., *J. Am. Chem. Soc.* **2001,** *123* (25), 6207-6208.
17. Lu, K.; He, C.; Lin, W., *J. Am. Chem. Soc.* **2014,** *136* (48), 16712-16715.
18. Lu, K.; He, C.; Lin, W., *J. Am. Chem. Soc.* **2015,** *137* (24), 7600-7603.
19. Huang, N.; Yuan, S.; Drake, H.; Yang, X.; Pang, J.; Qin, J.; Li, J.; Zhang, Y.; Wang, Q.; Jiang, D., *J. Am. Chem. Soc.* **2017,** *139* (51), 18590-18597.
20. (a) Deria, P.; Yu, J.; Balaraman, R. P.; Mashni, J.; White, S. N., *Chem Commun (Camb)* **2016,** *52* (88), 13031-13034; (b) Lim, J. M.; Kim, P.; Yoon, M.-C.; Sung, J.; Dehm, V.; Chen, Z.; Würthner, F.; Kim, D., *Chem. Sci.* **2013,** *4* (1), 388-397; (c) Piet, J. J.; Taylor, P. N.; Wegewijs, B. R.; Anderson, H. L.; Osuka, A.; Warman, J. M., *J. Phys. Chem. B* **2001,** *105* (1), 97-104.
21. Geier, G. R.; Haynes, D. M.; Lindsey, J. S., *Org. Lett.* **1999,** *1* (9), 1455-1458.
22. (a) Qu, W.; Ding, T.; Cetin, A.; Harvey, J. D.; Taschner, M. J.; Ziegler, C. J., *J. Org. Chem.* **2006,** *71* (2), 811-814; (b) Toganoh, M.; Yamamoto, T.; Hihara, T.; Akimaru, H.; Furuta, H., *Org. Biomol. Chem.* **2012,** *10* (22), 4367-4374.
23. Ikawa, Y.; Ogawa, H.; Harada, H.; Furuta, H., *Bioorg. Med. Chem. Lett.* **2008,** *18* (24), 6394-6397.

Chapter 3. Hierarchical Hybrid Metal-Organic Frameworks: Tuning the Visible/Near Infrared Optical Properties by Combination of Isomeric Porphyrin Ligands

3.1 Introduction

3.1.1 MOFs Based on N-Confused Porphyrin

As is introduced in former chapters, MOFs are one of the highly versatile and flexible materials possessing the potentials for the practical applications such as gas storage[1], catalysis[2], sensors[3], drug delivery system[4], energy storage[5] and so forth, due to their uniform and tailorable pore/surface structures. In particular, zirconium-based MOFs have attracted great attention due to the rich topological design, outstanding hydrothermal stability, and intriguing properties[6]. In chapter 2, the author succeeded in the synthesis of a novel porphyrinic Zr-MOF alternative (**NCP_{MOF}**) consisting of isomeric porphyrin linkers, N-confused porphyrins (NCP)[7] (Figure 3-1a). Due to the identical tetrapyrrolic backbone as the regular porphyrin (i.e., TPP) and a modified pyrrole ring moiety which is connecting to surrounding meso-carbons at the α and β'-position, **NCP_{MOF}** shows intriguing near-infrared optical absorption and emission up to λ_{max} ~900 nm, which are remarkably red-shifted compared to those of **TPP_{MOF}** (i.e., **MOF-525**[8]). These optical responses are originated from the destabilization of HOMO energy of NCP units caused by the electronic perturbation of the parent 18π-circuit of NCP[9]. Furthermore, NCP serves a unique organometallic coordination site at the NNNC core, which can give rise to the catalytic ability such as carbene-insertions into alkenes.[10]

3.1.2 Hybridized MOFs

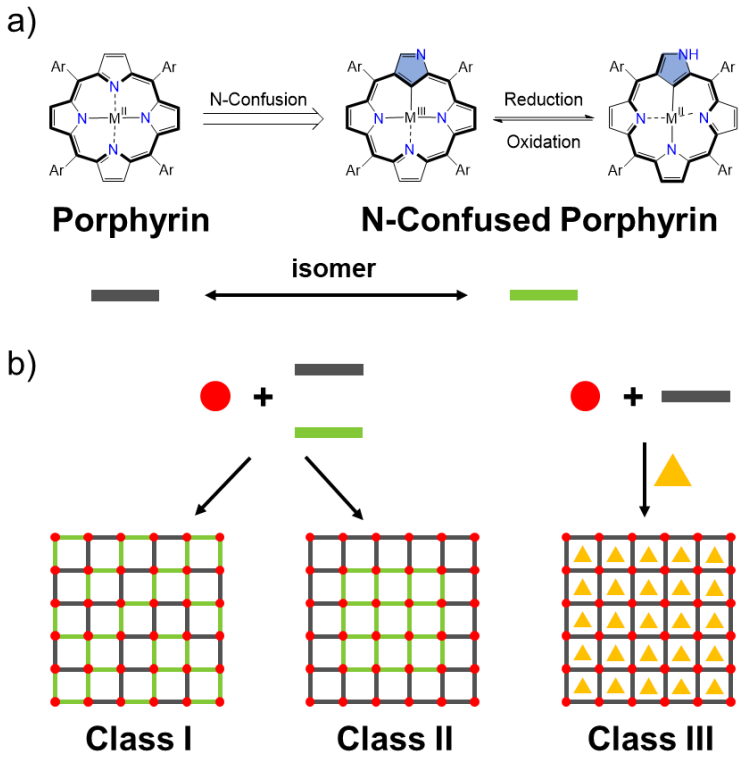

Figure 3-1. (a) Chemical structures of a regular porphyrin and an N-confused porphyrin used in this work: Ar = aryl groups, M = freebase or metals. (b) Schematic description of the classified structures of hybrid MOFs; Class I-III. The red circle, gray bar, green bar, and orange triangle indicate the metal ion, porphyrin linker, isomeric linker and guest molecule, respectively.[11]

The author has established the preparation of the most energetically stable "ftw" topology-pure crystals of **NCP$_{MOF}$** under the solvothermal conditions. The advanced procedure for the phase-pure synthesis of the porphyrinic Zr-MOFs via seed-mediated crystal growth[12] thus greatly encouraged us to create novel hetero-ligand hybrid MOFs combining both regular- and N-confused porphyrin building blocks.

To date, hybridization of different components in MOFs has been proved as an effective approach for fine-tuning of the intrinsic physical properties via combinations of distinct features of the materials[11]. These are generally classified into three types of hybrid MOFs; "solid-solution" Class I, core/shell Class II and guest-encapsulated Class III. (Figure 3-1b) Among them, the representative core/shell-type Class II hybrid MOF; ZIF-8@ZIF-67[13] was successfully synthesized by applying a seed-mediated growth. The kinetic analysis of the reaction system has revealed the construction of class I and class II hybrid MOF depends highly on the reaction conditions[14]. This strategy would produce new effective light-harvesting solid materials with switching[15] and energy transfer[16] functions as introducing two porphyrin ligands in our platform.

3.1.3 Purpose of This Chapter

In this chapter, the author reports the synthesis of novel hierarchical hybrid Zr-MOFs composed of TPP and the N-confused isomer (i.e., **NCP_{MOF}@TPP_{MOF}** and **TPP_{MOF}@NCP_{MOF}**) by seed-guided ligand exchange reactions. Through spectroscopic and microscopic analysis, these hybrid MOFs have Class II core/shell structures and exhibit distinct photophysical properties such as broad light photon collection from visible to near IR region by taking two dye components. Furthermore, dependent on the components at the surface of the MOFs, photo-sensitizing singlet oxygen generation was achieved using heterogeneous MOF solution.

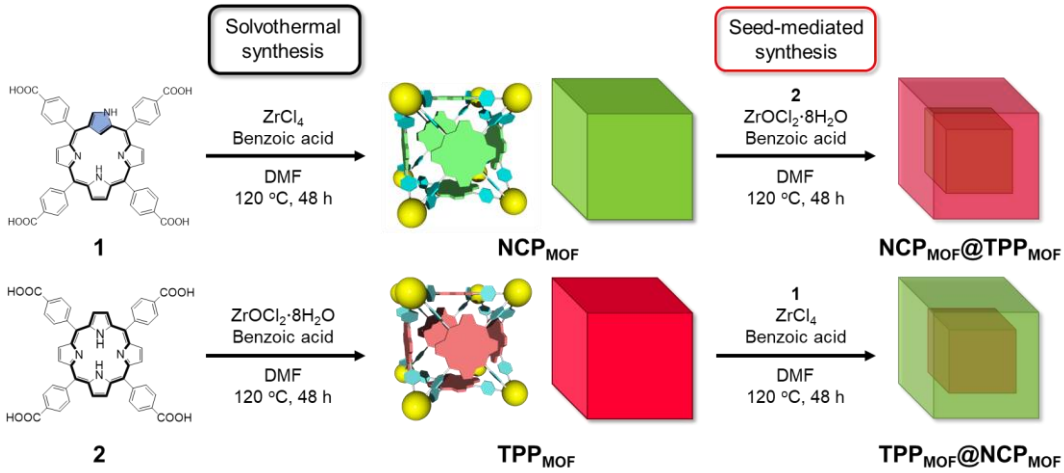

Scheme 3-1. Schematic description for synthetic strategies of hierarchical hybrid MOFs, **NCP_{MOF}@TPP_{MOF}**, and **TPP_{MOF}@NCP_{MOF}** through a seed-mediated ligand exchange reaction.

3.2 Synthesis of Hybrid MOFs

3.2.1 Synthesis of Porphyrin Ligands

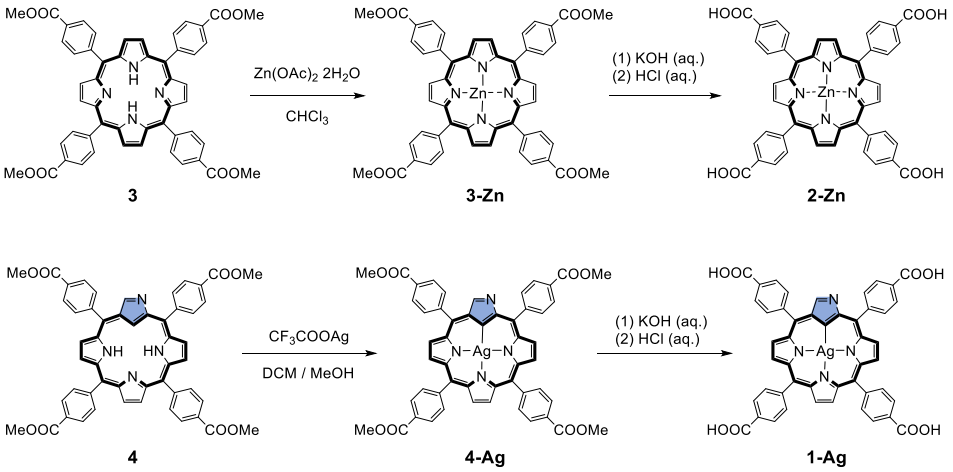

Scheme 3-2. Organic ligands synthesized in this Chapter.

Organic ligands **1** and **2** were synthesized the same way as chapter 2[17]. For the purpose of elementary analysis, metalated organic ligands (**1-Ag**[18] and **2-Zn**[19]) were also synthesized as reported. (Scheme 3-2)

2-Zn was synthesized by metalation of **3** with $Zn(OAc)_2 \cdot 2H_2O$ in $CHCl_3$ for 0.5 h, followed by the purification by silica gel column chromatography with an eluent of DCM/MeOH (99:1(v/v)). After crystallization, the hydrolysis of **3-Zn** was conducted to give **2-Zn**. (See the details in Section **3.6**)

1-Ag was synthesized by metalation of **4** with CF_3COOAg in dry CH_2Cl_2 and MeOH, followed by the purification by silica gel column chromatography, with an eluent of DCM/MeOH (99:1(v/v)). After crystallization, the hydrolysis of **4-Ag** was conducted to give **1-Ag**. (See details in section **3.6**).

3.2.2 Synthesis of MOFs and Characterization

3.2.2.1 Synthesis of Hybrid MOFs

Table 3-1. Reaction optimization for hybrid MOF fabrication using seed-mediated synthesis.

Entry	Organic linker / mg	DMF / mL	Zr reagent / mg	Seed / mg	Benzoic acid / mg	Reaction time / h	Results
1	50 [a]	8	103 [f]	20 [g]	2700	48	Crystalline powder
2	50 [a]	8	75 [e]	20 [h]	2700	48	Crystalline powder
3	50 [b]	8	103 [f]	20 [g]	2700	48	Crystalline powder
4	10 [b]	2	20 [f]	40 [g]	2700	48	Crystalline powder
5	50 [d]	8	75 [e]	20 [i]	2700	48	Crystalline powder
6	10 [c]	2	20 [f]	40 [j]	540	48	Crystalline powder
7	25 [a] + 25 [b]	8	75 [e]	20 [g]	2700	48	Amorphous powder

Organic linker: a) **1**, b) **2**, c) **2-Zn**, d) **1-Ag**; Zr reagent; e) $ZrCl_4$, f) $ZrOCl_2 \cdot 8H_2O$. Seed; g) $\mathbf{NCP_{MOF}}$, h) $\mathbf{TPP_{MOF}}$, i) $\mathbf{ZnTPP_{MOF}}$, j) $\mathbf{AgNCP_{MOF}}$.

Under the delicate preparation conditions for phase-pure ftw-topology crystalline products of $\mathbf{NCP_{MOF}}$ and $\mathbf{TPP_{MOF}}$, a seed-mediated approach was effective in the synthesis of the core/shell-type hybrid MOFs because of the kinetically favored nucleation in the MOF growth. In the preliminary reaction, the seed-guided reaction of the NCP carboxylate precursor **1** proceeded well to form the phase-pure MOFs even using an inappropriate combination of a zirconyl salt, i.e., $ZrOCl_2$, when the submicron crystalline $\mathbf{NCP_{MOF}}$ seeds are present in the reaction solution (Entry 1 in Table 3-1). Based on this observation, the author next tested the solvothermal reaction of the **1** with $ZrCl_4$ and benzoic acid in the presence of the guide seeds of $\mathbf{TPP_{MOF}}$ by

heating at 120 °C for 48 h (Entry 2 in Table 3-1). The solid was worked up in the same way with **NCP$_{MOF}$** through filtration and wash. The filtrate was collected and the absorption spectrum was measured. Judging from the UV/vis absorption spectrum of the filtrate obtained after the filtration of the **TPP$_{MOF}$@NCP$_{MOF}$** powder, the characteristic absorption peaks of **2** were observed, which suggests the part of TPP unit in a **TPP$_{MOF}$** seed was exchanged by external substrate **1** during the reaction (Figure 3-2).

This protocol was also applied for the inverted combination system; the hybrid as **NCP$_{MOF}$@TPP$_{MOF}$** by using the **NCP$_{MOF}$** seed and TPP carboxylate substrate **2** (Entry 3 in Table 3-1). During the structural analysis, the large coverage of **TPP$_{MOF}$** moiety was elucidated in the resulting hybrid, **NCP$_{MOF}$@TPP$_{MOF}$**. It is noted that the stronger affinity of the carboxylate groups of **2** could facilitate the ligand exchange reaction, in which case, further optimization was subjected to furnish the hybridization toward thin-TPP layered **NCP$_{MOF}$@TPP$_{MOF}$**. The change in the ratio of the seeds and the substrates of **2** were the key to afford the uniformly coated hybrid **NCP$_{MOF}$@TPP$_{MOF}$** with a pure-phase crystallinity (Entry 4 in Table 3-1).

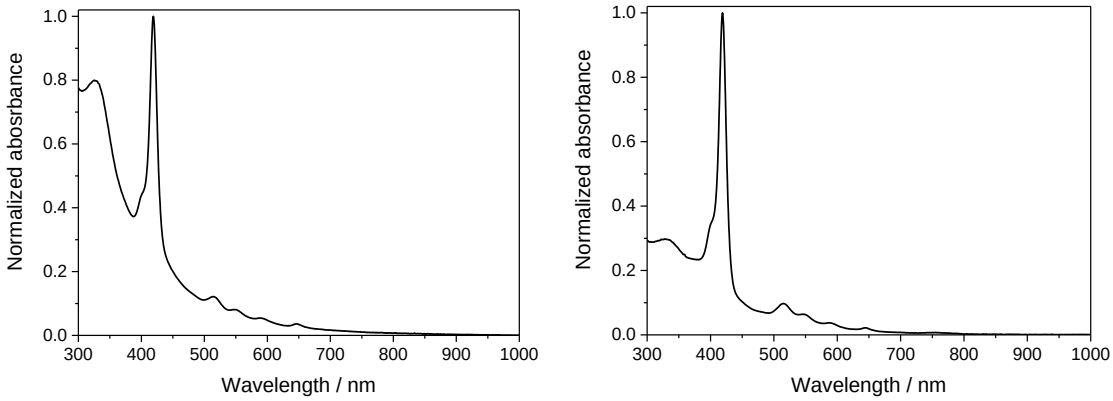

Figure 3-2. UV/vis/NIR spectra of filtrates after **NCP$_{MOF}$@TPP$_{MOF}$** (left) and **TPP$_{MOF}$@NCP$_{MOF}$** (right) was filtered.

In order to gain further structural insight into the core/shell hybrid MOFs, the author utilized the metal complexes of the porphyrins and N-confused isomers to prepare metalloporphyrin hybrids in the aforementioned protocol. Using tetra-carboxylate silver(III) NCP derivative (**1-Ag**) and zinc TPP derivative (**2-Zn**), the corresponding hybrid MOFs, namely, **ZnTPP$_{MOF}$@AgNCP$_{MOF}$** and **AgNCP$_{MOF}$@ZnTPP$_{MOF}$**, were obtained in the presence of **ZnTPP$_{MOF}$** and **AgNCP$_{MOF}$** (prepared under the appropriate conditions), respectively, as the topology-guide seeds. (Entries 5 and 6 in Table 3-1).

In another experiment, since the conditions for preparation of **TPP$_{MOF}$** and **NCP$_{MOF}$** are not identical (Scheme 3-3), the solvothermal reaction with the pre-mixed carboxylic acid precursors of **1** and **2** with zirconium salts, benzoic acid in DMF resulted in the precipitation of amorphous mixture of the coordinated products, but not the Class I hybrid MOFs as inferred from the faint signals in PXRD (Entry 7 in Table 3-1).

This result indicated that fast nucleation reaction of the porphyrinic MOF layer occurring with an aid of the seeds is likely crucial for the synthesis of the hybrid MOFs.

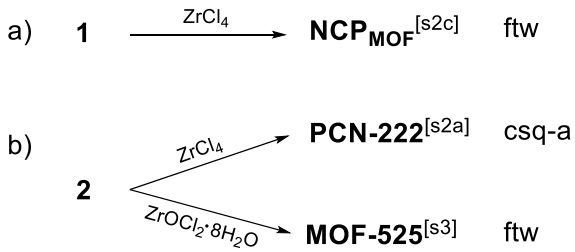

Scheme 3-3. Synthesis of a) $\mathbf{NCP_{MOF}}$ based on NCP ligand (**1**), b) PCN-222 and MOF-525 a based on TPP ligand (**2**).

3.2.2.2 Characterization

The scanning electron microscopy (SEM) and transmission electron microscopy (TEM) analysis revealed the formation of sub-micrometer sized cubic MOFs (Figure 3-3). The PXRD analysis of the resulting $\mathbf{NCP_{MOF}@TPP_{MOF}}$ revealed identical patterns of "ftw" topology to that of $\mathbf{TPP_{MOF}}$, and the SEM/TEM images of $\mathbf{NCP_{MOF}@TPP_{MOF}}$ likewise indicated the cubic structures. The resulting heterogeneous hybrid MOFs ($\mathbf{TPP_{MOF}@NCP_{MOF}}$) was brownish colored powders and identified as an ftw-topology microcrystalline product based on sharp PXRD pattern analysis, which is similar to that of $\mathbf{NCP_{MOF}}$

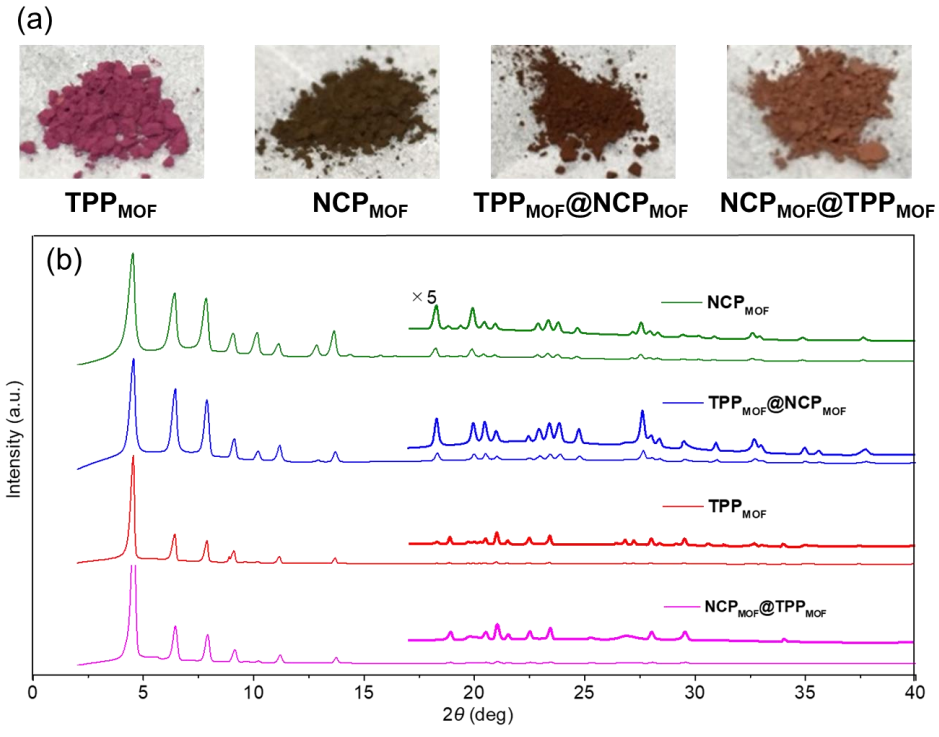

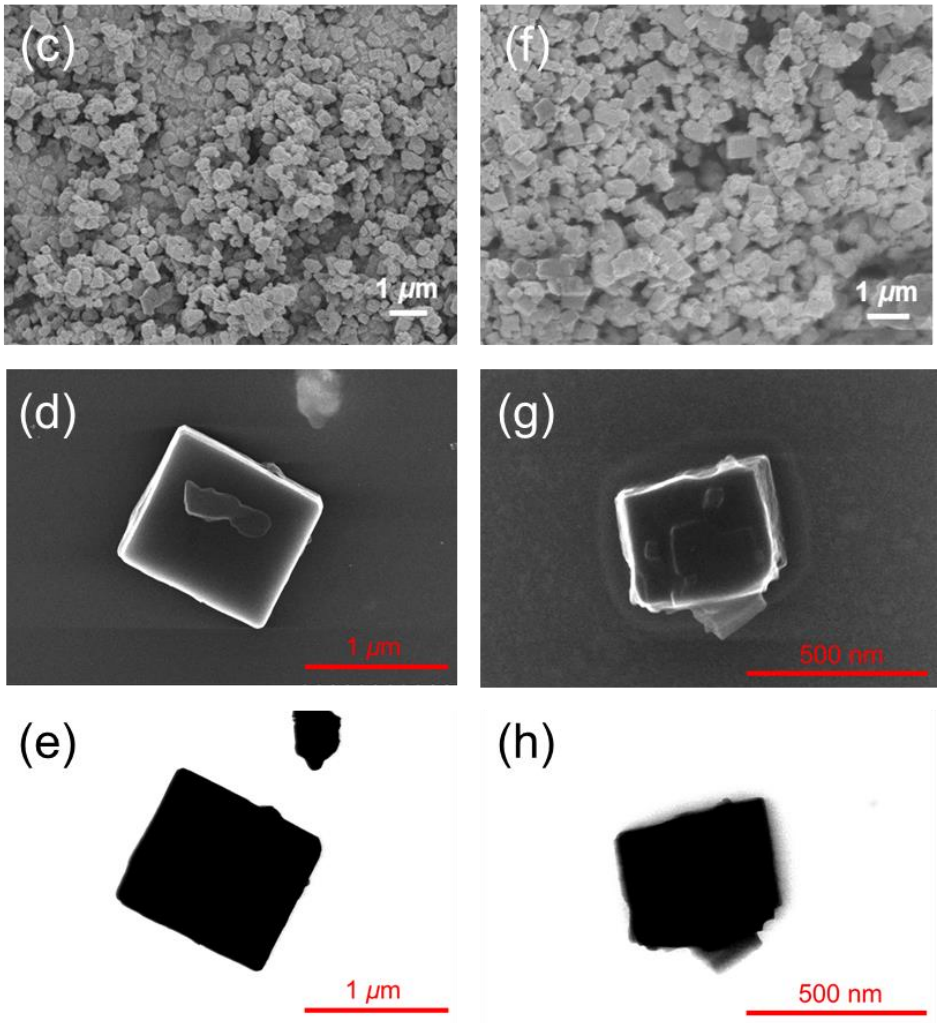

Figure 3-3. (a) Photographs and (b) PXRD patterns of **TPP_{MOF}**, **NCP_{MOF}**, **TPP_{MOF}@NCP_{MOF}**, and **NCP_{MOF}@TPP_{MOF}**. SEM/TEM images of (c-e) **NCP_{MOF}@TPP_{MOF}** and (f-h) **TPP_{MOF}@NCP_{MOF}**; The overview of SEM images (c/f) and the magnified views (d/g) are given. Scale bars are set to 1 μm for the images (c-f) and 500 nm for (g and h).

The same measurements were conducted on metalated hybrid MOFs. The PXRD analysis and SEM images of the resulting MOFs indicated the similar morphological features to those of freebase hybrids (Figure 3-3 and Figure 3-21). The presence of heterogeneous element compositions including the metal ions coordinated at the porphyrin cores within the frameworks of hybrid MOFs was visualized by energy-dispersive X-ray (EDX) analysis (Figure 3-4). The linear EDX analysis of two specific elements of **$ZnTPP_{MOF}$@$AgNCP_{MOF}$** and **$AgNCP_{MOF}$@$ZnTPP_{MOF}$** traced at red color lines of the SEM images revealed valley-shaped features for the components of the outer layered MOFs (e.g., silver for **$ZnTPP_{MOF}$@$AgNCP_{MOF}$** and zinc for **$AgNCP_{MOF}$@$ZnTPP_{MOF}$**). This result implies that the core-shell

structures with uniformly coated porphyrinic and isomeric MOFs were generated over the different component MOF as the cores, respectively.

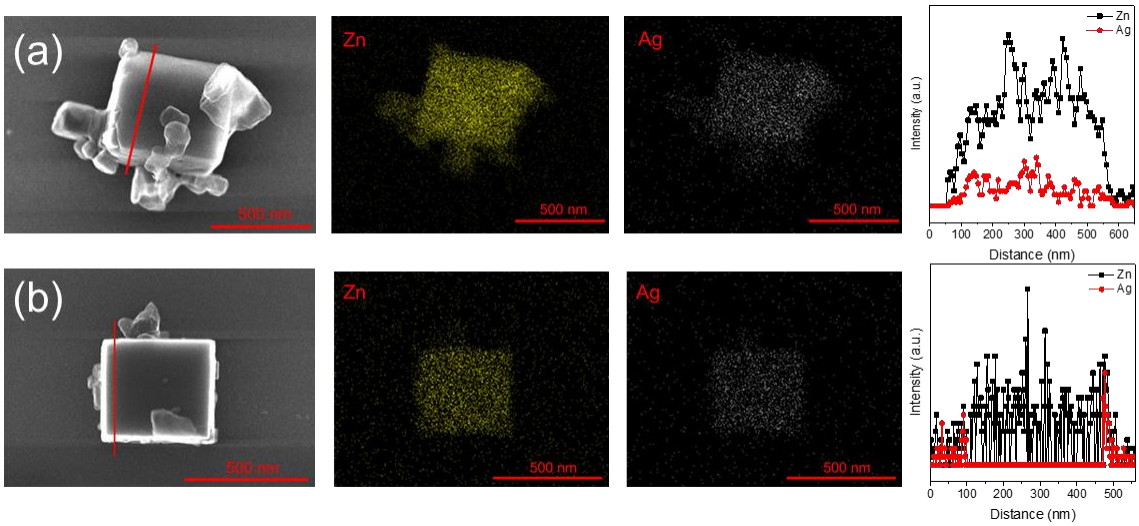

Figure 3-4. SEM images (left), elemental mappings for Zn and Ag (middle) and their linear analysis (right) for (a) **AgNCP$_{MOF}$@ZnTPP$_{MOF}$** and (b) **ZnTPP$_{MOF}$@AgNCP$_{MOF}$**. The scale bar is set to 500 μm.

Decomposition of the hybrid MOFs using strong base solution (0.1 M NaOH aq.) was conducted to find the ratio of NCP and TPP moiety in hybrid MOFs (Figure 3-5) based on the molar extinction coefficient of both NCP and TPP at 445 and 415 nm digested in NaOH solution. The ratio between NCP and TPP chromophore components in **TPP$_{MOF}$@NCP$_{MOF}$** is estimated to be approximately 1.74 (Figure 3-5 and 3-6), while it is estimated to be approximately 0.64 in **NCP$_{MOF}$@TPP$_{MOF}$** according to the spectra of digested MOFs (Figure 3-5 and 3-6).

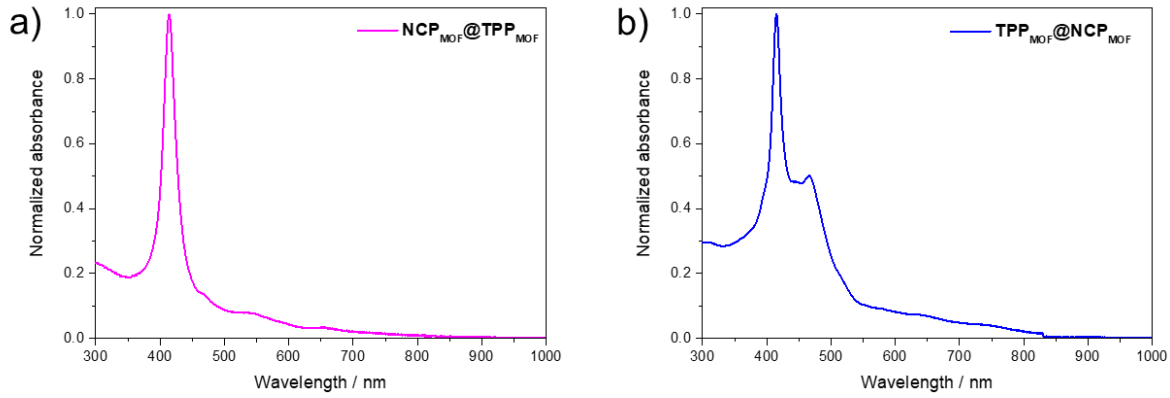

Figure 3-5. Absorption spectra of **NCP$_{MOF}$@TPP$_{MOF}$** (a) and **TPP$_{MOF}$@NCP$_{MOF}$** (b) dissolved in 0.1 M NaOH aqueous solution.

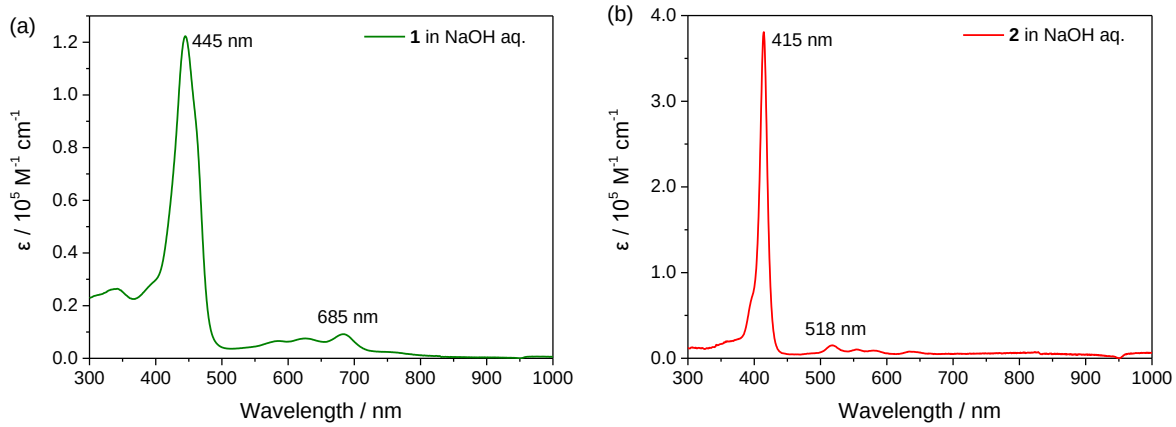

Figure 3-6. UV/vis absorption spectra of (a) **1** and (b) **2** in NaOH aq.

Based on the ratio, the theoretical core/shell structures of both hybrid MOFs were calculated, including the thickness of the shell phase and the volume of the core phase. The calculation was conducted on the hypothesis that $\mathbf{NCP_{MOF}}$ and $\mathbf{TPP_{MOF}}$ have identical densities. When a cubic particle with a diameter of 1 μm is used as the model, the $\mathbf{TPP_{MOF}}$ core in $\mathbf{TPP_{MOF}@NCP_{MOF}}$ is estimated to have a length of 0.71 μm, leaving the shell with a thickness of 0.145 μm. In the inverted case, the $\mathbf{NCP_{MOF}}$ core is estimated to be 0.73 μm in length, leading to a thinner shell phase with a thickness of 0.135 μm. (Figure 3-7)

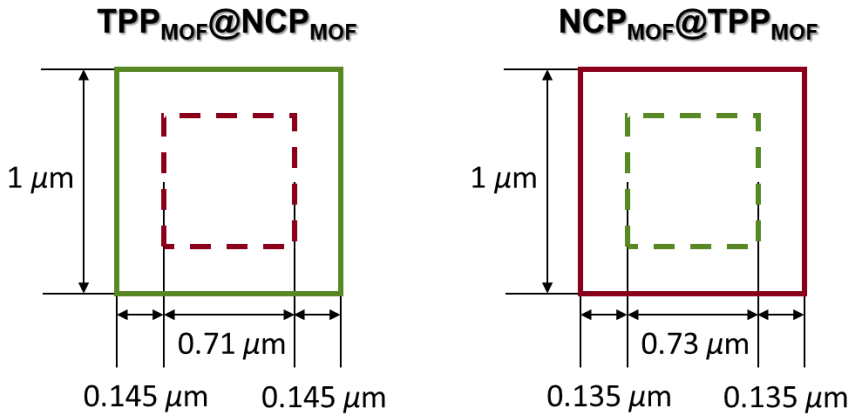

Figure 3-7. The calculated structure of $\mathbf{TPP_{MOF}@NCP_{MOF}}$ (left) and $\mathbf{NCP_{MOF}@TPP_{MOF}}$ (right).

3.3 Porosity

The porosity of these hybrid MOFs, $\mathbf{NCP_{MOF}@TPP_{MOF}}$ and $\mathbf{TPP_{MOF}@NCP_{MOF}}$ crystals was determined by N_2 adsorption-desorption isotherms at 77K (Figure 3-8). The samples displayed typical type I isotherms with small hysteresis between adsorption and desorption curves. This result indicates the permanent porosities of the MOFs without blocking the core-shell structures.

There is a negative slope in the adsorption of the hybrid MOFs at higher pressure, which may be attributed to the flexible skeletons of porphyrinic MOFs. The Brunauer-Emmett-Teller (BET) surface areas of **NCP$_{MOF}$@TPP$_{MOF}$** and **TPP$_{MOF}$@NCP$_{MOF}$** were calculated to be 323 and 351 m^3 g^{-1}, respectively, which are relatively smaller than the original single-component MOFs due to the existence of the solvated molecules within the pores. The results of elementary analyses also revealed the existence of solvent molecules in the solid samples. (See details in Section **3.8.2**) For comparison, the mixed MOFs (i.e., **TPP$_{MOF}$** and **NCP$_{MOF}$**) were also determined and exhibited similar type I isotherms, while slightly showing notable steps in the isotherms due to the presence of the slightly different mesoporous profiles for N_2 adsorption. Therefore, the hierarchical hybrid core structures can be expected for **TPP$_{MOF}$@NCP$_{MOF}$** and **NCP$_{MOF}$@TPP$_{MOF}$**.

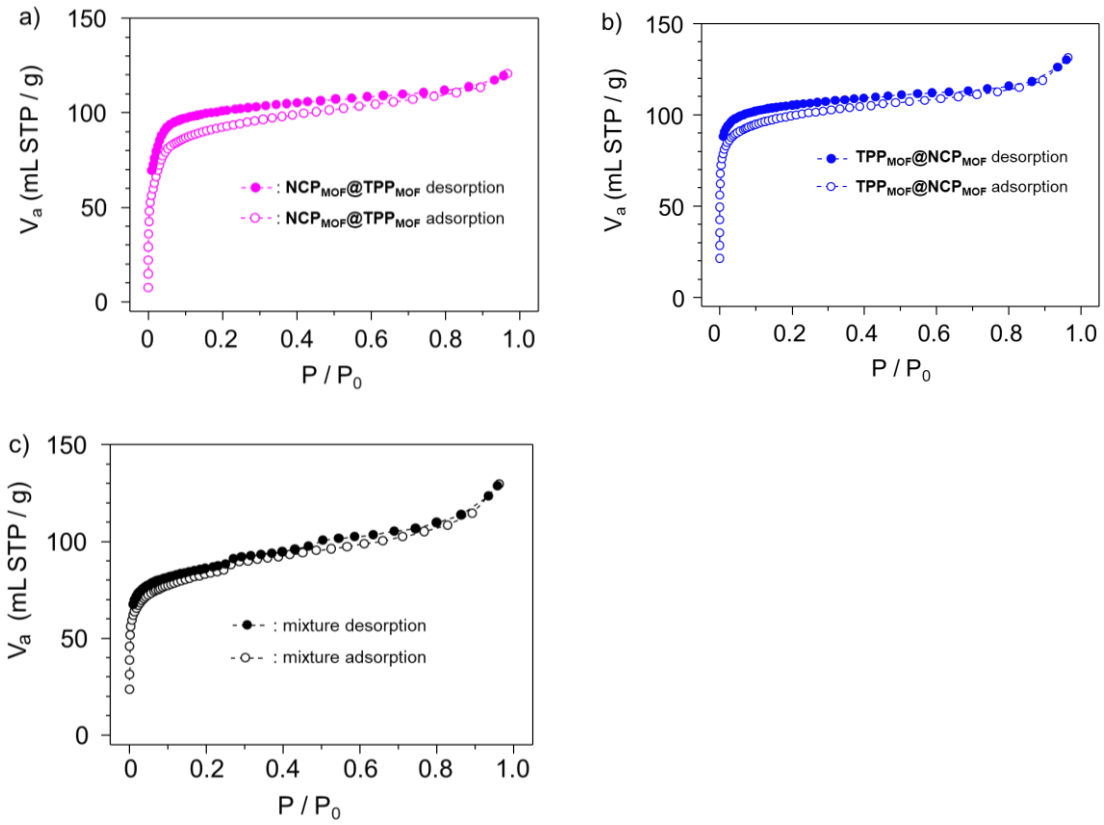

Figure 3-8. N_2 adsorption isotherms of a) **NCP$_{MOF}$@TPP$_{MOF}$**, b) **TPP$_{MOF}$@NCP$_{MOF}$** and c) mixture (**NCP$_{MOF}$** : **TPP$_{MOF}$** = 5:2) at 77 K.

3.4 Thermogravimetric Analysis

The thermogravimetric (TG) analysis was then utilized to confirm the removal of solvent molecules upon increasing the temperature. Both hybrid MOFs showed a first great mass loss at around 150-200 ºC, which can be attributed to the vaporization of DMF. Activation process failed as the reaction between ligands at

high temperature leads to a deterioration in the crystallinity. Both hybrid MOFs were observed to be decomposed at around 400 ºC (Figure 3-9).

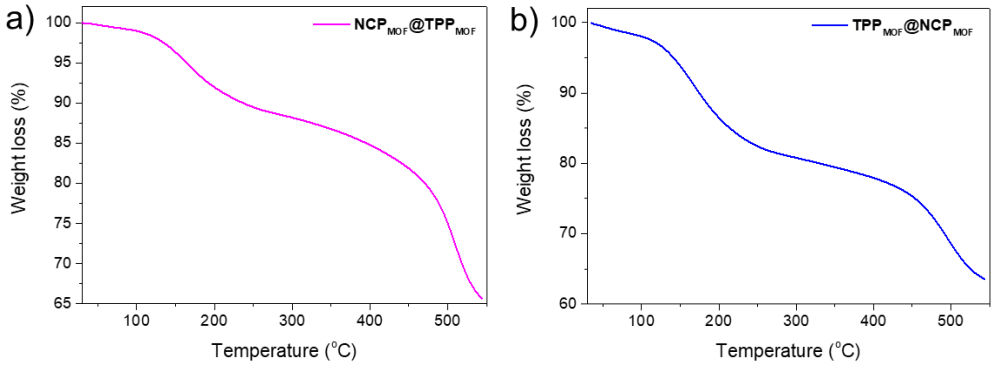

Figure 3-9. Thermogravimetric analyses of a) **NCP$_{MOF}$@TPP$_{MOF}$** and b) **TPP$_{MOF}$@NCP$_{MOF}$**.

3.5 Photophysical Properties

All the hybrid MOFs showed characteristic visible-to-near infrared absorption features with an intense Soret and broad Q-like bands originated from the corresponding porphyrin units (Figure 3-10). The individual spectrum of **NCP$_{MOF}$** in KBr pellet reveals the broad and redshifted spectral profiles compared with that of **TPP$_{MOF}$**. The corresponding hybrid, **TPP$_{MOF}$@NCP$_{MOF}$**, in turn, exhibits two Soret bands at λ_{max} = 427 nm and 472 nm and broad tailing band up to 1000 nm. On the other hand, the absorption spectrum of **NCP$_{MOF}$@TPP$_{MOF}$** shows distinct features for both components; Soret-like bands at λ_{max} 430 nm and resolved Q-like bands. However, the prominent spectral information for **TTP$_{MOF}$** was observed due to the intrinsic higher molar absorption coefficient of the TPP units than that of **NCP$_{MOF}$**.

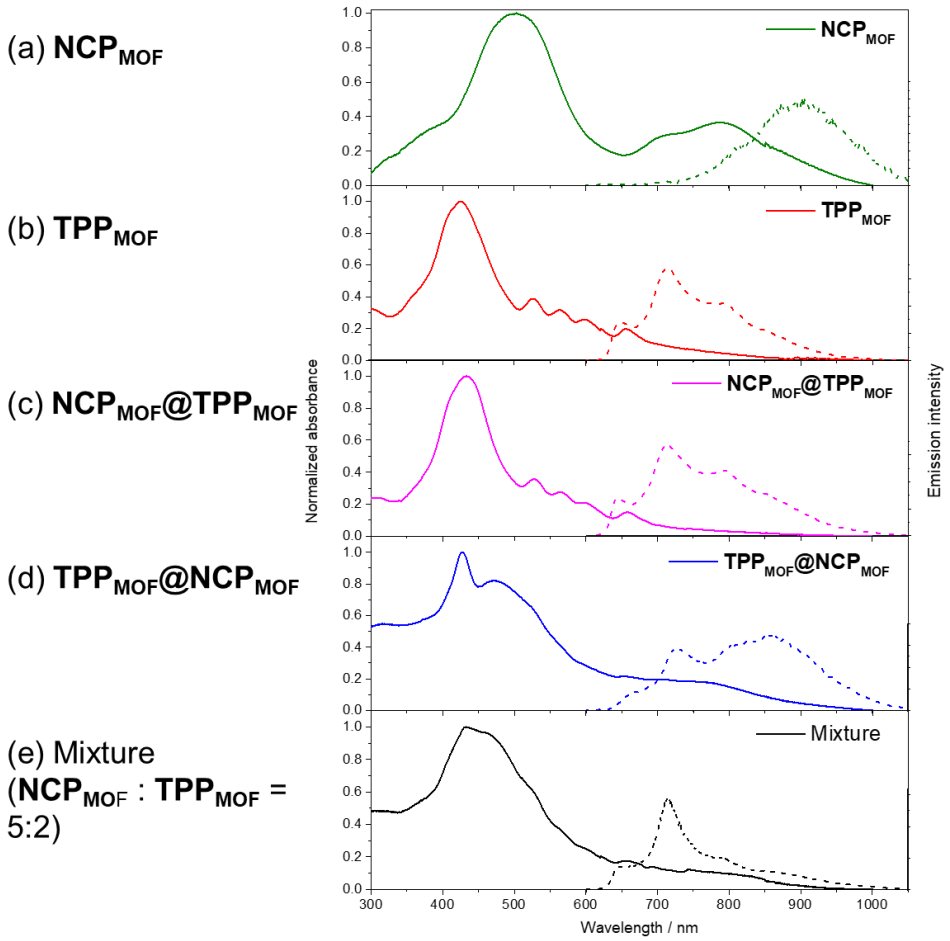

Figure 3-10. UV/vis absorption spectra (in KBr pellet, solid line) and fluorescent spectra (in DMF suspension, broken line) of (a) **NCP$_{MOF}$**, (b) **TPP$_{MOF}$**, (c) **NCP$_{MOF}$@TPP$_{MOF}$**, (d) **TPP$_{MOF}$@NCP$_{MOF}$** and (e) mixture of **NCP$_{MOF}$** and **TPP$_{MOF}$** (in 5:2 ratio). The excitation was excited at the maximum peak of the Soret band.

Along with the different absorption characteristics between pristine **TPP$_{MOF}$** and **NCP$_{MOF}$**, the steady-state fluorescence spectra of the hybrids (suspended in DMF solvent) exhibit two characteristic emissions at λ_{em} = ca. 900 nm (originating from **NCP$_{MOF}$**), and at λ_{em} = 645 nm and 715 nm (from **TPP$_{MOF}$**). In the case of **NCP$_{MOF}$@TPP$_{MOF}$**, the major resolved emission in the range between 650-800 nm is originated from outer-shell **TPP$_{MOF}$** and the tailing shoulder peak around 900 nm from inner core **NCP$_{MOF}$** moiety could be overlapped (Figure 3-10c). Both excitation spectra monitored at 730 nm and 910 nm are indeed consistent with the absorption spectra (Figure 3-11a and b), which implies that the stronger emission from TPP moiety is largely contributed. Similarly, the photo-excitation of **TPP$_{MOF}$@NCP$_{MOF}$** gave rise to the dual emissions from **NCP$_{MOF}$** and **TPP$_{MOF}$** units (Figure 3-10d). In this inverted system, the relatively larger intense NIR emission from **NCP$_{MOF}$** moiety was observed together with the red emission from **TPP$_{MOF}$** unit. The excitation spectral behavior of **TPP$_{MOF}$@NCP$_{MOF}$** probed at 900 nm are well corresponding to the actual absorptions for **NCP$_{MOF}$**. In contrast, the spectrum at 720 nm showed faint spectral feature presumably due to the intrinsically less effective excitation of TPP moieties. (Figure 3-11d) Estimation of the absolute

emission quantum yields for the MOFs was unsuccessful due to the intrinsically less emissive character. The large nonradiative decay process could have resulted from the decreased energy gap or an enhanced intersystem crossing rate.[20]

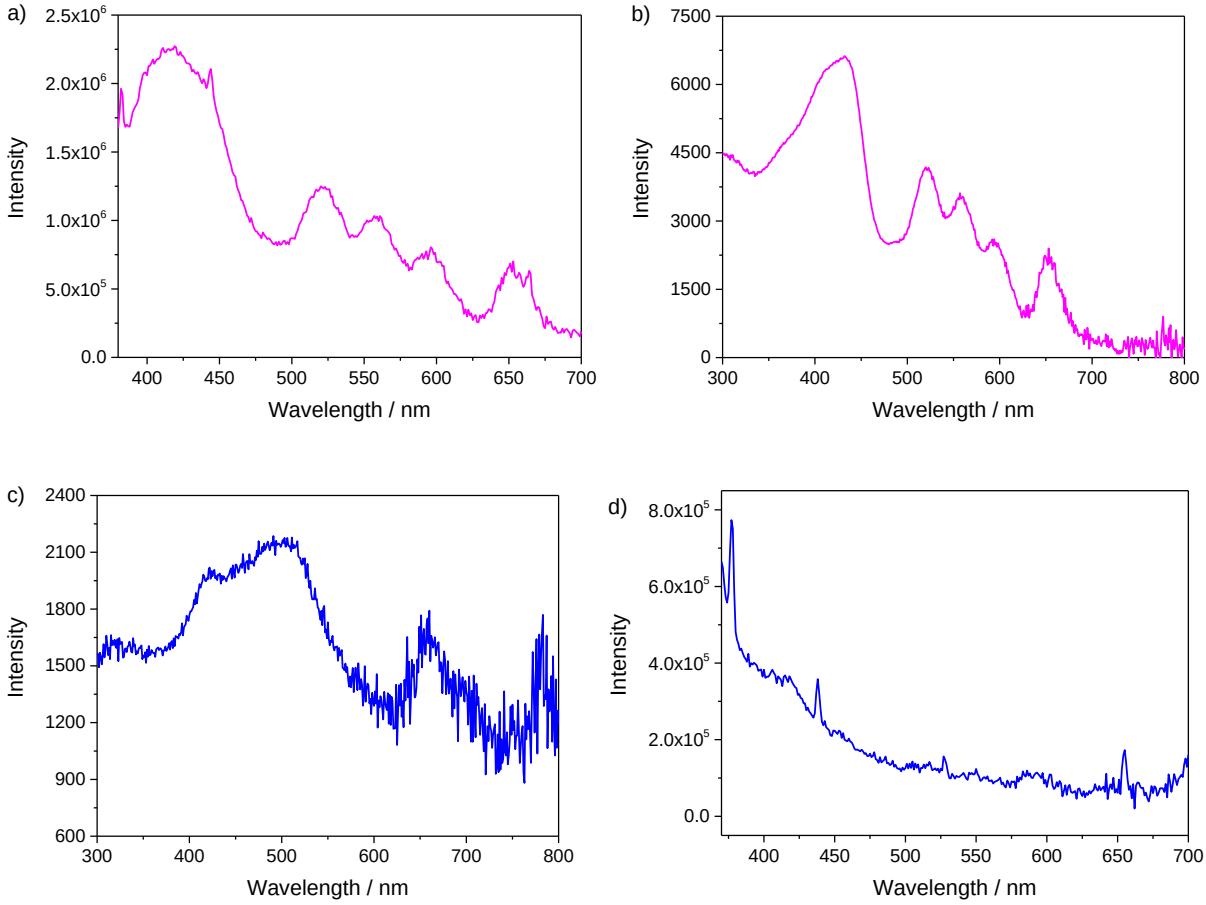

Figure 3-11. Photo-excitation spectra of **NCP$_{MOF}$@TPP$_{MOF}$** monitored at a) 730 nm and b) 910 nm. Photo-excitation spectra of **TPP$_{MOF}$@NCP$_{MOF}$** monitored at c) 900 nm and d) 720 nm.

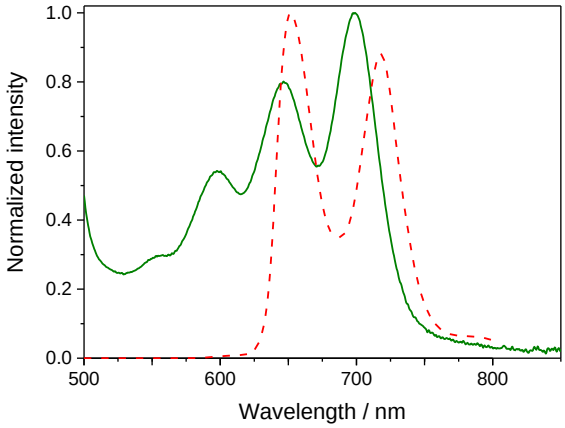

Figure 3-12. UV/vis absorption spectrum of **1** (green solid line) and emission spectrum of **2** (red dotted line) in DMF. (λ_{ex} = 420 nm).

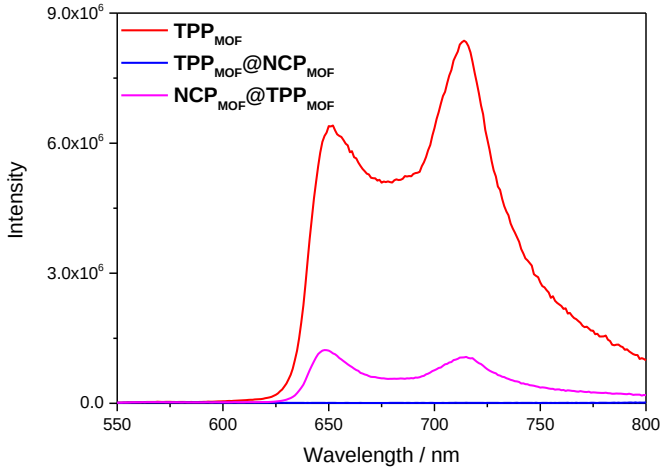

Figure 3-13. Emission spectra of **TPP$_{MOF}$** (red), **TPP$_{MOF}$@NCP$_{MOF}$** (blue), and **NCP$_{MOF}$@TPP$_{MOF}$** (purple). Excited at λ_{ex} = 455 nm.

Based on the large spectral overlap between the emission of TPP moiety and the absorption of NCP one, the energy transfer event within the hybrid MOFs is anticipated (Figure 3-12). Upon excitation at the TPP moieties at 455 nm, the notable lower emission intensities from the TPP moieties were observed for both **NCP$_{MOF}$@TPP$_{MOF}$** and **TPP$_{MOF}$@NCP$_{MOF}$** (Figure 3-13). Since the efficient Förster energy migration between two porphyrin chromophores in a phenylene-bridged porphyrin/N-confused porphyrin dyad molecule has been elucidated with the models, the preferred singlet energy transfers between the phase-orientated MOF layers can be assumed.[21] In an effort to elucidate the energy transfer phenomenon between two chromophores present within the hybrid MOFs, the time-resolved fluorescence spectra were measured in DMF suspension solution (Figure 3-14 and Figure 3-22). The decay curves were carefully analyzed by fitting with a bi-exponential decay equation as follows. (Figure 3-15)

$$F(t) = A_1 e^{-t/\tau_1} + A_2 e^{-t/\tau_2} \quad (1)$$

Here, A_1 and A_2 stand for the amplitudes, and τ_1 as well as τ_2 are the lifetimes of two decay components. The results of the hybrid MOFs are given in Table 3-2 and 3-3. The emission decays of the pure **TPP$_{MOF}$** and **NCP$_{MOF}$** are found to follow the mostly single-exponential fitting. The relatively long emission feature in the visible wavelength region (centered at 720 nm) was, in turn, estimated to be t = 1.14 ns (A_1 = 0.98) in **TPP$_{MOF}$** (Figure 3-14c). For **NCP$_{MOF}$**, the short-lived near infrared emission was captured with a decay constant of 0.62 ns (l_{em} = 880 nm), which is consistent with the relatively lower quantum yield estimated (Figure 3-14d). For the hybrid system, **NCP$_{MOF}$@TPP$_{MOF}$**, the dominant emission decay profile of the TPP moieties was observed in comparison with that of **TPP$_{MOF}$** because of the larger magnitude of the photoexcitation for the outer shell TPP moieties. Compared with the value of **TPP$_{MOF}$**, the slightly slower

decay kinetics of the emissions (t = 1.24 ns @720 nm and 1.33 ns @850 nm) could be attributed to the interchromophoric interactions of the excited state as a result of the exciton delocalization, or excited state trapped within the MOF lattice.[22] In contrast, the majority of the emission decays for **TPP$_{MOF}$@NCP$_{MOF}$** came from the NCP moieties at the initial time. The constant of 0.64 ns monitored at 880 nm is comparable to that of **NCP$_{MOF}$,** suggesting no chromophoric interactions due to the unfavorable reverse energy transfer from NCP to TPP moiety. The delayed emission from the TPP units were also observed with the constant 1.83 ns. In addition, the control experiment using the physical mixture of **TPP$_{MOF}$** and **NCP$_{MOF}$** revealed the simultaneous emission decay features for each component of TPP and NCP moieties with the almost same constants of 1.16-1.18 ns at 720 and 850 nm, respectively. These are assumed to be the predominant decay profile of **TPP$_{MOF}$**. Therefore, the observation indicates that the energy transfer process occurs for the ordered chromophores with special proximity within the hybrid MOFs.

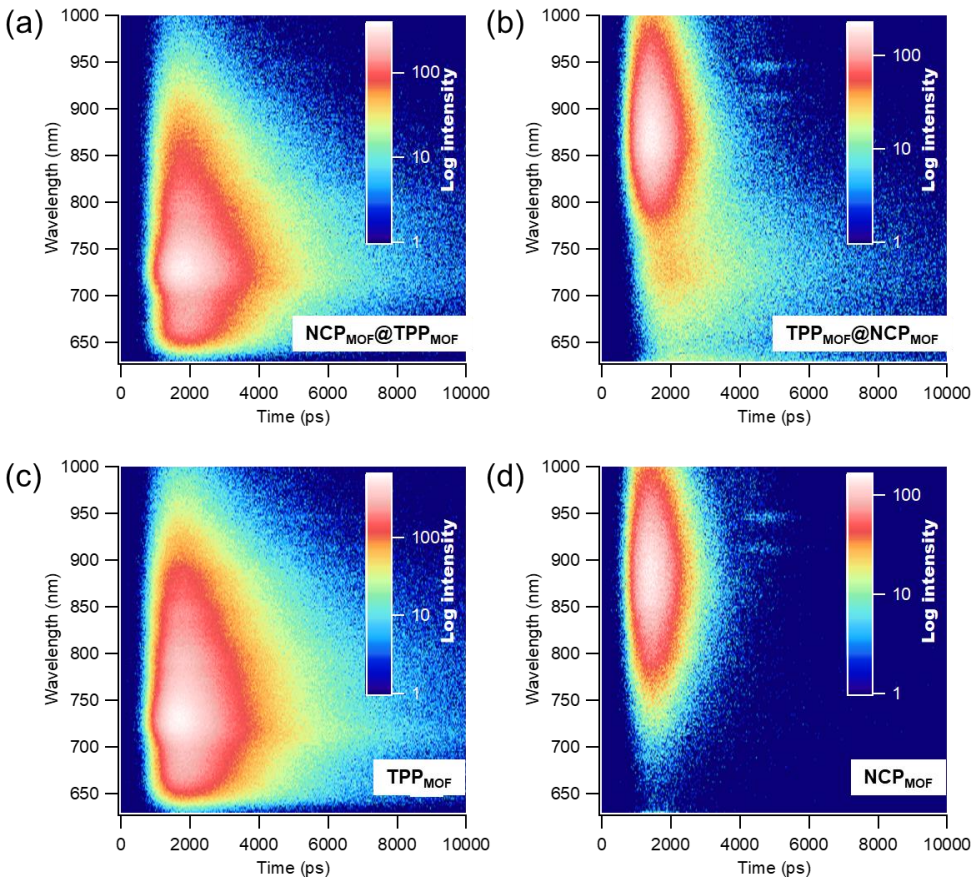

Figure 3-14. Time-resolved 2D fluorescence spectra of the hybrid MOFs; (a) **NCP$_{MOF}$@TPP$_{MOF}$** and (b) **TPP$_{MOF}$@NCP$_{MOF}$.** The data for the reference of (c) **TPP$_{MOF}$** and (d) **NCP$_{MOF}$** are shown. The excitation was subjected at λ_{ex} = 532 nm.

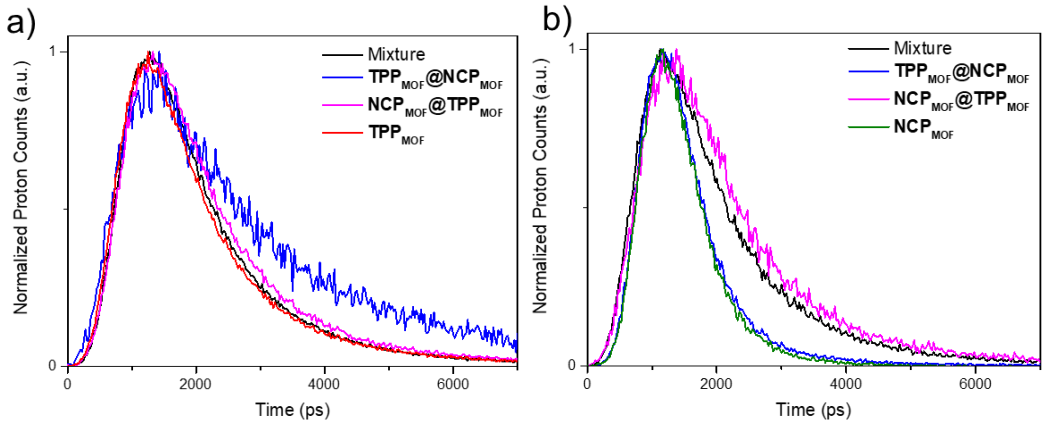

Figure 3-15. Emission decay curves of MOFs and a mixture (**NCP$_{MOF}$** : **TPP$_{MOF}$** = 5 : 2) in DMF excited at a) 720–730 nm and b) 850–880 nm.

Table 3-2. Summary of emission lifetimes of the MOFs probed at 720-730 nm and 850-880 nm regions.

Samples	τ_{em} (ns) probed at 720-730 nm	τ_{em} (ns) probed at 850-880 nm
TPP$_{MOF}$@NCP$_{MOF}$	1.83	0.64
NCP$_{MOF}$@TPP$_{MOF}$	1.24	1.33
TPP$_{MOF}$	1.14	-
NCP$_{MOF}$	-	0.62
Mixture*	1.16	1.18

*Note that the mixed sample contains **NCP$_{MOF}$** and **TPP$_{MOF}$** in 5:2 ratio. The lifetimes for the major amplitudes are given.

In order to obtain the further macroscopic structural information of the hybrid MOFs, hierarchical emissive characters of the hybrids, **TPP$_{MOF}$@NCP$_{MOF}$** and **NCP$_{MOF}$@TPP$_{MOF}$** were analyzed by using a confocal laser scanning microscopy (Figure 3-16). These images are taken by irradiating the suspension with a light at a wavelength of 430 nm and observing the wavelength at 650 nm. Therefore, the red emission of **TPP$_{MOF}$** can be visualized (while the near-IR emission from **NCP$_{MOF}$** is out of range for the detector in our experimental setup). In fact, red-fluorescence images of both particles of **NCP$_{MOF}$@TPP$_{MOF}$** and **TPP$_{MOF}$@NCP$_{MOF}$** were shown. The emission intensity of a selected particle of **NCP$_{MOF}$@TPP$_{MOF}$** is relatively higher than that of **TPP$_{MOF}$@NCP$_{MOF}$**, suggesting that the TPP moiety is present on the outer surface of the core (Figure 3-17)[22]. In contrast to the hybrid samples, the mixed sample of **TPP$_{MOF}$** and **NCP$_{MOF}$** (in approximately 5:2 ratio) clearly demonstrated that there are red-emissive and dark particles

shown in the image, which suggested that the core/shell hybrid MOFs obtained in the reactions are not a simple mixture.

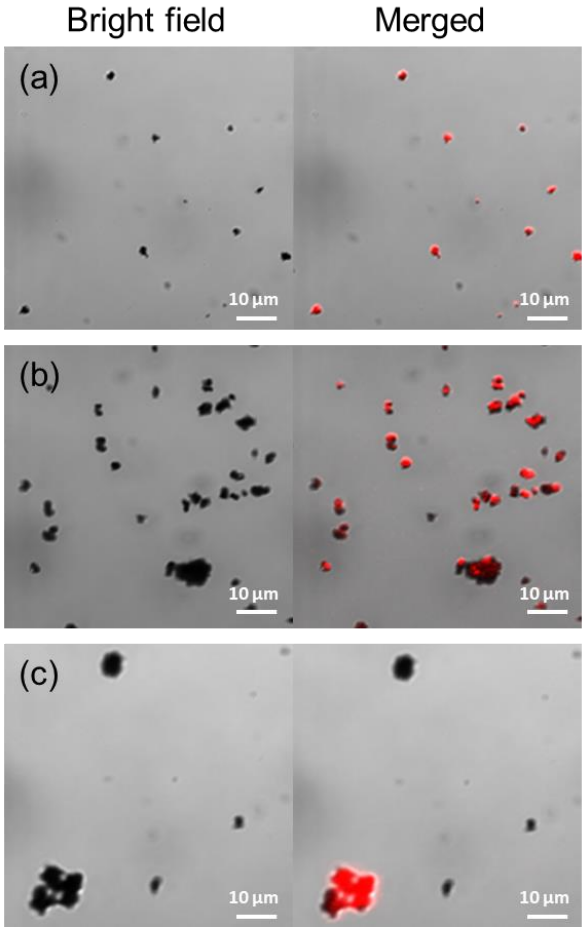

Figure 3-16. Fluorescent microscope images of (a) $\mathbf{NCP_{MOF}@TPP_{MOF}}$, (b) $\mathbf{TPP_{MOF}@NCP_{MOF}}$ and c) the mixture of $\mathbf{NCP_{MOF}}$ and $\mathbf{TPP_{MOF}}$ (5:2 ratio). The bright field images (left) and the merged fluorescent images (right, detect at 650 nm) are given with the scale bars of 10 μm.

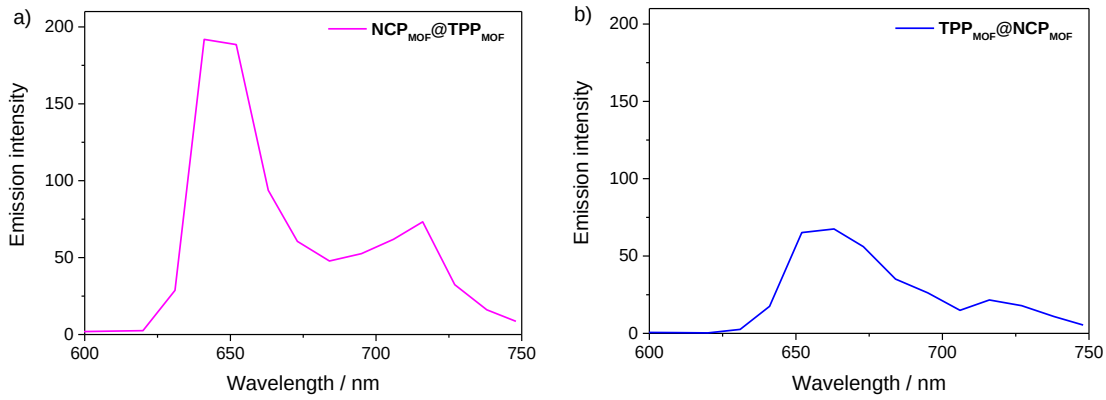

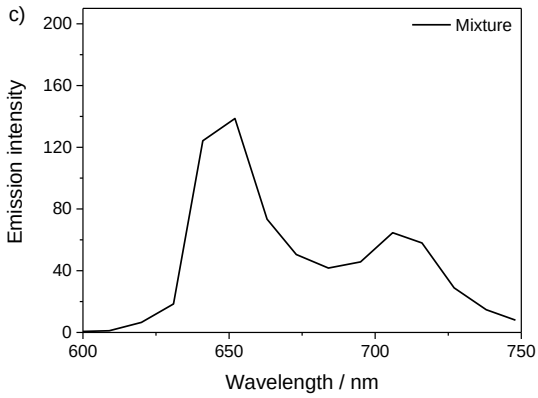

Figure 3-17. Emission spectra in the Confocal Laser Scanning Microscopy (CLSM) of a) **NCP$_{MOF}$@TPP$_{MOF}$**, b) **TPP$_{MOF}$@NCP$_{MOF}$** and c) mixture (λ_{ex} = 430 nm).

3.6 Photoinduced Singlet Oxygen Generation

The chemical robustness and the efficient light-harvesting ability of the porphyrinic Zr-MOFs have been paid attention for applications in the photosensitized singlet oxygen generation[23]. In fact, it is notable that the aforementioned energy transfer process affected the efficiency. Using a dihydroxynaphthalene (DHN) as a scavenger for $^1O_2$, visible photo-irradiation (300 W) induced the formation of photo-oxidized 5-hydroxy-1,4-naphthoquinone (namely, juglone) according to the decrease of DHN absorbance (λ_{max} ~ 300 nm, Figure 3-18). The absorbance at 430 nm of the resulting product, juglone was plotted against time to evaluate the efficiency of each MOFs. Consequently, the parent porphyrin MOFs, **TPP$_{MOF}$** has the highest efficiency for singlet oxygen generation as reported with PCN-222[17, 24]. In contrast, the efficiency of **NCP$_{MOF}$** was lower presumably due to the short excited-state lifetime. In the cases of the hybrid systems, lowering the photosensitizing ability of **NCP$_{MOF}$@TPP$_{MOF}$** was estimated compared with **TPP$_{MOF}$**. This can be understood by the involvement of the energy transfer process from the photo-excited TPP shell to the NCP core, which may decrease the spin-forbidden intersystem crossing rate. (Scheme 3-3) For **TPP$_{MOF}$@NCP$_{MOF}$**, the slight increase in the conversion yield was considered the resulting energy transfer phenomenon that can enhance the light-harvesting effect via complementary absorption, though a non-uniformity of the hybrid MOFs with a **TPP$_{MOF}$** core may be contributed to the partially enhanced efficiency. In the absence of MOFs or under dark conditions, there are no prominent photooxidized products as expected.

This detection only focuses on the spectral changes resulted from the reaction between $^1O_2$ and DHN, which gives a relatively accurate comparison on the kinetics of singlet oxygen generation regardless of the size or volume of MOFs. However, as the exciton interaction occurs on the interface between NCP and TPP phases, the ratio of TPP moiety included in the hybrid MOFs has a positive correlation with the efficiency.

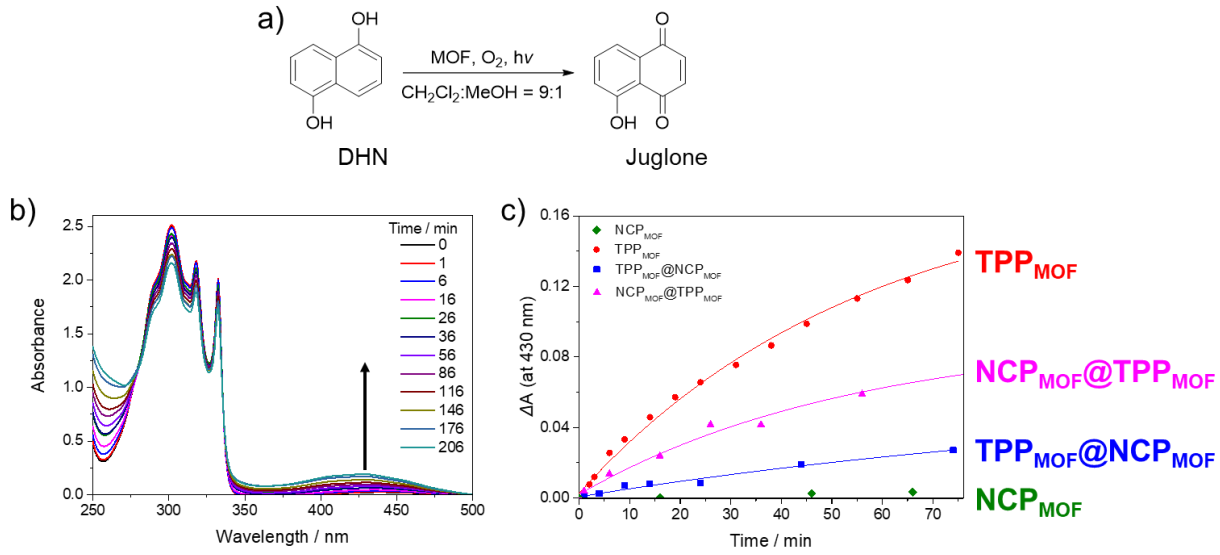

Figure 3-18. The monitoring of the generation of singlet oxygen by observing the change in the spectra of DHN.

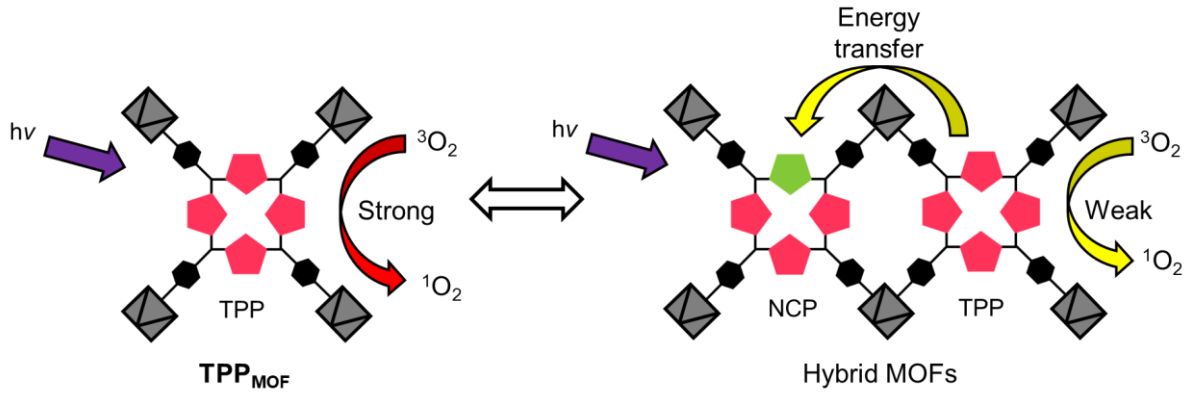

Scheme 3-3. Excitation of singlet oxygen weakens in hybrid MOFs due to the interaction between TPP and NCP moieties.

About the stability after the reaction, a recent report revealed that porphyrin-based MOF-525 have a better photostability than porphyrin monomer.[25] Upon irradiation, the fluorescent intensity of porphyrin decreased by 15% in 35 min while only 2% loss was seen in MOF-525. It is considered when irradiated, the $^1O_2$ generated from porphyrin ligand can cause the photo-oxidation of porphyrin itself, leading to degradation of the photosensitizer.

However, in MOF, the close distance among porphyrin molecules contributes to the process of triplet-triplet annihilation, which decreases the process of $^1O_2$ excitation, thus a high photostability was observed in the frameworks.

3.7 Conclusion

In summary, we have successfully synthesized novel hierarchically hybrid Zr-MOFs containing two isomeric ligands, **1**, and **2** under the seed-mediated solvothermal reaction. Simply heating the mixture component of **1** and **2** did not yield the desired hybrid MOFs. The powder XRD patterns and microscopic analysis of the resulting hybrid products suggested the formation of core/shell type Class II MOFs with "ftw" cubic topologies. Taking advantage of the efficient near-infrared optical properties of the N-confused porphyrin chromophore, the comprehensive visible-to-near infrared light absorption was achieved through the hybridization. The fine-tuning of the photoinduced energy transfer between TPP and NCP moieties is for improved efficiency of singlet oxygen photosensitization. These isomeric porphyrin-based MOFs could be regarded as mimics of the natural pigment systems, which should be useful motifs for specific applications in the solar energy conversion devices and photodynamic therapy.

3.8 Experimental Section

3.8.1 Materials and Instruments

Materials. The precursors, 5,10,15,20-Tetrakis(4-carboxyphenyl)-porphyrin (**TL**), [5,10,15,20-Tetrakis(4-carboxyphenyl)-porphyrinato]-Zn(II) (**ZnTL**), 2-aza-5,10,15,20-tetrakis(4-carboxyphenyl)-21-carbaporphyrin (**NL**), [2-aza-5,10,15,20-tetrakis(4-carbonylphenyl)-21-carbaporphyrinato]-Ag(III) (**AgNL**), were synthesized according to the reported procedures. The single-component zirconium-based MOFs, $\mathbf{TPP_{MOF}}$, $\mathbf{NCP_{MOF}}$ were also prepared by the literature procedure. Xx. Xx. Zirconium(IV) chloride ($ZrCl_4$) was purchased from Sigma-Aldrich Chemical Co. Silver trifluoroacetate (CF_3COOAg), zirconyl chloride hydrate ($ZrOCl_2 \cdot 8H_2O$) and benzoic acid were purchased from FUJIFILM Wako Pure Chemical Co. Zinc(II) trifluoromethanesulfonate, $Zn(CF_3SO_3)_2$ was purchased from Tokyo Chemical Industry Co., Ltd. *N*,*N*-Dimethylformamide (DMF) was purchased from Kanto Chemical Co., Inc.

Instruments. Powder X-ray diffraction (PXRD) measurements were carried out on Rigaku SmartLab Intelligent X-ray diffraction instrument at a scanning rate of 2^o/min. Scanning electron microscopy (SEM), transmission electron microscopy (TEM) and energy dispersion X-ray spectrometry (EDX) were used to characterize the morphology of the samples using a Hitachi Ultra-high Resolution Scanning Electron Microscope SU9000 instrument (at an accelerating voltage of 30 kV). UV/vis spectra were recorded on Shimadzu UV-3150PC and JASCO V-770 spectrophotometers. Fluorescent spectra were recorded on Horiba Modular Spectrofluorometer-Fluorolog-NIR. Confocal Laser Scanning Microscopy (CLSM) images were taken on Carl Zeiss Confocal Laser Scanning Microscope. Time-resolved emission measurements were performed in the time-correlated single photon counting mode using a NIR-sensitive photomultiplier (Hamamatsu H10330-75). The excitation source was a 532 nm frequency-doubled passive-Q-switched

Nd:YAG laser delivering a 1 μJ sub-nanosecond (<0.7 ns) pulse train at a repetition rate of 8 kHz. The sample solutions (DMF) in the cell cuvette were carefully degassed by argon bubbling with a septum. N_2 adsorption experiments were completed with high precision gas/vapor adsorption measurement instrument of MicrotracBEL BELSORP-aqua at 77 K.

3.8.2 Synthesis of Hybrid MOFs

Synthesis of Organic Ligands

Synthesis of [2-aza-5,10,15,20-tetrakis(*p*-methoxycarbonylphenyl)-21-carba-porphyrinato]-Ag(III) (1-Ag)

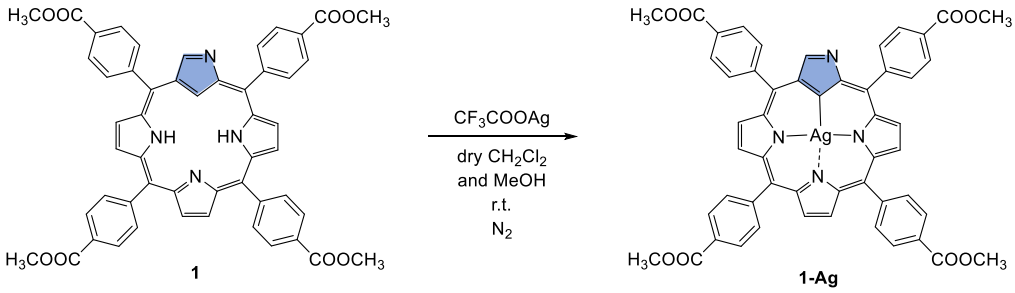

To a 200 mL of 3-necked flask 2-aza-5,10,15,20-tetrakis(p-methoxycarbonylphenyl)-21-carba-porphyrin **1** (150 mg, 0.18 mmol) was added and dissolved in 88 mL of dehydrated DCM under nitrogen atmosphere. Then CF_3COOAg (156 mg, 0.71 mmol) were dissolved in 1.6 mL of methanol and added in the flask. The mixture was stirred at room temperature overnight and monitored by thin layer chromatography (TLC). After completion of the reaction, the solvents were removed *in vacuo* and the residue was purified by a silica gel chromatography using an eluent of DCM/MeOH (99:1(v/v)). The brown solid compound **1-Ag** was obtained by recrystallization. Yield 140.05 mg, 0.15 mmol, 82% yield. ^{1}H NMR (500 MHz, $CDCl_3$); δ 9.46 (s, 1H, α-H), 8.93 (d, J = 5.4 Hz, 1H, β-H), 8.80 (d, J = 4.7 Hz, 1H, β-H), 8.69 (d, J = 5.0 Hz, 1H, β-H), 8.64 (d, J = 5.0 Hz, 1H, β-H), 8.63 (d, J = 5.3 Hz, 1H, β-H), 8.59 (d, J = 5.1 Hz, 1H, β-H), 8.45 (dd, J = 13.4, 6.3 Hz, 8H, Ar-H), 8.25 (dd, J = 13.3, 7.8 Hz, 4H, Ar-H), 8.21 (dd, J = 7.9, 2.4 Hz, 4H, Ar-H), 4.11 (d, J = 5.1 Hz, 9H, COOMe), 4.00 (s, 3H, COOMe); MALDI-TOF-MASS: calcd for $C_{53}H_{35}N_4O_8Ag$ ($[M]^+$), 950.1506, found 950.845; UV-vis (CH_2Cl_2, nm): λ_{max} = 383.5, 450, 522, 638.5.

Synthesis of [2-aza-5,10,15,20-tetrakis(*p*-carbonylphenyl)-21-carba-porphyrinato]-Ag(III) (1-Ag)

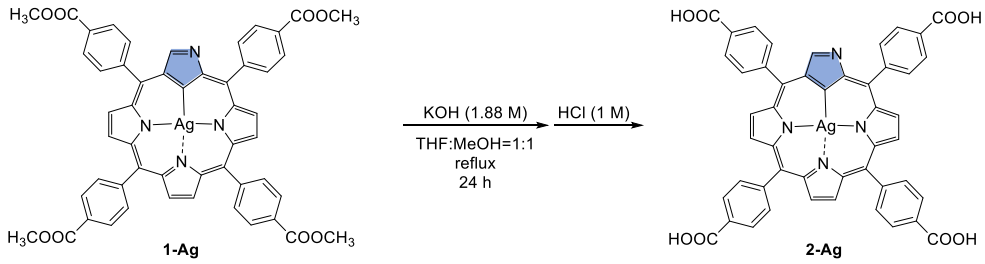

A solution of KOH (0.67 g, 12 mmol) in H_2O (25 mL) was added to a mixture of **1-Ag** (200 mg, 0.21 mmol) in THF/MeOH (50 mL, 1:1(v/v)). The mixture was stirred overnight under reflux. The resulting reaction mixture was cooled down to room temperature, and the organic solvents were evaporated *in vacuo*. Water was then added to the residue to dissolve completely. After solid impurity was removed by filtration, the precipitation was obtained via slow addition of 1 M HCl (aq.) to the filtrate to a final pH of 3. The dark brown solid was collected by filtration, washed with water and dried *in vacuo*. Yield of **1-Ag**; 146.65 mg, 0.16 mmol (78% yield). HRMS (FAB): calcd for $C_{48}H_{28}N_4O_8Ag$ ($[M+1]^+$), 895.0953, found 895.0958; UV-vis (*N*,*N*-dimethylformamide, nm): λ_{max} = 447.5, 586.5, 739.

Synthetic procedure for Porphyrinic Zr-MOFs and hybrids.

Synthesis of $ZnTPP_{MOF}$*:* 103 mg of $ZrOCl_2 \cdot 8H_2O$, 50 mg of ZnTPP, 2700 mg of benzoic acid were dissolved in 8 mL of DMF, ultrasonically for over 1 hour. The mixture was then heated and stirred in 120 ºC oven for 48 h. After cooling down to room temperature slowly, the violet solid was obtained by filtration

Synthesis of $AgNCP_{MOF}$ 75 mg of $ZrCl_4$, 50 mg NCP, 2700 mg of benzoic acid and 70 mg of CF_3COOAg were dissolved in 8 mL of DMF ultrasonically for over 1 hour. The mixture was then heated and stirred in 120 ºC oven for 48 h. After cooling down to room temperature slowly, the dark brown solid was obtained by filtration, followed by washes with DMF 3 times.

Synthesis of $ZnTPP_{MOF}$*@*$AgNCP_{MOF}$ 75 mg of $ZrCl_4$, 50 mg of (Ag)NCP, 2700 mg of benzoic acid were dissolved in 8 mL of DMF and 20 mg of $(Zn)TPP_{MOF}$ was also added into the solution, ultrasonically for over 1 hour. The mixture was then heated and stirred in 120 ºC oven for 48 h. After cooling down to room temperature slowly, the brown (dark red in the case of $ZnTPP_{MOF}$) solid was obtained by filtration, followed by washes with DMF 3 times.

Synthesis of $AgNCP_{MOF}$*@*$ZnTPP_{MOF}$ 21 mg of $ZrOCl_2$ $8H_2O$, 10 mg of (Zn)TPP, 540 mg of benzoic acid were dissolved in 2 mL of DMF and 40 mg of $(Ag)NCP_{MOF}$ was also added into the solution, ultrasonically for over 1 hour. The mixture was then heated and stirred in 120 ºC oven for 48 h. After cooling down to room temperature slowly, the solid was obtained by filtration, followed by washes with DMF 3 times.

Photosensitized singlet oxygen generation.

The photosensitized singlet oxygen generations using the hybrid MOFs were monitored through the change

in absorption of dihyroxynaphthalene (DHN) which was dissolved in dichloromethane /MeOH (10 mL, 9:1(v/v)). ZrMOF (1 mg) was dispersed in the solution and irradiated by Asahi Spectra MAX-301 Compact Xenon Light Source (300 W) equipped with band-path optical filters (450~750 nm).

3.9 Supporting Data

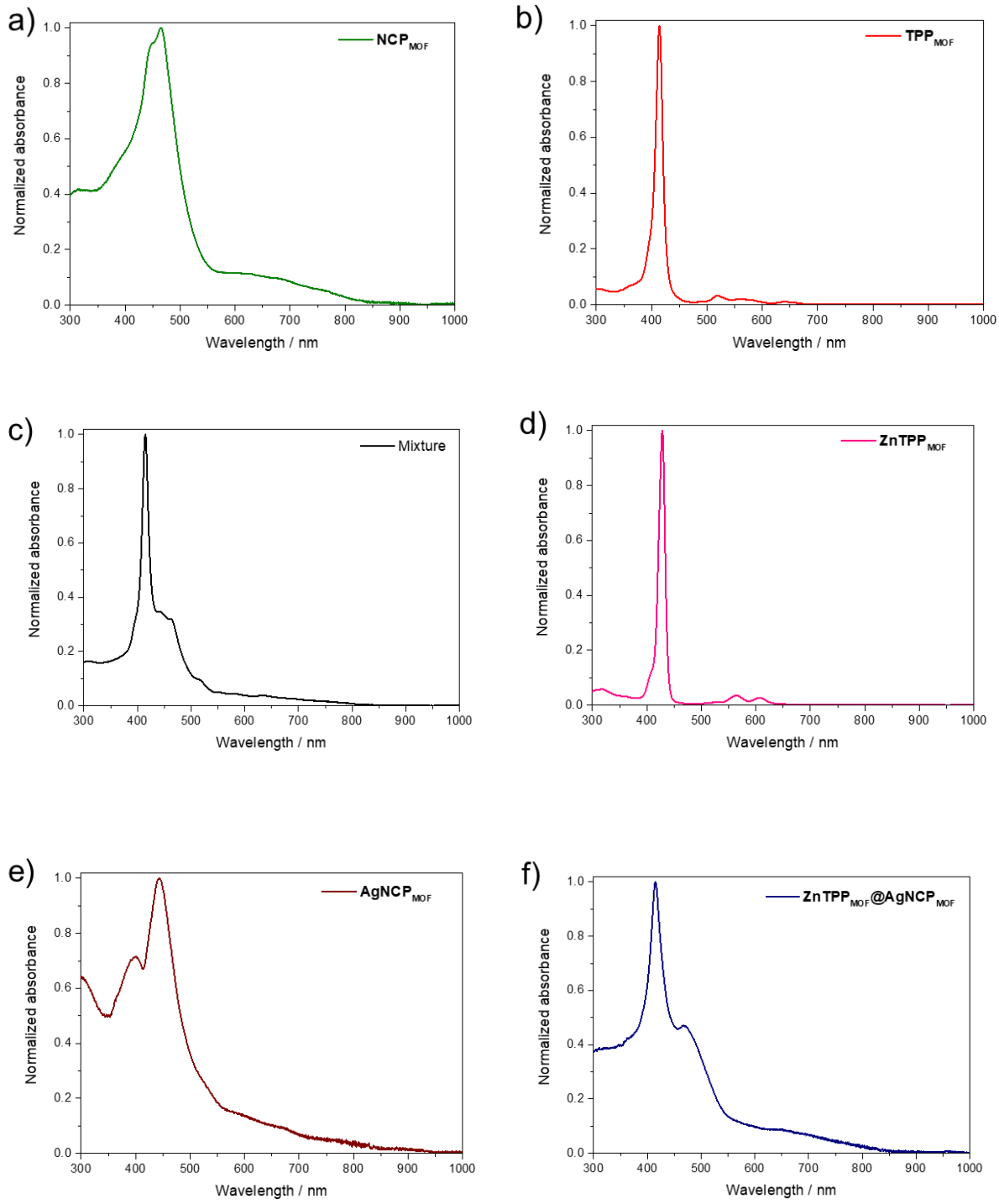

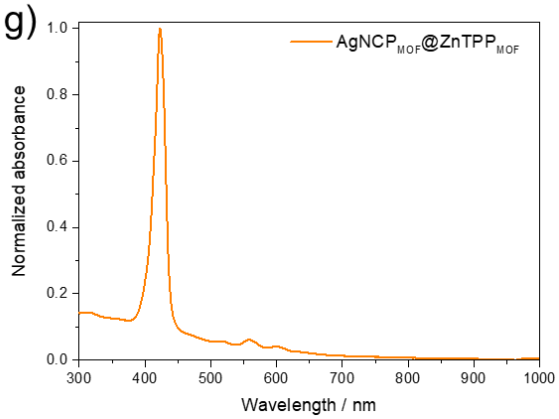

Figure 3-19. Absorption spectra of **NCP$_{MOF}$** (a), **TPP$_{MOF}$** (b), mixture (NCP$_{MOF}$:TPP$_{MOF}$=5:2) (c), **ZnTPP$_{MOF}$** (d), **AgNCP$_{MOF}$** (e), **ZnTPP$_{MOF}$@AgNCP$_{MOF}$** (f) and **AgNCP$_{MOF}$@ZnTPP$_{MOF}$** (g) dissolved in 0.1 M NaOH aqueous solution.

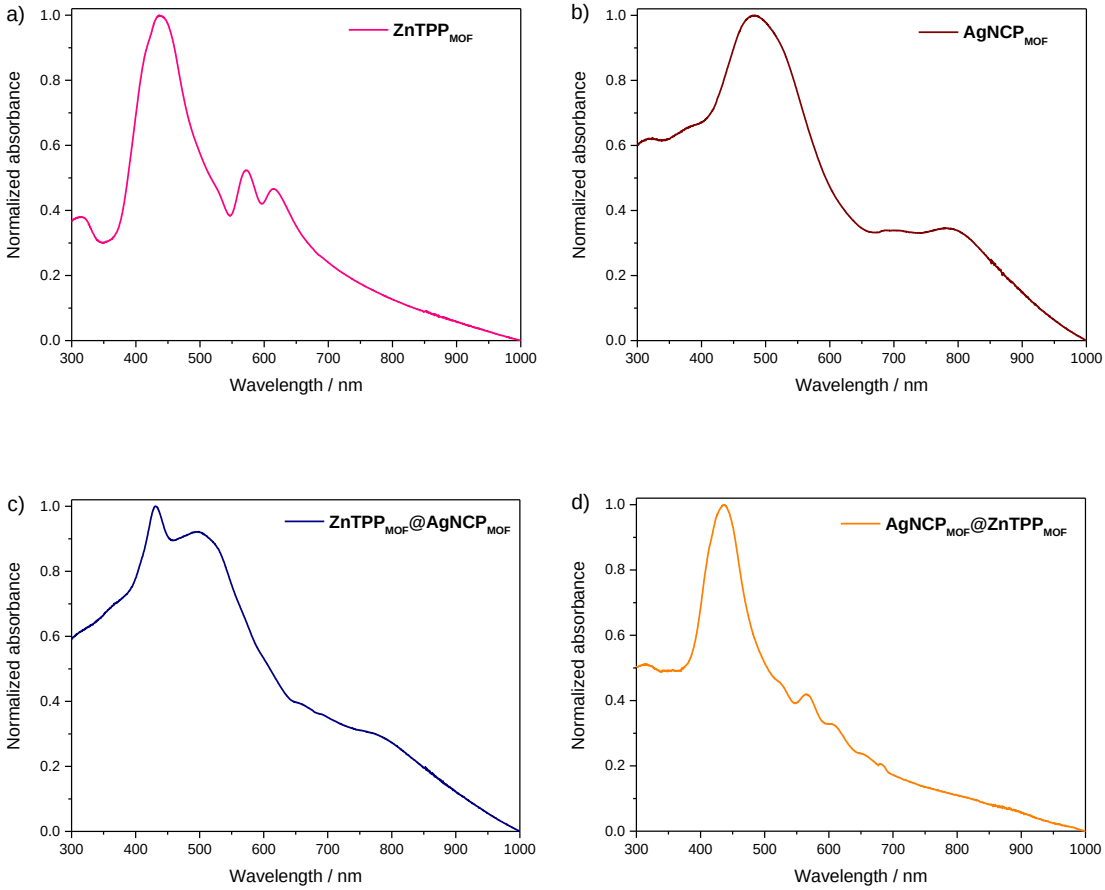

Figure 3-20. UV-vis absorption spectra of the KBr pellet containing (a) **ZnTPP$_{MOF}$**, (b) **AgNCP$_{MOF}$**, (c) **ZnTPP$_{MOF}$@AgNCP$_{MOF}$** and (d) **AgNCP$_{MOF}$@ZnTPP$_{MOF}$**.

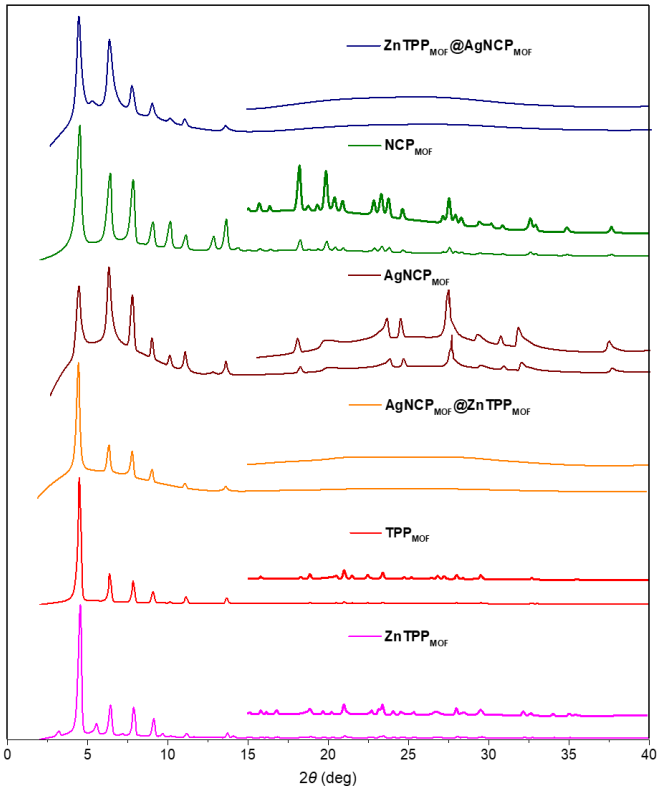

Figure 3-21. Wide-angle PXRD patterns of as-synthesized **ZnTPP$_{MOF}$@AgNCP$_{MOF}$**, **NCP$_{MOF}$**, **AgNCP$_{MOF}$**, **AgNCP$_{MOF}$@ZnTPP$_{MOF}$**, **TPP$_{MOF}$**, and **ZnTPP$_{MOF}$** crystals.

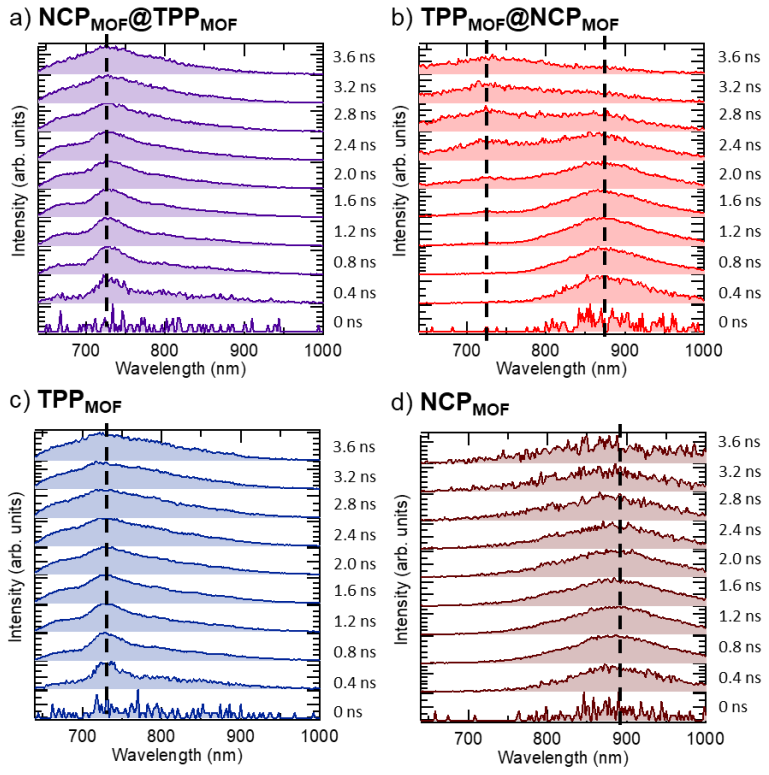

Figure 3-22. Time-resolved emission spectra of a) **NCP$_{MOF}$@TPP$_{MOF}$**, b) **TPP$_{MOF}$@NCP$_{MOF}$**, c) **TPP$_{MOF}$**, and d) **NCP$_{MOF}$** (all the intensities are normalized).

Table 3-3. Summary of emission lifetimes of the MOFs probed at 720–730 nm and 850–880 nm regions.

Sample	τ_{em} (ns) probed at 720–730 nm			τ_{em} (ns) probed at 850–880 nm		
	τ_1	τ_2	τ_{mean}	τ_1	τ_2	τ_{mean}
Mixture	1.16 (99.2%)	18.82 (0.8%)	1.30	1.18 (99.2%)	26.08 (0.8%)	1.38
NCP_{MOF}@TPP_{MOF}	1.24 (98.8%)	20.15 (1.2%)	1.46	1.33 (100%)		1.33
TPP_{MOF}@NCP_{MOF}	1.83 (86.5%)	6.07 (13.5%)	2.41	0.64 (100%)		0.64
TPP_{MOF}	1.14 (98.3%)	10.69 (1.7%)	1.30	-	-	-
NCP_{MOF}	-	-	-	0.62 (100%)		0.62

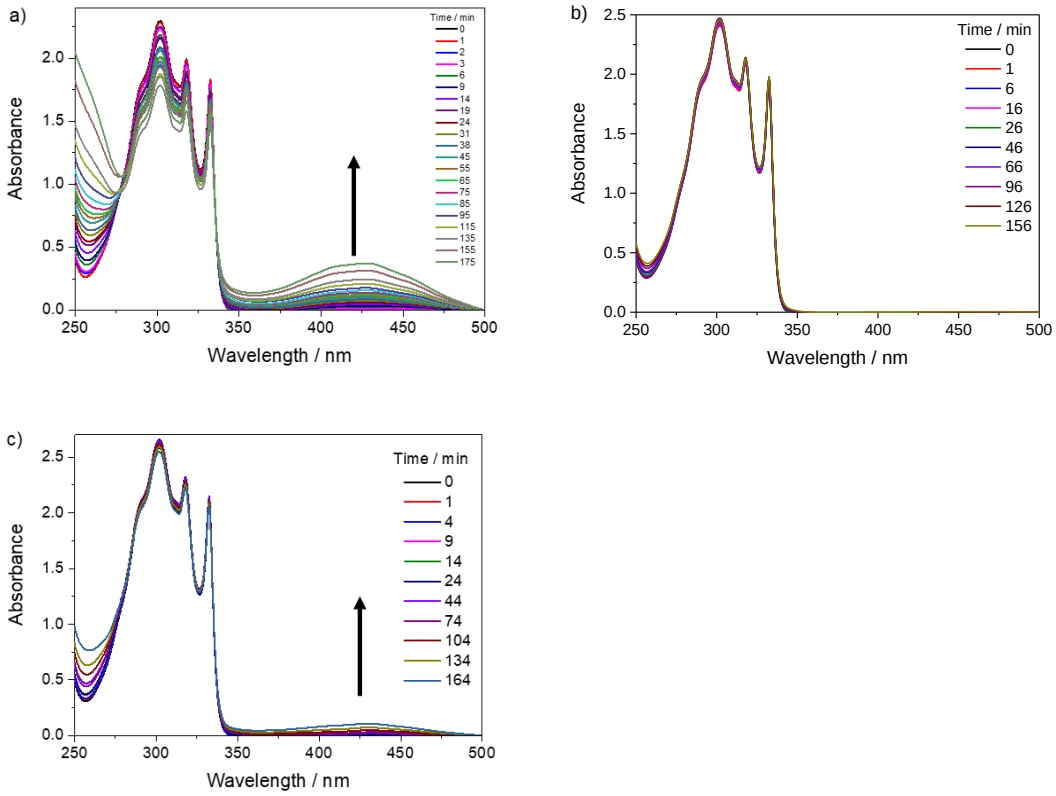

Figure 3-23. Spectral changes of DHN when treated with a) **TPP_{MOF}**, b) **NCP_{MOF}**, c) **TPP_{MOF}@NCP_{MOF}** and irradiated with light at wavelengths at 450-700 nm.

References

1. (a) Alezi, D.; Belmabkhout, Y.; Suyetin, M.; Bhatt, P. M.; Weselinski, L. J.; Solovyeva, V.; Adil, K.; Spanopoulos, I.; Trikalitis, P. N.; Emwas, A. H.; Eddaoudi, M., *J. Am. Chem. Soc.* **2015,** *137* (41), 13308-13318; (b) Ma, S.; Zhou, H. C., *Chem Commun (Camb)* **2010,** *46* (1), 44-53.
2. (a) Chughtai, A. H.; Ahmad, N.; Younus, H. A.; Laypkov, A.; Verpoort, F., *Chem. Soc. Rev.* **2015,** *44* (19), 6804-6849; (b) Corma, A.; García, H.; Llabrés i Xamena, F., *Chem. Rev.* **2010,** *110* (8), 4606-4655; (c) Deria, P.; Gomez-Gualdron, D. A.; Hod, I.; Snurr, R. Q.; Hupp, J. T.; Farha, O. K., *J. Am. Chem. Soc.* **2016,** *138* (43), 14449-14457; (d) Yuan, S.; Zou, L.; Li, H.; Chen, Y. P.; Qin, J.; Zhang, Q.; Lu, W.; Hall, M. B.; Zhou, H. C., *Angew. Chem. Int. Ed.* **2016,** *55* (36), 10776-10780.
3. (a) Fang, X.; Zong, B.; Mao, S., *Nano-Micro Letters* **2018,** *10* (4); (b) Ma, J.-P.; Yu, Y.; Dong, Y.-B., *Chem. Commun.* **2012,** *48* (24), 2946-2948; (c) Moon, S. Y.; Howarth, A. J.; Wang, T.; Vermeulen, N. A.; Hupp, J. T.; Farha, O. K., *Chem Commun (Camb)* **2016**.
4. Zheng, H.; Zhang, Y.; Liu, L.; Wan, W.; Guo, P.; Nystrom, A. M.; Zou, X., *J. Am. Chem. Soc.* **2016,** *138* (3), 962-968.
5. Wang, L.; Han, Y.; Feng, X.; Zhou, J.; Qi, P.; Wang, B., *Coord. Chem. Rev.* **2016,** *307*, 361-381.
6. (a) Bai, Y.; Dou, Y.; Xie, L. H.; Rutledge, W.; Li, J. R.; Zhou, H. C., *Chem. Soc. Rev.* **2016,** *45* (8), 2327-2367; (b) Deria, P.; Yu, J.; Balaraman, R. P.; Mashni, J.; White, S. N., *Chem Commun (Camb)* **2016,** *52* (88), 13031-13034; (c) Marshall, R. J.; Forgan, R. S., *Eur. J. Inorg. Chem.* **2016,** *2016* (27), 4310-4331.
7. Yang, Y.; Sakashita, R.; Yamasumi, K.; Ishida, M.; Yamada, T.; Furuta, H., *Chem. Lett.* **2017,** *46* (8), 1230-1232.
8. Morris, W.; Volosskiy, B.; Demir, S.; Gandara, F.; McGrier, P. L.; Furukawa, H.; Cascio, D.; Stoddart, J. F.; Yaghi, O. M., *Inorg. Chem.* **2012,** *51* (12), 6443-6445.
9. Lee, J. S.; Lim, J. M.; Toganoh, M.; Furuta, H.; Kim, D., *Chem. Commun.* **2010,** *46* (2), 285-287.
10. Miyazaki, T.; Yamamoto, T.; Mashita, S.; Deguchi, Y.; Fukuyama, K.; Ishida, M.; Mori, S.; Furuta, H., *Eur. J. Inorg. Chem.* **2018,** *2018* (2), 203-207.
11. Foo, M. L.; Matsuda, R.; Kitagawa, S., *Chem. Mater.* **2013,** *26* (1), 310-322.
12. Xu, H. Q.; Wang, K.; Ding, M.; Feng, D.; Jiang, H. L.; Zhou, H. C., *J. Am. Chem. Soc.* **2016,** *138* (16), 5316-5320.
13. Tang, J.; Salunkhe, R. R.; Liu, J.; Torad, N. L.; Imura, M.; Furukawa, S.; Yamauchi, Y., *J. Am. Chem. Soc.* **2015,** *137* (4), 1572-1580.
14. Guo, W.; Xia, W.; Cai, K.; Wu, Y.; Qiu, B.; Liang, Z.; Qu, C.; Zou, R., *Small* **2017,** *13* (41).
15. Park, J.; Feng, D.; Yuan, S.; Zhou, H. C., *Angew. Chem. Int. Ed.* **2015,** *54* (2), 430-435.
16. Park, K. C.; Seo, C.; Gupta, G.; Kim, J.; Lee, C. Y., *ACS Appl Mater Interfaces* **2017,** *9* (44), 38670-38677.

17. Feng, D.; Gu, Z. Y.; Li, J. R.; Jiang, H. L.; Wei, Z.; Zhou, H. C., *Angew. Chem. Int. Ed. Engl.* **2012,** *51* (41), 10307-10310.
18. Furuta, H.; Ogawa, T.; Uwatoko, Y.; Araki, K., *Inorg. Chem.* **1999,** *38* (11), 2676-2682.
19. Singto, S.; Tantayanon, S.; Zoto, C. A.; Connors, R. E., *J. Mol. Struct.* **2018,** *1154*, 114-130.
20. Caspar, J. V.; Meyer, T. J., *J. Phys. Chem.* **1983,** *87* (6), 952-957.
21. Toganoh, M.; Miyachi, H.; Akimaru, H.; Ito, F.; Nagamura, T.; Furuta, H., *Org. Biomol. Chem.* **2009,** *7* (15), 3027-3030.
22. Kent, C. A.; Mehl, B. P.; Ma, L.; Papanikolas, J. M.; Meyer, T. J.; Lin, W., *J. Am. Chem. Soc.* **2010,** *132* (37), 12767-12769.
23. Lismont, M.; Dreesen, L.; Wuttke, S., *Adv. Funct. Mater.* **2017,** *27* (14), 1606314.
24. (a) Hynek, J.; Ondrušová, S.; Bůžek, D.; Kovář, P.; Rathouský, J.; Demel, J., *Chem. Commun.* **2017,** *53* (61), 8557-8560; (b) Meng, A. N.; Chaihu, L. X.; Chen, H. H.; Gu, Z. Y., *Sci. Rep.* **2017,** *7* (1), 6297.
25. Hassan, G. F.; Saad, N. E. H.; Hmadeh, M.; Karam, P., *Dalton Trans.* **2018,** *47* (44), 15765-15771.

Chapter 4. Dissecting the Chloride–Nitrate Anion Transport Assay

4.1 Introduction

The design of synthetic anion receptors[1] that can carry biological anions, most importantly chloride, across phospholipid bilayers has been an active area of research in supramolecular chemistry[2]. These compounds have the future therapeutic potential to replace the function of faulty anion channels in genetic diseases[3] or to disrupt the ionic and pH gradients in cancer cells[4]. Efforts have been made to improve the potency of anion transporters, allowing them to function at low concentrations as required for therapeutic applications. When designing novel anion transporters, one must consider the target selectivity. As introduced in chapter 1, there are many ways to specifically target an anion, nevertheless one must also know the basic rule of relevant transport selectivity. In this chapter, the selectivity of transporters is discussed mainly by transmembrane transport experiments with a series of transporters.

4.1.1 Binding Affinity—Hofmeister Series

It takes two components to discuss the binding affinity, thus when considering the selectivity, one must also learn the properties of the target—anions in this case. Hofmeister series[5] is a rule that describes the ability ions of ions to salt out or salt in protein, meaning the effect of the ion on the solubility of proteins. It reflects the order of ion hydrophobicity. Hofmeister series are ordered:

$$ClO_4^- > I^- > NO_3^- > Br^- > Cl^- > HCO_3^-$$ (commonly seen monovalent anions)

In the series, HCO_3^- or Cl^- is the most hydrophilic anions, indicating they have higher affinities with organic compounds through a polar hydrogen bond. On the other hand, ClO_4^- has the highest hydrophobicity, leading to a low affinity with transporters.

Due to the Hofmeister Series, it is easier to design a compound binding strongly with the anions on the left of the series. However, anions such as NO_3^-, Br^-, Cl^-, HCO_3^- are of diagnostic and therapeutic significance, leaving chemist a huge challenge to design transporters capable of breaking the order.

4.1.2 Transport Selectivity

Now chemists have started to grasp the binding selectivity of anion toward various monovalent anions. However, it does not only depend on the binding affinity when it comes to transport selectivity. It is a more complex process in the lipid bilayer than in an organic solution due to the aqueous environment along with other factors including the stability and the overall hydrophobicity of the chelate formed by the transporter and anions and so forth. In the aqueous solution, hydrophilic anions tend to bind with surrounding water molecules through hydrogen bonding, which is also called solvation or hydration. When the transport occurs,

transporters are first forced to compete with water and bind with target anions. This process is also called dehydration, due to which the transport becomes more energy-consuming even though the binding is stronger, leading to a slower transport. On the other hand, anions on the left side of the Hofmeister series tend to be transported faster. All these factors taken together, anion transport selectivity shows uncertainty. Thus, one must conduct a real transport experiment to study the transport selectivity in the lipid bilayer. In order to do so, there are a few concepts about the experiment needed to be clarified which will be introduced as followed.

Lipid bilayer vesicle: Transport experiment are conducted on hand-made lipid bilayer vesicles before it can be conducted on the real cell. Vesicles are small particle formed by phospholipid bilayer[6]. It resembles cell membrane in structure and material. In addition, the inner and outer environment can be regulated by using different solutions to create the ideal experimental conditions. Vesicle suspension is usually made following the procedures below: (1) dissolve phospholipid in a volatile organic solvent, (2) remove the solvent to make an even film and desiccate the film completely, (3) make the wanted inner solution and add it into the lipid, shake the mixture until the lipid is dispersed evenly, (4) pass the suspension of lipid vesicles through a porous thin film to get an evenly distributed sizes of vesicles (extrusion). (Figure 4-1) Once the vesicle is made, it should be stored at low temperature and used quickly before the vesicles break. Different outer solutions can be achieved by dialysis.

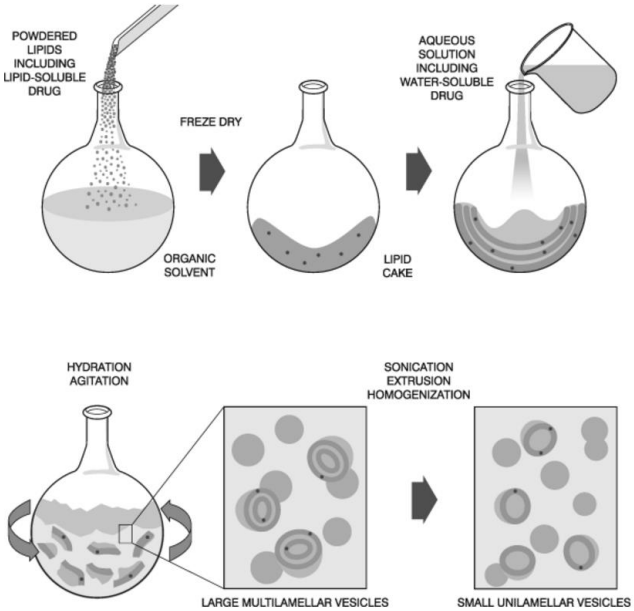

Figure 4-1. Procedures to make phospholipid bilayer vesicle suspension[6d].

Charge conservation: It is a premise of ion transport that the charge on both sides of the membrane must always stay equal, thus in the anion transport study, one also need to consider the transport other ions that can be other anions or cations. According to the other species transported, transport can be categorized into 2 types—symport and antiport. Symport is to transport another cation along with the target anions while

antiport is to transport another anion on the other side of the membrane backward at the same time. (Figure 4-2)

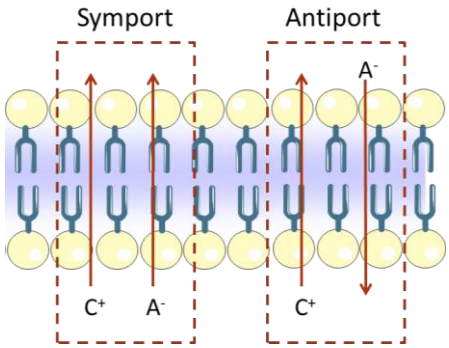

Figure 4-2. Schematic diagram of symport and antiport.

Efficiency evaluation: Like binding constant, the transport efficiency has to be quantified in the interest of further study. In the kinetic study of anion transport, half maximal effective concentration (EC_{50}), a parameter used as a measure of drug's potency, is usually calculated for comparison purpose. EC_{50} is the concentration (commonly in mol/L, M) of the tested transporter that transport 50% of the target anions in a certain amount of time, which shows a greater transport efficiency when the value is smaller.

Detection assay: Transport can occur spontaneously if there are transporter molecules and concentration difference. However, one needs also decide to use what assay to monitor the dynamic process. The assay chosen has a significant effect on the result due to the error during the monitor process. Hence, an appropriate assay must be utilized in accordance with the situation. For example, the ion-selective electrode (ISE)[7] is a typically used assay to monitor the anion concentration by the signal of the electrode. Despite the fact that it is an accurate assay, the choice is still limited due to limited types of electrodes. Thus, a rare anion needs another specific assay, which is usually the key point of the study.

Typically, chloride–nitrate exchange (antiport) assays have been used to evaluate the anion transport potency of the transporters.[8] In this assay, it is assumed that nitrate transport is unlikely to be the rate-limiting process due to the anion's high lipophilicity, and therefore this assay is assumed to indicate the chloride transport activity of the transporters.[9] However, in anion binding studies, chloride is almost always more strongly bound to hydrogen bond donor anion receptors than nitrate due to the higher charge density of Cl^-.[10] This could result in faster chloride transport than nitrate transport. The study of Cl^- vs. NO_3^- selectivity in membrane transport and its correlation with binding selectivity is thus of fundamental importance in addressing the question whether anion transport selectivity is dominated by anion lipophilicity[11] or anion affinity.[12] This information is also practically useful to unravel the potential limitations of the chloride–nitrate exchange assay. Recently, Gale and coworkers have developed membrane transport assays that could measure the rate of anion uniport mediated by anion transporters without the need for an anion exchange

process to occur.[13]

4.1.3 Purpose of This Chapter

In this chapter, the author makes use of two complementary vesicle-based assays created by Gale and coworkers to determine anion transport selectivity, in particular, Cl^-/NO_3^- selectivity of a library of hydrogen bond-based anion transporters**.** By comparing these results with association constants for anion complexation determined in acetonitrile, the author demonstrates for the first time a strong correlation between binding selectivity and transport selectivity across a series of structurally diverse anion transporters.

4.2 Molecular Design and Synthesis of Anion Transporters

The transporters **1**–**6** studied in this chapter are demonstrated in Figure 4-3. The increasing numbers of hydrogen bond donors help the strength of their bonding with anions. Different geometries help study the relationships between structure and selectivity.

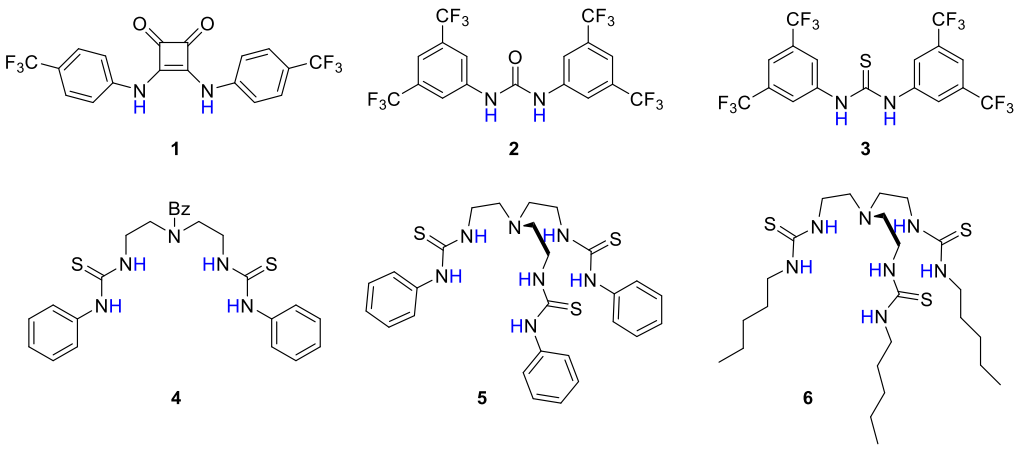

Figure 4-3. Structures of anion transporters **1**–**6**.

Compounds **1**, **2**, **3**, **5**, and **6** are examples of anion transporters previously studied by our group[12,13b,14]. These compounds represent two distinct design approaches to highly effective anion transporters. Compounds **1**–**3** contain highly acidic NH groups, leading to high anion binding affinity and the ability to disperse the negative charge of the bound anion. Compounds **5** and **6** are without the electron-withdrawing CF_3 groups but contain more hydrogen bond donors that are favorable for binding and transport because of multivalency[15] and encapsulation.[16] Their protonated cationic forms do not participate in anion transport as demonstrated previously.[13b] The author synthesized a new receptor **4** as a dipodal control of the tripodal thiourea **5**. The detailed synthesis strategies are demonstrated in the Experimental section.

4.3 Binding affinity

The affinities of these transporters towards anions including Cl^-, Br^- and NO_3^- in acetonitrile were determined by UV-vis absorption titrations using tetrabutylammonium (TBA^+) salts of the anions. UV-vis binding studies were performed by adding a CH_3CN solution containing both the host and the guest (TBACl, TBABr or $TBANO_3$) into a CH_3CN solution of the host in a quartz cuvette thermostated at 298 K. The UV-vis spectra of the host in the absence and presence of increasing concentration of the guest were measured. The absorbance values at a chosen wavelength were plotted against the guest concentration and fitted to a 1:1 binding model. (Experimental section)

From all compounds, similar anion binding selectivity trend was observed, which follows the anion charge density ($Cl^- > Br^- > NO_3^-$). Despite the same anion binding selectivity sequence, the actual extent of Cl^-/NO_3^- binding selectivity, i.e. the $S_b(Cl^-/NO_3^-)$ value, showed significant variation among different structure. The two tripodal compounds **5** and **6** have very high (41500-fold) binding selectivities for Cl^- over NO_3^-, whereas the other ureas and thioureas have a selectivity value of less than 150. A similar trend was found for the Br^-/NO_3^- binding selectivity. Compared with the dipodal thiourea **4**, the additional thiourea arm in **5** dramatically enhances the binding of Cl^- and Br^- but does not improve NO_3^- binding as much. These binding results give a hint that the tripodal compounds could behave differently in anion transport selectivity compared with other compounds. (Table 4-1 and Table 4-2)

Table 4-1. Anion binding data for compounds **1**–**6** in CH_3CN

Compound	$K_a(Cl^-)/M^{-1}$	$K_a(NO_3^-)/M^{-1}$	S_b (Cl^-/NO_3^-)
1	8.2×10^5	2.5×10^3	330
2	1.8×10^4	1.1×10^3	17
3	2.3×10^4	6.0×10^2	38
4	3.0×10^4	2.1×10^2	140
5	1.7×10^4	2.7×10^2	6200
6	8.3×10^4	4.9×10^2	1700

Association constant determined by UV-vis titration in acetonitrile at 298 K, using tetrabutylammonium anion salts. Errors were found to be < 10%. Cl^-/NO_3^- binding selectivity S_b (Cl^-/NO_3^-) = Ka(Cl^-)/Ka(NO_3^-).

Table 4-2. Br^- association constants and selectivities of compounds **1**−**6** in acetonitrile at 298 K.

Compound	K_a (Br^-) / M^{-1}	S_b (Br^-/NO_3^-)[a]	S_b (Cl^-/Br^-)[b]
1	3.3 × 10^4	13	25
2	1.9 × 10^3	1.8	9.8
3	1.7 × 10^3	2.8	14
4	1.4 × 10^3	6.8	21
5	1.7 × 10^4	62	100
6	2.2 × 10^4	44	38

[a] Br^-/NO_3^- binding selectivity S_b (Br^-/NO_3^-) = K_a (Br-) / K_a (NO_3^-). [b] Cl^-/Br^- binding selectivity S_b(Cl^-/Br^-) = K_a (Cl^-) / K_a (Br^-).

4.4 Transport Selectivity

4.4.1 Transport Selectivity Analysis

In this chapter, a traditional Ion Selective Electrode assay (ISE assay)[7] was first conducted. (See details in section **4.6.3**.) As was expected, ISE assay provides no information on Cl^-/NO_3^- selectivity. Then the author further conducted two additional assays to directly measure anion selectivity, which are called HPTS assay and Osmotic assay. (See details in section **4.6.4** and **4.6.5**)[17, 18]

In both HPTS and osmotic assays, the Cl^-/NO_3^- transport selectivity S_t(Cl^-/NO_3^-) was quantified by the ratio between EC_{50} of NO_3^- transport and EC_{50} of Cl^- transport, where an S_t(Cl^-/NO_3^-) value > 1 indicates Cl^- selectivity (Table 4-3). The results demonstrate that NO_3^- transport proceeds faster than Cl^- transport for monopodal transporters **1**–**3** and dipodal transporter **4**. This is consistent with the higher lipophilicity of NO_3^- than Cl^- while contrary to the $Cl^- > NO_3^-$ binding selectivity of the compounds in acetonitrile. The results suggest that in these cases transport selectivity is dominated by the ease of anion dehydration. In contrast to **1**–**4**, tripodal compounds **5** and **6** transported Cl^- faster than NO_3^-, with **5** showing an 8-fold Cl^-/NO_3^- selectivity in the HPTS assay and a 10-fold selectivity in the osmotic assay. Therefore, **5** and **6** are unusual examples of anion transporters that can break the normally observed $NO_3^- > Cl^-$ lipophilicity order. This cannot be explained as a general ‘‘anti-Hofmeister’’ selectivity as **5** and **6** transported the more lipophilic anion Br^- faster than Cl^-. It is interesting to note that the transport selectivity S_t (Cl^-/NO_3^-) in general shows a good correlation with the binding selectivity S_b(Cl^-/NO_3^-) (Figure 4-4). Both selectivities follow the trend of **5** > **6** > **1** > **2**–**4**. $Cl^- > NO_3^-$ selectivity is only observed for **5** and **6** that have the largest binding preference for Cl^- over NO_3^- among the library. Squaramide **1**, despite being a NO_3^--selective transporter, has a significantly larger S_t (Cl^-/NO_3^-) value compared with **2**–**4**, consistent with **1** being the third most $Cl^- > NO_3^-$ selective binder. The correlation, however, is not perfect with compounds **2**–**4**. This may be rationalized by

the idea that the rate of ionophore-catalyzed ion transport depends not only on the ion binding affinity (which determines the amount of ion–ionophore complex with respect to the free ionophore) but also on the ability of the chelate to move through lipid bilayers.[19]

Table 4-3. Anion transport data for compounds **1**–**6**

Compound	ISE exchange assay [a]	HPTS assay [d]			Osmotic assay [g]		
	$EC_{50}(Cl^-$-NO_3^- exchange)/mol%	$EC_{50}(Cl^-)$/ mol%	$EC_{50}(NO_3^-)$ /mol%	S_t (Cl^- /NO_3^-)	$EC_{50}(Cl^-)$ /mol%	$EC_{50}(NO_3^-)$ /mol%	S_t(Cl^- /NO_3^-)
1	0.060 [b]	0.0089 [e]	0.0073 [e]	0.82	0.093	0.078	0.85
2	0.30 [b]	0.043 [e]	0.0052 [e]	0.12	0.27	0.069	0.26
3	0.16 [b]	0.013 [e]	0.0014 [e]	0.11	0.12	0.031	0.26
4	>5	0.49 [f]	0.045 [f]	0.091	3.3	0.92	0.28
5	0.31 [c]	0.0044 [f]	0.036 [f]	8.1	0.055	0.56	10
6	0.11	0.0034 [f]	0.010 [f]	3.0	0.037	0.18	4.9

[a] Cl^-–NO_3^- exchange assay schematically shown in Figure 4, using POPC LUVs with a mean diameter of ~200 nm. EC_{50} calculated at 270 s. [b] Reported in ref. 9. [c] Reported in ref. 11a. [d] H^+–Cl^- cotransport assay schematically shown in Figure 4-5, using POPC LUVs with a mean diameter of ~200 nm. EC_{50} calculated at 200 s. Cl^-/NO_3^- transport selectivity in this assay: $S_t(Cl^-/NO_3^-) = EC_{50}(NO_3^-)/EC_{50}(Cl^-)$. [e] Determined in the absence of proton channel gramicidin D. The addition of gramicidin D did not affect the overall transport rate because these compounds are by themselves good H^+/OH^- transporters. See ref. 10b. [f] Determined in the presence of gramicidin D to remove the need of anion transporters to facilitate H^+/OH^- transport. Without gramicidin, H^-/OH^- transport facilitated by these compounds is slow and would rate-limit the overall transport process. See ref. 10b. [g] K^+–Cl^- cotransport assay schematically shown in Figure 4-6, using POPC LUVs with a mean diameter of ~400 nm. EC_{50} calculated at 600 s. Cl^-/NO_3^- transport selectivity in this assay: S_t (Cl^- /NO_3^-) = $EC_{50}(NO_3^-)/EC_{50}(Cl^-)$.

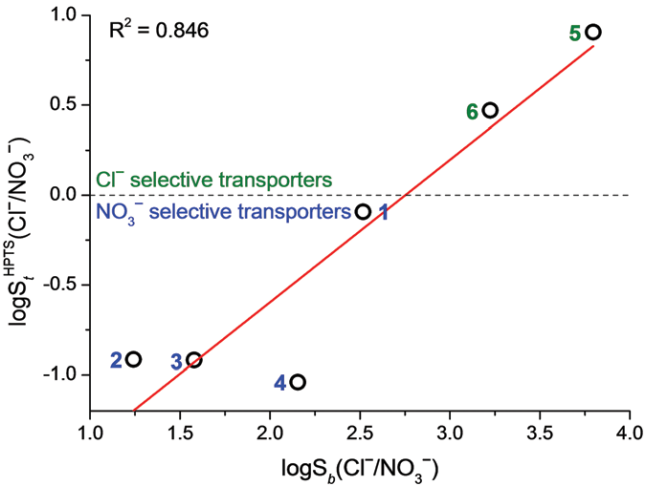

Figure 4-4. Correlation between transport selectivity logS_t (Cl^-/NO_3^-) and binding selectivity logS_b (Cl^-/NO_3^-). Compound numbers are shown next to the data points.

It is interesting to compare the activity determined in the three membrane transport assays. The data from HPTS and osmotic assays showed identical selectivities, with the EC_{50} value in the osmotic assay consistently being about an order of magnitude higher than that in the HPTS assay for the same compound transporting the same anion.[20] Both assays have revealed the Cl^- transport activity in the order of **6** > **5** > **1** > **3** > **2** > **4**, whereas NO_3^- transport activity in the sequence of **3** > **2** > **1** > **6** > **5** > **4**. The Cl^-–NO_3^- exchange assay showed the activity sequence of **1** > **6** > **3** > **2** ≈ **5** > **4**, which reflected the activity of transporting the "slower" anion (Cl^- in the cases of **1**–**4**, and NO_3^- in the cases of **5** and **6**). By converting the EC_{50} values to normalized activities, a reasonable agreement between the three transport assays can be observed. It is evident that the Cl^-–NO_3^- exchange assay gives a fair assessment of Cl^- transport activity of compounds **1**–**4** because the overall process is rate-limited by Cl^- transport in these cases. However, the Cl^- transport activity of **5** and **6** is clearly underestimated in the exchange assay. Both compounds are in fact better Cl^- transporters than the best Cl^-–NO_3^- exchanger **1**. Compound **1** turned out to be neither the best Cl^- transporter nor the best NO_3^- transporter (Figure 4-5).

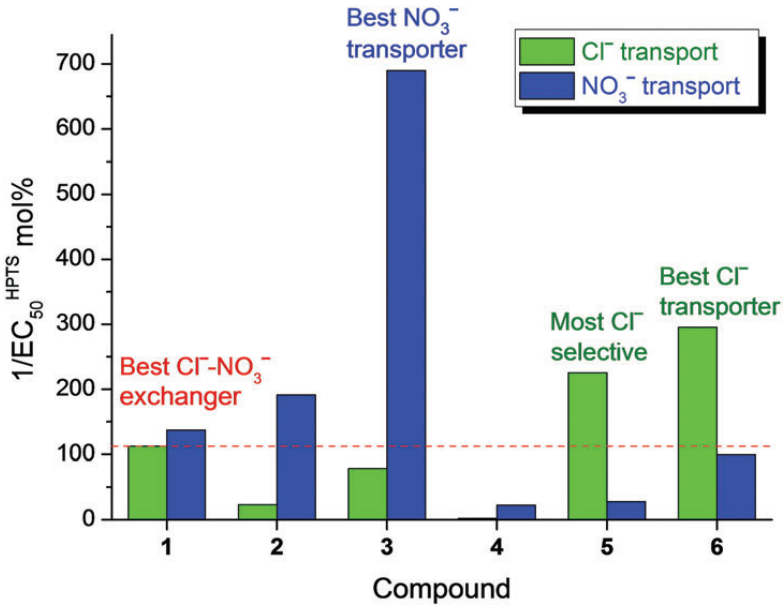

Figure 4-5. Histogram showing activities of **1**–**6** in facilitating uniport of Cl^- (green bars) and NO_3^- (blue bars). Activities are expressed as reciprocal of EC_{50} values (at 200 s) determined in the HPTS assay. The red dashed line shows that compound **1** has the highest activity in facilitating the slower anion uniport process, which explains its highest activity in the Cl^-–NO_3^- exchange assay.

4.4.2 Theoretical Calculation

For a better understanding of the $Cl^- > NO_3^-$ selectivity of the tripodal compound**s,** the author performed PM6-optimisation of the structures of the Cl^- and NO_3^- chelate of **5**. Figure 4-6 shows that the spherical anion Cl^- fits well and is well-encapsulated inside the cavity of the tripodal scaffold, whereas binding of the planar anion NO_3^- forces the scaffold to adopt a more open conformation leaving a significant part of the bound NO_3^- exposed to the solvent. Encapsulation of the anion is crucial for effective membrane transport as demonstrated by previous work [16, 13b] and therefore the poor encapsulation of NO_3^- could result in the $Cl^- > NO_3^-$ transport selectivity of the tripodal compounds.

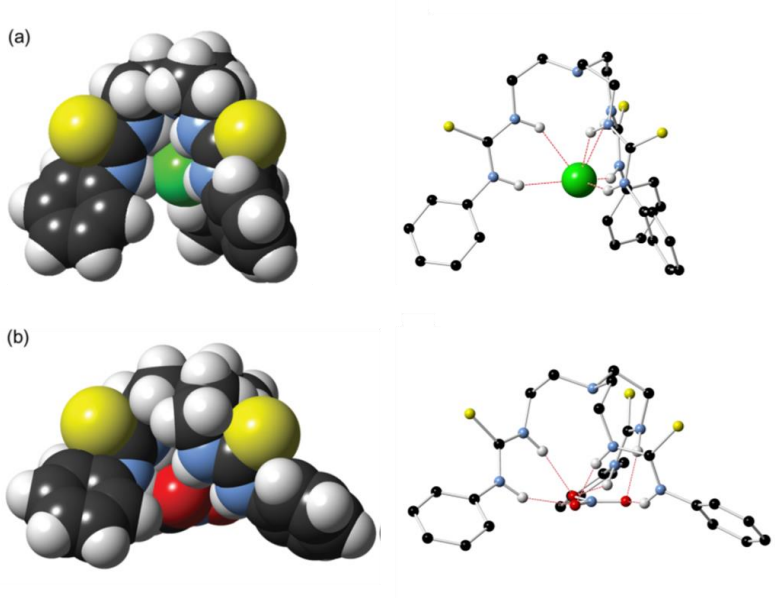

Figure 4-6. PM6-optimised structures of Cl^- (a) and NO_3^- (b) complexes of **5** shown in space-filling models and ball-and-stick models. Most hydrogen atoms have been omitted for clarity. Hydrogen bonds are represented by red dashed lines.

4.5 Conclusion

In this chapter, the author has examined the chloride vs. nitrate selectivity of representative hydrogen bond-based anion transporters in both binding and transport. A strong correlation between transport selectivity and binding selectivity has been found. Only the tripodal transporters **5** and **6** that have a large Cl^-/NO_3^- binding preference can overcome the Hofmeister hydrophobicity order to transport Cl^- selectively over NO_3^-. The author has compared the anion transport potency determined from different assays, showing that the commonly used Cl^-–NO_3^- exchange assay is valid in most cases for evaluating Cl^- transport activity but sometimes gives an underestimation in the case of a poor NO_3^- transporter. Importantly, the author has also demonstrated that compound **5** functions as a highly Cl^--selective transporter showing a ~10-fold Cl^- over NO_3^- selectivity in membrane transport, because of its complementary fit for Cl^-. The author believes that the structure-selectivity and binding-transport relationships demonstrated here, and the different assays provided in this work will provide valuable tools for future development of highly potent and selective anion transporters for biomedical applications.

4.6 Experimental Section

4.6.1 General

POPC was purchased from Avanti Polar Lipids. Other commercially available chemicals were purchased

from Sigma-Aldrich, Alfa-Aesar, or Fisher Scientific, and used as received. UV-vis absorption spectra were obtained on an Agilent Cary-100 UV-vis Spectrophotometer equipped with a stirrer plate and a temperature controller. Fluorescence and light scattering measurements were performed using an Agilent Cary Eclipse Fluorescence Spectrophotometer equipped with a stirrer plate and a temperature controller. Compounds **1**[21], **2**[22], **3**[23], **5**[24] and **6**[25] were synthesized following reported procedures.

Abbreviations

DMSO	Dimethyl sulfoxide
HEPES	4-(2-Hydroxyethyl)-1-piperazineethanesulfonic acid
HPTS	8-Hydroxypyrene-1,3,6-trisulfonic acid
LUV	Large unilamellar vesicles
NMDG	*N*-methyl-D-glucamine
POPC	1-Palmitoyl-2-oleoyl-*sn*-glycero-3-phosphocholine
TBA	Tetrabutylammonium
UV-vis	Ultraviolet-visible
Vln	Valinomycin

4.6.2 Synthetic Procedures

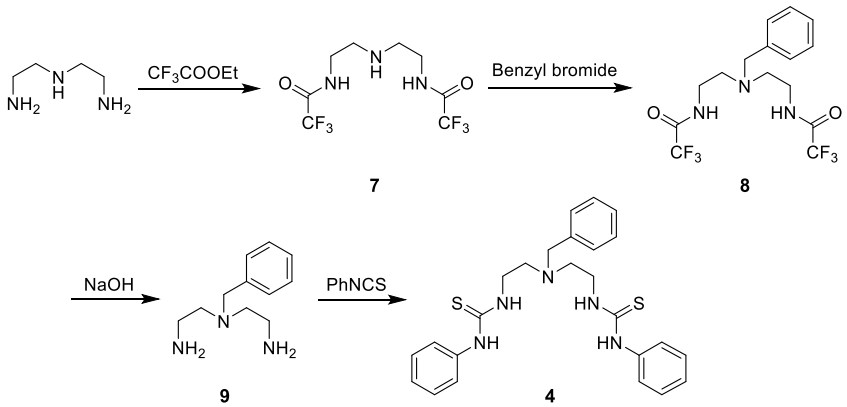

***N*,*N*'-(azanediylbis(ethane-2,1-diyl))bis(2,2,2-trifluoroacetamide) (7)**. A mixture of 2.68 mL diethylenetriamine (25 mmol) and 10.1 mL ethyltrifluoro acetate (85 mmol, 3.5 eq) in 50 mL acetonitrile containing 0.5 mL water was refluxed for 18 h. The solvents were removed under reduced pressure and the residue was recrystallised from 1:1 MeCN-Et_2O. The precipitate was filtered off and washed with cold Et_2O to give a white solid (7.35 g, 24.8 mmol). Yield: 99%; ^{1}H NMR (300 MHz, DMSO-d_6) δ ppm 3.14 (t, J = 6.22 Hz, 4 H), 3.50 (q, J = 5.85 Hz, 4 H), 8.70 (br. s., 1 H), 9.59 (br. s., 2 H); ^{13}C NMR (75 MHz, DMSO-d_6) δ ppm 35.70, 45.17, 115.65 (q, J=288.60 Hz), 156.60 (q, J = 35.38 Hz), 158.96; LRMS (ESI+): m/z = 296.2 $[M+H]^+$.

***N*,*N*'-((benzylazanediyl)bis(ethane-2,1-diyl))bis(2,2,2-trifluoroacetamide) (8)**. A mixture of 4.00 g compound **4** (13.5 mmol) and 4.00 mL triethylamine (28.7 mmol) in acetonitrile (50 mL) was stirred for 2 h at 50°C under nitrogen. 2.50 mL benzyl bromide (21.0 mmol) was added and the solution was stirred for 48 h at 50°C under nitrogen. Acetonitrile was removed under reduced pressure and the residue was purified by column chromatography (5% methanol in dichloromethane), followed by recrystalisation from 1:1 dichloromethane-hexane. The resulting precipitate was filtered off and washed with hexane to give a white solid (2.72 g, 7.04 mmol). Yield: 53%; ^{1}H NMR (300 MHz, DMSO-d_6) δ ppm 2.59 (t, J = 6.59 Hz, 4 H), 3.29 (q, J = 6.03 Hz, 4 H), 3.60 (s, 2 H), 7.25 (m, 5 H), 9.21 (br. s., 2 H); ^{13}C NMR (75 MHz, DMSO-d_6) δ ppm 37.06, 51.53, 57.49, 115.90 (q, J = 289.70 Hz), 126.83, 128.04, 128.38, 139.06, 156.19 (q, J = 35.38 Hz); LRMS (ESI+): *m/z* = 386.2 $[M+H]^+$, 408.2 $[M+Na]^+$; HRMS (ES) for $C_{15}H_{18}F_6N_3O_2$ $[M+H]^+$: *m/z* = 386.1298 (calcd), 386.1304 (found).

***N*^{1}-(2-aminoethyl)-*N*^{1}-benzylethane-1,2-diamine (9)**. Compound **8** (2.50 g, 6.4 mmol) was dissolved in 25 mL methanol. A solution of 2.50 g NaOH in 25 mL water was added and the mixture was stirred overnight at room temperature. Methanol was removed under reduced pressure and the remaining aqueous phase was extracted with DCM (3 × 50 mL). The combined organic phases were dried with $MgSO_4$ and the $MgSO_4$ was subsequently removed by filtration. DCM was removed under reduced pressure and dried overnight *in vacuo* to give a clear oil (0.94 g, 4.83 mmol). Compound **9** was used without further purification. Yield: 75%; ^{1}H NMR (300 MHz, $CDCl_3$) δ ppm 2.52 (br. s., 4 H), 2.76 (br. s., 4 H), 3.56 (br. s., 2 H), 7.20 (m, 5 H); ^{13}C NMR (75 MHz, $CDCl_3$) δ ppm 38.92, 55.55, 58.17, 127.09, 128.29, 129.10, 138.45.

1,1'-((benzylazanediyl)bis(ethane-2,1-diyl))bis(3-phenylthiourea) (4). A mixture of 0.30 g compound **9** (1.55 mmol), 0.50 g Na_2SO_4 and 2 equivalents of phenyl isothiocyanate in 50 mL DCM was stirred overnight at room temperature under nitrogen. 20 mL water was added to remove Na_2SO_4. The DCM layer was removed and the aqueous phase was further extracted with DCM (2x50 mL). The combined organic layers were dried with $MgSO_4$ and the $MgSO_4$ was subsequently removed by filtration. DCM was removed under reduced pressure and the crude oil was recrystallized from 1:1 DCM-hexane. The precipitate was filtered off and washed with hexane. The white solid was then dried overnight *in vacuo* (0.66 g, 1.42 mmol). Yield: 92%; Mp: 156.0-156.4°C; ^{1}H NMR (300 MHz, DMSO-d_6) δ ppm 2.64 (t, J=6.59 Hz, 4 H), 3.60 (q, J=5.65 Hz, 4 H), 3.64 (s, 2 H), 7.14 (m, 2 H), 7.22 (m, 5 H), 7.35 (m, 8 H), 7.55 (br. s., 3 H), 9.62 (br. s., 3 H); ^{13}C NMR (75 MHz, DMSO-d_6) δ ppm 41.60, 51.55, 57.61, 123.41, 124.42, 126.75, 128.09, 128.52, 128.77, 138.96, 138.96, 180.00; IR (film): ν = 3160 (*br*, NH stretch), 1520 (CS stretch) cm^{-1}; LRMS (ESI+): *m/z* = 464.2 $[M+H]^+$, 486.2 $[M+Na]^+$; HRMS (ES) for $C_{25}H_{30}N_5S_2$ $[M+H]^+$: *m/z* = 464.1937 (calcd), 464.1939 (found).

4.6.3 Ion Selective Electrode (ISE assay)

A traditional Cl^-–NO_3^- exchange assay was conducted on all compounds (Figure 4-4). 1-palmitoyl-2-oleoylsn-glycero-3-phosphocholine (POPC) large unilamellar vesicles (LUVs) were loaded with NaCl (490 mM) buffered at pH 7.2, and suspended in $NaNO_3$ (490 mM) buffered at pH 7.2. The anion transporter was added to the vesicle suspension as a DMSO solution. Chloride efflux (due to Cl^-–NO_3^- exchange induced by the anion transporters) was monitored via the appearance of Cl^- in the external solution, measured by a chloride ion-selective electrode (ISE). The activity of a transporter was quantified by EC_{50} at 270 s, which was calculated by applying Hill plot.

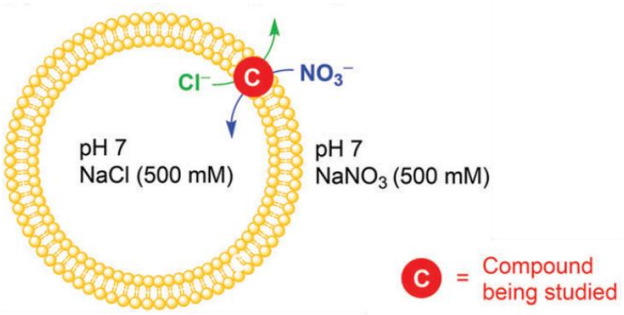

Figure 4-7. Schematic diagram of ISE Cl^-—NO_3^- exchange assay.

Hill plot analyses were performed with the test compound loaded at different concentrations. The chloride efflux at 270 s was plotted as a function of the compound concentration. Hill coefficients (n) and EC_{50} (270 s) values were calculated by fitting the curves to the following equation:

$$y = y_0 + (y_{max} - y_0)\frac{x^n}{K+x^n} \quad (1)$$

where y is chloride efflux (270 s) value with the compound loaded at concentration x, y_0 is the chloride efflux (270 s) value obtained without the compound, y_{max} is the maximum chloride efflux (270 s) value, n is the Hill coefficient, and K is the EC_{50} (270 s) value. The results are demonstrated in Table 3.

4.6.4 HPTS Assay

HPTS assay is a detection that utilizes 8-hydroxypyrene-1,3,6-trisulfonic acid (HPTS, a fluorescent dye that is sensitive to the pH change) to monitor the dynamic behavior through the spectral changes due to pH change[27]. In the assay, POPC LUVs with a mean diameter of 200 nm were loaded with and suspended in a solution of the N-methyl-D-glucamine salt of the target anion (NMDG-X, 100 mM, X^- = Cl^- or NO_3^-) buffered at pH 7.0 with HEPES. The external pH was brought to ~8 by addition of a base pulse (5 mM of N-methyl-D-glucamine), and then the transporter-induced dissipation of the pH gradient across vesicle membranes was

measured using an intravesicular fluorescent pH indicator HPTS. The overall process leading to pH gradient dissipation is H^+–X^- symport or OH^-—X^- antiport, which may be rate-limited by H^+ or OH^- transport. However, the need for an anion transporter to facilitate H^- or OH^- transport can be eliminated by using the natural proton channel gramicidin,[13b] allowing this assay to reveal the ability of an anion transporter to facilitate X^- transport (Figure 4-5).

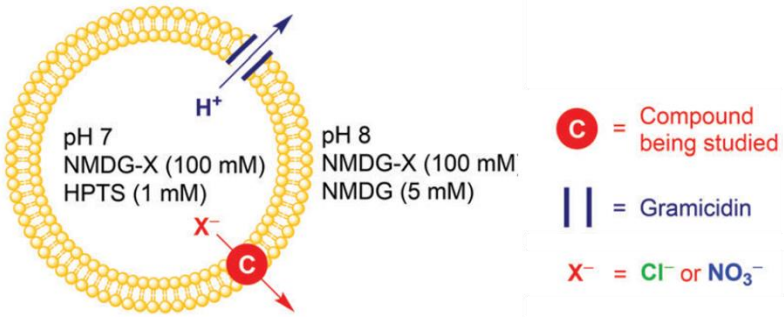

Figure 4-8. Schematic diagram of the HPTS assay.

At the end of each measurement, a detergent (22 μL of 11% (w%) Triton X-100 in 7 : 1 (v/v) H_2O-DMSO) was added to destroy the pH gradient to calibrate the assay. The fractional fluorescence intensity (I_f) was calculated using the following equation:

$$I_f = \frac{R_t - R_0}{R_f - R_0} \quad (2)$$

where R_t is the fluorescence ratio at time t, R_0 is the fluorescence ratio at time 0, and R_f is the final fluorescence ratio after detergent addition.

Hill plot analyses were performed with the test compound loaded at different concentrations. The fractional fluorescence intensity I_f at 200 s was plotted as a function of the compound concentration. Hill coefficients (n) and EC_{50} (200 s) values were calculated by fitting the curves to equation (1), where y is I_f (200 s) value with the compound loaded at concentration x, y_0 is the I_f (200 s) value obtained without the compound, y_{max} is the maximum I_f value, n is the Hill coefficient, and K is the EC_{50} (200 s) value. The results are shown in Table 3.

4.6.5 Osmotic Assay

Osmotic assay is another detection to monitor the dynamic transport behavior by utilizing the osmotic pressure, where larger POPC LUVs are needed. When a symport of species inside vesicles transported out occurs, the overall concentration decreases on the inside, resulting in an increase in the osmotic pressure. Due to the nature of semipermeable membrane, water is forced to diffuse out of the vesicles under the

pressure, leading to a shrink in the volume of the vesicles which can be detected by changes in the intensity of the scattering light. Using this scattering light intensity signal as the indicator, the kinetic study of the anion transport can be achieved.

In this assay, POPC LUVs (mean diameter 400 nm) were loaded with a buffered KX (300 mM) solution and suspended in a buffered K^+ gluconate (300 mM) solution. A combination of valinomycin (for transporting K^+) and an anion transporter give overall K^+–X^- cotransport (Figure 4-6), leading to water efflux to balance the osmotic difference and the resultant shrinkage of vesicles, which can be monitored by following the light scattering of vesicles using a fluorometer.[18]

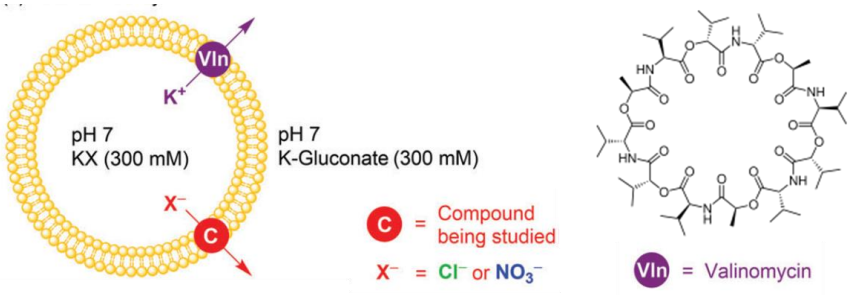

Figure 4-9. Schematic diagram of the osmotic assay and the structure of valinomycin.

The fractional intensity (I_f) was calculated using the following equation:

$$I_f = \frac{I_t - I_0}{I_{final} - I_0} \quad (3)$$

where I_t is the light scattering intensity at time t, I_0 is the light scattering intensity at time 0, and I_{final} is the final light scattering intensity after the addition of ionophores at the end of each measurement. And then hill plot was used to calculate the EC50 value. The fractional intensity I_f at 600 s was plotted as a function of the compound concentration. Hill coefficients (n) and EC_{50} (600 s) values were calculated by fitting the curves to equation (1), where y is I_f (600 s) value with the compound loaded at concentration x, y_0 is the I_f (600 s) value obtained without the compound, y_{max} is the maximum I_f value, n is the Hill coefficient, and K is the EC_{50} (600 s) value. The results are shown in Table 4-3.

4.7 Supporting Data

4.7.1 Characterization of Compounds

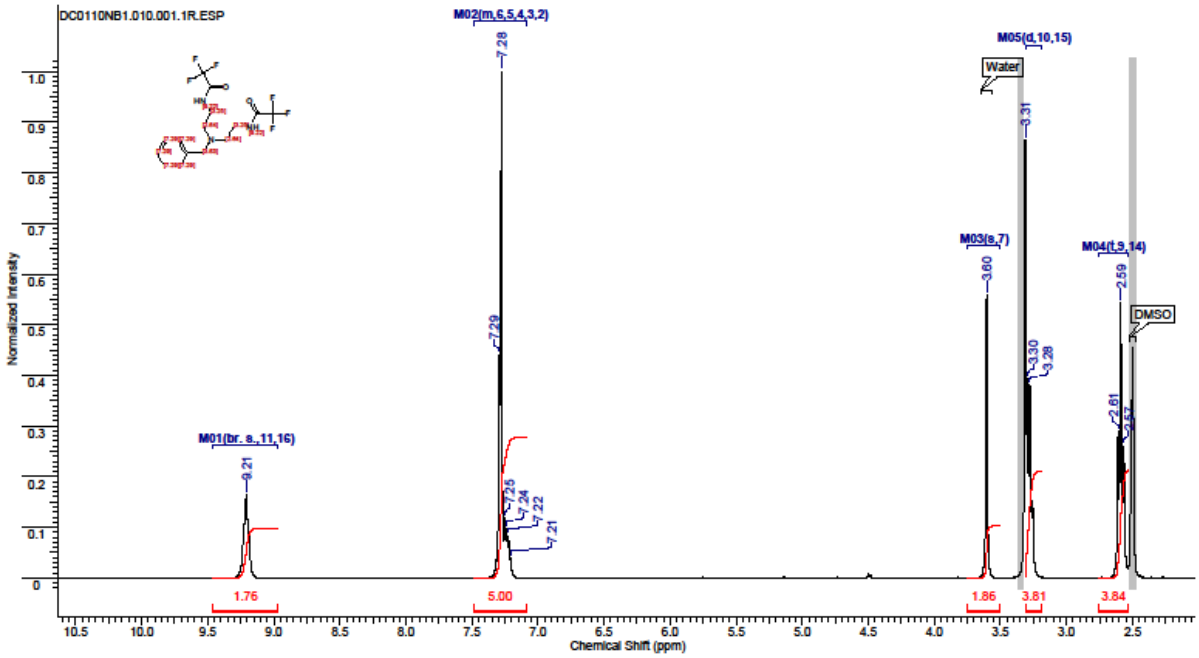

Figure 4-10. ^{1}H NMR (300 MHz) spectrum of **4** in DMSO-d_6.

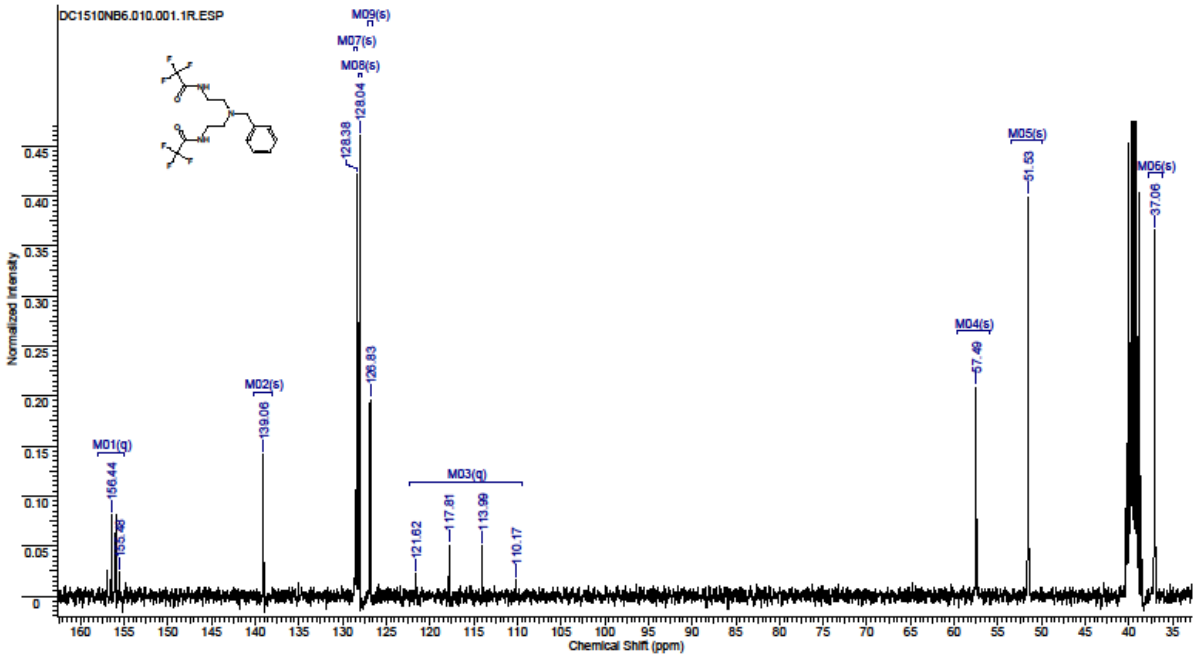

Figure 4-11. ^{13}C NMR (75 MHz) spectrum of **4** in DMSO-d_6.

4.7.2 Titration Experiments and Calculation of Binding Constants

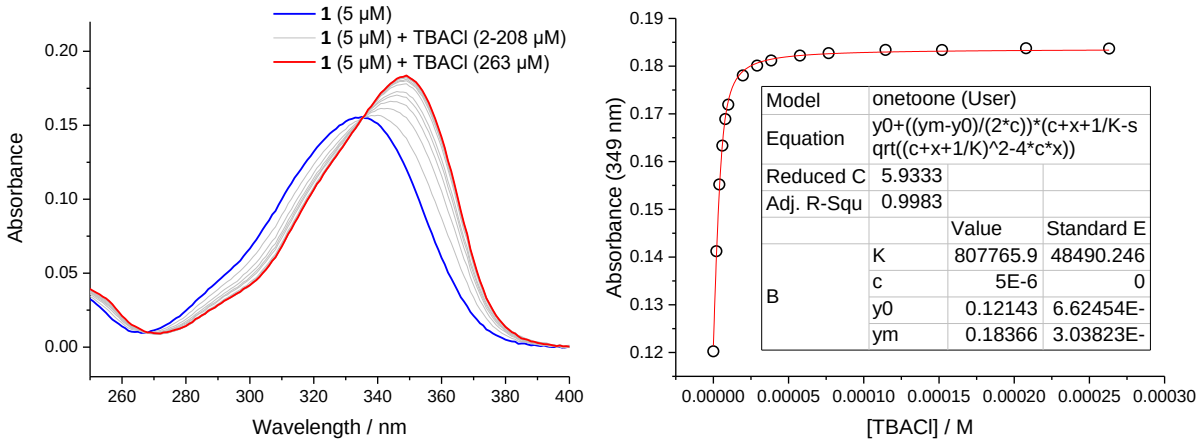

Figure 4-12. UV-vis titration of **1** (5 μM) with TBACl (0–263 μM) in CH_3CN at 298 K.

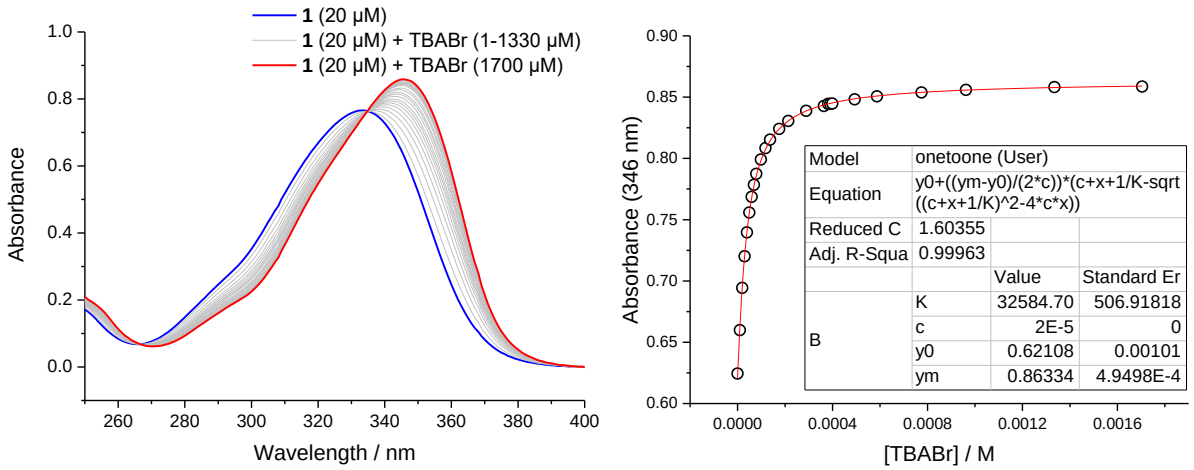

Figure 4-13. UV-vis titration of **1** (20 μM) with TBABr (0–1700 μM) in CH_3CN at 298 K.

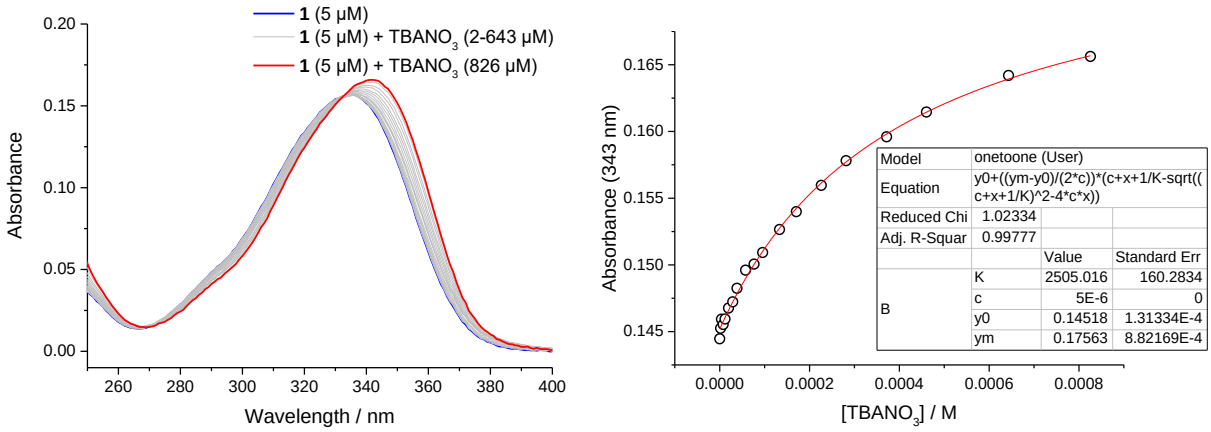

Figure 4-14. UV-vis titration of **1** (5 μM) with $TBANO_3$ (0–826 μM) in CH_3CN at 298 K.

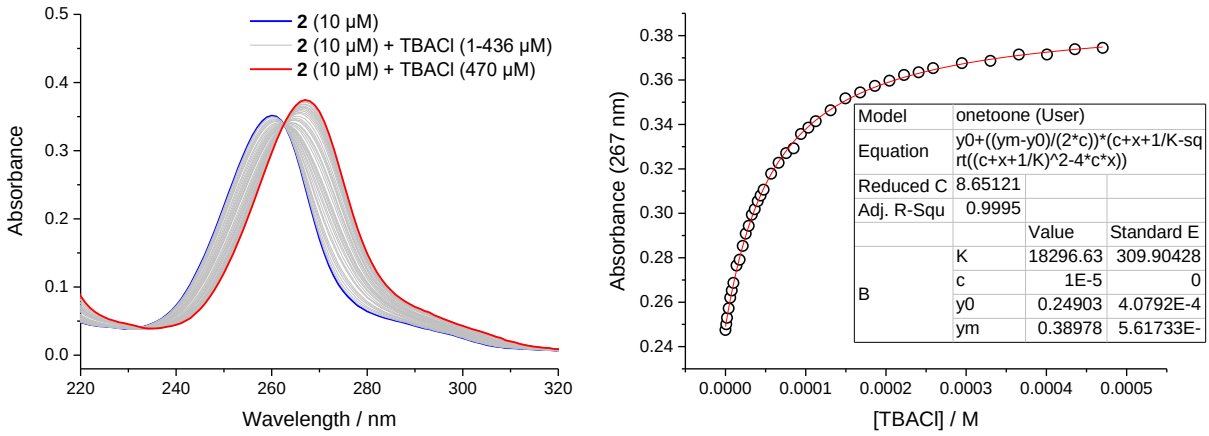

Figure 4-15 UV-vis titration of **2** (10 μM) with TBACl (0–470 μM) in CH_3CN at 298 K.

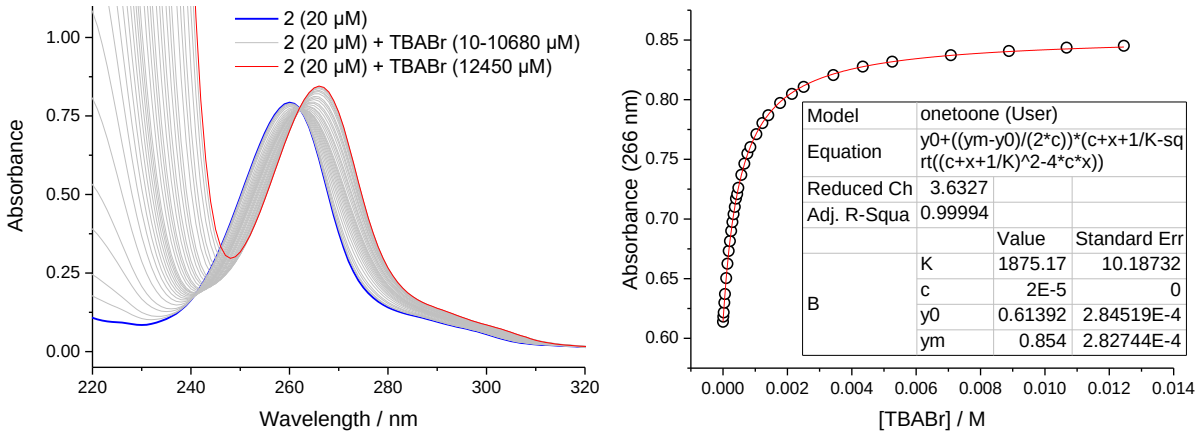

Figure 4-16 UV-vis titration of **2** (20 μM) with TBABr (0–12450 μM) in CH_3CN at 298 K.

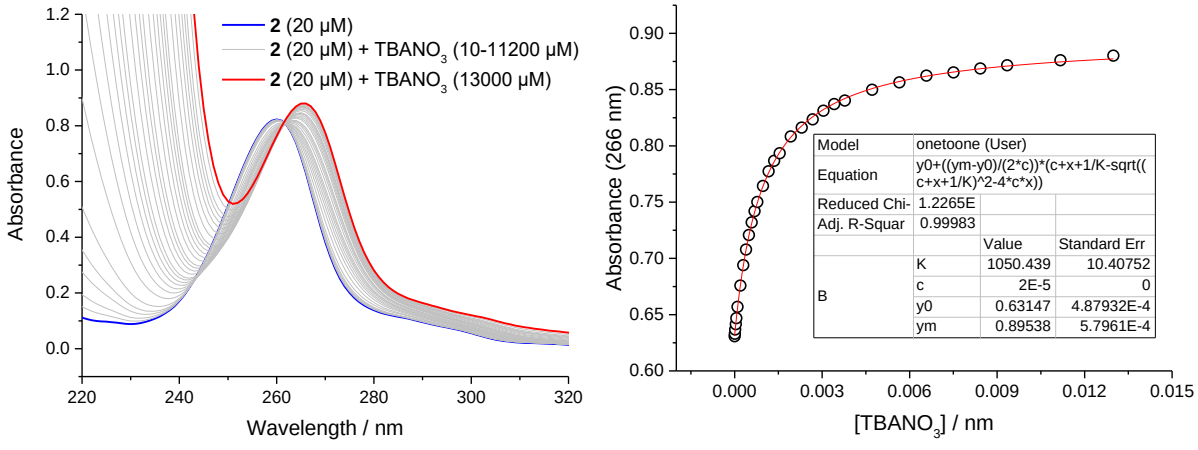

Figure 4-17 UV-vis titration of **2** (20 μM) with $TBANO_3$ (0–13000 μM) in CH_3CN at 298 K.

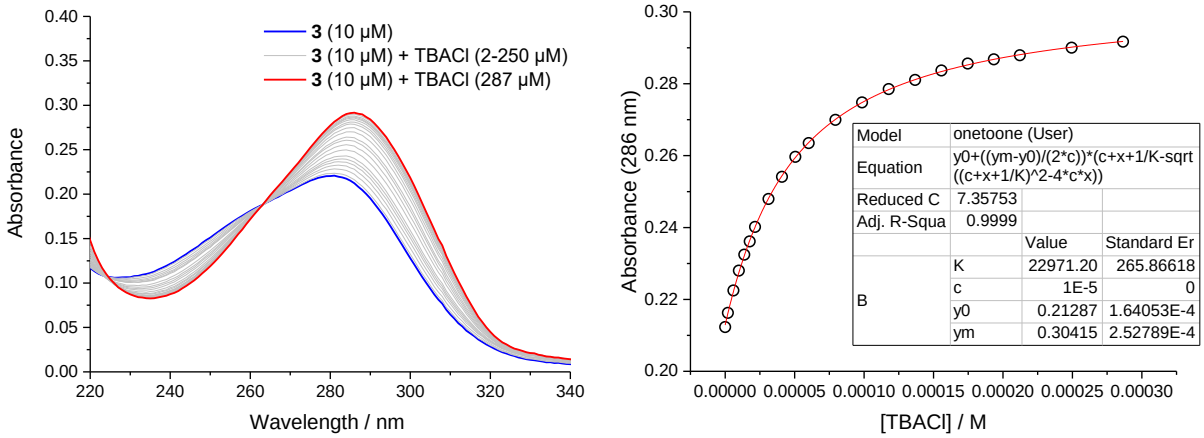

Figure 4-18. UV-vis titration of **3** (10 μM) with TBACl (0–287 μM) in CH_3CN at 298 K.

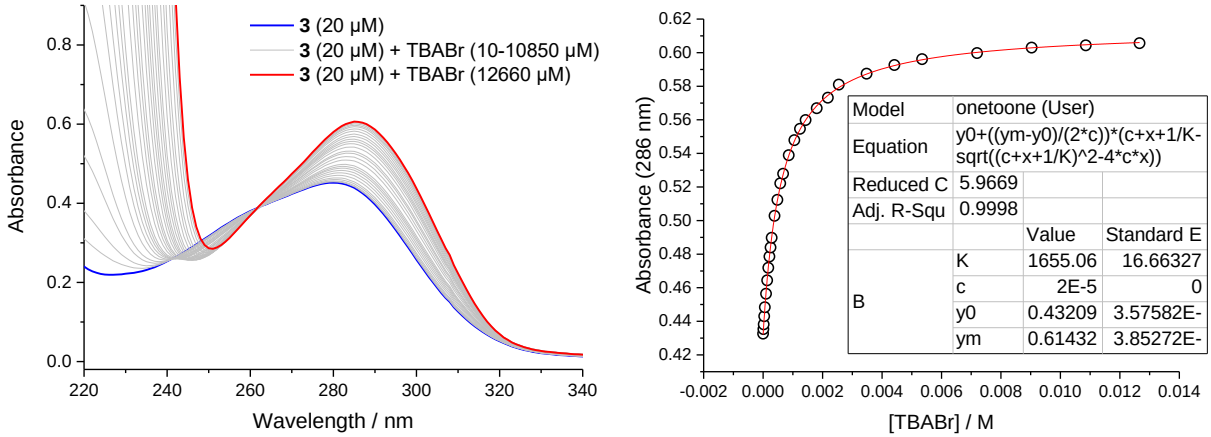

Figure 4-19. UV-vis titration of **3** (20 μM) with TBABr (0–12660 μM) in CH_3CN at 298 K.

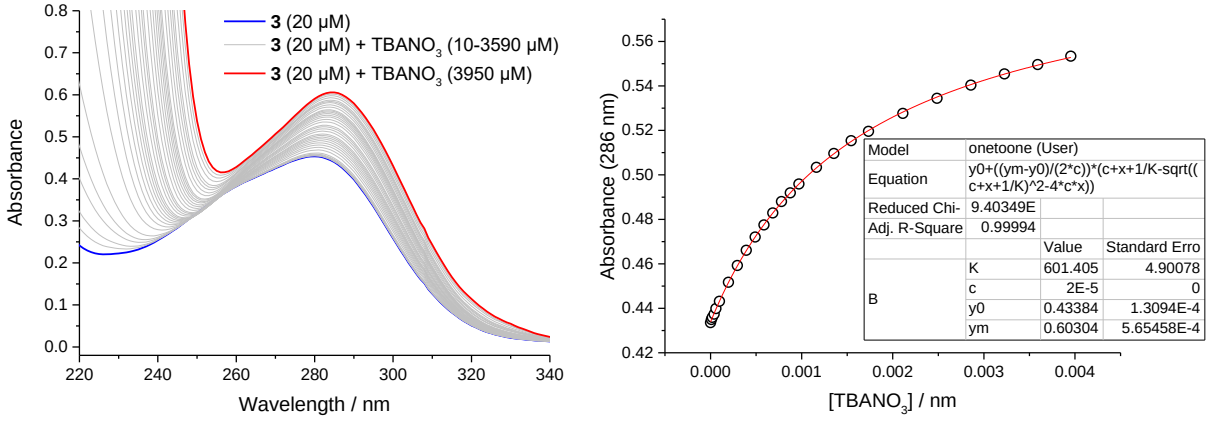

Figure 4-20. UV-vis titration of **3** (20 μM) with $TBANO_3$ (0–3950 μM) in CH_3CN at 298 K.

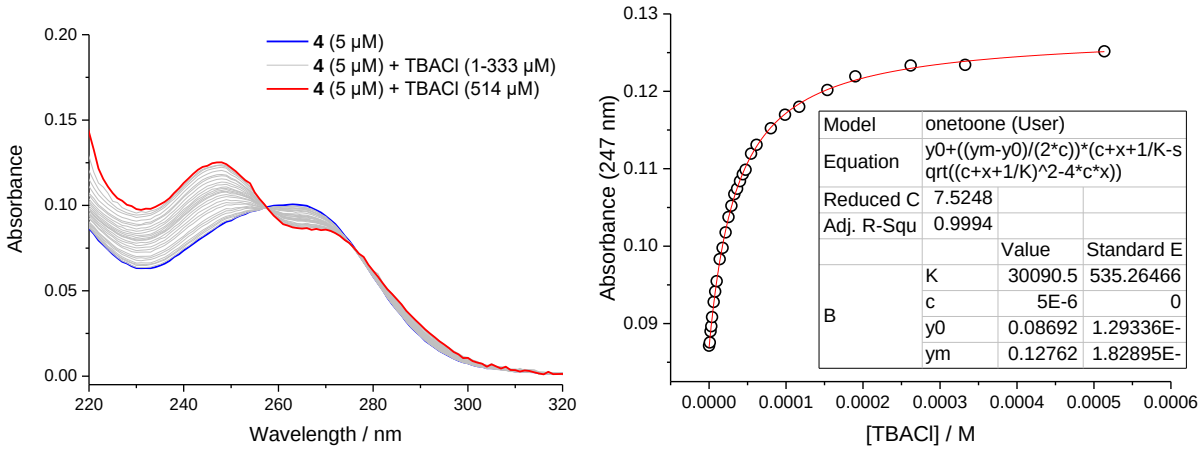

Figure 4-21. UV-vis titration of **4** (5 μM) with TBACl (0–514 μM) in CH_3CN at 298 K.

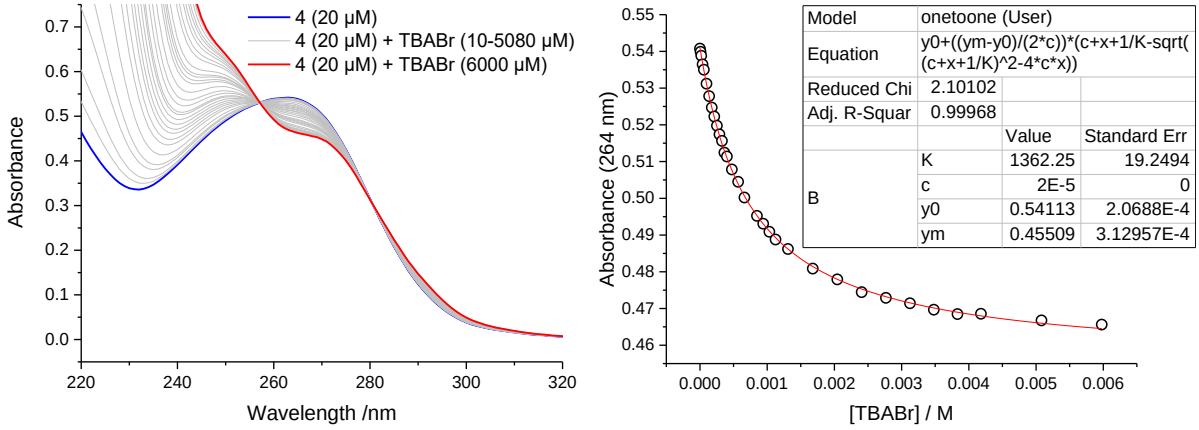

Figure 4-22. UV-vis titration of **4** (20 μM) with TBABr (0–6000 μM) in CH_3CN at 298 K.

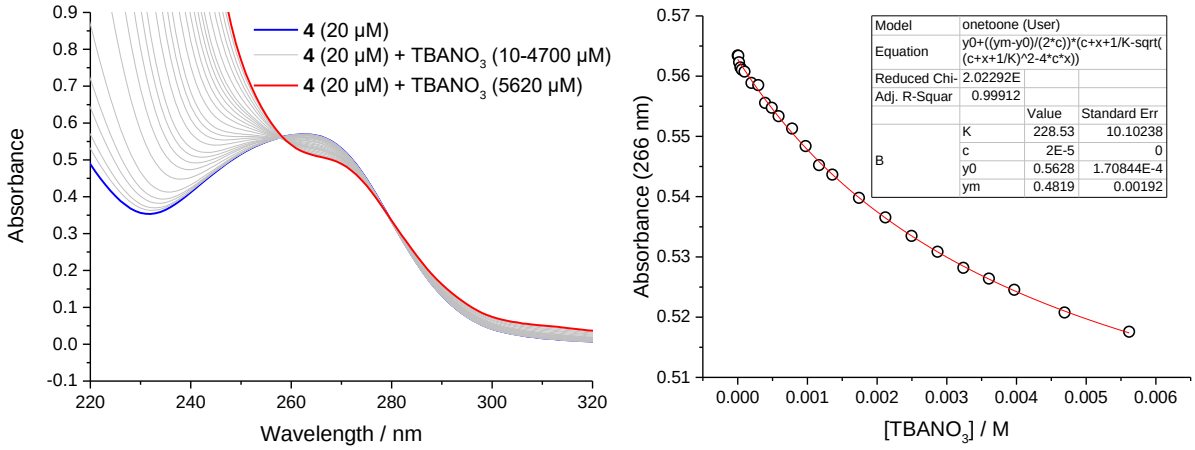

Figure 4-23. UV-vis titration of **4** (20 μM) with $TBANO_3$ (0–5620 μM) in CH_3CN at 298 K.

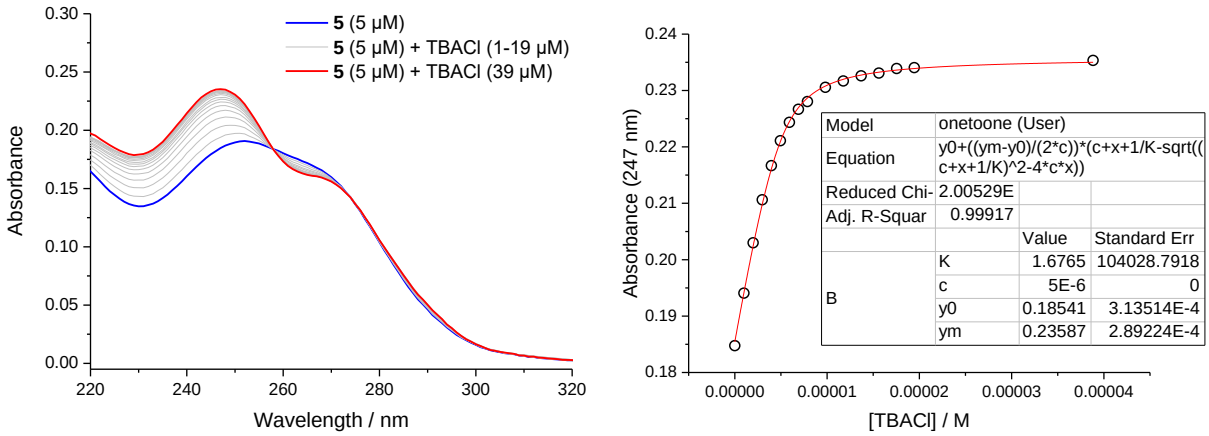

Figure 4-24. UV-vis titration of **5** (5 μM) with TBACl (0–39 μM) in CH_3CN at 298 K.

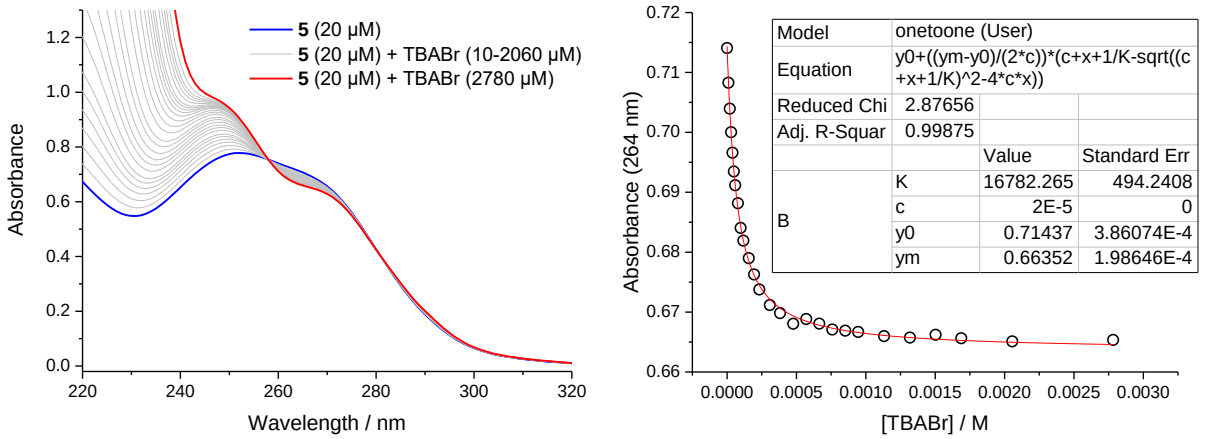

Figure 4-25. UV-vis titration of **5** (20 μM) with TBACl (0–2780 μM) in CH_3CN at 298 K.

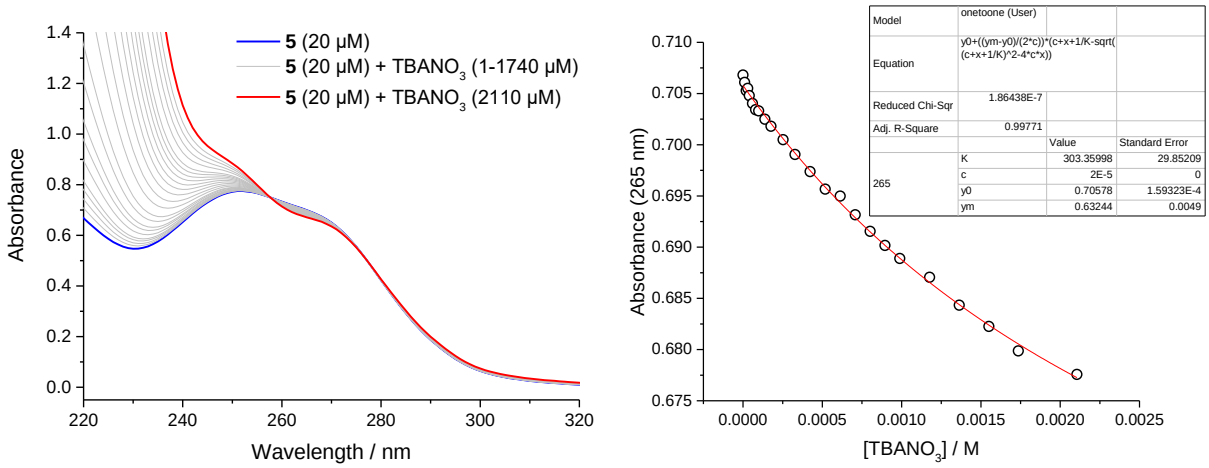

Figure 4-26. UV-vis titration of **5** (20 μM) with $TBANO_3$ (0–2110 μM) in CH_3CN at 298 K.

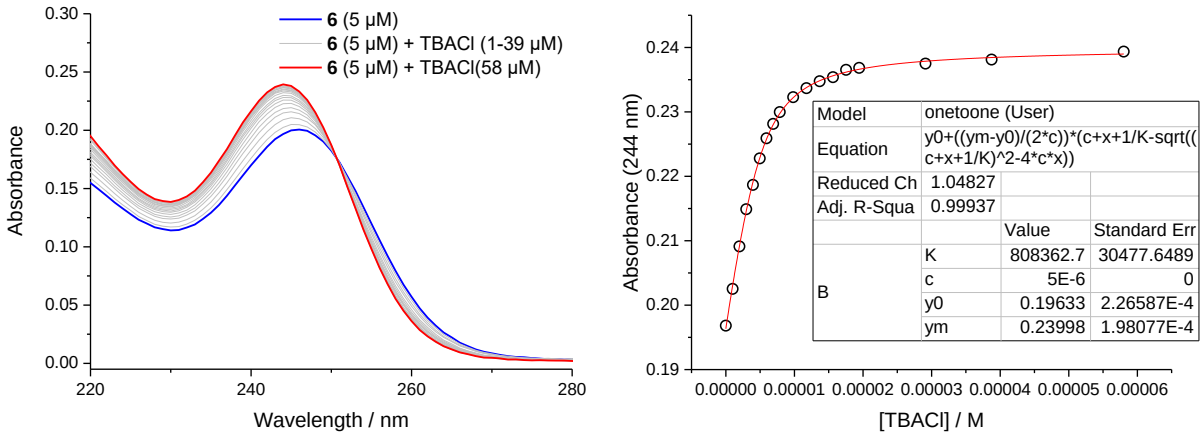

Figure 4-27. UV-vis titration of **6** (5 μM) with TBACl (0–58 μM) in CH_3CN at 298 K.

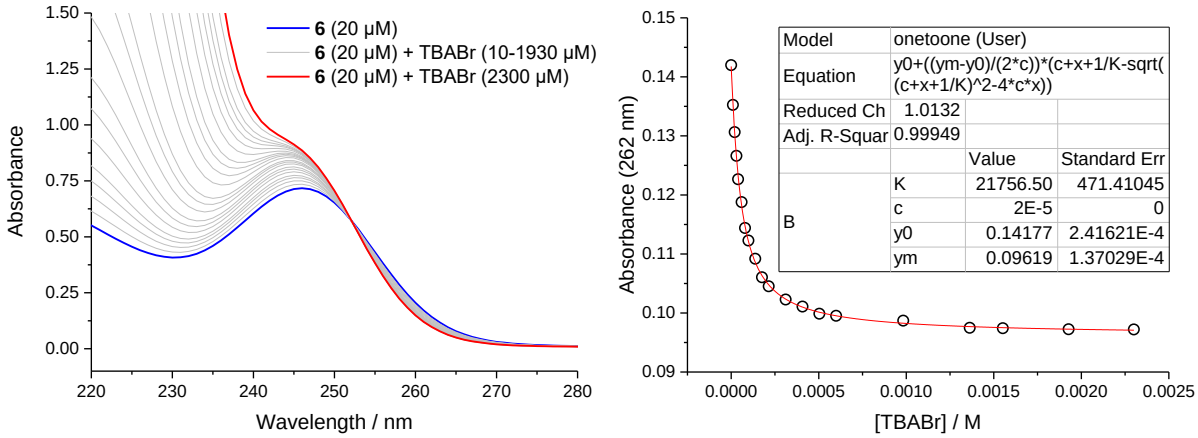

Figure 4-28. UV-vis titration of **6** (20 μM) with TBABr (0–2300 μM) in CH_3CN at 298 K.

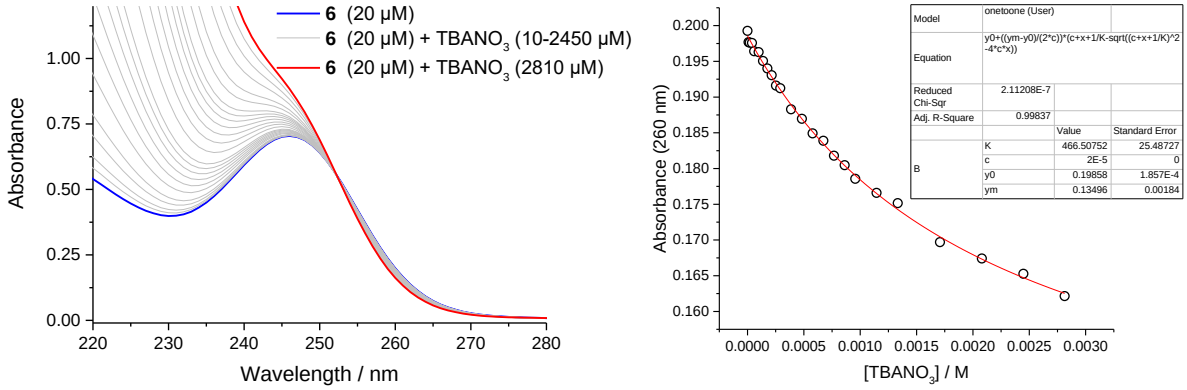

Figure 4-29. UV-vis titration of **6** (20 μM) with $TBANO_3$ (0–2810 μM) in CH_3CN at 298 K.

4.7.3 Transport Kinetic Results

4.7.3.1 ISE Assay

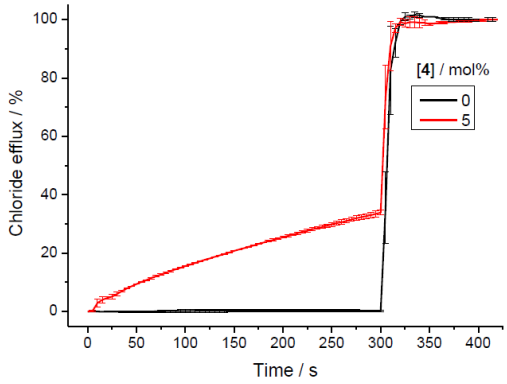

Figure 4-30. Cl^- efflux facilitated by compound **4** measured in the ISE anion exchange assay. The vesicles were loaded with an internal solution of NaCl (490 mM) buffered at pH 7.2 with 5 mM sodium phosphate salts and suspended in an external solution of NaNO3 (490 mM) buffered at pH 7.2 with 5 mM sodium phosphate salts. Compound **4** was added at 0 s, and detergent at 300 s. Compound concentrations are shown as compound-to-lipid molar ratios. Error bars represent standard deviations from at least two repeats.

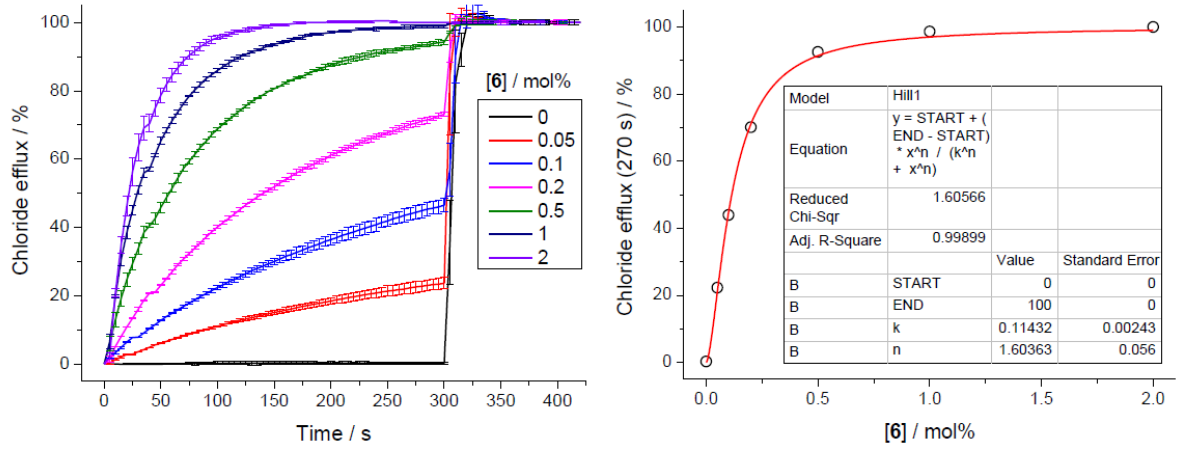

Figure 4-31. Hill plot for Cl^-/NO_3^- exchange facilitated by compound **6** measured in the ISE anion exchange assay. The vesicles were loaded with an internal solution of NaCl (490 mM) buffered at pH 7.2 with 5 mM sodium phosphate salts and suspended in an external solution of $NaNO_3$ (490 mM) buffered at pH 7.2 with 5 mM sodium phosphate salts. Compound **6** was added at 0 s, and detergent at 300 s. Compound concentrations are shown as compound-to-lipid molar ratios. Error bars represent standard deviations from at least two repeats.

4.7.3.2 HPTS Assay

Hill Plots for Cl^- Transport

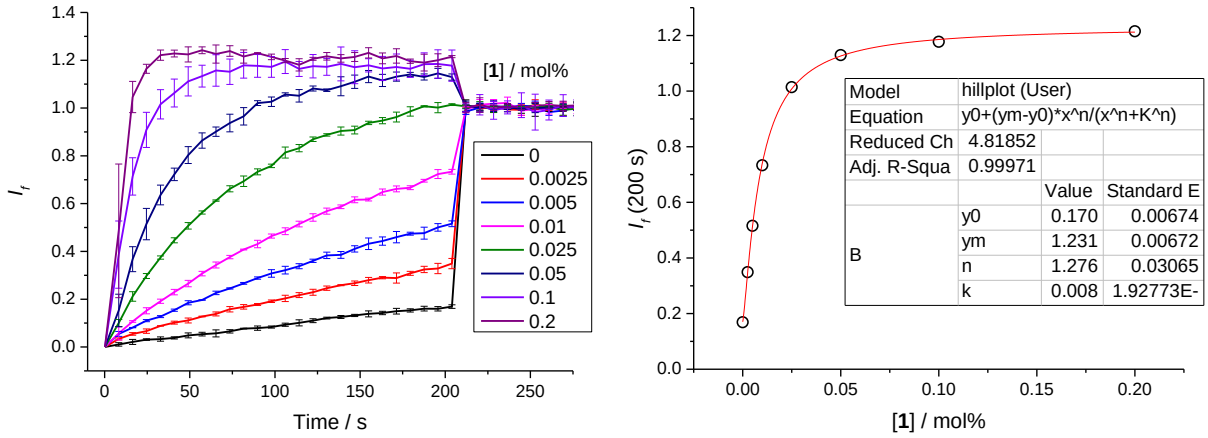

Figure 4-32. Hill plot analysis of H^+/Cl^- symport (or Cl^-/OH^- antiport) facilitated by compound **1** measured in the HPTS assay. NMDG (5 mM) was added before the addition of **1** at 0 s, and detergent was added at 200 s. Compound concentrations are shown as compound-to-lipid molar ratios. Error bars represent standard deviations from at least two repeats.

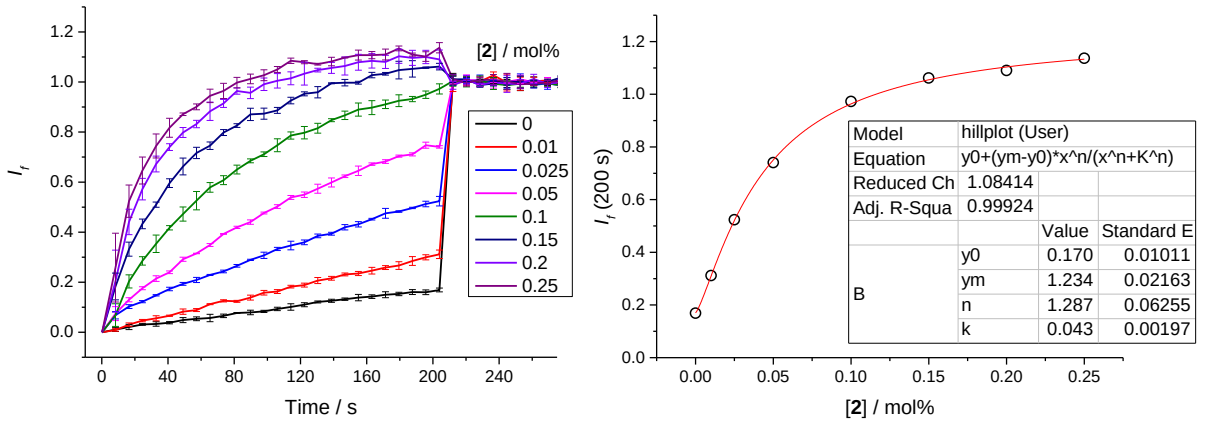

Figure 4-33. Hill plot analysis of H^+/Cl^- symport (or Cl^-/OH^- antiport) facilitated by compound **2** measured in the HPTS assay. NMDG (5 mM) was added before the addition of **2** at 0 s, and detergent was added at 200 s. Compound concentrations are shown as compound-to-lipid molar ratios. Error bars represent standard deviations from at least two repeats.

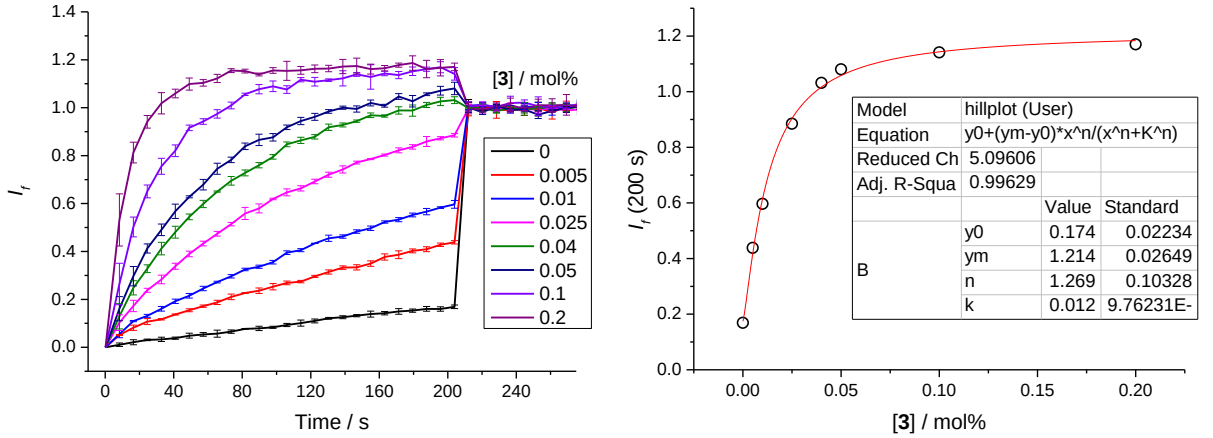

Figure 4-34. Hill plot analysis of H^+/Cl^- symport (or Cl^-/OH^- antiport) facilitated by compound **3** measured in the HPTS assay. NMDG (5 mM) was added before the addition of **3** at 0 s, and detergent was added at 200 s. Compound concentrations are shown as compound-to-lipid molar ratios. Error bars represent standard deviations from at least two repeats.

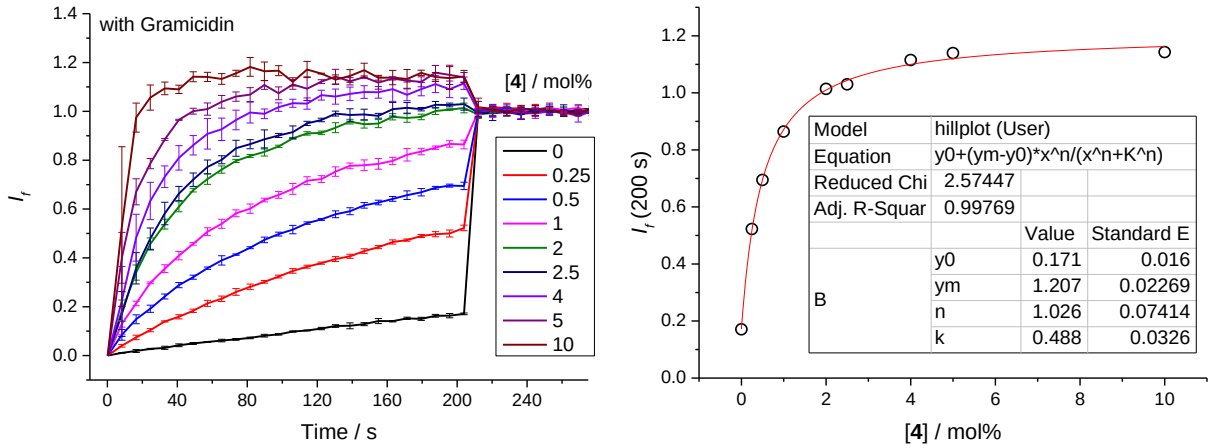

Figure 4-35. Hill plot analysis of H^+/Cl^- symport (or Cl^-/OH^- antiport) facilitated by compound **4** measured in the HPTS assay. NMDG (5 mM) was added before the addition of **4** at 0 s, and detergent was added at 200 s. Compound concentrations are shown as compound-to-lipid molar ratios. Error bars represent standard deviations from at least two repeats.

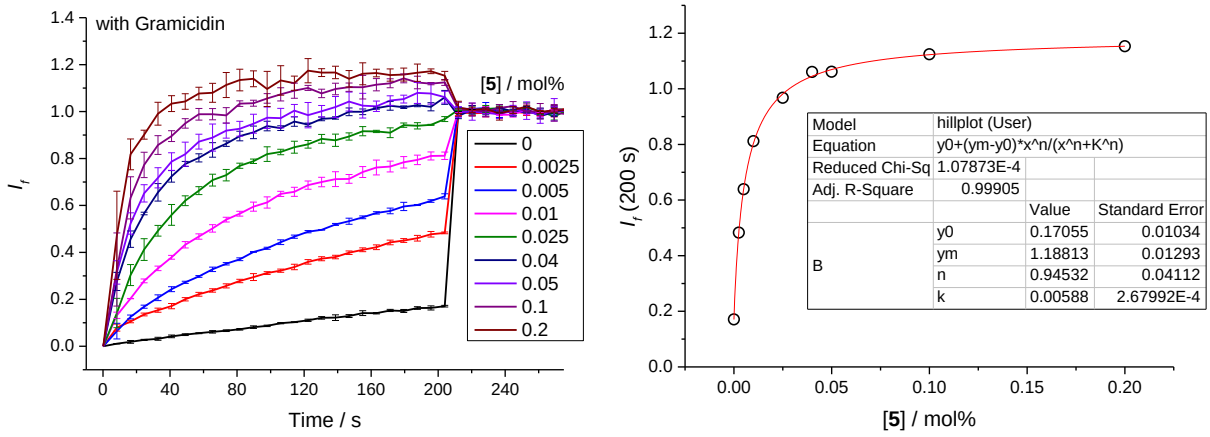

Figure 4-36. Hill plot analysis of H^+/Cl^- symport (or Cl^-/OH^- antiport) facilitated by compound **5** measured in the HPTS assay. NMDG (5 mM) was added before the addition of **5** at 0 s, and detergent was added at 200 s. Compound concentrations are shown as compound-to-lipid molar ratios. Error bars represent standard deviations from at least two repeats.

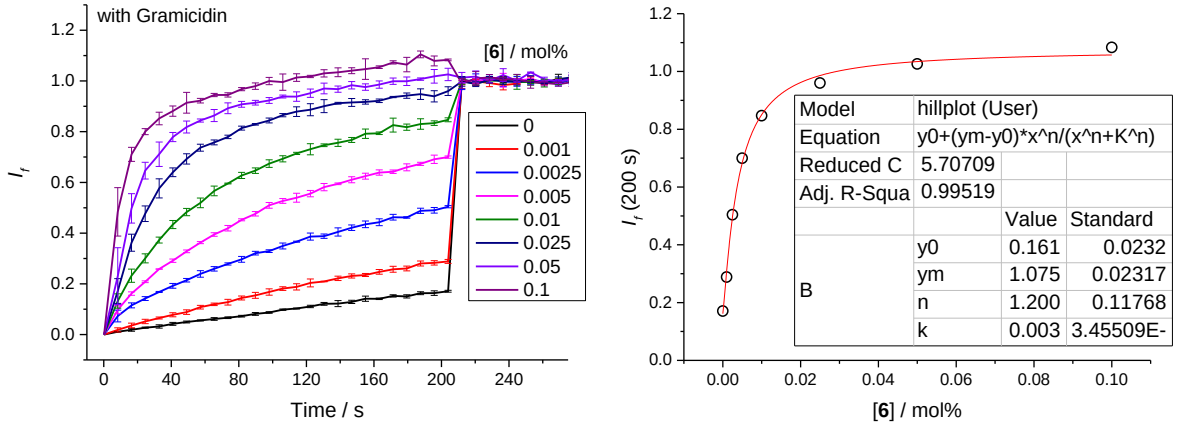

Figure 4-37. Hill plot analysis of H^+/Cl^- symport (or Cl^-/OH^- antiport) facilitated by compound **6** measured in the HPTS assay. NMDG (5 mM) was added before the addition of **6** at 0 s, and detergent was added at 200 s. Compound concentrations are shown as compound-to-lipid molar ratios. Error bars represent standard deviations from at least two repeats.

Hill Plots for NO_3^- Transport

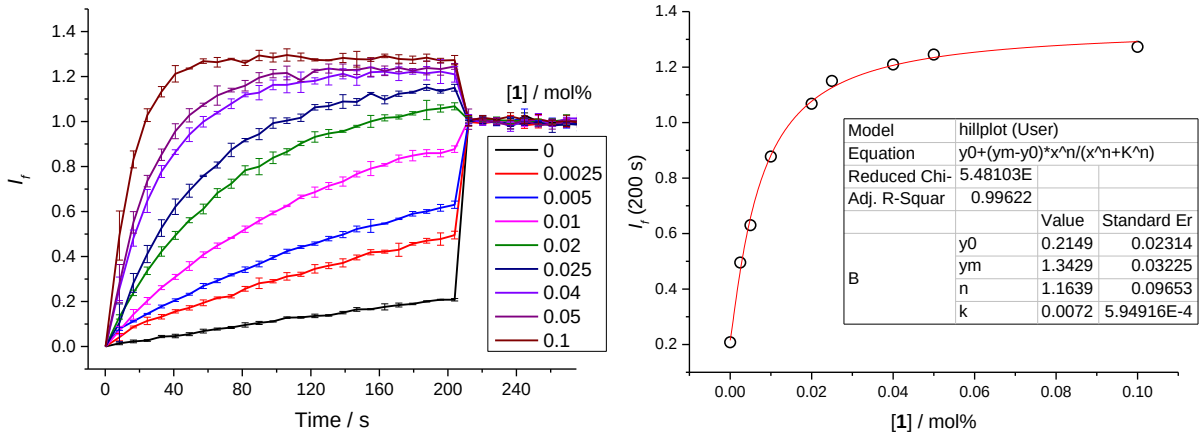

Figure 4-38. Hill plot analysis of H^+/NO_3^- symport (or NO_3^-/OH^- antiport) facilitated by compound **1** measured in the HPTS assay. NMDG (5 mM) was added before the addition of **1** at 0 s, and detergent was added at 200 s. Compound concentrations are shown as compound-to-lipid molar ratios. Error bars represent standard deviations from at least two repeats.

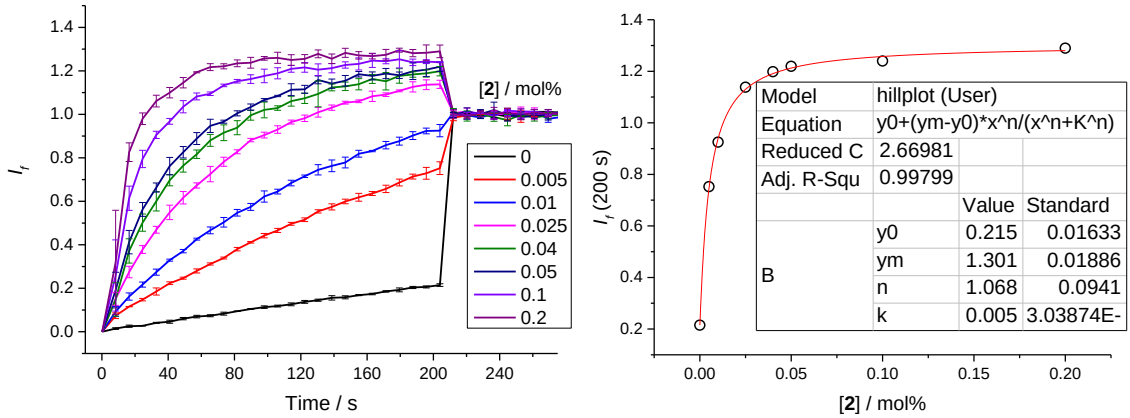

Figure 4-39. Hill plot analysis of H^+/NO_3^- symport (or NO_3^-/OH^- antiport) facilitated by compound **2** measured in the HPTS assay. NMDG (5 mM) was added before the addition of **2** at 0 s, and detergent was added at 200 s. Compound concentrations are shown as compound-to-lipid molar ratios. Error bars represent standard deviations from at least two repeats.

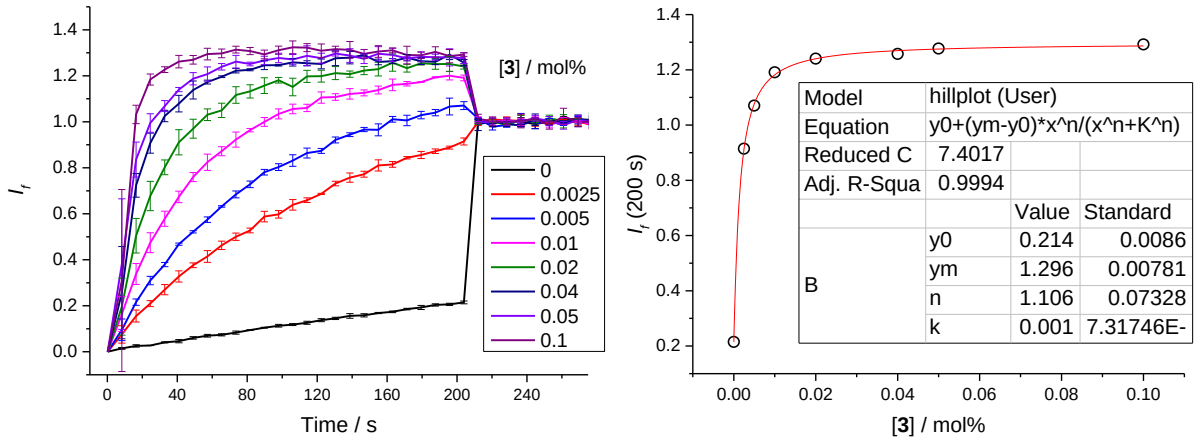

Figure 4-40. Hill plot analysis of H^+/NO_3^- symport (or NO_3^-/OH^- antiport) facilitated by compound **3** measured in the HPTS assay. NMDG (5 mM) was added before the addition of **3** at 0 s, and detergent was added at 200 s. Compound concentrations are shown as compound-to-lipid molar ratios. Error bars represent standard deviations from at least two repeats.

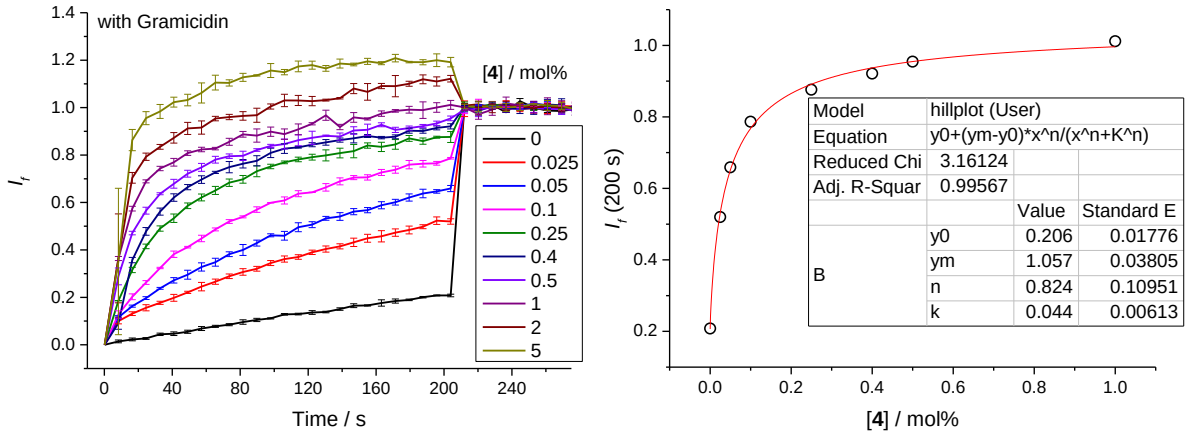

Figure 4-41. Hill plot analysis of H^+/NO_3^- symport (or NO_3^-/OH^- antiport) facilitated by compound **4** measured in the HPTS assay. NMDG (5 mM) was added before the addition of **4** at 0 s, and detergent was added at 200 s. Compound concentrations are shown as compound-to-lipid molar ratios. Error bars represent standard deviations from at least two repeats.

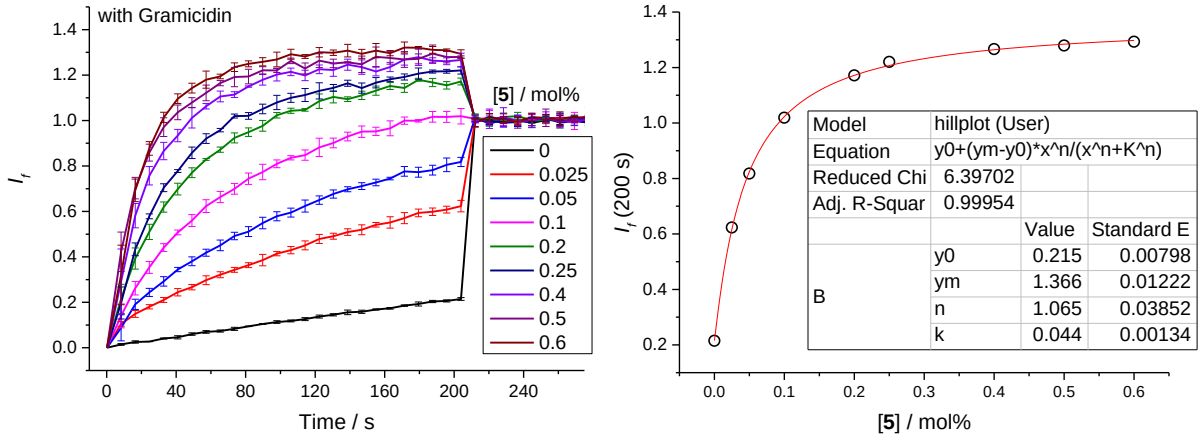

Figure 4-42. Hill plot analysis of H^+/NO_3^- symport (or NO_3^-/OH^- antiport) facilitated by compound **5** measured in the HPTS assay. NMDG (5 mM) was added before the addition of **5** at 0 s, and detergent was added at 200 s. Compound concentrations are shown as compound-to-lipid molar ratios. Error bars represent standard deviations from at least two repeats.

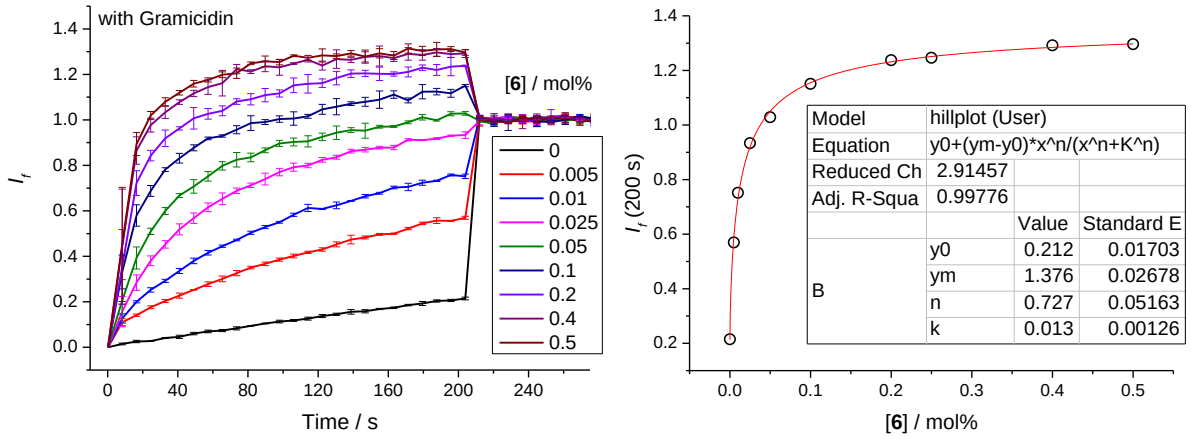

Figure 4-43. Hill plot analysis of H^+/NO_3^- symport (or NO_3^-/OH^- antiport) facilitated by compound **6** measured in the HPTS assay. NMDG (5 mM) was added before the addition of **6** at 0 s, and detergent was added at 200 s. Compound concentrations are shown as compound-to-lipid molar ratios. Error bars represent standard deviations from at least two repeats.

4.7.3.3 Osmotic Assay

Hill Plots for Cl^- Transport

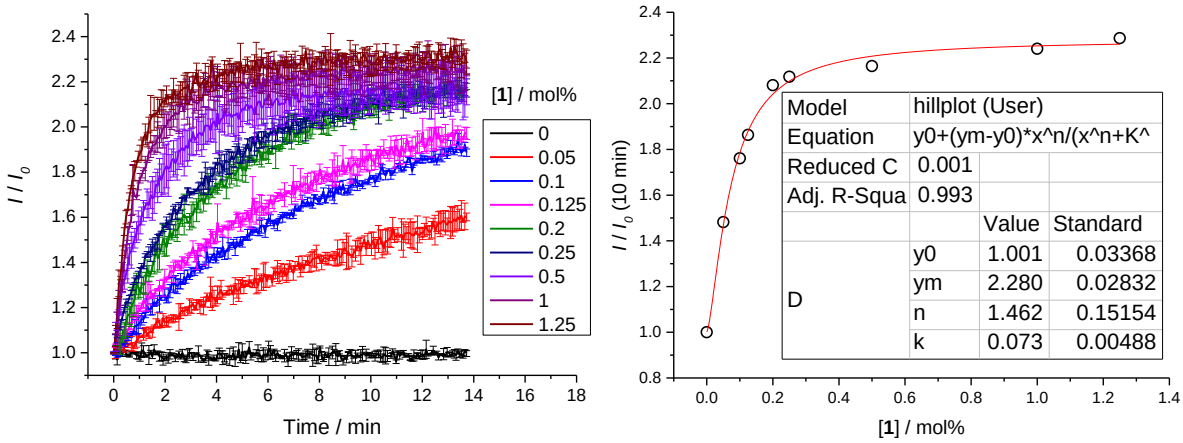

Figure 4-44. Hill plot analysis of Cl^- transport facilitated by compound **1** measured in the Osmotic assay. Vln (0.1 mol%) was added, before the addition of **1** at 0 s. Compound concentrations are shown as compound-to-lipid molar ratios. Error bars represent standard deviations from at least two repeats.

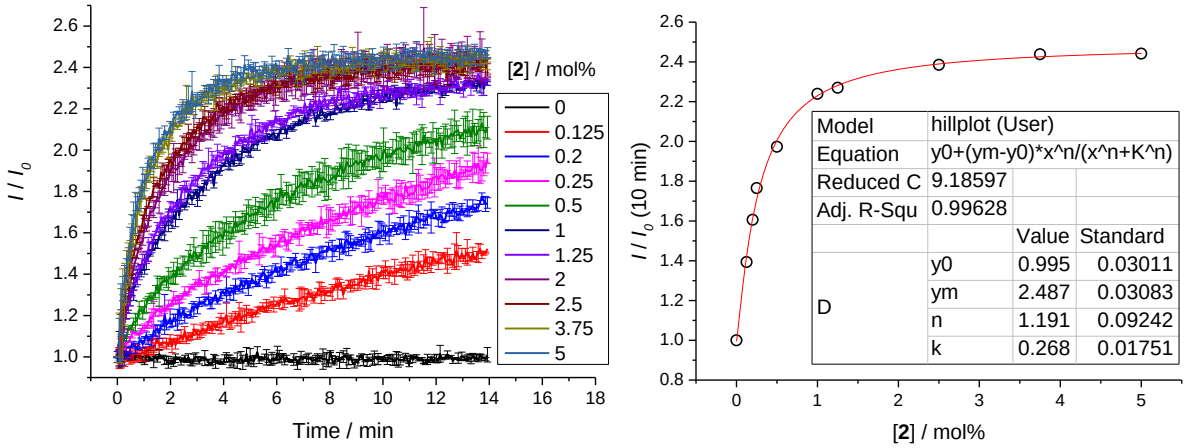

Figure 4-45. Hill plot analysis of Cl^- transport facilitated by compound **2** measured in the Osmotic assay. Vln (0.1 mol%) was added, before the addition of **2** at 0 s. Compound concentrations are shown as compound-to-lipid molar ratios. Error bars represent standard deviations from at least two repeats.

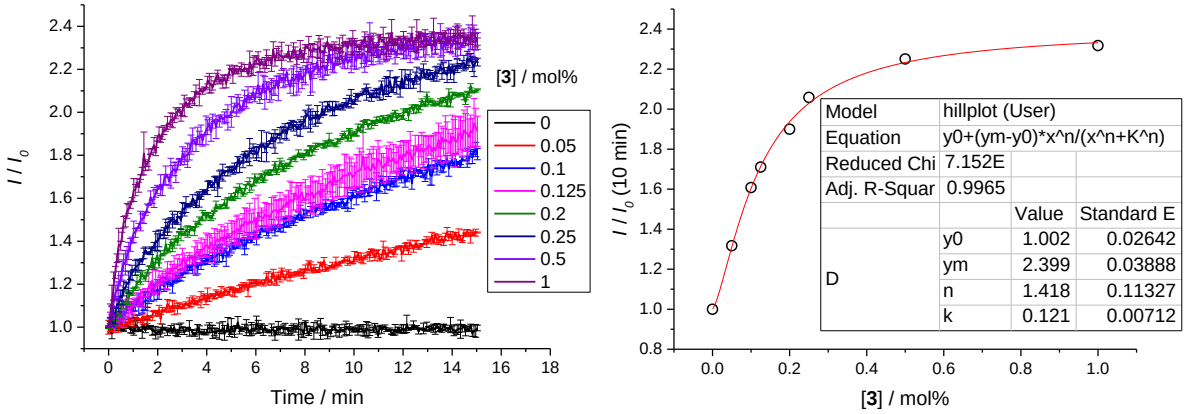

Figure 4-46. Hill plot analysis of Cl^- transport facilitated by compound **3** measured in the Osmotic assay. Vln (0.1 mol%) was added, before the addition of **3** at 0 s. Compound concentrations are shown as compound-to-lipid molar ratios. Error bars represent standard deviations from at least two repeats.

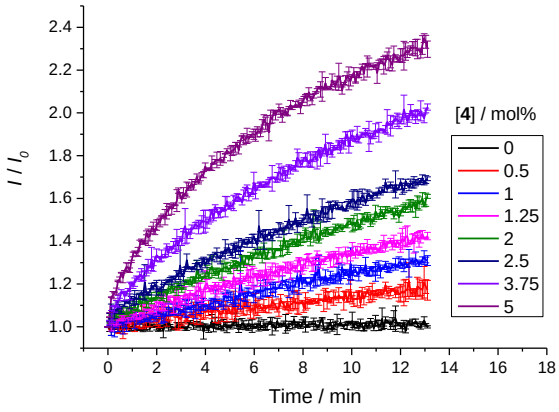

Figure 4-47. Hill plot analysis of Cl^- transport facilitated by compound **4** measured in the Osmotic assay. Vln (0.1 mol%) was added, before the addition of **4** at 0 s. Compound concentrations are shown as compound-to-lipid molar ratios. Error bars represent standard deviations from at least two repeats.

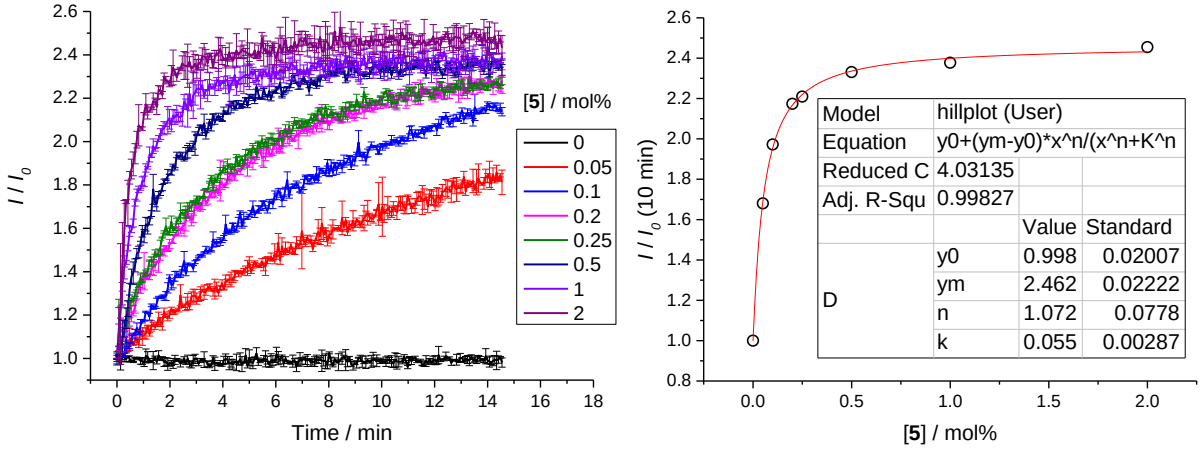

Figure 4-48. Hill plot analysis of Cl^- transport facilitated by compound **5** measured in the Osmotic assay. Vln (0.1 mol%) was added, before the addition of **5** at 0 s. Compound concentrations are shown as compound-

to-lipid molar ratios. Error bars represent standard deviations from at least two repeats.

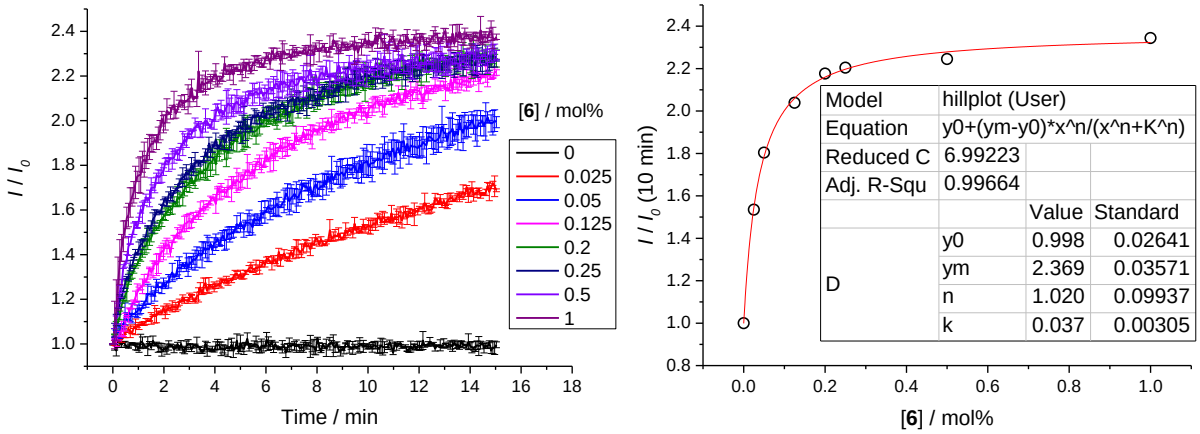

Figure 4-49. Hill plot analysis of Cl^- transport facilitated by compound **6** measured in the Osmotic assay. Vln (0.1 mol%) was added, before the addition of **6** at 0 s. Compound concentrations are shown as compound-to-lipid molar ratios. Error bars represent standard deviations from at least two repeats.

Hill Plots for NO_3^- Transport

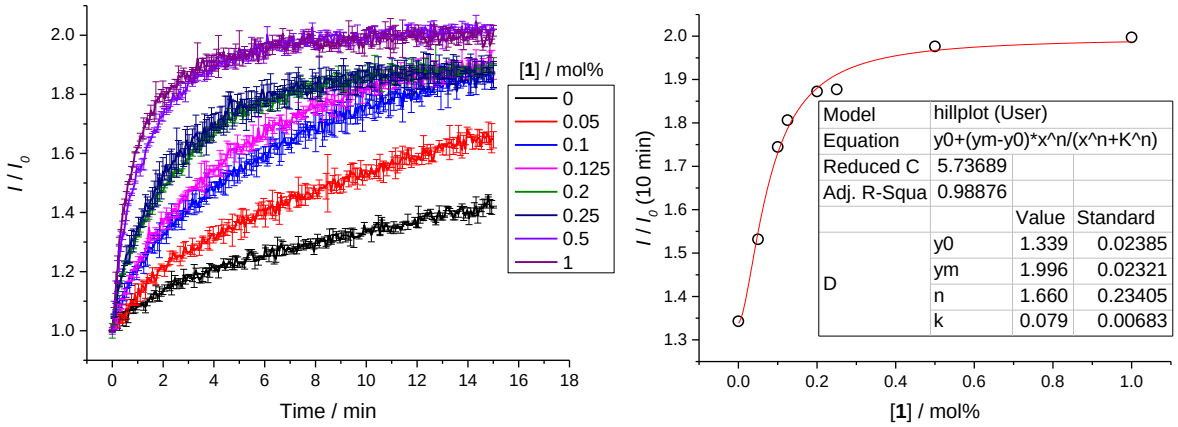

Figure 4-50. Hill plot analysis of NO_3^- transport facilitated by compound **1** measured in the Osmotic assay. Vln (0.1 mol%) was added, before the addition of **1** at 0 s. Compound concentrations are shown as compound-to-lipid molar ratios. Error bars represent standard deviations from at least two repeats.

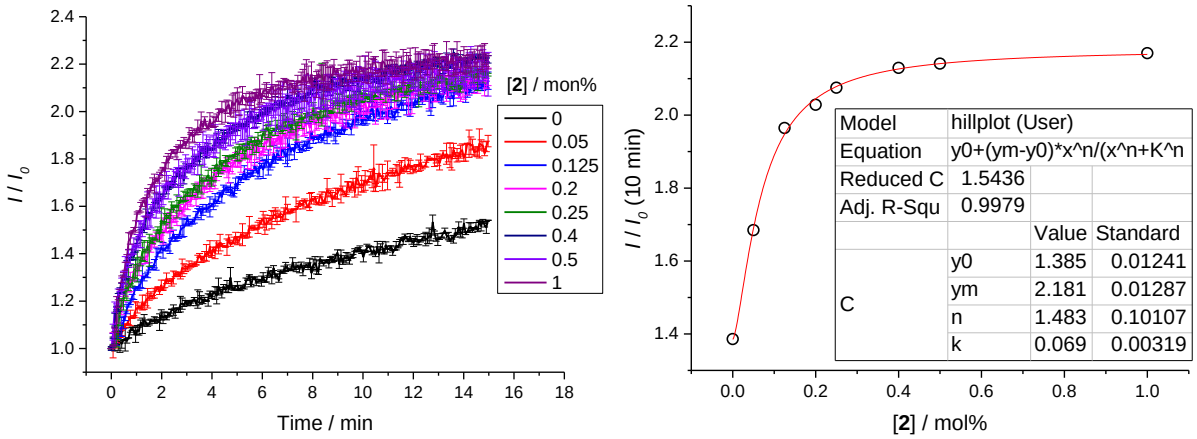

Figure 4-51. Hill plot analysis of NO_3^- transport facilitated by compound **2** measured in the Osmotic assay. Vln (0.1 mol%) was added, before the addition of **2** at 0 s. Compound concentrations are shown as compound-to-lipid molar ratios. Error bars represent standard deviations from at least two repeats.

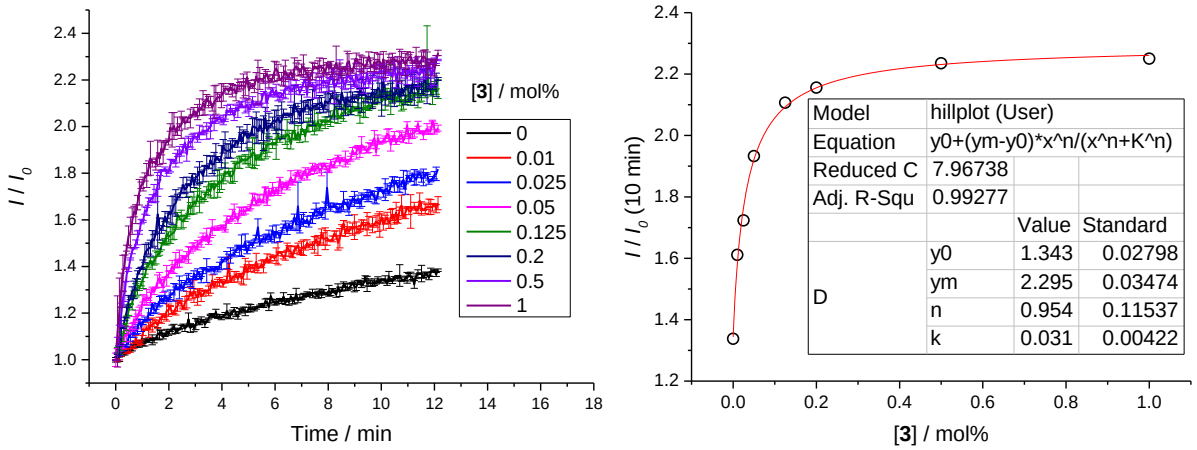

Figure 4-52. Hill plot analysis of NO_3^- transport facilitated by compound **3** measured in the Osmotic assay. Vln (0.1 mol%) was added, before the addition of **3** at 0 s. Compound concentrations are shown as compound-to-lipid molar ratios. Error bars represent standard deviations from at least two repeats.

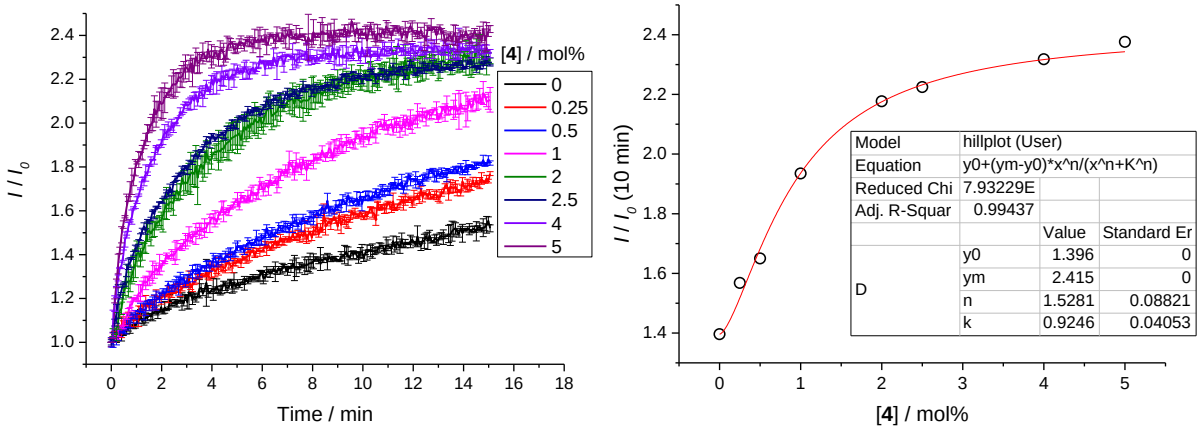

Figure 4-53. Hill plot analysis of NO_3^- transport facilitated by compound **4** measured in the Osmotic assay.

Vln (0.1 mol%) was added, before the addition of **4** at 0 s. Compound concentrations are shown as compound-to-lipid molar ratios. Error bars represent standard deviations from at least two repeats.

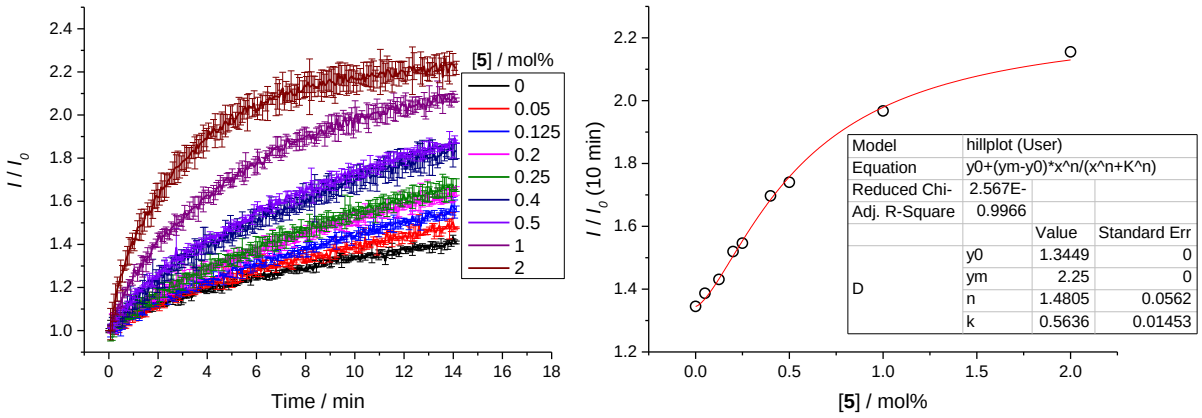

Figure 4-54. Hill plot analysis of NO_3^- transport facilitated by compound **5** measured in the Osmotic assay. Vln (0.1 mol%) was added, before the addition of **5** at 0 s. Compound concentrations are shown as compound-to-lipid molar ratios. Error bars represent standard deviations from at least two repeats.

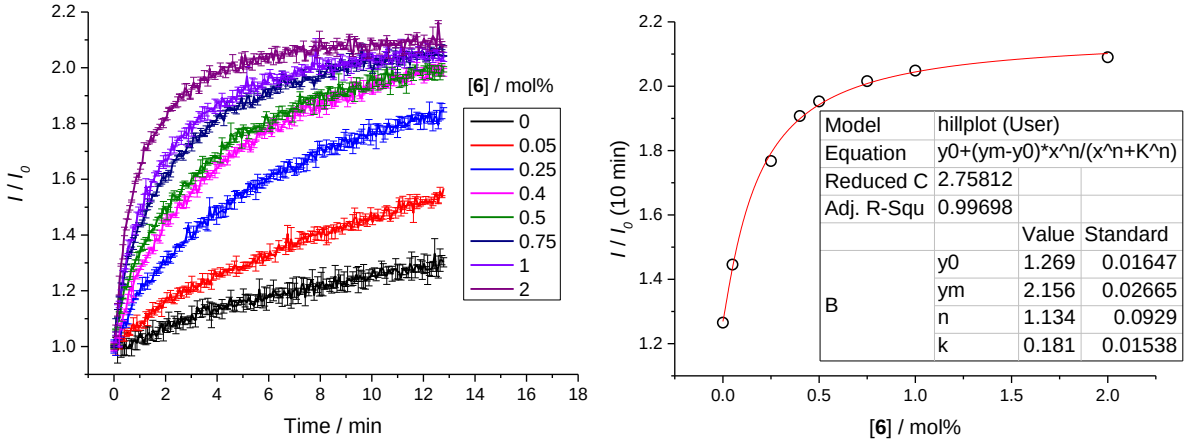

Figure 4-55. Hill plot analysis of NO_3^- transport facilitated by compound **6** measured in the Osmotic assay. Vln (0.1 mol%) was added, before the addition of **6** at 0 s. Compound concentrations are shown as compound-to-lipid molar ratios. Error bars represent standard deviations from at least two repeats.

4.7.3.4 Br^- Transport

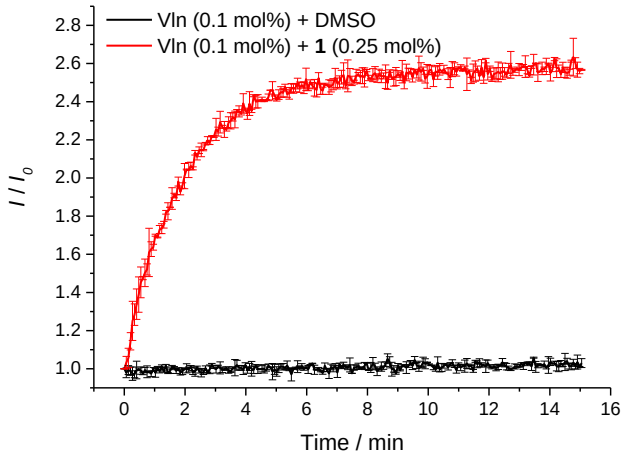

Figure 4-56. KBr efflux facilitated by a combination of Vln and compound **1**. Vln (0.1 mol%) was added, before the addition of **1** at 0 s. Compound concentrations are shown as compound-to-lipid molar ratios. Error bars represent standard deviations from at least two repeats.

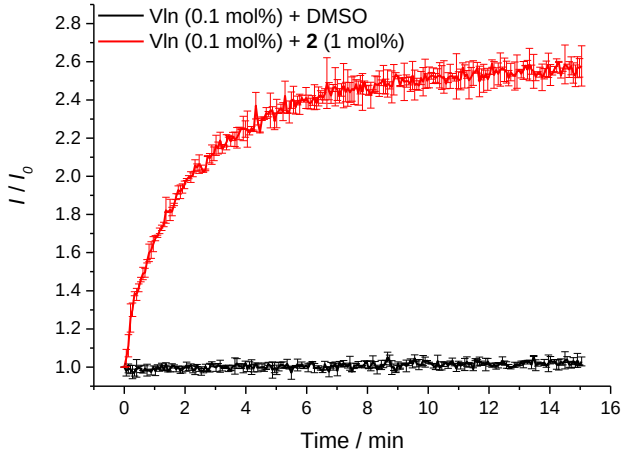

Figure 4-57. KBr efflux facilitated by a combination of Vln and compound **2**. Vln (0.1 mol%) was added, before the addition of **2** at 0 s. Compound concentrations are shown as compound-to-lipid molar ratios. Error bars represent standard deviations from at least two repeats.

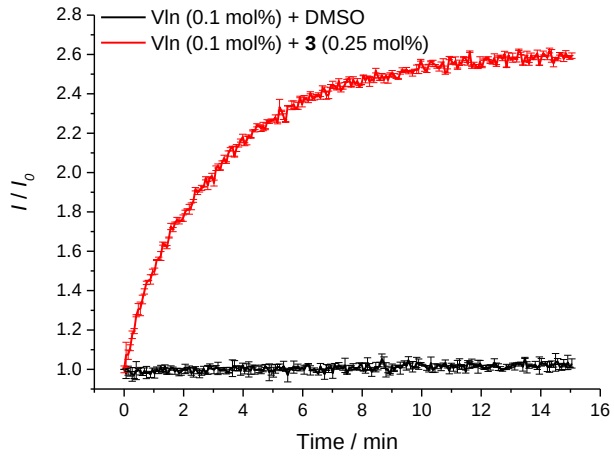

Figure 4-58. KBr efflux facilitated by a combination of Vln and compound **3**. Vln (0.1 mol%) was added, before the addition of **3** at 0 s. Compound concentrations are shown as compound-to-lipid molar ratios. Error bars represent standard deviations from at least two repeats.

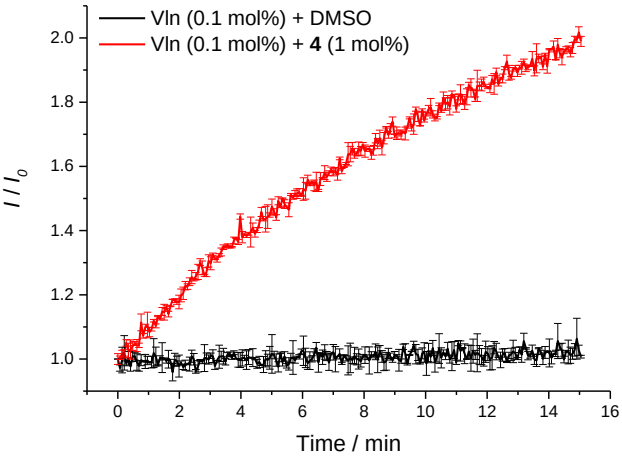

Figure 4-59. KBr efflux facilitated by a combination of Vln and compound **4**. Vln (0.1 mol%) was added, before the addition of **4** at 0 s. Compound concentrations are shown as compound-to-lipid molar ratios. Error bars represent standard deviations from at least two repeats.

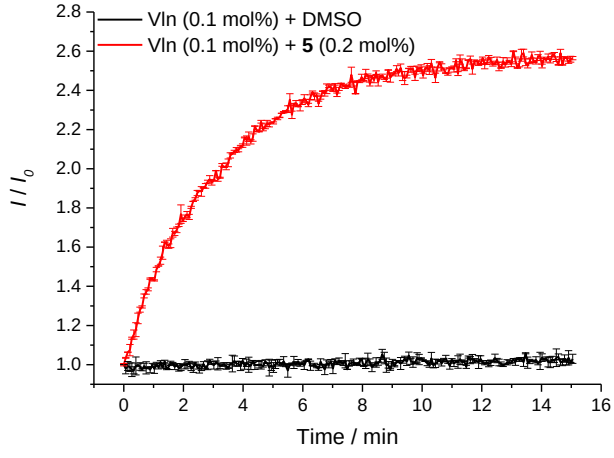

Figure 4-60. KBr efflux facilitated by a combination of Vln and compound **5**. Vln (0.1 mol%) was added, before the addition of **5** at 0 s. Compound concentrations are shown as compound-to-lipid molar ratios. Error bars represent standard deviations from at least two repeats.

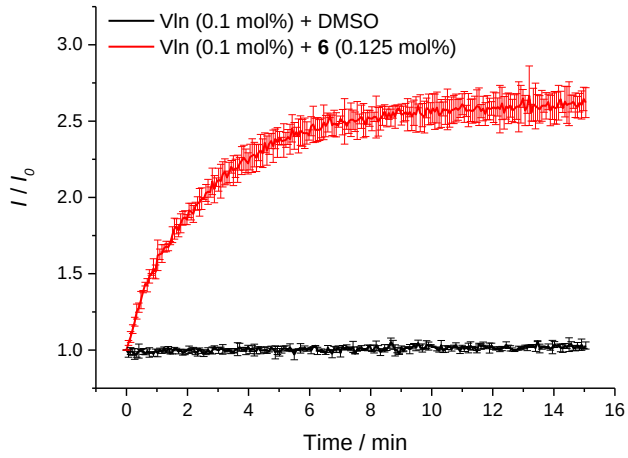

Figure 4-61. KBr efflux facilitated by a combination of Vln and compound **6**. Vln (0.1 mol%) was added, before the addition of **6** at 0 s. Compound concentrations are shown as compound-to-lipid molar ratios. Error bars represent standard deviations from at least two repeats.

References

1. Gale, P. A.; Howe, E. N. W.; Wu, X. *Chem*., **2016**, *1*, 351–422.
2. (a) Gale, P. A.; Davis, J. T.; Quesada, R. *Chem. Soc. Rev*., **2017**, *46*, 2497–2519; (b) Benz, S.; Macchione, M.; Verolet, Q.; Mareda, J.; Sakai, N.; Matile, S. *J. Am. Chem. Soc*., **2016**, *138*, 9093–9096; (c) Vargas Jentzsch, A.; Hennig, A.; Mareda, J.; Matile, S. *Acc. Chem. Res*., **2013**, *46*, 2791–2800; (d) Davis, J. T.; Okunola, O.; Quesada, R. *Chem. Soc. Rev*., **2010**, *39*, 3843–3862.
3. Li, H.; Valkenier, H.; Judd, L. W.; Brotherhood, P. R.; Hussain, S.; Cooper, J. A.; Jurcˇek, O.; Sparkes, H. A.; Sheppard, D. N.; Davis, A. P. *Nat. Chem*., **2016**, *8*, 24–32.
4. (a) Busschaert, N.; Park, S.-H.; Baek, K.-H.; Choi, Y. P.; Park, J.; Howe, E. N. W.; Hiscock, J. R.; Karagiannidis, L. E.; Marques, I.; Fe´lix, V.; Namkung, W.; Sessler, J. L.; Gale, P. A.; Shin, I. *Nat. Chem*., **2017**, *9*, 667–675; (b) Rodilla, A. M.; Korrodi-Grego´rio, L.; Hernando, E.; Manuel-Manresa, P.; Quesada, R.; Pe´rez-Toma´s, R.; Soto-Cerrato, V. *Biochem. Pharmacol*., **2017**, *126*, 23–33; (c) Soto-Cerrato, V.; Manuel-Manresa, P.; Hernando, E.; Calabuig-Farin˜as, S.; Martı´nez-Romero, A.; Ferna´ndez-Duen˜as, V.; Sahlholm, K.; Kno¨pfel, T.; Garcı´a-Valverde, M.; Rodilla, A. M.; Jantus-Lewintre, E.; Farra`s, R.; Ciruela, F.; Pe´rez-Toma´s, R.; Quesada, R. *J. Am. Chem. Soc*., **2015**, *137*, 15892–15898; (d) Ko, S.-K.; Kim, S. K.; Share, A.; Lynch, V. M.; Park, J.; Namkung, W.; Van Rossom, W.; Busschaert, N.; Gale, P. A.; Sessler, J. L.; Shin, I. *Nat. Chem.*, **2014**, *6*, 885–892.
5. Zhang, Y.; Cremer, P. S., *Curr. Opin. Chem. Biol.* **2006,** *10* (6), 658-663.

6. (a) Ishii, F.; Takamura, A.; Ishigami, Y., *Langmuir* **1995,** *11* (2), 483-486; (b) Miyamoto, V. K.; Stoeckenius, W., *J. Membr. Biol.* **1971,** *4* (1), 252-269; (c) Szoka, F.; Papahadjopoulos, D., *Proc. Natl. Acad. Sci. U. S. A.*, **1978,** *75* (9), 4194-4198, (d) Kammari, R.; Das, N. G.; Das, S. K., Elsevier: 2017; pp 105-144.
7. Oesch, U.; Ammann, D.; Simon, W., *Clin. Chem.* **1986,** *32* (8), 1448-1459.
8. (a) Olivari, M.; Montis, R.; Berry, S. N.; Karagiannidis, L. E.; Coles, S. J.; Horton, P. N.; Mapp, L. K.; Gale, P. A.; Caltagirone, C. *Dalton Trans.*, **2016**, *45*, 11892–11897; (b) Lang, C. Zhang, X.; Luo, Q.; Dong, Z.; Xu, J.; Liu, J. *Eur. J. Org. Chem*., **2015**, 6458–6465; (c) Choi, Y. R.; Kim, G. C.; Jeon, H.-G.; Park, J.; Namkung, W.; Jeong, K.-S. *Chem. Commun*., **2014**, *50*, 15305–15308; (d) McNally, B. A.; Koulov, A. V.; Smith, B. D.; Joos, J.-B.; Davis, A. P. *Chem. Commun*., **2005**, 1087–1089.
9. Valkenier, H.; Davis, A. P. *Acc. Chem. Res*., **2013**, *46*, 2898–2909.
10. (a) McNally, B. A.; Koulov, A. V.; Lambert, T. N.; Smith, B. D.; Joos, J.-B.; Sisson, A. L.; Clare, J. P.; Sgarlata, V.; Judd, L.W.; Magro, G.; Davis, A. P. *Chem. – Eur. J*., **2008**, *14*, 9599–9606; (b) Nishizawa, S.; Bu¨hlmann, P.; Iwao, M.; Umezawa, Y. *Tetrahedron Lett*., **1995**, *36*, 6483–6486.
11. (a) Busschaert, N.; Bradberry, S. J.; Wenzel, M.; Haynes, C. J. E.; Hiscock, J. R.; Kirby, I. L.; Karagiannidis, L. E.; Moore, S. J.; Wells, N. J.; Herniman, J.; Langley, G. J.; Horton, P. N.; Light, M. E.; Marques, I.; Costa, P. J.; Felix, V.; Frey, J. G.; Gale, P. A. *Chem. Sci*., **2013**, *4*, 3036–3045; (b) Berezin, S. K.; Davis, J. T. *J. Am. Chem. Soc*., **2009**, *131*, 2458–2459.
12. Busschaert, N.; Kirby, I. L.; Young, S.; Coles, S. J.; Horton, P. N.; Light, M. E.; Gale, P. A. *Angew. Chem., Int. Ed.*, **2012**, *51*, 4426–4430.
13. (a) Wu, X.; and Gale, P. A. *J. Am. Chem. Soc*., **2016**, *138*, 16508–16514; (b) Wu, X.; Judd, L.W.; Howe, E. N. W.; Withecombe, A.M.; Soto-Cerrato, V.; Li, H.; Busschaert, N.; Valkenier, H.; Pe´rez-Toma´s, R.; Sheppard, D. N.; Jiang, Y.-B.; Davis, A. P.; Gale, P. A. *Chem*, **2016**, *1*, 127–146.
14. (a) Busschaert, N.; Wenzel, M.; Light, M. E.; Iglesias-Herna´ndez, P.; Pe´rez-Toma´s, R.; Gale, P. A. *J. Am. Chem. Soc*., **2011**, *133*, 14136–14148; (b) Marques, I.; Colaco, A. R.; Costa, P. J.; Busschaert, N.; Gale, P. A.; Felix, V. *Soft Matter*, **2014**, *10*, 3608–3621.
15. Fasting, C.; Schalley, C. A.; Weber, M.; Seitz, O.; Hecht, S.; Koksch, B.; Dernedde, J.; Graf, C.; Knapp, E.-W.; Haag, R. *Angew. Chem., Int. Ed*., **2012**, *51*, 10472–10498.
16. Judd, L. W.; Davis, A. P. *Chem. Commun*., **2010**, *46*, 2227–2229.
17. N.B. there are transporters that are incapable of (or have a poor activity in) mediating anion uniport. Examples include prodigiosin and an analogue of **5** with cyano substituents. In those cases, the HPTS assay showed no gramicidin-induced enhancement of transport rate and the valinomycin-coupled assay showed little or no activity.
18. Stockbridge, R. B.; Lim, H.-H.; Otten, R.; Williams, C.; Shane, T.; Weinberg, Z.; Miller, C. *Proc. Natl. Acad. Sci. U. S. A*., **2012**, *109*, 15289–15294.

19. La¨uger, P. *Science*, **1972**, 178, 24–30.
20. The difference in EC_{50} between the two assays is mainly due to the fact that the HPTS assay measures a much smaller flux of X^- (5 mM) compared with the osmotic assay (300 mM) and also in part due to the different vesicle sizes. As a result, the transport process in the HPTS assay completes more quickly than in the osmotic assay. For a discussion of transport rate dependence on vesicle size, see Valkenier, H.; Mora, N. L.; Kros, A.; Davis, A. P.; *Angew. Chem., Int. Ed*., **2015**, *54*, 2137–2141.
21. Busschaert, N.; Gale, P. A.; Haynes, C. J. E.; Light, M. E.; Moore, S. J.; Tong, C. C.; Davis, J. T.; Harrell, W. A., Jr. *Chem. Commun.* **2010**, *46*, 6252-6254.
22. Busschaert, N.; Bradberry, S. J.; Wenzel, M.; Haynes, C. J. E.; Hiscock, J. R.; Kirby, I. L.; Karagiannidis, L. E.; Moore, S. J.; Wells, N. J.; Herniman, J.; Langley, G. J.; Horton, P. N.; Light, M. E.; Marques, I.; Costa, P. J.; Felix, V.; Frey, J. G.; Gale, P. A. *Chem. Sci.* **2013**, *4*, 3036-3045.
23. Busschaert, N.; Kirby, I. L.; Young, S.; Coles, S. J.; Horton, P. N.; Light, M. E.; Gale, P. A. *Angew. Chem., Int. Ed.* **2012**, *51*, 4426-4430.
24. Jakab, G.; Hosseini, A.; Hausmann, H.; Schreiner, P. R. *Synthesis* **2013**, *45*, 1635-1640.
25. Wu, X.; Judd, L. W.; Howe, E. N. W.; Withecombe, A. M.; Soto-Cerrato, V.; Li, H.; Busschaert, N.; Valkenier, H.; Pérez-Tomás, R.; Sheppard, D. N.; Jiang, Y.-B.; Davis, A. P.; Gale, P. A. *Chem* **2016**, *1*, 127-146.

Chapter 5. Conclusion

In this thesis, the author explored the novel functional MOF world by using N-confused porphyrin as an organic ligand, which demonstrates unique properties such as red-shifted absorption and emission. The novel NCP-based MOF was expected to exhibit NIR-absorption thus an efficient NIR responsive photosensitizer with high stability and crystalline structure. Furthermore, by incorporating both NCP and porphyrin into a hybrid MOF through a seed-mediated synthesis, MOFs possessing core/shell structure and high light harvesting ability was designed. In chapter 1, basic knowledge and information related to MOFs are introduced to elucidate the history and development of MOF research. The chemistry of NCP is also introduced by starting with the description of porphyrin and its applications in MOFs.

In chapter 2, the synthesis of novel $\mathbf{NCP_{MOF}}$ is addressed in detail. Strong binding of COO-Zr(IV) was utilized to obtain high thermal and chemical stability. After optimization of the conditions, a crystalline powder was obtained which was confirmed by PXRD and SEM. Through theoretical calculation, it was confirmed that the topology of $\mathbf{NCP_{MOF}}$ is similar to the reported porphyrin-based MOF-525, with a cubic ftw topology. Chemical and thermal stabilities were confirmed by PXRD and TG. Through spectroscopic measurement, the absorption and emission spectra were observed, which are broadened due to the bulky structure of MOFs. Compared with $\mathbf{TPP_{MOF}}$, $\mathbf{NCP_{MOF}}$ showed red-shifted absorption and emission band, which is suitable for applications such as bioimaging or photocatalysis.

In chapter 3, two class II hybrid MOFs with core/shell structure were synthesized based on both TPP and NCP through seed-mediated synthesis. the cubic ftw topology of resulting MOFs was confirmed by PXRD TEM SEM. To confirm the core/shell structure of these hybrid MOFs, both NCP and TPP organic ligands were metalated in the center with Ag(III) and Zn(II) respectively. Then EDX elementary analyses and confocal laser scanning microscopy were utilized to observe the hybrid MOFs constructed with metalated ligands, from which the core/shell structure was observed. The spectroscopic analyses were also conducted to detect energy transfer process between the two ligands, which was then found significant in the photoinduced singlet oxygen generation efficiency.

In addition to the synthesis of MOFs, transmembrane transport selectivity of anions by synthetic transporters was also discussed in the thesis. The correlations between anion binding selectivity and transport selectivity were explored for future selective transporter design. In chapter 1, the basics of transmembrane transport are introduced. Moreover, the various designs of anion transporters are described according to the binding.

In chapter 4, a series of compounds, including squaramide, urea, and thiourea, along with dipodal and tripodal thiourea were tested for their selectivity toward different anions, among which Cl^- and NO_3^- are the most significant due to their application in the anion transport selectivity experiment. The binding constants are calculated through titration. Then the anion transport selectivity was analyzed through two different

assays, which explained that the correlations between the binding and transport. This study will provide more essential perspective for the design of novel transporter molecules.

In the future, MOFs based on NCP metal complexes can also be synthesized using the same strategy, which will provide more flexibility in the design or even new topologies of MOFs. With a NIR-responsiveness, $\mathbf{NCP_{MOF}}$ is considered to be an efficient and stable photosensitizer. Besides, metallic $\mathbf{NCP_{MOF}}$s with high oxidation state metal center is expected to be an active and green heterogeneous catalyst. At last, the result of transmembrane anion transport selectivity provides a theoretical basis for the future selective transporter design, which benefits therapy of disease resulting from disorders of anion diffusion.

List of Publication

1) Yufeng Yang, Ryuichi Sakashita, Kazuhisa Yamasumi, Masatoshi Ishida, Teppei Yamada and Hiroyuki Furuta, *Chem. Lett*. **2017**, *46*, 1230-1232. (Chapter 2)

2) Yufeng Yang, Masatoshi Ishida, Yusuke Yasutake, Susumu Fukatsu, Chihoko Fukakusa, Masa-aki Morikawa, Teippei Yamada, Nobuo Kimizuka and Hiroyuki Furuta, *Manuscript in Preparation*. (Chapter 3)

3) Yufeng Yang, Xin Wu, Nathalie Busschaert, Hiroyuki Furuta, Philip A. Gale, *Chem. Commun*. **2017**, *53*, 9230-9233. (Chapter 4)

References

1) Jiaying Yan, Makoto Takakusaki, Yufeng Yang, Shigeki Mori, Bao Zhang, Yaqing Feng, Masatoshi Ishida and Hiroyuki Furuta, *Chem. Commun*. **2014**, *50*, 14593-14596.

2) Jiaying Yan, Yufeng Yang, Masatoshi Ishida, Shigeki Mori, Bao Zhang, Yaqing Feng, H. Furuta, *Chem. Eur. J*. **2017**, *23*, 11375-11384.

Acknowledgment

First, I would like to express my deep gratitude to my supervisor—Prof. Furuta, who always inspires me to challenge my limit and be a better chemist. In the beginning, Prof. Furuta accepted me as a graduate student and gave me the chance to study in Japan. After that, not only did he give me tons of mentoring and directions on my researches in this thesis and life in Japan but also, he helped me with the application for Kyushu University Leading Program and research fellowship for young scientists of Japan Science Promotion Society (JSPS). He even gave many pieces of advice on my job searching process in Japan. I will always be thankful for what he has taught me.

Secondly, I would like to thank the reviewers of my thesis—Prof. Fujigaya and Prof. Shimakoshi, who kindly reviewed my thesis and gave me precious advice and discussions on my study related to MOFs and nanoparticles.

Then, I would like to give my deep gratitude to Prof. Gale from the University of Sydney. Prof. Gale accepted me as a visiting student at the University of Southampton and gave me the opportunity to study and conduct researches in the UK even when he was busy moving to Sydney. He was also very caring about my progress in the new chemical field that I had had almost no knowledge of. I am thankful for the priceless experience he has given me.

I would also like to thank my advisor—Dr. Ishida, who has been caring for my life in Furuta lab since the first day I came. Dr. Ishida has given me lots of advice on my experiments and taught me many basic pieces of knowledge regarding organic chemistry experiments. He helped me with my application for Kyushu University Leading Program and research fellowship for young scientists of Japan Science Promotion Society (JSPS). He also helped me with my job searching process in Japan. I am beyond grateful for everything he has taught me.

I am very grateful to Prof. Shimizu for having given me advice on my experiments and the kindness of communicating with me.

I would like to thank the people who have helped me with my experiments in this thesis. This includes Dr. Yasutake, Prof. Fukatsu, Ms. Fukakusa, Dr. Morikawa, Prof. Yamada, and Prof. Kimizuka. I am thankful for every second they have spent on my research.

I would like to thank Dr. Miyazaki who helped me with my experiment skills in Furuta lab.

I would also like to express my deep thankfulness to my seniors—Dr. Sakashita, Dr. Yan and Dr. Wu, who have taught me many organic experiment skills and given me the ideas to further conduct my research.

Finally, I am grateful to my fellow labmates for creating and keeping a neat and tidy experiment environment for me to conduct my research.